THE MICROSTRUCTURE OF AMORPHOUS POLYMERS

A Wide Angle X-ray Diffraction Study

by

Andrew Colebrooke

A thesis submitted for the degree of
Doctor of Philosophy in the University of London

Department of Metallurgy and Materials Science,
Royal School of Mines,
Imperial College,
London, S.W.7.

February 1975

To Hazel with love

CONTENTS

CONTENTS

CHAPTER THREE : Experiment Procedure

CHAPTER FOUR : Experiment Results

CHAPTER FIVE : Discussion of the Results

APPENDIX A : A Fortran IV Programme to Generate Radial Distribution Functions

ABSTRACT

Radial distribution functions have been generated from the wide angle X-ray diffraction from atactic polystyrene:

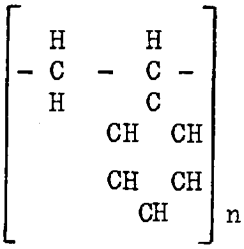

$$\left[\begin{array}{ccccc} & H & & H & \\ - & C & - & C & - \\ & H & & C & \\ & & & CH\quad CH & \\ & & & CH\quad CH & \\ & & & CH & \end{array}\right]_n$$

and from atactic polymethyl methacrylate:

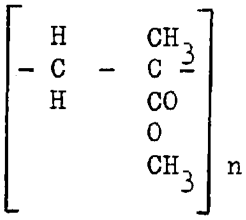

$$\left[\begin{array}{cccc} & H & & CH_3 \\ - & C & - & C\ - \\ & H & & CO \\ & & & O \\ & & & CH_3 \end{array}\right]_n$$

The functions were extremely sensitive to systematic normalisation errors in the region $r < 3$Å whilst in the region $r > 3$Å they were relatively free of such errors. Preferred molecular orientation was induced in these polymers so that strong equatorial and meridional arcing of the diffraction pattern was obtained. Intramolecular scattering effects are shown to predominate in both orientated polymers although pronounced intermolecular scattering was detected. Possible molecular conformations and packing arrangements are discussed for atactic polystyrene whilst the effects of annealing below T_g and the swelling of polymethyl methacrylate are explained in terms of changes in intra- and inter-molecular ordering.

ACKNOWLEDGEMENTS

I am indebted to Dr. A.H. Windle for his help and guidance throughout this project. Thanks are due also to Professor J.G. Ball, for the use of research facilities, and to the laboratory staff, in particular Mr. L. Walden and Mr. F. Huggins, for their assistance. Finally I would like to thank the staffs of the departmental photographic section and Imperial College Computer Centre for their help and co-operation.

This project was financed by the Science Research Council and Imperial College.

CHAPTER ONE

A Survey of the Literature Dealing with the Morphology of the Amorphous State of Synthetic Polymers

1.1 Introduction

The kinetic theory of high elasticity which was developed in the early 1930's has been successful in quantitatively explaining rubber elasticity and the properties of dilute polymer solutions[1]. In particular the Flory-Bueche's statistical random coil model has predicted the mean-square end-to-end distance and radius of gyration of polymer chains in dilute solutions. In the condensed state, linear amorphous polymer molecules are assumed to display the same "unperturbed" conformational properties as isolated macromolecules in an ideal solvent[2-4]. The success of this model has fostered the view that bulk amorphous polymers are totally disordered systems consisting of deeply entangled molecular coils possessing large amounts of free volume.

This model does however suffer from some considerable drawbacks. It assumes that the distribution of chain segments about the centre of mass of an isolated molecule is Gaussian in nature and predicts that the segmental density at any point decreases as the length of the molecule increases. Since the specific density of a polymer is not seen to decrease with increasing molecular weight and since there is no evidence of significant density modulations, the number of intermolecular segmental interpenetrations (i.e. entanglements) per unit volume must increase with increasing chain length. To overcome the forces involved in entanglements, energy must be invested when untangling the molecules. Thus if the entanglement density is a function of the chain length, the heat of mixing of the polymer with a solvent should be also. This is not observed experimentally.

Secondly Fox et al.[5,6] have shown that the maximum Newtonian melt viscosity η depends on the polymer molecular weight M in the following manner

$$\eta = \begin{cases} K_1 M & \text{for} \quad M < M_c \\ K_2 M^{3.4} & \text{for} \quad M > M_c \end{cases}$$

where K_1 and K_2 are constants and M_c is a "critical" value of M. The visco-elastic maximum relaxation time also has this molecular weight dependence. Neither phenomenon can be satisfactorily explained by the model.

The concept of entanglements is subject to objections on the grounds of polymer crystallisation. Polarised light studies[7] of the crystallisation of natural rubber and polybutadiene have been reported in which samples were repeatedly melted and recrystallised. If the melting temperature was not too high, the same spherulitic patterns were completely and precisely reproduced. From pure geometrical considerations this would imply that deep entanglement is unlikely.

It is known that polymers crystallise from the melt in lamellar structures in which the molecular chains are more or less perpendicular to the flat surfaces. The chains fold on these surfaces and re-enter the lamellae either adjacent to or close to their points of exit. The time periods involved in the crystallisation process are thought to be much shorter than the maximum relaxation times of the polymers in question[8]. How therefore can a polymer crystallise each molecule separately onto the growing lamellae over time periods shorter than it takes the same polymer to untangle itself?

In the light of such arguments the validity of the random coil as an accurate picture of the amorphous states of crystallisable polymers at least has been seriously questioned. The possibility that non-crystalline polymers such as unstretched natural rubber and amorphous polystyrene contain some form of ordered elements has been suggested on and off since the 1920's. This view originated from X-ray and electron diffraction studies of organic liquids and their polymers, and has been supported by work on magnetic susceptibility[9], differential thermal analysis[10], crystallisation kinetics[11], calorimetry[12], density[13] and dark-field diffraction microscopy[14].

To date no really conclusive demonstration of short range ordering in glassy polymers has been made. However, several structure models which assume various degrees of chain ordering have been proposed and these are discussed in this chapter. A full review of the literature on WAXD and SAXD regarding amorphous studies is given in later sections. We now consider some electron microscopy experiments which have probably been the most spectacular and controversial of the studies of the morphologies of polymer glasses.

1.2 Electron Microscope Studies of Amorphous Polymer Films

Recent electron microscope studies have created considerable excitement because of the appearance of tiny structures on the surfaces of thin polymer films. In the mid 1950's several Russian workers, notably Kargin[15-18], reported seeing structures from a few hundred Angstroms to several microns in size on solution cast films. These studies led Kargin to propose that amorphous polymers contain quite ordered elements which he envisaged as being bundles or packets of molecular chain segments orientated more or less parallel to one another. Studies of fluorinated rubbers cast from solution showed very clear 1000Å diameter particles irrespective of the solvent used[17]. Kargin calculated that these particles probably contained up to a thousand molecular chains. Unfortunately many of the published micrographs of this period as well as some of the specimen preparation techniques were somewhat controversial.

Schoon et al.[19] have observed small spherical particles 30-55Å in diameter on the surface of a number of amorphous films including natural rubber and a copolymer of butadiene and acrylonitrile. They also reported seeing larger structures of the order of hundreds of Angstroms in size on films of the non-crystallisable polymers atactic polystyrene and atactic polymethyl methacrylate[20,21]. Again these micrographs were considered by many to be unreliable since they were obtained by an iridium replication technique, the resolution of which is comparable to the particle size reported.

In 1967 Yeh and Geil[22,23] published their now famous papers on the crystallisation of polyethylene terephthalate (PET) in which they reported seeing ball-like structures or "nodules" 45-100Å in size on the surfaces of films cast from solution and quenched from the melt. When the PET films were annealed just below the glass transition temperature, T_g, the nodules were reported to aggregate in small clusters. Depending upon the annealing temperature, time and film thickness, large structures suggesting the initial growth stages of spherulites were formed and the $(\bar{1}11)$ and (011) reflections appeared. Several other crystallisable polymers including bisphenol-A polycarbonate[24-26] and isotactic polystyrene[14] have now been reported as possessing similar nodular structures which appear to be the first stages of the spherulite crystal growth pattern. Yeh and Geil tentatively proposed that the glassy state of crystallisable polymers at least should be likened to the Fringed Micelle Model of crystalline polymers; the crystallites would be replaced by the nodules, which were suggested to possess some kind of paracrystalline order (possibly of the kind proposed by Hosemann[27]).

Strain-induced crystallisation studies of PET[23] showed that after stretching the nodules were more or less aligned in short rows of 2-5 nodules at approximately 50° to the stretch direction (at this stage the electron diffraction pattern was that of a highly orientated fibre). If the drawing was performed at an elevated temperature (260°C) the angle of inclination of the rows to the stretch direction was increased to 90°. Yeh and Geil argued that the alignment was achieved by nodule rotation so that the partially ordered chain segments within each nodule became aligned parallel to the draw direction.

Further studies of the deformation behaviour of PET films were performed by Klement and Geil[28] in which they investigated both uniaxial and biaxial stretching. The uniaxial stretching showed similar effects to those described above while the biaxially drawn films showed no evidence of row alignment. Occasionally large clusters of nodules were seen (250-300Å in diameter) similar to those reported for annealed PET which they christened "supernodules". Gold decoration experiments suggested that these structures were several nodules tied together by internodular links which upon drawing rotated the nodules parallel to the draw direction.

Yeh[29] has proposed a detailed two-phase model based on his morphological studies of various amorphous polymers called the Folded-Chain Fringed Micellar Grain Model (Fig.1.1). It consists of two major elements: the grain (G) and the region between the grains or the intergrain region (IG). The grain is subdivided into an ordered domain (OD) about 20 to 40Å in diameter and a grain boundary (GB). Within each ordered domain the chain segments are more or less parallel to one another with nearly constant spacings (so that the order is regarded to be better than nematic). The degree of order may vary with each grain and from one polymer to another depending upon thermal history, chemical structure, etc. The grain boundaries are considered to be about 10 to 20Å thick and contain mostly folds, a few chain ends and some entanglements. The intergrain regions vary from 10 to 50Å in size and consist of more randomly packed molecules, including low molecular weight molecules and portions of molecules going from grain to grain (internodular links). Yeh has argued that several physical phenomena such as viscous behaviour and lamella formation are consistent with this two-phase model.

Interesting as these e.m. studies are, they have on their own, so far failed to convince the majority of scientists of the existence of chain ordering in the amorphous state. Part of the problem lies in the difficulty of the technique itself: limiting resolution, specimen contamination, beam damage, etc. In particular these experiments have failed to give us information about the details of the proposed structures, since they refer to their outline only. Dark-field diffraction microscopy is now being used to help in this aspect[14]. Polymer chemists have been particularly reticent about chain ordering. Ciferri, Hoeve and Flory[3] in their paper on stress-temperature coefficients and conformational energies of polymer chains state that: "These results are at variance with the often postulated pseudo ordering of chains in molten polymers such as polyethylene. The molecular shape of the polyethylene dilutent must surely be quite incompatible with any conceivable ordered arrangement of chains of this polymer".

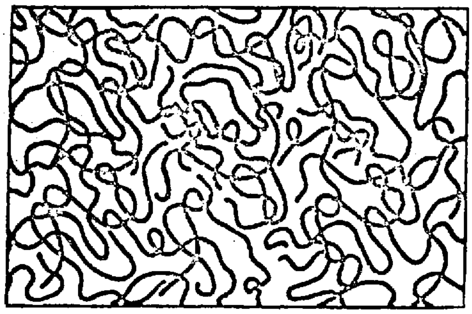

Fig. 1. 1a Schematic representation of the random-coil model.

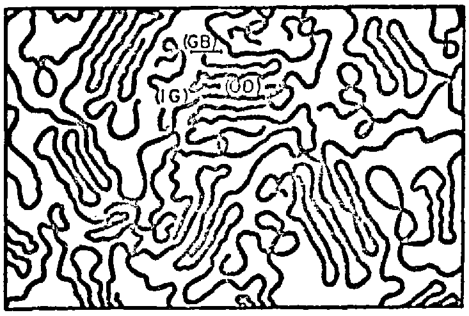

Fig. 1. 1b Schematic representation of the folded-chain fringed micellar grain model showing the ordered domain (OD), the grain boundary layer (GB), and the intergrain region (IG). (Yeh[29]).

1.3 The Density of Amorphous Polymers : Robertson's Model

Table 1.1 lists the densities of several common synthetic polymers in both their amorphous and crystalline states. Robertson[30] has argued that the relatively high densities of the amorphous polymers demands a fairly large amount of ordering to occur within them. Using a simple model consisting of strings of cylindrical beads, he attempted to develop a means of assessing the order in an amorphous polymer from its density.

Polymer	d_c	d_a	d_a/d_c	$\theta^*(l=d)$
Polyethylene	1.00	0.855	0.855	15.0°
Polypropylene	0.937	0.854	0.911	8.4
Polystyrene (isotactic)	1.111	1.054	0.947	4.8
Polyvinyl alcohol	1.345	1.269	0.943	5.2
Polyethylene terephthalate	1.455	1.335	0.917	7.8
Bisphenol-A polycarbonate	1.30	1.20	0.92	7.5
Nylon 66	1.220	1.069	0.876	12.4

Table 1.1 A comparison of the amorphous and crystalline densities d_a and d_c of several synthetic polymers[30].

These cylindrical beads of length l and diameter d are assumed to be jammed together with each bead touching its neighbour's but not necessarily parallel to them. The angle between two neighbouring beads is considered to be randomly distributed between 0° and some cut off angle θ^* (Fig.1.2). Robertson estimated that for chains which tend to pack in a planar zigzag fashion, the ratio of the densities of the amorphous and crystalline states is given by

$$\frac{d_a}{d_c} = \left(\frac{3}{2}\right)^2 \left\{ \left[\frac{1 - \cos^3 \frac{\theta^*}{2}}{\sin^3 \frac{\theta^*}{2}} + \frac{l}{d} \right]^2 \left(1 - \cos^3 \frac{\theta^*}{2}\right) \right\}^{-1}$$

where d_a and d_c are the densities of the amorphous and crystalline phases.

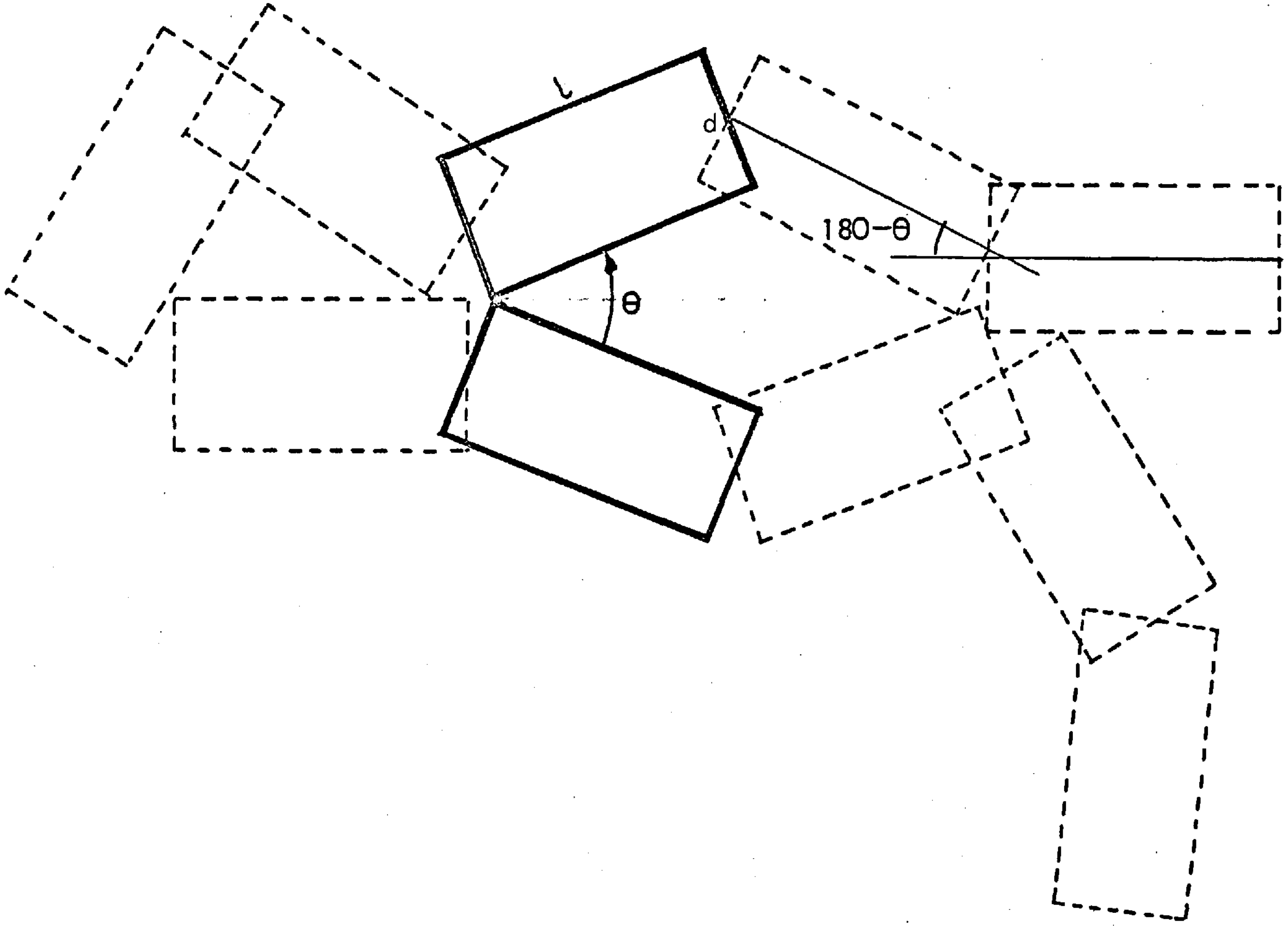

Fig.1.2 Robertson's model for calculating the densities of amorphous polymers.[30]

If the polymer chains tend to pack in helices, the ratio is

$$\frac{d_a}{d_c} = \left(\frac{3}{2}\right)^2 \left\{ \left[\frac{1 - \cos^3 \frac{\theta^*}{2}}{\sin^3 \frac{\theta^*}{2}} + \frac{l}{d} \right]^2 \sin^2 \frac{\theta^*}{2} \right\}^{-1}$$

By lifting the restriction on θ , we have that in the case of the amorphous state being that of a random coil:

$$\frac{d_a}{d_c} = 0.652 \qquad (\text{using } l = d)$$

This is much smaller than the ratio for real polymers (Table 1.1). Using the reasonable assumption that $l = d$, Robertson computed the value of the "order parameter" θ^* for each polymer from the known d_a/d_c values (Table 1.1). The small values of θ^* obtained indicated that a fairly high degree of order exists in the amorphous state. If the root-mean-squared end-to-end distance is calculated for polyethylene assuming $\theta^* = 15^\circ$ and $l = 2.51$Å, a value fifteen times larger than that found by intrinsic viscosity measurement is obtained[31]. To overcome this difficulty Robertson proposed that there is a certain small probability that the chain will fold back on itself as in crystal lamellae so that at each junction the next bead can be within a cone either 0° to θ^* or $(180^\circ - \theta^*)$ to 180°. The root-mean-squared distance calculated using this assumption is reduced to about one quarter of that of the viscosity measurement, without affecting the density.

Thus this model goes a long way in simultaneously meeting the requirements of both chemists interested in chain statistics and morphologists interested in short range ordering. The order postulated here is strictly one dimensional in nature. The polymer chains tend to lie parallel to one another but there is no particular correlation between neighbouring chains about their axes or along their length.

1.4 Recent Models of the Amorphous State of Polymers

Numerous new models for the amorphous state of linear polymers and polymer melts have been suggested within the last year which assume some degree of chain folding. Pechhold and Blasenbury[32] have described a "Meander model" in which supermolecular structures are composed of tightly folded separate bundles of nearly straight chains. An increasing concentration of kink defects is introduced into these otherwise aligned chains until their overall properties approach that of a melt. These supermolecular structures have been shown to be thermodynamically stable. Using this model they have shown that the Gibbs free energy, the geometry and the radius of gyration of the folded molecules depend only on molecular parameters such as the interchain distance, the length of a kink segment and the energy of a fold.

Privalko and Lipatov[33] have suggested that the sharp change in the molecular weight dependence of the Newtonian viscosity of polymer melts at M_c as described in section 1.1, can be explained by the onset of "kinetic" chain folding as the molecules make the transition between a chain-extended conformation to a statistically chain-folded conformation. This suggestion has been supported by recent magnetic susceptibility measurements[9]. A sketchmatic representation of the Privalko-Lipatov model is shown in Fig. 1.3. All chain conformations above the polymer melting point are assumed to be essentially unperturbed (as in the Flory-Bueche's random coil). The mean-squared end-to-end distance is therefore given by

$$\langle h^2 \rangle = Nb^2 \sigma^2$$

where N is the number of main chain bonds, b the length of each single bond and σ the steric factor (a measure of the hindrance to internal rotation). The molecules are assumed to have chain folded conformations, so that the mean value of $\langle h \rangle$ is approximately

$$\langle \bar{h} \rangle = naA$$

where a is the chain thickness (a^2 = the cross-sectional area of a chain, end on), n-1 is the number of folds in the chain folded entity with a given

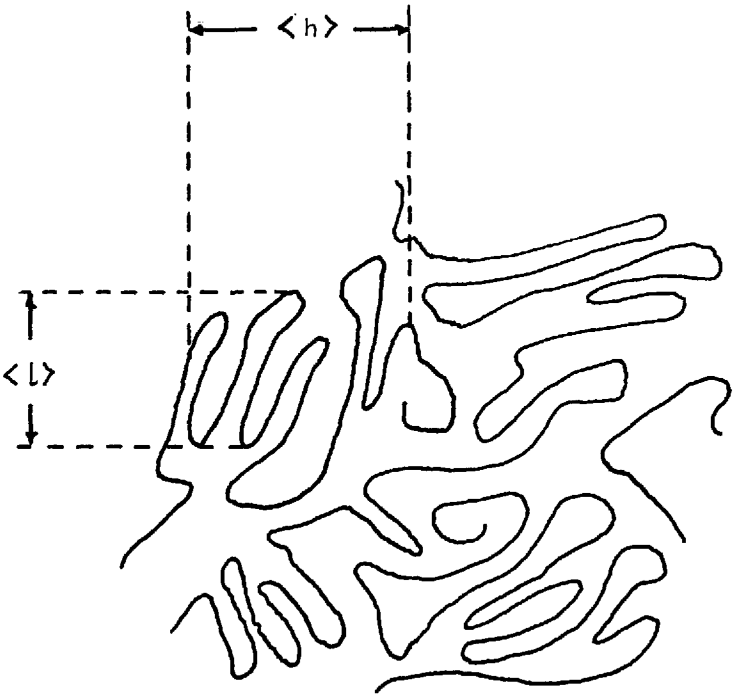

Fig.1.3 Privalko-Lipatov model for the polymer amorphous state.[33]

fold length $\langle l \rangle$ and A is a numerical constant. These equations are correct only on the condition that the randomly folded molecules display the conformational properties of unperturbed random coils. This is imagined by assuming that both the size and the location of the regions of short range order depend upon the temperature and the time of observation. That is, the instantaneous structure of the polymer corresponds to one of many possible randomly folded chain conformations. When the time of observation is sufficiently long as for example an equilibrium stress-strain experiment or an experiment to measure solvent diffusion, the experiment "sees" a time average of chain conformations which behaves like an unperturbed random coil. By borrowing a term from statistical mechanics we can say that the experiment measures the ensemble average of a large number of thermodynamically-identical folded chain conformations.

Thus to date the following models of the polymer amorphous state have been proposed:

Flory-Bueche's statistical random coil.
Robertson's bead model.
Yeh's two-phase, nodule model.
Pechold and Blasenbury's meander model.
Privalko and Lipatov's ensemble of randomly folded chains.

all of which can find experimental evidence to support them.

Since it is not really surprising that ordered elements have been reported in the amorphous states of crystallisable polymers, interest in the fundamental questions concerning the polymer amorphous state is now centred on the non-crystallisable polymers such as polymethyl methacrylate and atactic polystyrene.

After brief descriptions of recent small-angle X-ray diffraction and wide-angle light scattering studies the final sections of this chapter deal in detail with the literature concerning wide-angle X-ray and electron diffraction studies of amorphous polymers.

1.5 Small-Angle X-Ray Diffraction (SAXD) Experiments

Some of the scepticism about the reports of nodule structure has arisen because electron microscopy deals only with thin films or surface replicas. It may be that nodules are peculiar to free surfaces where the molecular chains may be free from certain conformational constraints. To assert that nodules are also typical of the bulk material, confirmation must be sought from other techniques. Since nodules presumably have higher electron densities than their surroundings, SAXD which is sensitive to local electron density fluctuations $\Delta\rho$, is an obvious tool for investigating the bulk properties.

Harget and Seigmann[34] have reported SAXD studies of amorphous PET and have shown them to be consistent with the nodule structure seen by Carr, Geil and Baer[24]. Intensities were recorded over the 2θ range 17min. to 4° for CuKα radiation, corresponding to Bragg spacing of 300Å to 22Å. Unfortunately they used the Guinier's law approximation for single particle scattering (which is valid only for very small angles and very dilute systems) to calculate the radius of gyration of the scatterers. Their data was at all points, above the angles for which Guinier's law should hold and the nodules observed by electron microscopy can hardly be considered dilute. However they showed that the SAXD observed was slightly dependent upon the thermal history of the specimens, i.e. the annealing time below Tg or the quench rate from the melt.

Lin and Kramer[35] have reported that the SAXD from amorphous polycarbonate exhibited a sharp rise in intensity at ultrasmall angles ($2\theta < 0.08^{\circ}$ for CuK radiation). At much higher angles the SAXD was superimposed on a diffuse halo centred at an angle corresponding to a spacing of 10Å. Since SAXD depends only on the electron density difference $\Delta\rho$, microvoids as well as local density fluctuations within the sample could cause the detected intensity. By doping the specimen with small amounts of iodine (1.3%), a reversible uniform decrease in the SAXD intensity was observed, corresponding to a decrease in $\Delta\rho$. Lin and Kramer argued that if microvoids were responsible for the SAXD, the addition of such small quantities of I_2 could only increase $\Delta\rho$ and therefore the scattered intensity. They accordingly ruled out the possibility that microvoids are the primary scattering centres. From absolute intensity measurements the minimum relative density fluctuation between nodules and their surroundings was estimated to be 1.6% with an upper limit of 1.8% (from fcc close packing of nodules). This would suggest that the Yeh model which assumes an almost crystalline density for the nodules and predicts a relative density fluctuation of 21% is much too extreme.

Since these experiments were performed it has been shown that the SAXD observed from polymers is very sensitive to impurities within the samples. Kirste[36] has reported that studies on purified polymers has shown that the bulk of the SAXD observed from commercial grade samples is due to additives such as inhibitors and plastiziers.

1.6 Birefringence and Light Scattering Experiments

In anisotropic media, light generally has two refracted paths and the media are said to be doubly refracting or birefringent. Changes in birefringence may sometimes be used as a measure of the orientation processes within molecules or of strain at various bonds. Strain birefringence measurements have shown that the optical anisotropies due to strained or swollen polymers were much smaller than those on the unswollen polymers. Nagai[37], Gent and Vickroy[38] attribute this reduction in optical stress coefficient to the disappearance of short-range segmental order of swelling. Yeh[39] interpreted these results in terms of the disappearance of short-range interactions between one ordered region and another when the polymer was swollen.

Addleman[40] has shown that inhomogeneities exist within pure polymethyl methacrylate. Pure methyl methacrylate monomer was polymerised in sunlight while its structure was continuously monitored using wide-angle light scattering. Three parameters were measured throughout the experiment:

1. The Rayleigh ratio (scattering cross-section per unit volume) of the light scattered through 90^o with its electric vector parallel to that of the incident radiation (R_{90}).

2. The depolarisation ratio ρ_{90} : the ratio of the intensities of light scattered through 90° with electric vectors perpendicular and parallel to that of the incident radiation.

3. The dissymmetry Z_{60} : the ratio of the intensity of light scattered through 60° to that scattered through 120° (the electric vector of the scattered beam parallel to that of the incident beam).

Fig.1.4 shows how these parameters varied with time together with the percentage polymerisation. For a given size of discrete inhomogeneity R_{90} is proportional to the product of the number of inhomogeneities per unit volume, and the square of the refractive index difference between the inhomogeneity and the matrix. It is also a function of the size and distribution of the heterogeneities. Z_{60} is directly related to the size of inhomogeneities (the larger the value of Z_{60} the larger the inhomogeneity). ρ_{90} is for small-scale inhomogeneities a measure of the isotropy of the scattering entities. It takes the value of zero for a perfectly isotropic scattering entity and gets numerically larger with increasing anistropy until the limiting value of unity is reached.

Fig.1.4 shows that after an induction period of several days the scattering was typical of that found for high molecular weight polymers in dilute solution. After this Z_{60} decreased monotonically whereas R_{90} increased to a peak value and then decreased. This behaviour indicated that the polymer molecules pervaded the entire volume of the solution and no longer scattered as separate entities. At this stage less than 1% polymer was present (this is consistent with random-chain statistics[41]). With further polymerisation (up to 15% polymer) R_{90} continued to decrease as did Z_{60} indicating that either the molecules became compressed to very small sizes or were completely interpenetrating so that the mixture exhibited only small scale refractive index discontinuities. After this both R_{90} and Z_{60} increased until the system was solid. From the final scattered intensity distribution a value of ~500Å was obtained for the correlation distance (a measure of the size of the scattering heterogeneities).

Addleman has proposed a differential contraction model for amorphous polymers in which inherent density heterogeneities are assumed to correspond

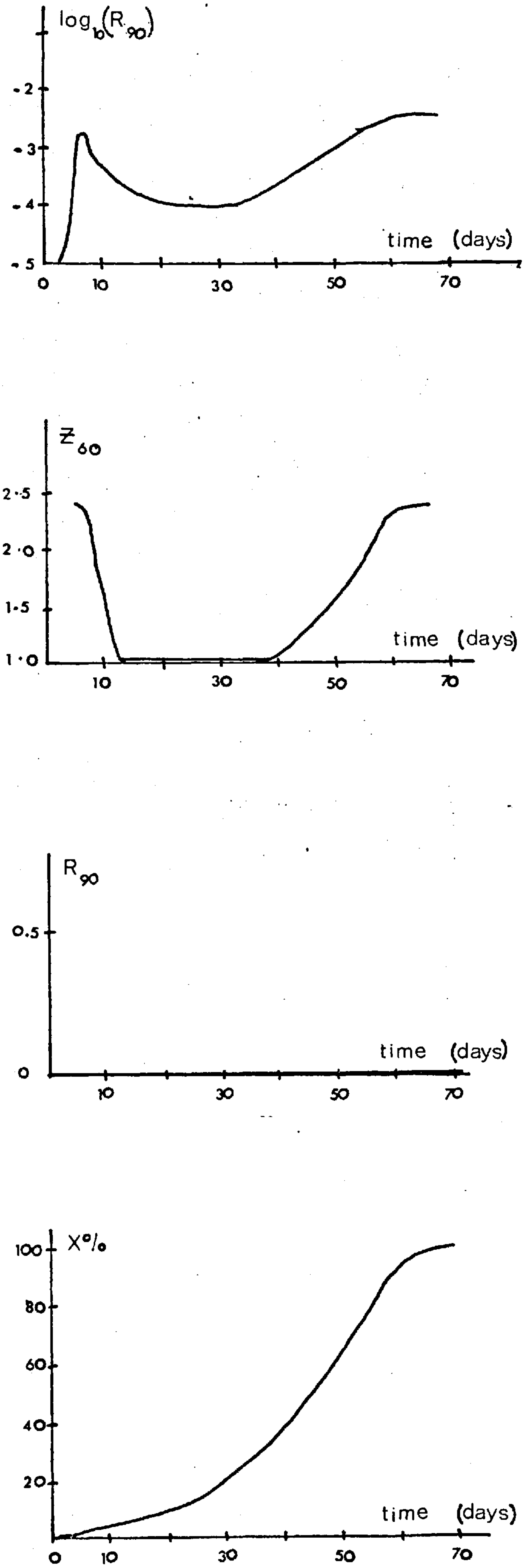

Fig.1.4 Light scattering from methyl methacrylate during polymerisation at 20°C.

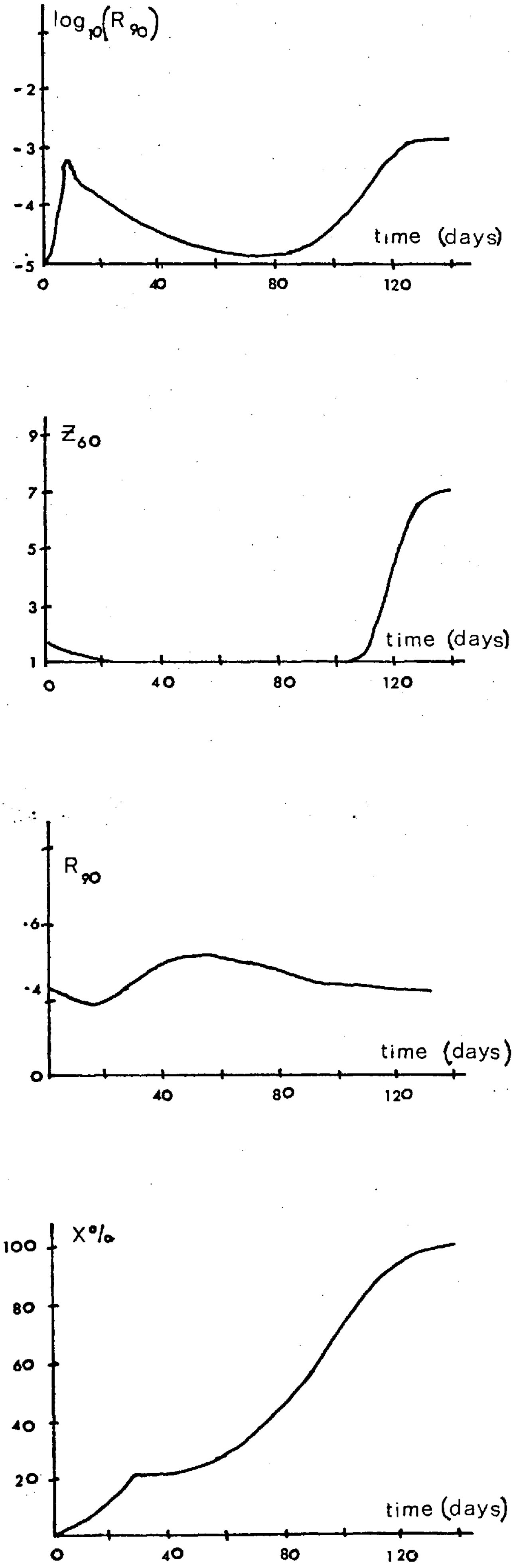

Fig.1.5 Light scattering from styrene during polymerisation at 40°C (Addleman[40]).

to mechanical heterogeneities within the material (i.e. relatively low density regions also have low modulus). During the required volume change on polymerisation high internal stresses would be generated. If internal equilibrium is maintained the low density (low modulus) regions would expand by more than the higher density regions, increasing the density difference between the high and low density regions and hence the intensity of light scattered.

Fig.1.5 shows the results of an identical experiment on the polymerisation of styrene. The general scattering behaviour was similar to that during the polymerisation of methyl methacrylate with two major exceptions:

1. The final scattering was very much lower in intensity than that from the polymethyl methacrylate. This is consistent with the model since it predicts that the final scattering will depend upon the contraction during polymerisation (the contraction of styrene being about 60% that of methyl methacrylate).

2. The depolarisation of the scattered radiation which was absent in the polymethyl methacrylate, remained in the polystyrene.

1.7 Wide-Angle X-Ray and Electron Diffraction Experiments

The first extensive study of the wide-angle X-ray diffraction (WAXD) from rubbers and polymer glasses was made in 1925 by J.R. Katz[42,43]. In a paper published in 1927 he stated that in a number of cases the polymer diffraction pattern exhibited one more ring than the corresponding unpolymerised liquid. For example, liquid styrene had just one diffuse diffraction halo corresponding to a Bragg spacing of ~4.8Å, while polystyrene had two: one at ~4.8Å and a smaller one at ~10Å. This extra diffraction halo was termed the "polymerisation ring". Upon stretching the polystyrene samples the extra ring was seen to split into two broad equatorial maxima. Katz therefore concluded that the polymerisation ring in polystyrene arose from interferences between neighbouring main chain segments which were aligned roughly parallel an average distance of 10Å apart. However the absence of sharp Bragg reflections suggested that this alignment was far from perfect.

In 1943 G.D. Coumoulos[44] investigated the electron diffraction from a series of amorphous polymers (Table 1.2) and found that the diffraction halos he obtained were characteristic of the polymer side chains.

Polymer	d-spacings of halos in Å				
	A	B	C	D	E
methyl methacrylate	1.2	2.2	2.8	-	6.6
ethyl methacrylate	1.2	2.2	2.8	4.6	7.5
n-butyl methacrylate	1.2	2.2	2.8	4.8	9.0
β-ethoxy-ethyl methacrylate	1.2	2.2	2.8	4.8	9.5
methyl acrylate	1.2	2.2	-	4.1	6.5
ethyl acrylate	1.2	2.2	-	4.3	8.0
polyvinyl acetate	1.2	2.2	-	4.0	7.0

Intensities of halos as D > E > B > A > C

Table 1.2 Electron diffraction data from selected amorphous polymers[44].

The two outer halos (A and B) are common to all the polymers considered while the dimensions of the two inner ones (D and E) vary from polymer to polymer. The polymers in the methacrylate series are distinguished by an extra ring (C) at a d-spacing of 2.8Å. Halos A and B correspond to d-spacings of 1.2Å and 2.2Å respectively and appear in the diffraction patterns of all long chain organic molecules. They were first reported by Stewart[45] in 1928 in connection with X-ray scattering from liquid n-paraffins and have been attributed to the spacings between carbon atoms chemically bonded to nearest neighbours (1.54Å) and to second nearest neighbours (2.5Å) in a polymer chain. Halo C appeared only in the methacrylate polymers of Table 1.2 and was always of weak intensity. Since it only appeared when a hydrogen atom in the main chain was replaced in each unit by a methyl group it was suggested that this represents the mean distance between methyl groups along the main chain. The two remaining halos D and E were suggested as being inter-molecular in nature on the grounds of the following observations:

1. A "sharpening" of the D ring occurred when the specimens were orientated by stretching.

2. The Bragg spacings for the E rings corresponded to the calculated size of each side chain.

Coumoulos proposed that the E ring corresponds to the distance of closest mutual approach of two main chains when they are separated by a single side chain. He concluded that scattering by side chains is responsible for the characteristic halos and that the polymer molecules would have to be grouped into clusters with their chains lying roughly parallel in an otherwise random system.

In 1953 Krimm[46] investigated the WAXD from glassy polystyrene and observed two broad halos at d-spacings of 8.84Å and 4.67Å. At room temperature the 4.67Å ring was approximately twice as intense as the 8.84Å ring. Orientation of the sample by drawing produced a concentration of scattering at the equator for the 8.84Å ring and a concentration of scattering at the meridian for the 4.67Å ring. When the WAXD from unorientated polystyrene was measured as a function of temperature the Bragg spacings and the relative intensities of the halos changed as the temperature was increased (Table 1.3).

Temperature °C	Relative intensities $I_{4.67}/I_{8.84}$	Bragg spacing Å	
26	2.0	8.84	4.67
70	2.0	8.84	4.67
90	2.0	8.84	4.67
135	1.5	8.84	4.67
170	1.4	9.03	4.77
200	1.35	9.50	4.92

Table 1.3 The effect of temperature on the WAXD from glassy polystyrene[46].

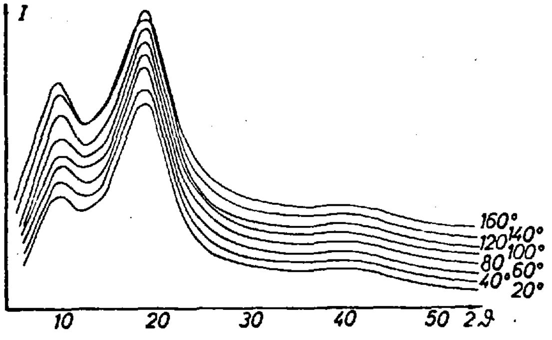

Fig.1.6 The WAXD from amorphous atactic polystyrene as a function of temperature (Kilian and Boueke[51]). The curves have been arbitrarily displaced.

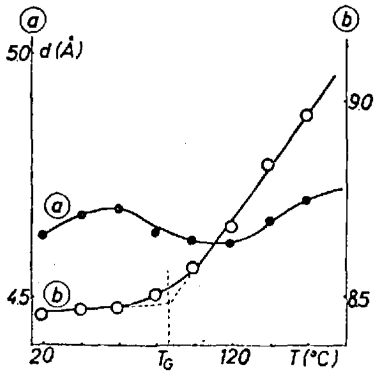

Fig.1.7 The variation in Bragg spacings of the first two halos of atactic polystyrene with temperature: (a) the most intense; (b) the second most intense. (Kilian and Boueke[51]). This is strong evidence that (a) arises from intramolecular interferences while (b) arises from intermolecular interferences.

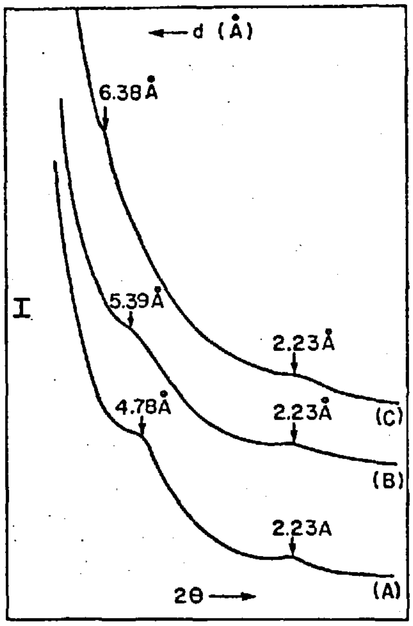

Fig.1.8a Examples of densitometer tracings obtained from electron diffraction patterns of an atactic polystyrene (mol.wt.1,800,000) upon successive increase of exposure to electron irradiation or degree of cross-linking. Curve (A) 60; (B) 120; and (C) 240 seconds exposure to 80-kV electrons at a low beam intensity. Each curve is displaced arbitrarily upward for clarity. (Yeh[14]).

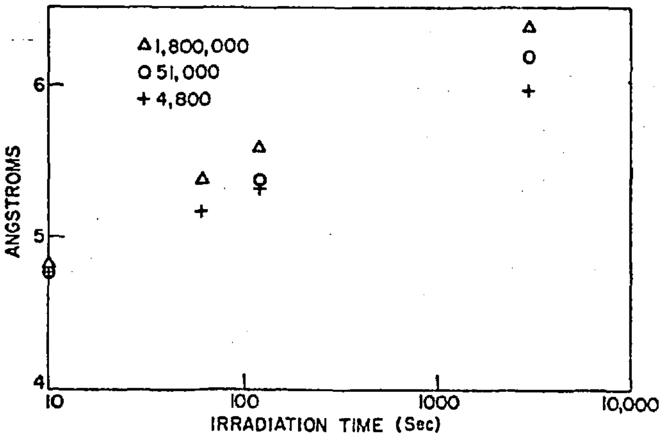

Fig.1.8b Increase in d-spacing of the 4.78Å ring as a function of degree of cross-linking or irradiation time of exposure to 80-kV electrons at a low beam intensity for various molecular weight atactic polystyrenes. (Yeh[14]).

Kilian and Boueke[51] have also measured the WAXD from amorphous polystyrene as a function of temperature over the range 20°–160°C (Fig.1.6). The Bragg spacing of the strongest peak ($\sim$4.6Å) was found to be approximately constant with temperature while that of the weaker peak rose rapidly as the temperature exceeded the glass transition temperature T_g (Fig.1.7). Thus it was concluded that the halo at $\sim$8.8Å was due entirely to intermolecular interferences while the one at $\sim$4.6Å was probably almost all due to intramolecular effects.

More recently Yeh[14] has reported the results of an electron diffraction study of both atactic and isotactic polystyrene. In both cases he detected four diffuse rings at Bragg spacings of 9Å, 4.78Å, 2.23Å and 1.26Å. Neither the tacticity nor the molecular weight appeared to cause any difference to the electron diffraction pattern. By irradiating samples with 80KV electrons he was able to cross-link the sample and induce a detectable change in the pattern. In all samples the major change observed was an irreversible shift in the position of the 4.78Å ring (4.78→6.38Å) i.e. a pronounced increase in the d-spacing as the amount of cross-linking increased (Fig.1.8). Evidence for a slight broadening of this ring and a decrease in its intensity was also found. No detectable change was observed in either the 2.23Å or the 1.26Å ring. Due to experimental difficulties the 9Å ring was not monitored.

1.8 Radial Distribution Analysis of the WAXD

In section 1.7 we have seen that most of the early X-ray studies of amorphous polymers were concerned with the size of the diffraction halos and their possible interpretation in terms of intra- and inter-molecular spacings. This led some of the early workers to conclude that polymers in their non-crystalline state probably contain a fair degree of short range order. That these materials might have a definite structure led a few crystallographers to attempt structure determinations by performing a Fourier synthesis on the experimental X-ray intensities. The application of Fourier-synthesis to X-ray data from non-crystalline materials was originally proposed by Zernicke and Prins[47] and their method has been employed in a

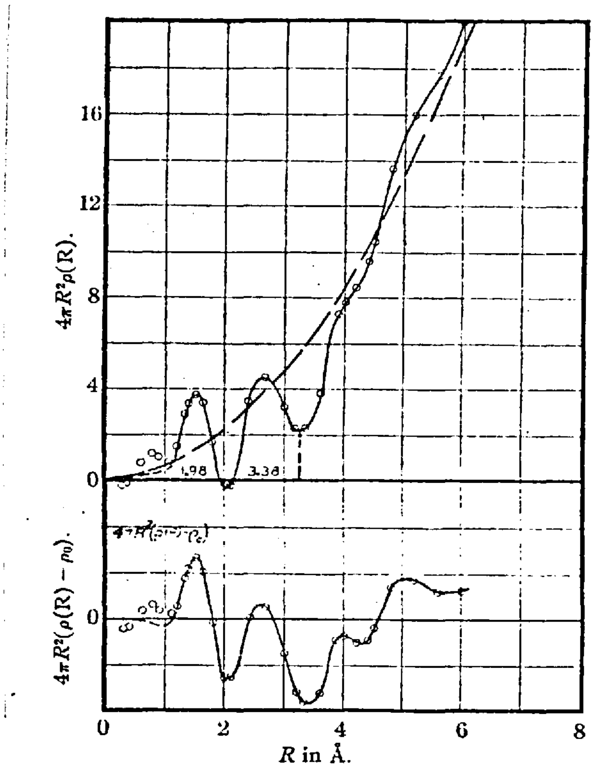

Fig. 1.9 The atomic radial distribution function for natural rubber obtained by Simard and Warren.[48]

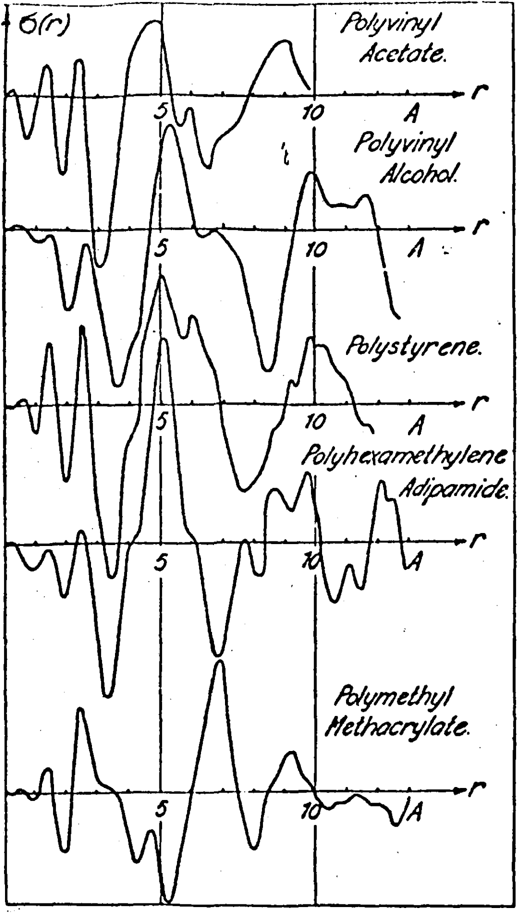

Fig.1.10 Electronic radial distribution functions for several amorphous polymers obtained by Bjornhaug et al.[50]

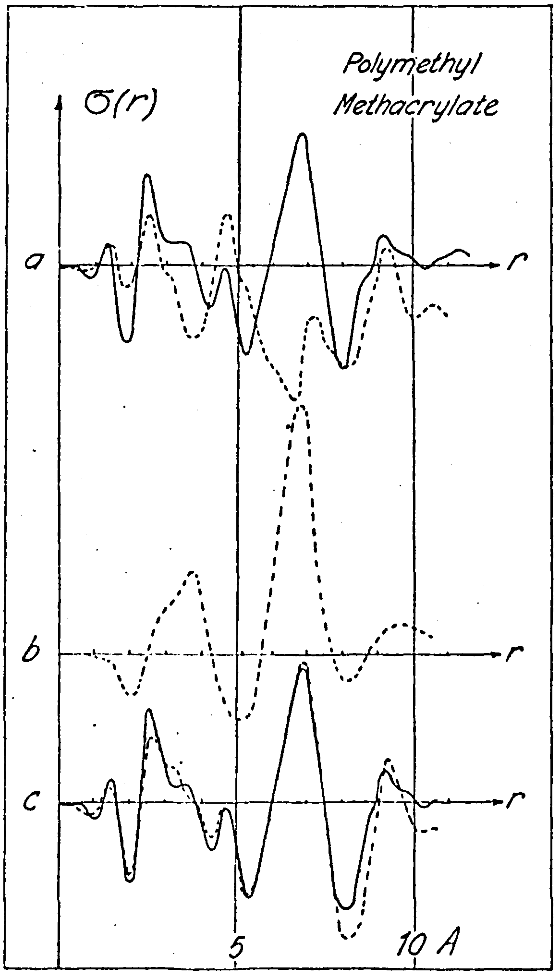

Fig.1.11 (a) Experimental electronic radial distribution function for polymethyl methacrylate (solid line) compared with the theoretical (dotted) curve for an infinite, non-planar zigzag chain. (b) The theoretical curve which was assumed to correspond to inter-molecular distances. (c) Comparison of the experimental curve with a theoretical distribution curve (dotted) which is the sum of the dotted curves in (a) and (b).

somewhat modified form by Simard and Warren[48] in 1936 to obtain the atomic radial distribution function (RDF) of unstretched natural rubber. The RDF will be discussed in detail in the remaining chapters and represents the density of atoms (or electrons) $\rho(r)$ in a spherical shell of thickness dr at a distance r from an "average" reference atom. The RDF has maxima for r values corresponding to distances between greatest densities of atoms or electrons in the system and thus represents the average structure of the sample.

Fig.1.9 shows the RDF obtained by Simard and Warren for natural rubber. The four peaks in the RDF out to 6Å were explained in terms of the individual hydrogen chains in rubber without the need for considering the conformation or relative orientation of the chains.

In 1954 Bjornhaug, Ellefsen and Tonneson[50] published several electronic radial distribution functions from atactic polymers including polyvinyl acetate, polystyrene, polymethyl methacrylate and polyvinyl alcohol obtained from photo-metric measurements of X-ray films (Fig.1.10). Their analysis showed peaks at 1.5Å and 2.5Å as expected. In the case of polymethyl methacrylate, the experimental distribution was compared with a theoretical distribution curve calculated from atomic distances obtained from a molecular model building set. Fig.1.11a shows the experimental RDF (solid line) compared with a theoretical RDF (dotted line) which corresponds to an infinite non-planar zigzag chain having a repetition period of 4.7Å. The very distinct differences between the two curves of Fig.1.11a were assumed by the authors to be due to the contribution from distances between molecular chains. Fig.1.11b shows the difference of the two curves, assumed to correspond to inter-molecular distances.

Kilian and Boueke[51] have examined the scattering from glassy polystyrene at several temperatures and showed that the RDF's obtained were similar to those expected for model compounds as diverse as phenolphthalein and poly(meta-methylstyrene) (Fig.1.12 and Fig.1.13). This comparison indicated the importance of steric effects involving the bulky phenyl substituents on the macromolecules in determining chain conformation in the non-crystalline state. They showed that intra-molecular effects dominate the diffraction of polystyrene.

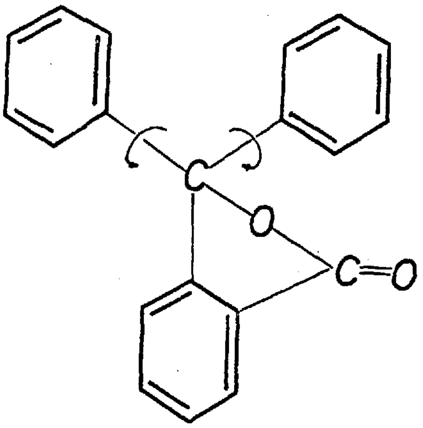

Schematic representation of Phenolphthalein.

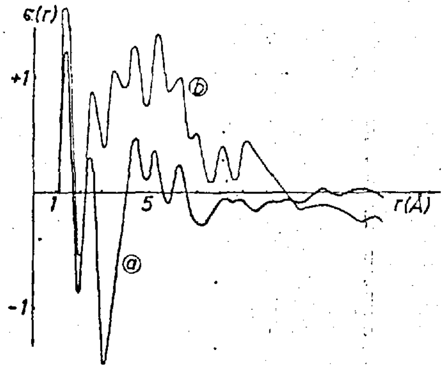

Fig.1.12 The experimental atomic radial distribution function for atactic polystyrene (a) compared with that calculated for amorphous phenolphthalein (b). (Kilian and Boueke[51]).

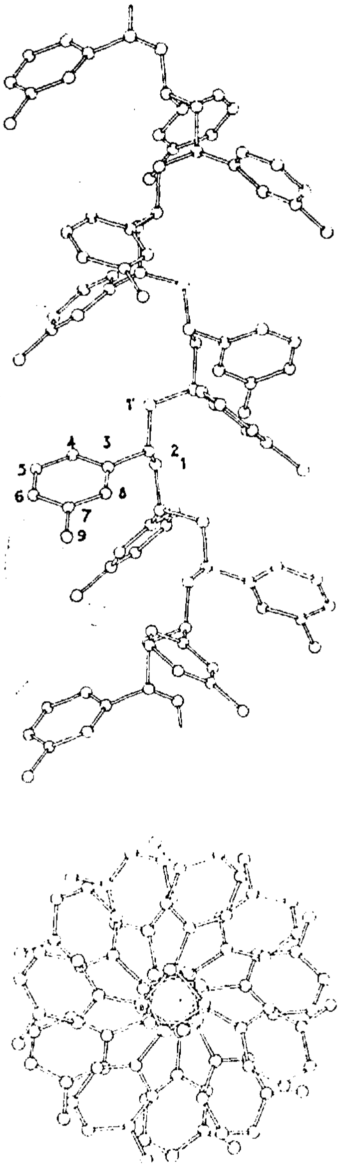

The helical structure of isotactic poly(meta-methylstyrene).

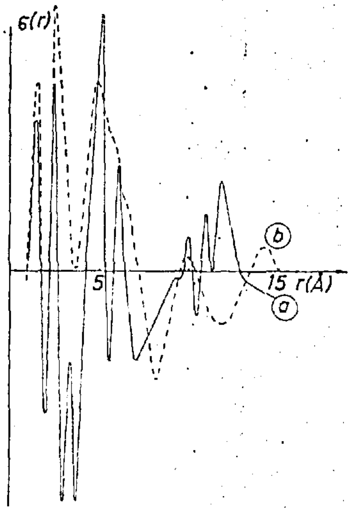

Fig.1.13 The experimental radial distribution function for atactic polystyrene at 160°C (a) compared with that calculated for isotactic poly(meta-methylstyrene) (b). (Kilian and Boueke[51]).

More recently Wecker, Davidson and Cohen[52] have obtained atomic RDF's from three polystyrene glasses: quenched and slowly cooled atactic polystyrene and isotactic polystyrene (Fig.1.14). The RDF's exhibit five principal peaks centred at 1.5, 2.5, 5, 6, and 10Å in all of the glasses.

Polystyrene sample	Density	Peak 1	Peak 2	Peak 3	Peak 4	Peak 5	Peak 6
Quenched atactic	1.048	1.51Å	2.53	5.05	6.11	10.1	14.7
Slowly cooled atactic	1.048	1.51	2.53	5.01	6.09	10.0	14.6
Quenched isotactic	1.056	1.51	2.53	5.00	6.13	10.3	14.9
Annealed isotactic	1.069	1.43	2.49	4.94	6.42	10.7	-

Table 1.4 The Peaks in the atomic RDF's of Wecker, Davidson and Cohen[52].

In an attempt to analyse the peaks beyond 2.5Å a "theoretical" RDF was calculated based on the crystal structure of isotactic polystyrene. Using the crystallographic data the distances to all carbon atoms in one repeat unit were computed. Fig.1.15 shows this theoretical RDF superimposed on the RDF for annealed isotactic polystyrene. The authors could identify their theoretical peaks as follows:

First peak (1.5Å) : caused exclusively by bonding neighbours along the chain and in the phenyl rings.

Second peak (~2.5Å) : caused by second nearest neighbours in the molecule and some distances across the phenyl ring to third nearest neighbour atoms.

Third peak (~3.7Å) : involved almost equal numbers of inter- and intramolecular contributions. The intra-spacings were almost all between phenyl atoms and chain atoms while the inter-spacings were all phenyl-phenyl spacings between neighbouring chains.

Fourth peak (4.7Å) : causes very similar to the third: closely divided between inter- and intra-spacings, nearly all inter-spacings being phenyl-phenyl while almost all intra-spacings were phenyl-chain.

The third and fourth peaks taken together covered the range of 3.4 to 5.2Å and involved 164 spacings of which 86 were interchain. All but ten

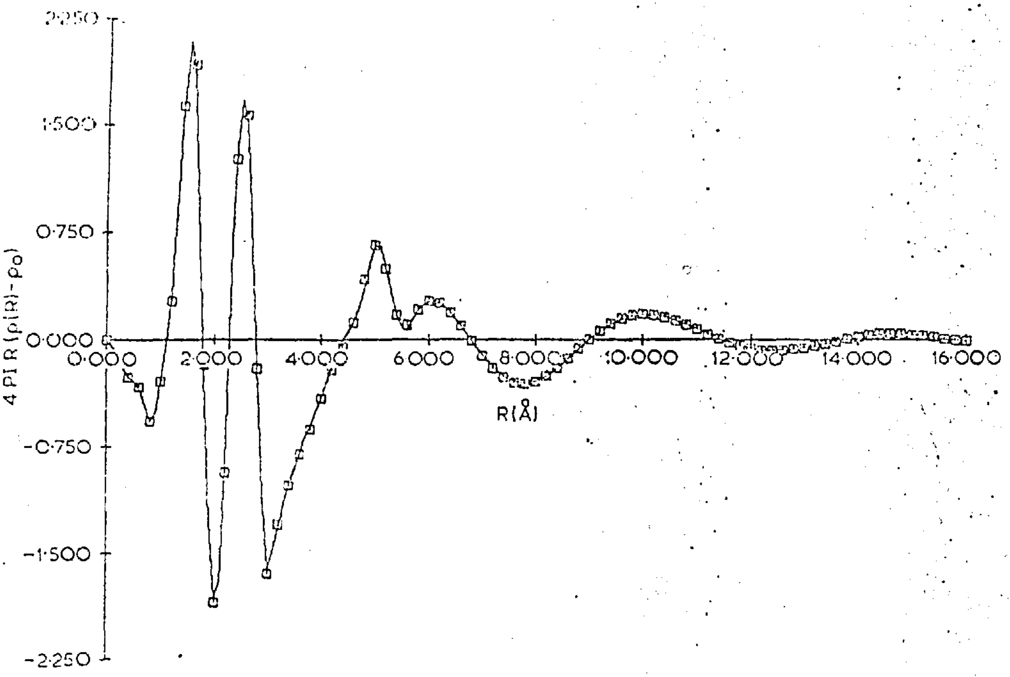

Fig.1.14(a) Atomic radial distribution functions for quenched atactic (line) and slowly cooled atactic (squares) polystyrene obtained by Wecker, Davidson and Cohen[52].

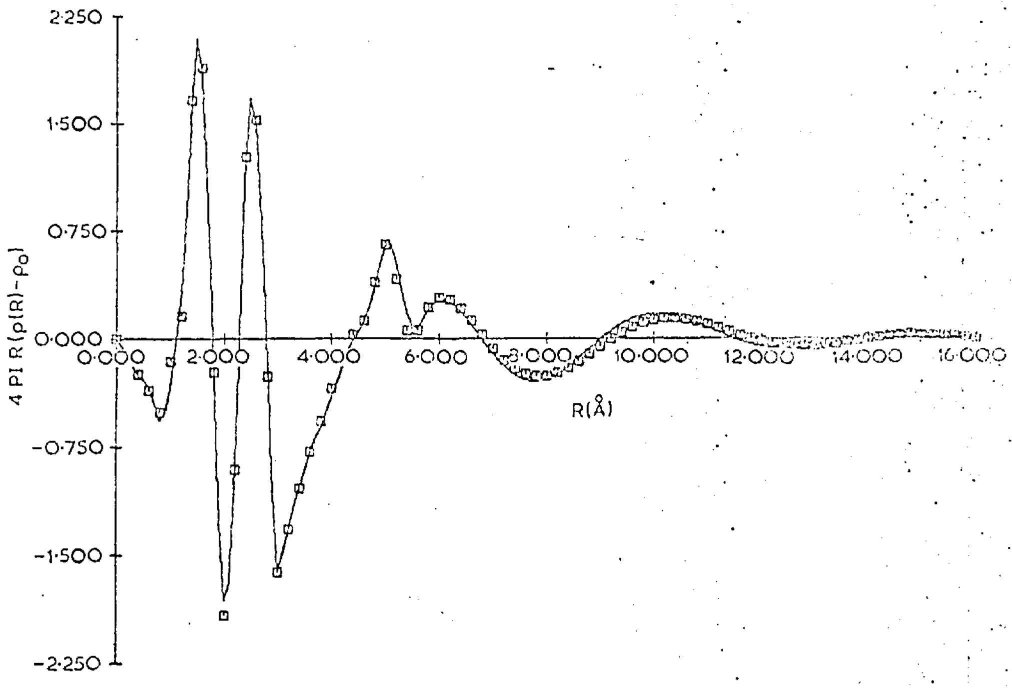

Fig.1.14(b) Atomic radial distribution function for quenched isotactic polystyrene (squares) compared with quenched atactic polystyrene (line). (Wecker, Davidson and Cohen[52]).

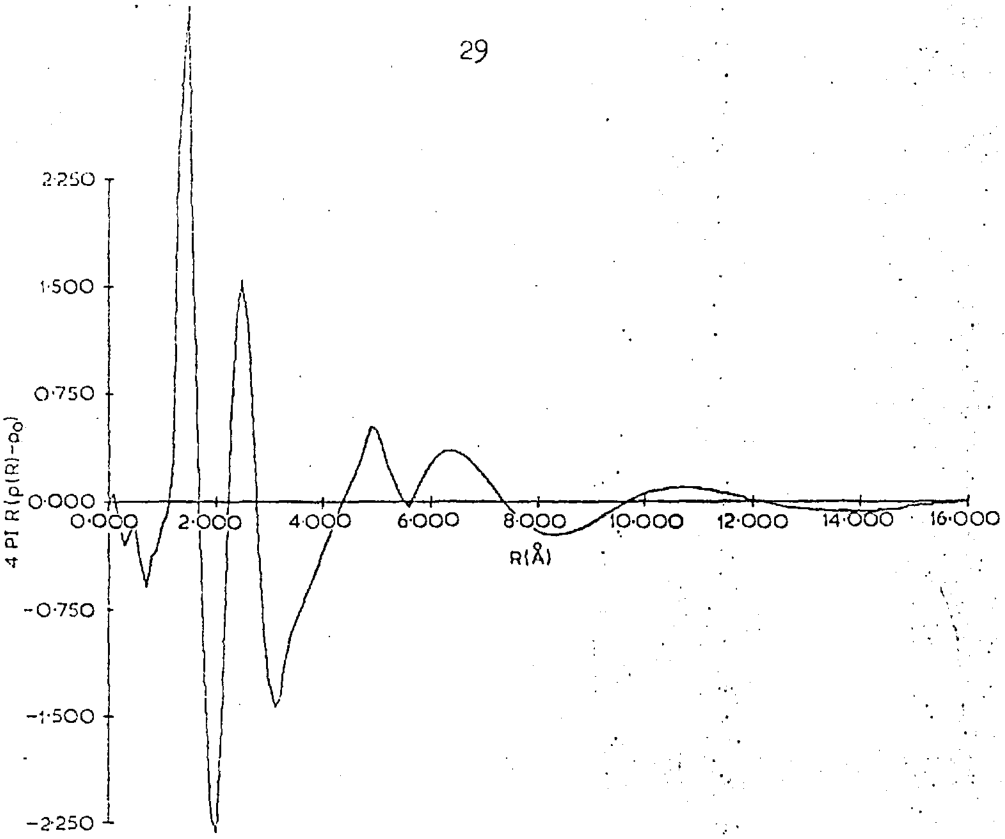

Fig.1.14(c) Atomic radial distribution function for annealed isotactic polystyrene. (Wecker, Davidson and Cohen[52]).

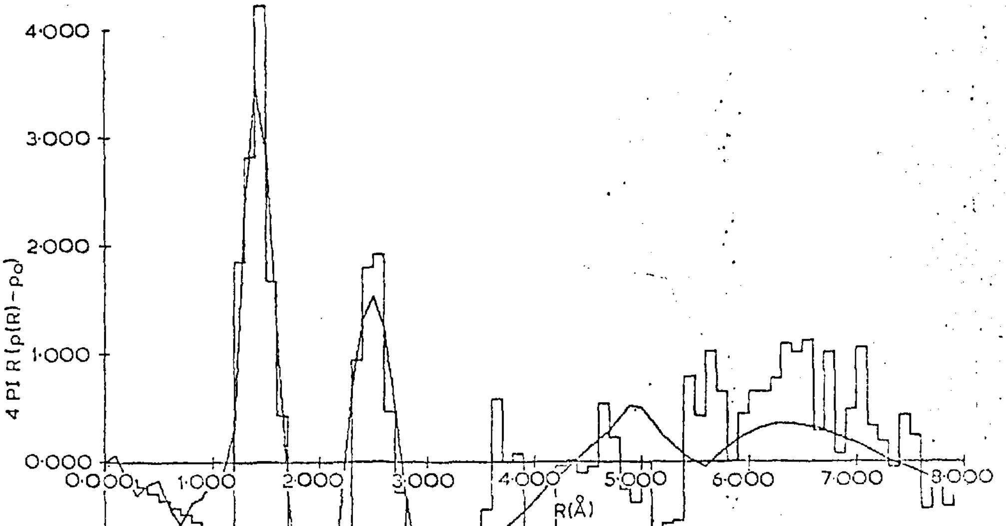

Fig.1.15 Experimental radial distribution function for annealed isotactic polystyrene superimposed on a calculated distribution function based on the crystal structure as determined by Natta and Corradini[55]. (Wecker, Davidson and Cohen[52]).

of the interchain spacings were between phenyl atoms, and all but twenty of the intrachain spacings were between phenyl and chain atoms. In the light of this information Wecker, Davidson and Cohen concluded that the 5Å peak in the experimental RDF was due very largely (~87%) to phenyl-phenyl interchain and phenyl-chain intrachain spacings.

Fifth peak (5.2Å - 8Å) : involved nearly 700 spacings two thirds of which were interchain. The separation of spacing types into phenyl-phenyl (for interchain) and phenyl-chain (for intrachain) present in the third and fourth peaks breaks down here. 70% of the phenyl-chain distances were interchain and 4% of the phenyl-phenyl distances were intrachain. This was caused largely by

(a) c-axis at 6.65Å places phenyl rings directly above and below the reference atom resulting in many intrachain phenyl-phenyl contributions.

(b) interchain axis spacing of 7.3Å places two chains in the proper interchain position for phenyl-chain spacing to occur. If only these two features were considered half of the observed spacings were left unaccounted for.

There were numerous contributions to the scattering at separations beyond 8Å, most of which were intermolecular in origin.

Markova, Ovchinnikov and Bokhyan[53] have studied the electron diffraction from high density polyethylene melts over a wide temperature range and have obtained the radial density plots shown in Fig.1.16. By comparing their functions with the scheme of the distribution of interatomic distances in crystalline polyethylene and by calculating model RDF's the authors claimed to have established that the broad maxima at radii of larger than 4Å are all intermolecular in nature. They concluded that such a number of intermolecular maxima is possible only with the parallel packing of neighbouring sections of chain molecules on a scale not less than 50Å (in the direction perpendicular to the molecular axis).

Finally Wignall and Longman[54] have recently reported the results of a WAXD study of bisphenol-A polycarbonate. Three samples were examined: sample A an "as received" injection moulded sheet, sample B a similar sheet

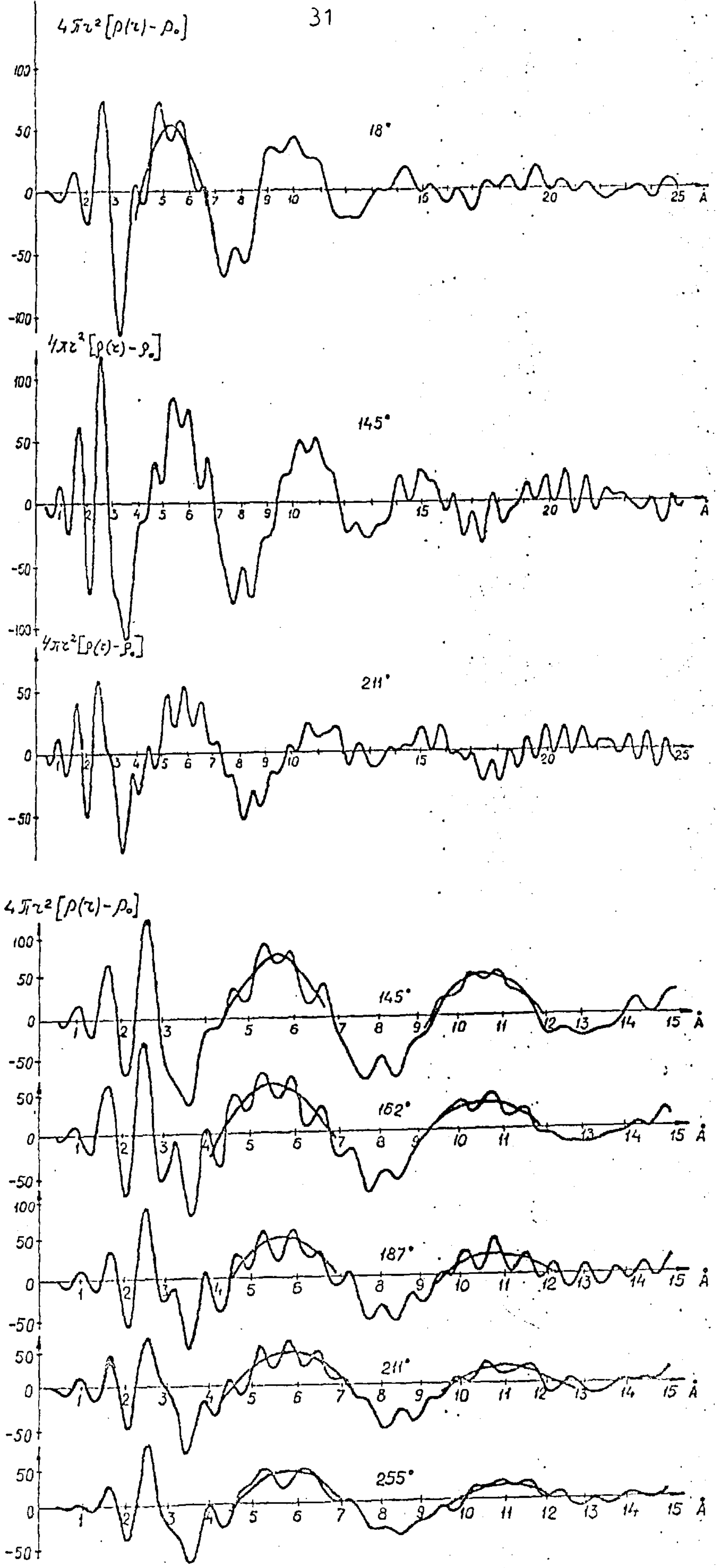

Fig.1.16 Radial density functions for polyethylene melts over a wide temperature range. (Markova, Ovchinnikov and Bokhyan[53]).

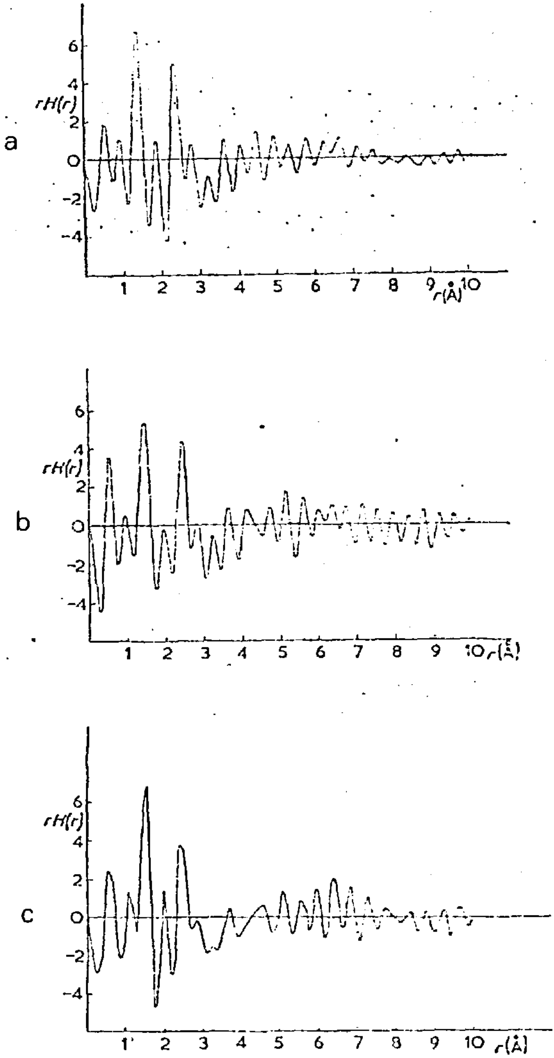

Fig.1.17 Atomic radial distribution functions for bisphenol-A polycarbonate: (a) for sample A; (b) for sample B; (c) for sample C. (Wignall and Longman[54]).

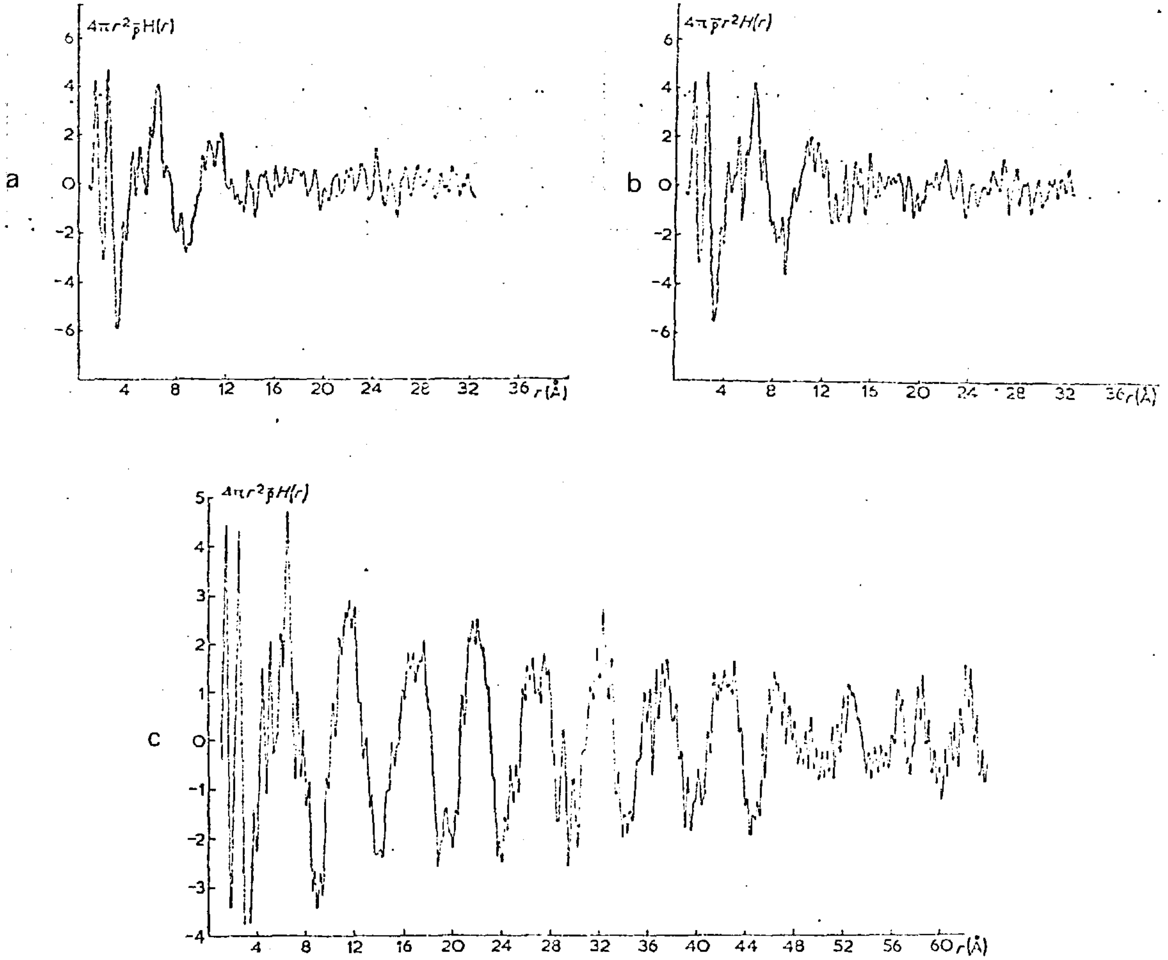

Fig.1.18 Radial density functions for bisphenol-A polycarbonate: (a) for sample A; (b) for sample B; (c) for sample C. (Wignall and Longman[54]).

subsequently annealed at 120°C for three hours and sample C, a sheet annealed for 122 hours at 190°C. The latter two samples showed slight increases in their densities and marked changes in their impact properties. The atomic radial distribution functions obtained are shown in Fig.1.17. By assuming that the molecular conformation of a repeat unit of the chain was the same in the amorphous state as in the polycarbonate crystal, the authors claimed to have shown that all the observed peaks up to r = 6.0Å together with their approximate relative intensities may be accounted for by intramolecular spacings. The peaks falling at r = 4.95Å and r = 5.17Å for samples A and B respectively could not be attributed by this model and were therefore suggested as possible candidates for inter-atomic distances resulting from the average intermolecular chain spacings in polycarbonate. A suggestion which is supported by the observation that the interchain spacing in the polycarbonate unit cell is 5.05Å. No attempt was made to index the peaks occurring at values of $r > 6$Å. The peaks at $r < 1$Å were believed to arise from truncation error in the Fourier transform process. (It is shown in Chapter III that this is more likely to be due to faulty normalisation).

Fig.1.18 shows the radial density plots obtained for the three samples. There is little significant difference between the plots for A and B which appears to eliminate any explanation of the change in the impact properties due to intermolecular re-ordering. This is consistent with the very small difference in density between samples A and B. However the radial density plot of sample C showed a marked periodicity of interval ~ 5.5Å. This extended over a radial distance of 50Å to 60Å.

1.9 Concluding Remarks

In this chapter I have attempted to describe the kinds of experiments that have been performed to help to elucidate the true nature of the glassy state of synthetic polymers. Various new models of this state have now been proposed which require varying degrees of local segmental order on the microscale. Density considerations alone appear to require that the chain packing in the condensed state is highly efficient. Diffraction experiments appear to be the most fruitful approach to the study of this problem but classical WAXD has been largely neglected.

CHAPTER TWO

The Fundamentals of X-ray Diffraction and the Interatomic Distance Function

2.1 Introduction

Studies of atomic structure are based on the diffraction of X-rays, electrons or neutrons. In principle the theory of structure analysis is the same for all radiations; however, certain differences in the nature of the physical interactions mean that each method has an optimum range of application. Electrons are scattered by electrostatic interactions with the nuclei and electron shells, whereas X-rays are scattered by the electron shells only. Neutrons are scattered by nuclear forces and are unaffected by the electron shells. For example, in the case of electron scattering the diffraction data gives a picture of the distribution of electric potential, whose peaks correspond to the positions of the nuclei.

In spite of its limitations (e.g. low accuracy in locating H atoms) X-ray diffraction is the method most universally used because of its experimental simplicity. In this chapter the fundamentals of X-ray diffraction are presented with the aid of Fourier Transform methods and the concept of the interatomic distance function is introduced.[56,57]

2.2 Scattering Amplitude

X-rays are electromagnetic waves of very short wavelength which are generated when high-energy electrons impinge on a metal target. Typical X-ray wavelengths used in diffraction studies range from 0.56Å for a Gold target to 2.29Å for a Chromium target. The direction of propagation of a beam of such waves can be specified by the wave vector $\underline{k}$ where $|\underline{k}| = 2\pi/\lambda$, and λ is the wavelength. The position of a point in three dimensional space may be specified by a vector $\underline{r}$, so that the wave can be described by $A\cos 2\pi(\underline{k}.\underline{r} + \alpha)$ or more conveniently $A\exp[i(\underline{k}.\underline{r} + \alpha)]$ in which A is the amplitude and α the initial phase.

When a beam of such X-rays is incident upon an assembly of atoms, the electrons within each atom become secondary emitters of X-rays and the incident beam is said to be "scattered". The major part of the incident intensity is scattered coherently, and this intensity can be used for structural studies because it occurs without change of wavelength and without loss of the phase relationship between the incident and scattered rays.

Scattering by a crystal may be considered simply as "reflections" from crystal lattice planes. These reflections occur only when the scattered waves are in phase (Fig.2.1), the reflection condition being

$$n\lambda = 2d_{hkl}\sin\theta \tag{1}$$

This is Bragg's Law, which relates the direction θ of the scattered beam to the interplanar distance d_{hkl}. Reflections occur whenever the path difference is an integral number of wavelengths $n\lambda$. In this simple geometrical derivation however, the process of interaction of secondary waves is not evident. The rigorous approach is to consider the secondary waves as coming from every point in the scattering object. Consider two such scattering centres (Fig.2.2), the origin ($\underline{r} = 0$) is located at one centre, the position of the other being specified by the vector $\underline{r}$. The initial plane wave falls on these centres, each of which becomes the source of a secondary spherical wave. In general, the initial wave arrives with different phases at the two centres, so that the scattered waves will have a corresponding phase difference. Constructive interference will occur in directions for which the phases are the same, destructive interference for those in which they are opposite. The resulting intensity distribution has a strict relationship to the structure of the scattering system.

If λ is very large relative to the distance r between the centres the two scattered waves will have nearly the same phase in all directions, in which case the scattered intensity would be independent of angle. Interference occurs only if the separation is comparable with the wavelength; it does not occur if λ is very much greater than r.

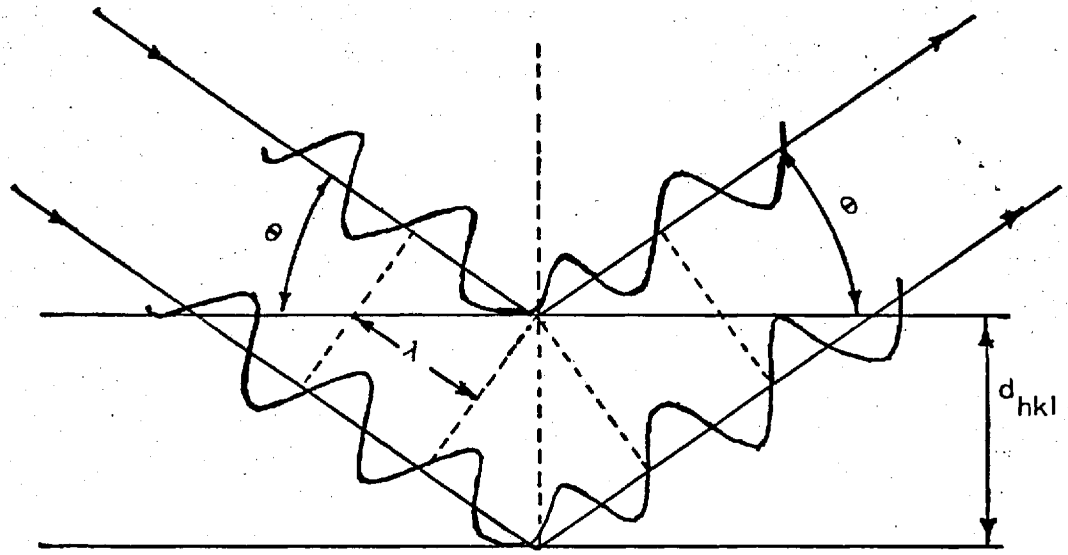

Fig.2.1 Scattering from a crystal considered as reflections from lattice planes.[56]

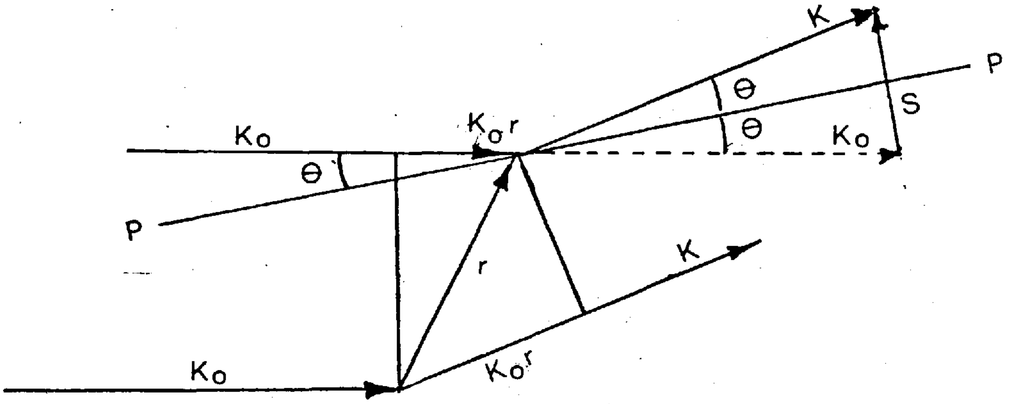

Fig.2.2 Scattering from two point centres.[56]

In Fig.2.2 the wave scattered at $\underline{r}$ in the direction $\underline{k}$ has a path difference relative to the wave scattered at $\underline{r} = 0$ in the same direction of

$$\underline{k}.\underline{r} - \underline{k}_o.r = (\underline{k} - \underline{k}_o).\underline{r} \tag{2}$$

So if the initial wave is of unit amplitude (A = 1), the centre at $\underline{r}$ produces a wave

$$f\exp\left[i(\underline{k} - \underline{k}_o).\underline{r}\right] = f\exp i(\underline{s}.\underline{r}) \tag{3}$$

The factor f indicates the scattering power of the centre. The amplitude of the scattered wave is proportional to f. Furthermore, in equation (3) we have the vector

$$\underline{S} = \underline{k} - \underline{k}_o \tag{4}$$

It is also convenient to use the vector

$$\underline{S} = \frac{\underline{s}}{2\pi} = \frac{\underline{k} - \underline{k}_o}{2\pi} \tag{5}$$

In Cartesian co-ordinates $\underline{s}(x,y,z)$ and S(X,Y,Z) are related by

$$\begin{aligned} x &= 2\pi X \\ y &= 2\pi Y \\ z &= 2\pi Z \end{aligned} \tag{6}$$

If the angle of deviation of the scattered beam from the initial direction is designated by 2θ then the scattering of the initial beam $\underline{k}_o$ in the direction of $\underline{k}$ can be represented by analogy with Bragg's Law for crystals as a reflection at an angle θ from a plane 'p' (Fig.2.2), although there is actually no such reflection.

$\underline{s}$ and $\underline{S}$ are perpendicular to 'p' and from Fig.2.2 we have

$$\frac{|\underline{s}|}{2} / \underline{k} = \frac{\lambda s}{4\pi} = \sin\theta$$

$$s = \frac{4\pi}{\lambda}\sin\theta \quad \text{and} \quad S = \frac{2\sin\theta}{\lambda} \tag{7}$$

The scattering object contains a large number (n) of such scattering centres so that the resultant wave is a summation of expressions of the type of (3):

$$\sum_{j=1}^{n} f_j e^{2\pi i(\underline{S}.\underline{r}_j)} = F(\underline{S}) \qquad (8)$$

$F(\underline{S})$ is called the scattering amplitude. Equation (8) extends the concept of f (the scattering power) for a single centre to any physical scattering object.

The set of discrete points in positions $\underline{r}_j$ can be replaced by an object whose scattering power has a continuous distribution $\rho(\underline{r})$. Since X-rays are scattered by electrons we take $\rho(\underline{r})$ as the time-average of the electron density within the object. This continuous function will have maximum values at the atoms and values close to zero between them. The electron density within a single atom is defined by the corresponding function $\rho_a(\underline{r})$. Thus equation (8), which is the sum over discrete centres f_j, can be replaced by an integral for the continuous function $\rho(\underline{r})$:

$$F(\underline{S}) = \int_V \rho(\underline{r}) e^{2\pi i(\underline{S}.\underline{r})} dv_r \qquad (9a)$$

in which dv_r is an element of the scattering volume V. This gives the amplitude as a function of $\underline{S}$ or $\underline{s}$ and so defines the amplitude for any direction $\underline{k} = \underline{k}_o + \underline{s}$. In Cartesian co-ordinates

$$F(X,Y,Z) = \iiint_{-\infty}^{+\infty} \rho(x,y,z) e^{2\pi i(xX+yY+zZ)} dxdydz \qquad (9b)$$

The integrals of (9a) and (9b) are Fourier integrals and these are considered in detail below. $F(\underline{S})$ is specified in the space of the vector $\underline{S}$ (reciprocal space) and is the "image" of $\rho(\underline{r})$ in that space. These two functions have a unique relationship.

2.3 Scattering by an Isolated Atom

Inserting $\rho_a(\underline{r})$ in (9), the atomic scattering amplitude is

$$f(\underline{s}) = \int_V \rho_a(\underline{r}) e^{i(\underline{s}.\underline{r})} dv_r \qquad (10a)$$

It is sufficient to assume here that the atom has spherical symmetry, i.e. $\rho_a(\underline{r}) = \rho_a(r)$, so it is convenient to express this amplitude in spherical co-ordinates. It is simple to show that

$$f(s) = \int_0^\infty 4\pi r^2 \rho_a(r) \frac{\sin sr}{sr} dr \qquad (10b)$$

f is therefore a function of the modulus of $\underline{s}(\sin\theta/\lambda)$ and thus spherically symmetric in reciprocal space. Curves of $f(\sin\theta/\lambda)$ have been calculated for all atoms and Fig.2.3 shows a few of interest in polymer science. The characteristic feature of these curves is a smooth fall off of f towards large angles.

Since $\frac{\sin sr}{sr} \rightarrow 1$ as $s \rightarrow 0$ we have

$$f(0) = \int_0^\infty 4\pi r^2 \rho_a(r) dr = Z \qquad (11)$$

f at zero scattering angle is simply the integral of the atomic electron density, i.e. Z (the number of electrons present). This is to be expected since regardless of the positions of the electrons, no phase shift occurs in the primary beam direction.

2.4 Scattering from a Group of n Atoms

The electron density for a set of n atoms at points $\underline{r}_1, \underline{r}_2, \underline{r}_3, \ldots \underline{r}_j, \ldots \underline{r}_n$ is given by

$$\sum_{j=1}^{n} {}_j(\underline{r} - \underline{r}_j) \qquad (12)$$

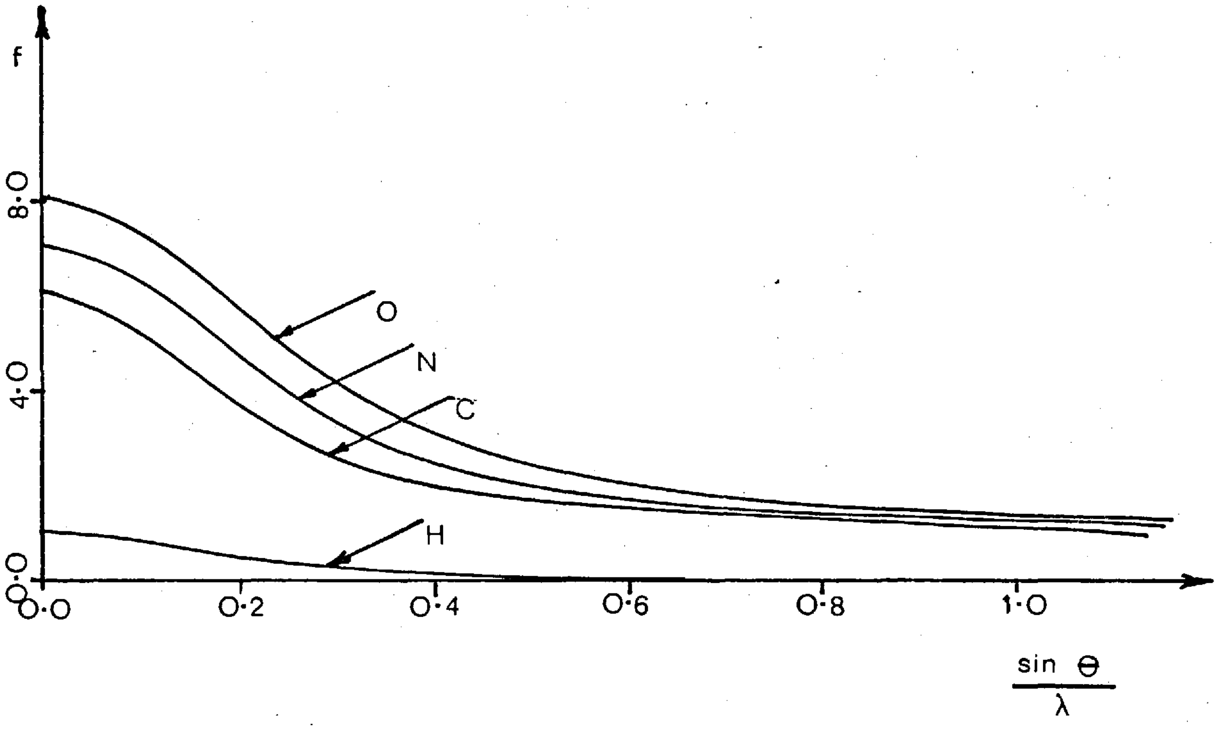

Fig.2.3 The atomic scattering amplitudes for hydrogen, carbon, nitrogen and oxygen.

Using (9) and (10) we have for the scattering amplitude of a set of n atoms

$$F(\underline{S}) = \sum_{j=1}^{n} f_j(\underline{S})\, e^{2\pi i \underline{S}\cdot\underline{r}} \tag{13}$$

Equation (13) is almost precisely the same as equation (8) for scattering point centres. Thus diffraction from a set of atoms can be reduced to the problem of diffraction from a set of points making allowance for the angular variation in the atomic scattering amplitude. From (13) we can compute the scattering amplitude for any molecule or set of molecules and also for crystals.

2.5 Scattering from a Crystal

A crystal consists of groups of atoms repeated periodically in three dimensions. The electron density $\rho(x,y,z)$ is therefore a periodic function of all three co-ordinates x,y,z. The crystal structure can be described by reference to the array of atoms in the unit cell, whose edges have lengths $\underline{a}$, $\underline{b}$ and $\underline{c}$. Repetition of the unit cell along the translations $\underline{a}$, $\underline{b}$, $\underline{c}$ generates the entire crystal lattice. The array inside the unit cell therefore determines the diffraction pattern of the crystal. Thus for a crystal, the Fourier integral of (9) for a general function must be replaced by an analogous integral for a periodic function.

In a one-dimensional crystal where the electron density has a period a, the scattering amplitude is

$$F_h = \frac{1}{a} \int_0^a \rho(x) e^{i(2\pi \frac{h}{a})} dx \tag{14}$$

where h in an integer. In contrast to a general (aperiodic) function $\rho(\underline{r})$ which produces a continuous set of values for $F(\underline{S})$, the periodic function $\rho(x)$ results in a discrete set of Fourier coefficients F_h. The Fourier transform of a periodic function is zero if h is not an integer.

$F(\underline{S})$ for a function of period a differs from zero only when $\underline{S} = \frac{h}{a}$ so that

$$F(\underline{S}) = F\left(\frac{h}{a} \right) \tag{15}$$

Thus, F_h have a certain mutual separation $\left(\frac{h}{a} \right)$ in reciprocal space.

Similarly, the Fourier coefficients for a three-dimensional crystal are

$$F_{hkl} = \frac{1}{abc} \int_0^a \int_0^b \int_0^c \rho(x,y,z) e^{2\pi i\left(\frac{hx}{a} + \frac{ky}{b} + \frac{lz}{c} \right)} dxdydz$$

$$= \frac{1}{\Omega} \int \rho(\underline{r}) e^{2\pi i(\underline{r}.\underline{H})} dv_r \tag{16}$$

where h,k,l are integers and Ω is the volume of the unit cell. The components of $\underline{S}$ (which here is denoted by $\underline{H}$) are $\frac{h}{a}$, $\frac{k}{b}$, and $\frac{l}{c}$. Thus in the case of scattering from a non-periodic object, the distribution of $F(\underline{S})$ in reciprocal space is continuous, i.e. scattering with some intensity is possible in any direction, whereas scattering from a crystal produces only certain definite diffracted intensities.

The points at which F differs from zero and takes the values F_{hkl} form a periodic distribution in reciprocal space, known as the reciprocal lattice (Fig.2.4). Each point (h,k,l) is characterised by a reciprocal-lattice vector

$$\underline{H} = h\underline{a}^* + k\underline{b}^* + l\underline{c}^* \tag{17}$$

whose origin is at (0,0,0). Comparison of (17) with the argument of the exponent of (16) shows that

$$\begin{aligned} a^* &= 1/a \\ b^* &= 1/b \\ c^* &= 1/c \end{aligned} \tag{18}$$

for orthogonal unit cells. Therefore the diffraction conditions for a crystal are

$$\underline{S} = \underline{H} \quad ; \quad \underline{k} = \underline{k}_o + \underline{s} = \underline{k} + 2\pi\underline{H} \tag{19}$$

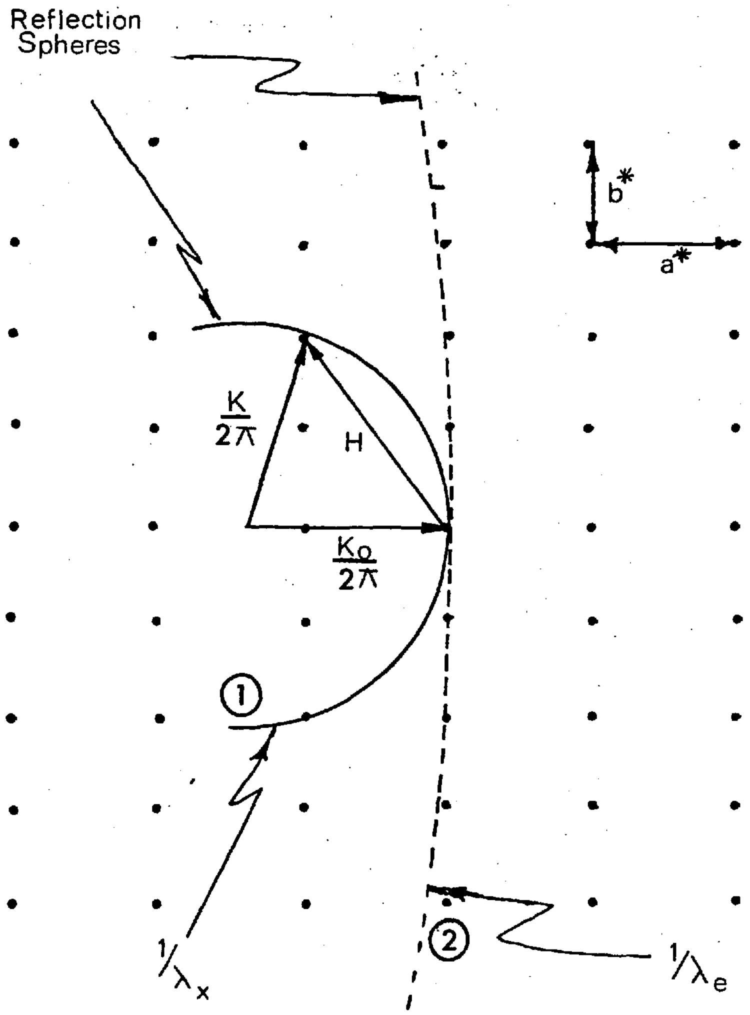

Fig.2.4 Reciprocal lattice and the reflection sphere: 1) for X-rays; 2) for electrons.[56]

This defines the possible $\underline{k}$ directions for the diffracted beams. Any given position of the crystal gives rise only to those beams corresponding to an intersection between the reflecting sphere and reciprocal lattice points (Fig.2.4). Thus the conditions for the occurrence of the diffracted beams are dependent upon the orientation of the crystal relative to the primary beam and on the radius $1/\lambda$ of the reflecting sphere.

From equations (1), (7) and (19) we have

$$|\underline{H}_{hkl}| = 1/d_{hkl} \qquad (20)$$

i.e. the vector $\underline{H}_{hkl}$ in the reciprocal lattice has a length $1/d_{hkl}$ and is perpendicular to the hkl planes of the crystal lattice.

Since the arrangement of atoms in the unit cell is repeated throughout the crystal, the scattering amplitude may be found by summing equation (13) over just one unit cell.

$$F(hkl) = \sum f_j e^{2\pi i(\underline{rj}.\underline{H})} = \sum f_j e^{2\pi i(hxj + kyj + lzj)} \qquad (21)$$

This gives the structure amplitude for the hkl reflection ($\underline{S}$ is replaced by $\underline{H}$ for crystals).

In a crystal, large values of F_{hkl} (strong reflections) are obtained when $\underline{H}_{hkl}$ is perpendicular to hkl planes which are densely populated. Also in any object which lacks true crystallographic planes but contains layers or rows of atoms, large values of $F(\underline{S})$ will arise whenever $\underline{S}$ is perpendicular to them.

2.6 Intensity

The scattering amplitude $F(\underline{S})$ is governed by the electron density $\rho(\underline{r})$ and thus the absolute value of $F(\underline{S})$ must be deduced from the scattering characteristics for a single electron. Classical electrodynamics gives this as

$$f_e = \frac{e^2}{m\,c^2} P \qquad (22)$$

where e and m are the charge and mass of an electron and c is the velocity of light. P is a function of θ which describes the degree of polarisation produced within the scattered beam. For unpolarised incident radiation, the square of (22) is

$$f_e^2 = \left(\frac{e^2}{m\,c^2}\right)^2 \frac{1 + \cos^2 2\theta}{2} \tag{23}$$

The amplitude of the scattered wave is proportional to that of the incident wave and inversely proportional to the distance $\underline{r}$ from the object. The intensity is always proportional to the square of the modulus of $F(\underline{S})$

$$F(\underline{S})\ ^2 = F(\underline{S})F^*(\underline{S}) \propto I(S) \tag{24}$$

so that

$$I = I_o \frac{e^4}{m^2 c^4 r^2} \left(\frac{1 + \cos^2 2\theta}{2}\right) \tag{25}$$

Equation (25) gives the intensity of classical scattering by a single free electron and it is often called the Thomson scattering equation. The factor $\left(\frac{1 + \cos^2 2\theta}{2}\right)$ is called the polarisation factor for an unpolarised beam. If the primary beam is not unpolarised, the polarisation factor takes a different form. The numerical factor

$$\frac{e^4}{m^2\ c^4} = 7.94 \times 10^{-26}\ \mathrm{cm}^2 \quad \text{in (25)} \tag{26}$$

is best excluded from equations describing the scattering amplitude and intensity, by expressing them in terms of a single electron (i.e. in electron units). It is assumed in what follows that F is in such units.

2.7 Fourier Transforms

The integral of equation (9) which connects $F(\underline{S})$ with the electron density $\rho(\underline{r})$ is a Fourier integral which has the important property of reciprocity. That is, $\rho(\underline{r})$ can be calculated by the inverse Fourier transform if $F(\underline{S})$ is known:

$$\rho(\underline{r}) = \int F(\underline{S})\ e^{-2\pi i(\underline{S}.\underline{r})} dv_s \tag{27}$$

This property is widely exploited in diffraction theory since (27) is basic to the solution of structure problems. The prime difficulty of this analysis is that the observed intensity gives only the modulus of the scattering amplitude $|F(\underline{S})| = \sqrt{I(\underline{S})}$ whereas the $F(\underline{S}) = |F|\exp(i\alpha)$ of (27) also has a certain phase (The Phase Problem).

$F(\underline{S})$ is called the Fourier transform of the function $\rho(\underline{r})$ and $\rho(\underline{r})$ is called the inverse Fourier transform of $F(\underline{S})$. $\rho(\underline{r})$ and $F(\underline{S})$ are said to form a reciprocal pair of transforms. We shall represent this operation by the Fourier operator $\mathfrak{F}$:

$$F(\underline{S}) = \mathfrak{F}\left[\rho(\underline{r})\right] \tag{28a}$$

$$\rho(\underline{r}) = \mathfrak{F}^{-1}\left[F(\underline{S})\right] \tag{28b}$$

It follows that

$$\mathfrak{F}^{-1}\left[\mathfrak{F}[\rho(\underline{r})]\right] = \rho(\underline{r}) \tag{29}$$

i.e. the double operation restores the original function. Since $\exp ix = \cos x + i\sin x$ we can separate the complex operator $\mathfrak{F}$ into its real and imaginary parts

$$\mathfrak{F} = \mathfrak{F}_c + i\,\mathfrak{F}_s \tag{30}$$

$\mathfrak{F}_c$ and $\mathfrak{F}_s$ give the Fourier cosine and sine transforms

$$\begin{aligned}\mathfrak{F}_c\left[\rho(\underline{r})\right] &= A(\underline{S}) \;:\; \text{real component of } F(\underline{S})\\ \mathfrak{F}_s\left[\rho(\underline{r})\right] &= B(\underline{S}) \;:\; \text{imaginary component of } F(\underline{S})\end{aligned} \tag{31}$$

so that

$$\begin{aligned}F(\underline{S}) = \mathfrak{F}\left[\rho(\underline{r})\right] &= \int \rho(\underline{r})\cos 2\pi\,\underline{S}.\underline{r}\;dv_r + i\int \rho(\underline{r})\sin 2\pi\,\underline{S}.\underline{r}\;dv_r \\ &= A(\underline{S}) + iB(\underline{S})\end{aligned} \tag{32}$$

In general $F(\underline{S})$ is complex and can therefore be represented in terms of its modulus $|F|$ and a phase :

$$F = |F|\exp i\alpha = |F|\cos\alpha + i|F|\sin\alpha \qquad (33)$$

so that

$$|F|^2 = A^2 + B^2 \qquad (34)$$

and

$$\cos\alpha = \frac{A}{|F|} \quad \text{and} \quad \sin\alpha = \frac{B}{|F|} \qquad (35)$$

A diffraction experiment yields $|F|^2$, so that if α is deduced in some way, the Fourier synthesis of (27) can be performed and the structure of the scattering object is obtained.

Equation (27) which expresses the function $\rho(\underline{r})$ as a Fourier integral with respect to $\exp[2\pi i(\underline{S}.\underline{r})]$ having a continuously variable coefficient $F(\underline{S})$, is the generalisation of the representation of a periodic electron density as a Fourier series

$$\rho(x,y,z) = \frac{1}{\Omega}\sum\sum\sum F_{hkl}\exp\left[-2\pi i\left(\frac{hx}{a} + \frac{ky}{b} + \frac{lz}{c}\right)\right] \qquad (36)$$

We may imagine the period of $\rho(\underline{r})$ of (36) to increase indefinitely, in which case the functions $F(\frac{h}{a}, \frac{k}{b}, \frac{l}{c})$ become infinitely close together and go over to a continuous function $F(\underline{S})$, causing (36) to become (27).

2.8 The Microscope Analogy

Image formation in optical and electron microscopes may be summarised as

a) scattering of incident waves by the object to produce a diffraction pattern.

b) focussing of the diffraction pattern by lenses to produce an image.

a) is a Fourier expansion while b) is a Fourier synthesis. Unfortunately no lenses capable of focussing X-rays are available so that the synthesis must be done by calculation. Thus a Fourier synthesis is really a mathematical X-ray microscope with a magnification of about 100 million capable of showing us atomic structure. The main disadvantage of this microscope is that it gives us no direct indication of the phases: these must be found by calculation from the most probable models.

The microscope analogy may be taken a step further to illustrate another property of (27). $F(\underline{S})$ cannot be measured throughout the whole volume of reciprocal space but is limited by the wavelength of X-rays used, that is $S_{max} = 2/\lambda$. This means that $\rho(\underline{r})$ cannot be calculated with infinite limits as in (27) but only for a sphere of finite radius S_{max}

$$\rho'(\underline{r}) = \int_{|S| < \frac{2}{\lambda}} F(\underline{S}) e^{-2\pi i(\underline{S}\cdot\underline{r})} dv_s \tag{37}$$

This is equivalent to a reduction in the resolving power of a microscope; the image being distorted by the so-called "termination waves". However, if $F(\underline{S})$ becomes vanishingly small on a sphere of radius $2/\lambda$ which is dependent on the form of $\rho(\underline{r})$ then (37) becomes equivalent to (27) and no resolution is lost. This termination effect is considered in more detail in Chapter III.

2.9 Convolution

The operation of convolution or folding of a function is widely used in diffraction theory. The convolution is the result of distributing a function $f_1(x)$ in accordance with a law specified by another function $f_2(x)$.

The convolution operation is most readily explained by reference to some properties of the Dirac δ-function. The integral of the product of some function with the δ-function, samples the value of the first at $x = o$

$$\int_{-\infty}^{+\infty} f(x)\,\delta(x)dx = f(o) \tag{38}$$

The δ-function may be specified at $x = x'$ instead of $x = o$, in which case the value of $f(x)$ is sampled at $x = x'$:

$$\int_{-\infty}^{+\infty} f(x)\,\delta(x - x')dx = f(x') \tag{39}$$

Now consider an analogous integral with the sum of two δ-functions having certain weights, say 1 : 2, at the points x' and x''

$$f_2 = \delta(x - x') + 2\,\delta(x - x'') \tag{40a}$$

in which $x'' = x' + a$, as in Fig.2.5.

From (39) we have

$$\int_{-\infty}^{+\infty} f(x)f_2dx = f(x') + 2f(x' + a) \tag{40b}$$

Here $f(x)$ is distributed in accordance with the f_2 of (40a), it is displaced to the points at which $f_2$exists and its values at those points are multiplied by 1 and 2. Here f_2 in "x'-space" is inverted with respect to the x-space in which it was originally specified. This is clear in (39) in which the x' in the argument of the δ-function has a negative sign. Extending (39) to any $f_2(x)$, we have the integral

$$\int_{-\infty}^{+\infty} f_1(x)f_2(x - x')dx = Q(x') \tag{41}$$

which we shall call the Q-convolution. It gives the distribution of one function in accordance with a second function inverted relative to the convolution space. Therefore it is readily seen that

$$\int_{-\infty}^{+\infty} f_1(x)f_2(x' - x)dx = P(x') \tag{42}$$

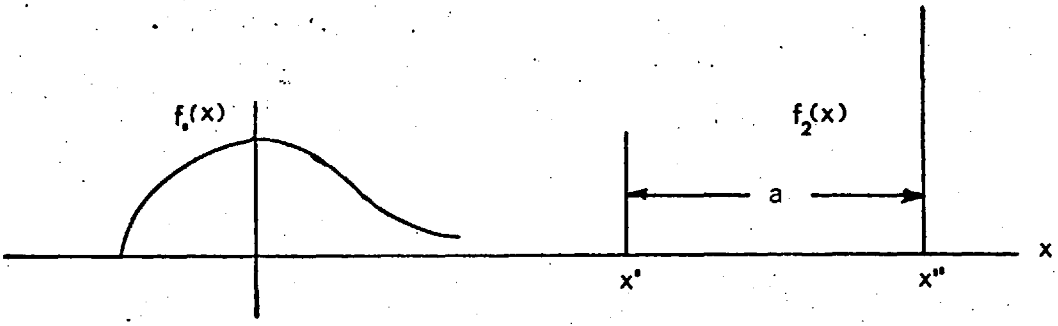

a) functions $f_1(x)$ and $f_2(x)$

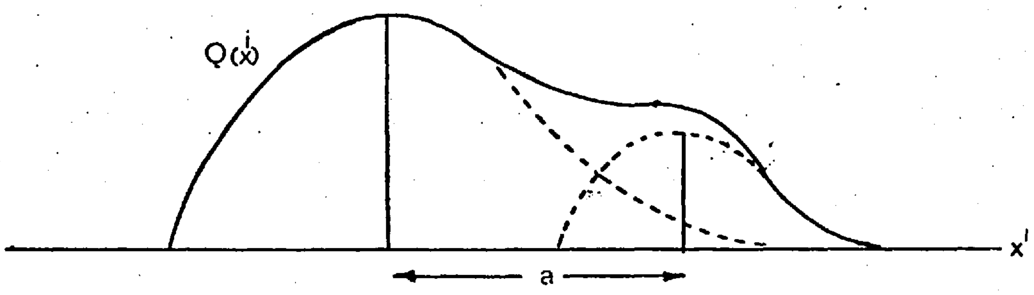

b) Q - convolution $Q(x') = \int f_1(x) f_2(x - x') dx$

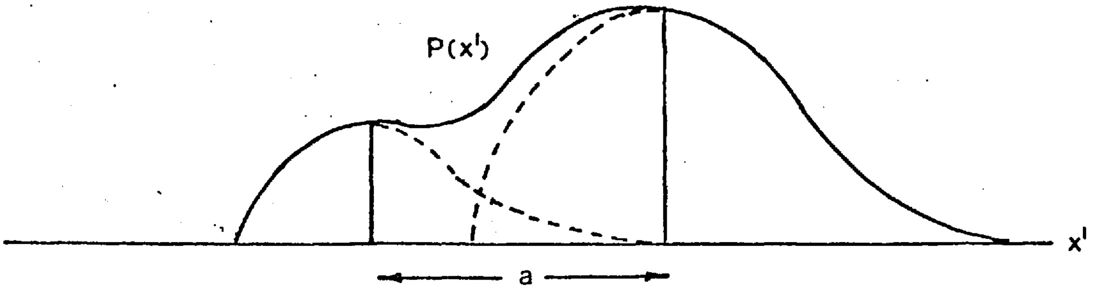

c) P - convolution $P(x') = \int f_1(x) f_2(x' - x) dx$

Fig.2.5 The P and Q convolution of the functions $f_1(x)$ and $f_2(x)$.[56]

gives the distribution of one function in accordance with a second function not inverted with respect to the convolution space. We shall call this the P-convolution. The inversion is without importance if one of the functions has an inversion centre; then P = Q. If no sharp peaks are present in f_1 and f_2 their general features are less apparent in the convolution although the general rule is still fulfilled; one function is distributed according to a law specified by the other.

2.10 Convolution Theorem

This theorem states that the Fourier transform of the convolution of two functions is the product of the transforms of each separate function. This may be written in brief as

$$\mathcal{F}\left[f_1(x) \circledast f_2(x)\right] = \mathcal{F}\left[f_1(x)\right] \mathcal{F}\left[f_2(x)\right] \tag{43}$$

where the symbol $\circledast$ is used to denote convolution. The converse statement is

$$\mathcal{F}\left[f_1(x) f_2(x)\right] = \mathcal{F}\left[f_1(x)\right] \circledast \mathcal{F}\left[f_2(x)\right] \tag{44}$$

The convolution theorem plays an important role in transforming functions which can be recognised as the convolution of two others or as the product of two others.

2.11 Self-Convolution and the Interatomic-Distance Function

An especially important case of Q-convolution is the convolution of a function with itself, which is called self-convolution or convolution square and is denoted by $\overset{2}{\sim}$. For a three dimensional electron density function $\rho(\underline{r})$, the self-convolution is

$$Q(\underline{r}') = \overset{2}{\tilde{\rho}}(\underline{r}') = \int \rho(\underline{r})\, \rho(\underline{r} - \underline{r}')\, dv_r \tag{45a}$$

The value of $Q(\underline{r}')$ is unaffected by rewriting as

$$Q(\underline{r}') = \int \rho(\underline{r})\,\rho(\underline{r} + \underline{r}')dv_r \tag{45b}$$

Also the primed and unprimed arguments can be interchanged so that

$$Q(\underline{r}) = \overset{2}{\tilde{\rho}}(\underline{r}) = \int \rho(\underline{r}')\,\rho(\underline{r}' - \underline{r})dv_{r'}, \tag{46a}$$

$$Q(\underline{r}) = \overset{2}{\tilde{\rho}}(\underline{r}) = \int \rho(\underline{r}')\,\rho(\underline{r}' + \underline{r})dv_{\underline{r}'}, \tag{46b}$$

$Q(\underline{r})$ is in the same space as $\rho(\underline{r})$.

$Q(\underline{r}) = \overset{2}{\tilde{\rho}}(\underline{r})$ takes large values whenever $\underline{r}'$ of (46a) and (46b) corresponds to a distance between points $\underline{r}$ and $\underline{r} + \underline{r}'$ such that $\rho(\underline{r})$ has large values at both points. Since $\rho(\underline{r})$ represents the electron density of a set of atoms $\sum \rho_j(\underline{r} - \underline{r}_j)$ and has its largest values at the centres of these, ($Q(\underline{r})$ is large whenever $\underline{r}' = \underline{r}_j - \underline{r}_k$, i.e. whenever $\underline{r}$ is equal to the vectors joining points $\underline{r}_1$, $\underline{r}_2$, $\underline{r}_3$, ... and so on. The self-convolution $\overset{2}{\tilde{\rho}}(\underline{r})$ is therefore called the Interatomic-Distance Function.

The functions of (46a) and (46b) are identical so their transforms are identical and therefore

$$\mathcal{F}\left[\overset{2}{\tilde{\rho}}(\underline{r})\right] = F(\underline{S})F^*(\underline{S}) = I(\underline{S}) \tag{47}$$

Thus we have the useful result that the diffracted intensity and the interatomic-distance function are reciprocal Fourier transforms. Fourier transformation of $I(\underline{S})$ gives a function which is directly related to the atomic structure of the object. Fig.2.6 illustrates the relationship between $\rho(\underline{r})$ and the system of interatomic vectors $Q(\underline{r})$. The array of atoms is not shown by $\overset{2}{\tilde{\rho}}(\underline{r})$ itself but it does provide valuable information.

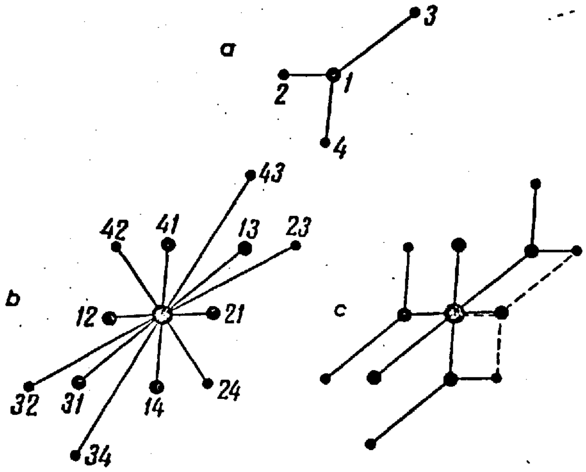

Fig.2.6 a) Structure containing four atoms, b) interatomic distance function $Q(\underline{r}) = \overset{2}{\tilde{\rho}}(\underline{r})$ for this structure, c) the representation of $Q(\underline{r})$ as the sum of displaced and inverted $\rho(\underline{r})$ [56]

The main properties of the interatomic distance function are as follows

1. the vector joining each pair of atoms in $\rho(\underline{r})$ is represented in $Q(\underline{r})$ by a vector arising from the origin.
2. $Q(\underline{r})$ always has a centre of symmetry (so that (47) is a cosine transform).
3. the height of peak jk in $Q(\underline{r})$ is proportional to the product of the peak heights of atoms j and k in $\rho(\underline{r})$.
4. the origin ($\underline{r} = o$) is always the site of the strongest peak (the distances of the atoms from themselves).
5. if $\rho(\underline{r})$ contains n atoms, then $\overset{2}{\tilde{\rho}}(\underline{r})$ contains n^2 peaks of which n fuse at the origin and the other $n(n - 1)$ are distributed over the volume of $Q(\underline{r})$.

2.12 Conservation of Intensity

Since $I(\underline{S})$ is real and everywhere positive, its transform is free from the basic difficulty encountered with the scattering amplitudes, namely the need to know the phases. $Q(\underline{r})$ is centrosymmetric, i.e. it does not alter when $-\underline{r}$ replaces $\underline{r}$. $I(\underline{S})$ is also centrosymmetric and the transforms of $Q(\underline{r})$ and $I(\underline{S})$ are thus cosine transforms.

From equation (13)

$$I(\underline{S}) = |F(\underline{S})|^2 = \sum_{j=1}^{N} \sum_{k=1}^{N} f_j f_k e^{2\pi i \underline{S}\cdot(\underline{r}_j - \underline{r}_k)} \tag{48}$$

The centrosymmetry of $I(\underline{S})$ now becomes obvious if we pair off terms containing $\underline{r}_j - \underline{r}_k$ and $\underline{r}_k - \underline{r}_j$, and pick out terms having $j = k$.

This gives

$$I(\underline{S}) = \sum_{j=k} f_j^2 (\underline{S}) + 2 \sum_{j>k}\sum f_j f_k \cos 2\pi (\underline{S}.\underline{r}_{jk}) \tag{49}$$

using $\underline{r}_{jk} = \underline{r}_j - \underline{r}_k$. The first sum of (49) is always present and is sometimes called the gas component of the intensity since it describes the scattering of isolated atoms as may be observed with monoatomic gases.

Each term in the second sum represents a plane wave in reciprocal space having $\underline{r}_{jk}$ normal to it. This wave has positive and negative parts, the mean being zero so that the mean of the double sum is also zero. The interferences described by this double sum cannot alter the total intensity provided by the isolated atoms; they only alter its distribution. Thus the integral of the intensity over the whole of reciprocal space equals the integral of the intensities given by the isolated atoms. Since for our purposes $f^2(\underline{S})$ has spherical symmetry, the integration may be performed for spherical belts of area $4\pi S^2$ and thickness dS :

$$\int I(\underline{S}) dv_{\underline{S}} = \sum_{j=1}^{N} \int_0^{\infty} f_j^2 (\underline{S})\, 4\pi S^2 \, dS \tag{50}$$

This value of the amount of intensity is independent of the distribution of atoms in space.

The second sum of (49) describes for a particular atomic array, the distribution of the total available intensity. This is illustrated in Fig.2.7. The effect is very pronounced for crystals where the intensity is concentrated into isolated sharp peaks, while in liquids the intensity maxima are broad and isotropic.

Equation (50) may be called the Law of Conservation of Intensity and it may be used to normalize experimental intensities to the scattering by a molecule or a unit cell of a crystal since the number of scattering atoms in the object is scarcely ever known.

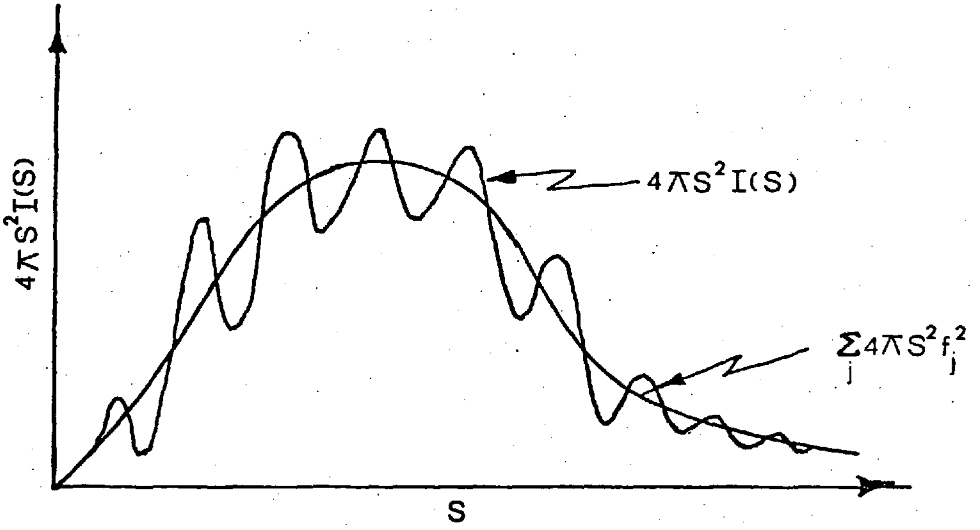

Fig.2.7 The law of conservation of intensity.[56]

2.13 The Radial Distribution Function

Objects such as amorphous polymers which have spherically symmetric intensity distributions may be described by a single parameter $s = 2\pi S = 4\pi \sin\theta/\lambda$, the distance in reciprocal space from the origin. I(S) is transformed to Q(r) by the Fourier integral and thus Q(r) is also symmetric by virtue of the reciprocity theorem.

From (47) :

$$I(\underline{S}) = \mathcal{F}\left[\overset{2}{\tilde{\rho}}(\underline{r})\right] = \int Q(r)e^{2\pi i(\underline{S}\cdot\underline{r})}dv_r \qquad (51)$$

Transforming to spherical co-ordinates as in Fig.2.8 we have

$$I(s) = \int_0^{2\pi} d\Psi \int_0^{\pi} \int_0^{\infty} Q(r)e^{isr\cos\alpha}\, r^2 \sin\alpha \, dr d\alpha \qquad (52)$$

now let $t = sr\cos\alpha \quad ; \quad \sin\alpha \, d\alpha = -\frac{dt}{sr}$

so that $$I(s) = 2\pi \int_0^{\infty} dr \int_{-sr}^{sr} e^{it}\, Q(r)\, \frac{r^2}{sr}\, dt \qquad (53)$$

$$= 4\pi \int_0^{\infty} Q(r)r^2 \, \frac{\sin sr}{sr}\, dr \qquad (54)$$

Thus

$$Q(r) = \frac{1}{2\pi^2} \int_0^{\infty} I(s)s^2 \, \frac{\sin sr}{sr}\, ds \qquad (55)$$

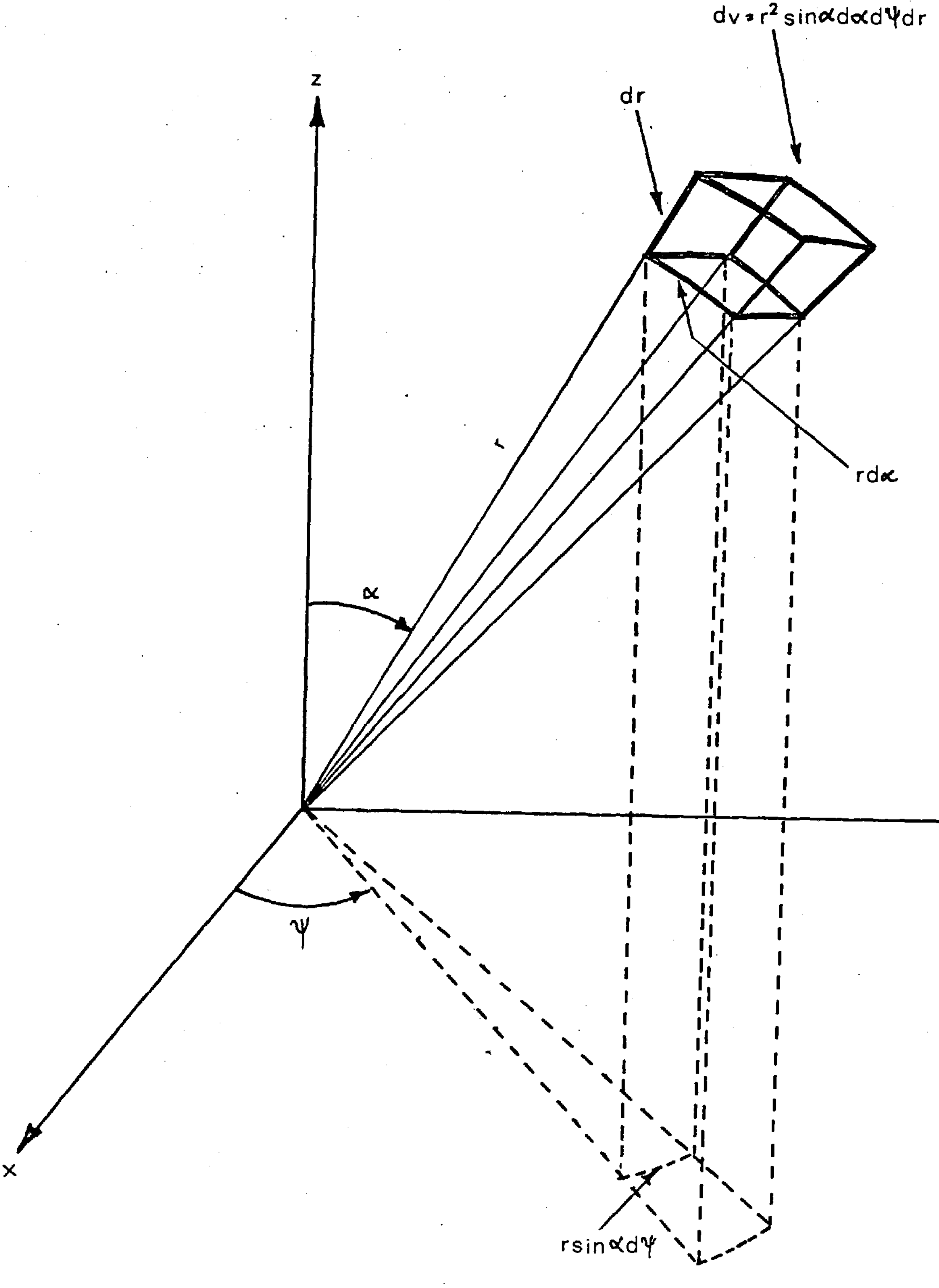

Fig.2.8 Spherical Polar co-ordinates (r, α, Ψ).

The vector $\underline{r}$ loses all indications of its spatial position in the spherically symmetrical function. The vectors for the various pairs of atoms are superimposed by spherical rotation, and so we can establish only the distances between atoms, not the spatial orientation of the distances.

Equation (55) may be rewritten as

$$Q(r) = \frac{1}{2\pi^2 r} \int_0^\infty sI \sin rs \, ds \tag{56}$$

Multiplying both sides by $4\pi r$ we have

$$4\pi r Q(r) = \frac{2}{\pi} \int_0^\infty sI \sin rs \, ds \tag{57}$$

Since $Q(r) = \overset{2}{\tilde{\rho}}(\underline{r})$ and each vector joining pairs of atoms in $\rho(\underline{r})$ is represented in $Q(r)$ by a vector arising from the origin, (57) is usually rewritten as

$$4\pi r(\rho(r) - \rho_o) = \frac{2}{\pi} \int_0^\infty sI \sin rs \, ds \tag{58}$$

where ρ_o is the macroscopic number density and $\rho(r)$ is defined as the most probable time average electron density at a distance r from an atom arbitrarily selected as the origin. Equation (58) is referred to as the Radial Distribution Function (RDF).

In equation (58) and all previous equations, all X-ray photons are assumed to be elastically scattered, that is, I is assumed to be completely coherent. However, in experiments, I is never completely coherent and several corrections have to be applied to the observed intensity before the integration of (58) can be performed.

Equation (58) is the self-convolution of the time-average electron density within the sample, and is thus sometimes called the electronic radial distribution function. It will be shown in Chapter III that to avoid disasterous termination effects (58) must be replaced by

$$4\pi r\left[\rho(r) - \rho_o\right] = \frac{2}{\pi}\int_0^\infty s(I - \sum_{uc} f^2)\sin rs\, ds \qquad (59)$$

where $\sum_{uc} f^2$ is the independent coherent scattering for a unit of composition of the material and I is normalised to that composition. (59) is a radial distribution function, which, exclusive of the intra-atomic electron distributions, represents a measure of the probability of finding electrons mutually separated by a distance between r and r + dr.

In an attempt to improve resolution the interference function of (59) is usually replaced by the function

$$\frac{I - \sum f^2}{\sum f^2}$$

From the convolution theorem of (44) it is readily seen that this has the effect of deconvoluting (59) with the distribution function of an "average" atom. This drastically sharpens all peaks in the function since they now represent distances between atom centres. This sharpening effect tends also to exaggerate spurious details and may lead to serious difficulties in the interpretation of the experimental distribution curves. For this reason electronic distribution functions of the type of (59) have been used throughout this study.

In addition to the interatomic distance function or radial distribution function $4\pi r\left[\rho(r) - \rho_o\right]$, the radial density function

$$4\pi r^2\left[\rho(r) - \rho_o\right] = \frac{2r}{\pi}\int_0^\infty s(I - \sum f^2)\sin rs\, ds \qquad (60)$$

is also used. This function represents the probable number of electrons (or atoms) within a spherical shell of thickness dr at a distance r from an "average" point in the sample. The radial density functions reflect more directly the atomic distribution. A common application of such data involves the evaluation of the quantity

$$C_i = \int_{r_i-\Delta}^{r_i+\Delta} 4\pi r^2 \rho \, dr \qquad (61)$$

in the vicinity of each of the peaks, thus obtaining the number of first, second, third, etc. nearest neighbours about the average atom. This procedure is always uncertain however because of the overlapping of the peaks.

To conclude this section we will summarise the nomenclature used in radial distribution analysis:

Electronic radial distribution function

$$4\pi r \rho(r) = 4\pi r \rho_o + \frac{2}{\pi} \int_0^\infty s(I - \sum_1 f^2) \sin rs \, ds$$

Electronic radial density function

$$4\pi r^2 \rho(r) = 4\pi r^2 \rho_o + \frac{2r}{\pi} \int_0^\infty s(I - \sum_1 f^2) \sin rs \, ds$$

Reduced electronic radial distribution function (RDF)

$$4\pi r \left[\rho(r) - \rho_o\right] = \frac{2}{\pi} \int_0^\infty s(I - \sum_1 f^2) \sin rs \, ds$$

Reduced atomic radial distribution function

$$4\pi r\left[\rho(r) - \rho_o\right] = \frac{2}{\pi}\int_0^\infty s\left(\frac{I - \sum f^2}{\sum f^2}\right)\sin rs\, ds$$

The reduced form $4\pi r\left[\rho(r) - \rho_o\right]$ is most commonly employed (interatomic distance function) and is the easiest to present graphically.

2.14 The Cylindrical Distribution Function

An assembly of chain molecules often has statistical cylindrical symmetry. The averaging of a distribution function $z(\underline{r})$ on account of cylindrical symmetry gives rise to the electronic cylindrical distribution function (CDF) or more precisely the projection of this function on the basal plane

$$2\pi r\ z_c(r)$$

This function represents the density, in the basal plane, of neighbours at a distance r, where r is the polar radius from the axis r = 0.

To $z_c(r)$ there corresponds in reciprocal space a cylindrically symmetrical interference function

$$i_c(R) = i_c(R,\ Z = 0) = I_c(R,\ 0) - \sum f^2 \qquad (62)$$

This means that the intensity must be measured along the equator of the diffraction pattern. The two functions are related by the Fourier-Bessel transform

$$2\pi r\ z_c(r) = 2\pi r\ z_{av} + 4\pi^2 r^2 \int_0^\infty i(R)J_o(2\pi rR)RdR \qquad (63)$$

in which $R = \frac{s}{2\pi}$.

Note that the zero order Bessel functions:

$$J_o(2\pi rR) = \frac{1}{2\pi}\int_0^{2\pi} \exp\left[i\ 2\pi rR \cos\phi\right] d\phi \tag{64}$$

arise from the cylindrical averaging of the exponent in the transform

$$\int I(\underline{s})\exp(i\ \underline{r}.\underline{s})dv_s$$

(c.f. radial averaging which produced the function $\frac{\sin rs}{rs}$).

The intensity distribution I(0,Z) along the meridian of the diffraction pattern provides information about the internal structure of the molecules and enables us to construct a distribution function for the atoms within them. A one-dimensional Fourier transformation gives us the one-dimensional distribution function, by analogy with (59) and (63)

$$H_3(z) = H_{3(o)} + \frac{1}{\pi}\int_0^{s_{max}} (I(0,Z) - \sum f^2)\cos zs\ ds \tag{65}$$

which is the function for a line distribution of the atoms within the molecule in projection on the principal axis.

2.15 The Distribution Function for a Distorted Lattice

An ideal periodic three dimensional lattice of points can in general be distorted in two different ways:

a) Distortions of the first kind: a lattice distorted in this way has points which have a certain probability of being displaced slightly from their ideal positions but on average the assembly retains its crystalline order throughout the volume (the long-range order is preserved). A typical example of this is the thermal vibrations of the atoms in a metal crystal (Fig.2.9a).

b) Distortions of the second kind: a lattice distorted in this way has only statistical mean translations $\bar{a}$ and $\bar{b}$ which merely give the probable relative positions of adjacent atoms and does not extend to a description of the entire volume. This type of lattice is called paracrystalline (Fig.2.9b).

Fig.2.9c shows that distortions of the first kind in an ideal two dimensional lattice leave the distribution function (self-convolution of the lattice) still ideally periodic but the peaks become diffuse.

Distortions of the second kind cause the distribution function to take the form shown in Fig.2.9d. The distribution of nearest neighbours is reasonably distinct: there is short-range order. Distances to second nearest neighbours vary more widely since there is addition of the variations in the distances from one molecule to the next and from the second to the third. The more distant the neighbour the more diffuse becomes the distribution function and the probability of finding a molecule becomes the same everywhere.

Distortions of the second kind are characteristic of liquids and are often found in chain molecule assemblies. The essential point in the discussion of these distortions is the allowance for short-range order, the entire distribution function can be deduced if the distribution law for nearest neighbours is known. Fig.2.10 shows the distribution function z(x) for an ideal one dimensional lattice with paracrystalline distortions. The peaks are equally spaced at intervals of

$$\bar{a} = \int x \, H_1(x) \, dx \tag{66}$$

where $H_1(x)$ is the distribution function for nearest neighbours. The peak at $x = \bar{a}$ is the distribution for nearest neighbours $H_1(x)$ while the peak at $x = m\bar{a}$ is the distribution for the m^{th} nearest neighbours and is given by the m^{th} convolution of $H_1(x)$ with itself. Peak width is specified via the mean-square fluctuation which for $H_1(x)$ is

$$\int_0^{\infty} H_1(x) \, (x - \bar{a})^2 \, dx = \Delta^2 \tag{67}$$

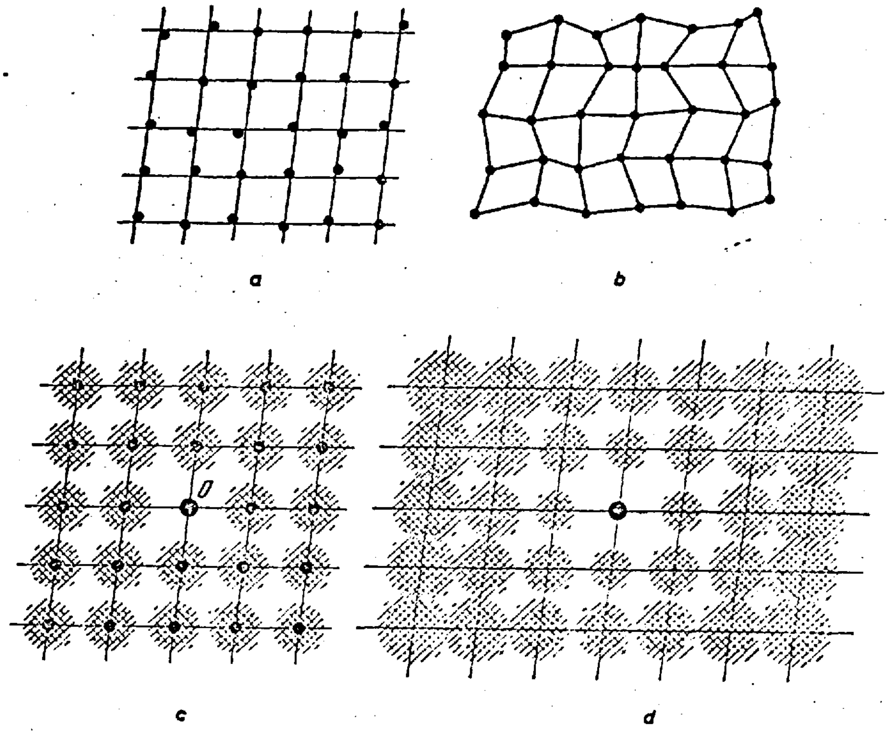

Fig.2.9 Distortions of a) the first, and b) the second kind in an ideal two-dimensional lattice; distribution functions of c) the first, and d) the second kinds

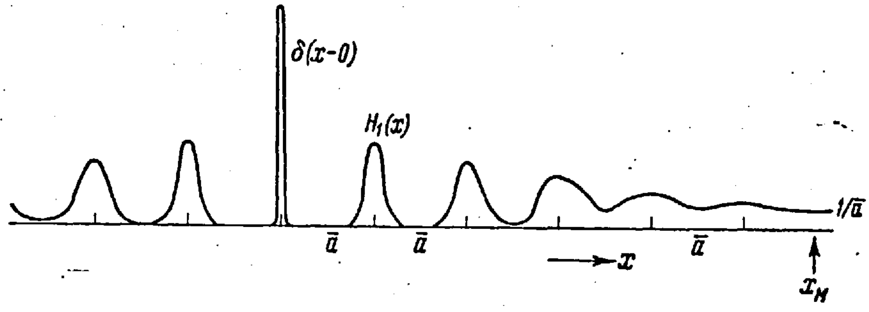

Fig.2.10 Distribution function of the second kind, z(x) [56]

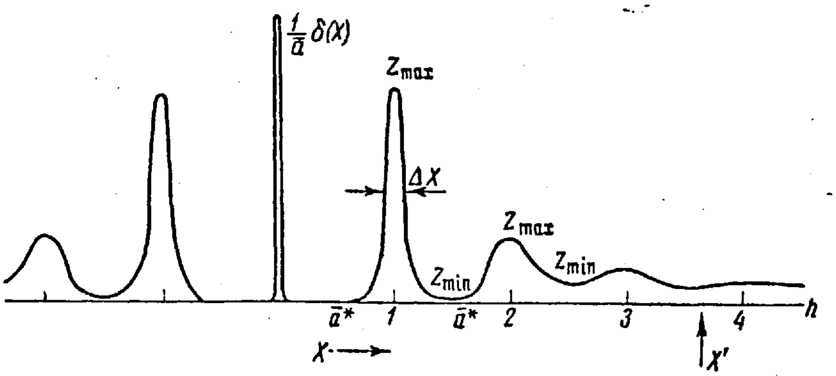

Fig.2.11 Z(X), the interference function of the second kind

This is the measure of statistical fluctuations in distances between first nearest neighbours.

The general features of the interference function Z(X) for paracrystalline distortion are shown in Fig.2.11. The peaks here are equally spaced at $\bar{a}^*$ and decrease uniformly in intensity in similar fashion to z(x).

It has been shown that the height of interference maxima is given approximately by

$$Z_{max}(h\bar{a}^*) \approx \frac{1}{\pi^2 h^2 (\Delta/\bar{a})^2} \tag{68}$$

where $\Delta/\bar{a}$ is the ratio of the width of fluctuations of the distance between first neighbours to the mean distance between them. The height is inversely proportional to the square of this ratio and to the square of h (the order of reflection). The integral half-width of the diffraction maxima is given by

$$\Delta X = \frac{1}{\bar{a}} \pi^2 h^2 \left(\frac{\Delta}{\bar{a}}\right)^2 \tag{69}$$

The existence of separate maxima in the interference function result from the region of order in z(x) which is bounded by the "radius of interaction" x_M, outside which z(x) becomes practically smooth. This arises when H_m becomes so broad that it has attained half its peak value at the distance $x = \bar{a}/2$ and overlaps its neighbours so much that z(x) becomes almost constant. It can be shown that the critical value of m is given by

$$M = \frac{1}{(2.5\Delta/\bar{a})^2} \tag{70}$$

and

$$x_M = M\bar{a} \tag{71}$$

CHAPTER THREE

Experimental Procedure

3.1 Brief Description of Apparatus

X-ray measurements were made on a Philip's vertical powder diffractometer (goniometer type PW 1050/25; X-ray generator type PW 1310). The intensity data was obtained with both CuKα (λ = 1.5418 Å) and MoKα (λ = 0.7107 Å) radiation using a McLean's curved graphite monochromator in the diffracted beam. A Xenon filled proportional counter (PW 1965/20) employing pulse height discrimination was used to detect the X-rays. The generator supplied 60 KV maximum at 2 KW giving highly stable tube current and voltage (stabilised to within 0.03% for mains fluctuations of ± 10%). An angular range of $0^{\circ} - 160^{\circ} 2\theta$ was possible on the goniometer which had facilities for both continuous-line and discrete-step scanning.

The electronic counting and measuring cabinet consisted of high and low voltage supplies, pulse amplifier and analyser, scaler and timer combination, ratemeter and strip chart recorder, step-scan control and digital printer. Fig.3.1 is a schematic block diagram of the arrangement of these receiving circuits. Low voltage pulses from the proportional counter were first amplified and sharpened in a pre-amplifier mounted in the counter housing. These then passed via a transmission cable to a pulse shaper where each pulse was shaped to 1 μ sec. All the received pulses were then amplified again, but only those with pulse heights above a certain threshold or between certain chosen limits were transmitted further. This discrimination meant that practically all pulses due to electronic noise were rejected together with X-ray harmonics passed by the monochromator. Thus only pulses of almost equal amplitude were applied to the scaler. The output from the amplifier could also be applied to the ratemeter, which smoothed out the pulses into a fluctuating current recordable on the strip chart.

The scaler and timer worked in conjunction and both could be pre-set to operate the printer in the step-scan mode. Intensities were measured

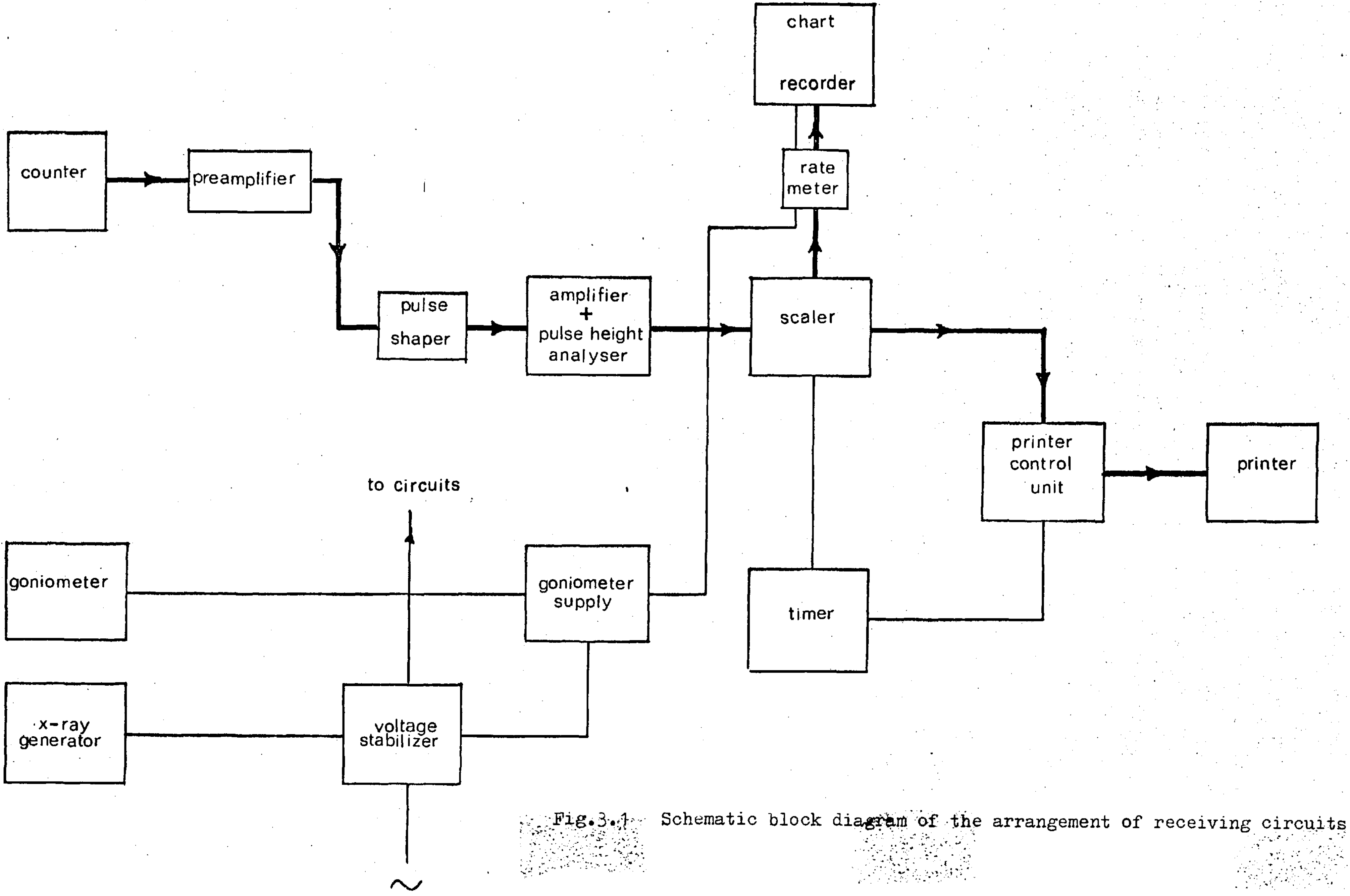

Fig.3.1 Schematic block diagram of the arrangement of receiving circuits.

in the reflection geometry over the range 2° - $160^{\circ}2\theta$ at angular intervals of $0.5^{\circ}2\theta$ up to $50^{\circ}2\theta$ and $1.0^{\circ}2\theta$ up to $160^{\circ}2\theta$. This gave $s = 4\pi \sin\theta/\lambda$, a range of .14 - 8.03 for CuKα and of .31 - 17.41 for MoKα. Data was collected by point counting for fixed time periods, both from "single slit runs" and runs where the high angle data was obtained on larger slits in order to improve the accuracy of the counting in this region.

3.2 The Diffraction Geometry

The X-ray diffractometer is a device for obtaining scattered X-ray intensities as a function of angle between the incident and diffracted beams. The relative positions of the X-ray source, sample and receiver satisfy a modified Seeman-Bohlin parafocussing arrangement so as to obtain maximum intensities. The essential features of the parafocussing arrangement are shown in Fig.3.2. In the Seeman-Bohlin parafocussing geometry, all X-rays scattered through 2θ degrees from the curved sample S will be brought to a focus at G. In the symmetrical reflection diffractometer, the receiver, G, pivots about a flat sample, S, so as to maintain a constant sample-to-receiver distance SG. The circle ESH is called the focussing circle, and in principle every photon detected at G will have been scattered through 2θ degrees. In practice this focussing condition is only approximately met since the sample is flat and not curved. Fig.3.3 shows that as the detector at G is rotated about S towards larger 2θ the radius of the focussing circle decreases, since FS and GS are constant. Thus to maintain the focussing conditions the flat sample must be rotated at half the angular speed of the detector so that it remains tangential to the circle.

The focus at G is not perfect since the whole of the sample surface cannot lie on the circle and because of the finite dimensions of the source and slits. However aberrations may be kept acceptably small by limiting the beam divergence.

The circle described by the detector is called the goniometer circle and is shown in Fig.3.4. The triangle SGG' is an axial section through

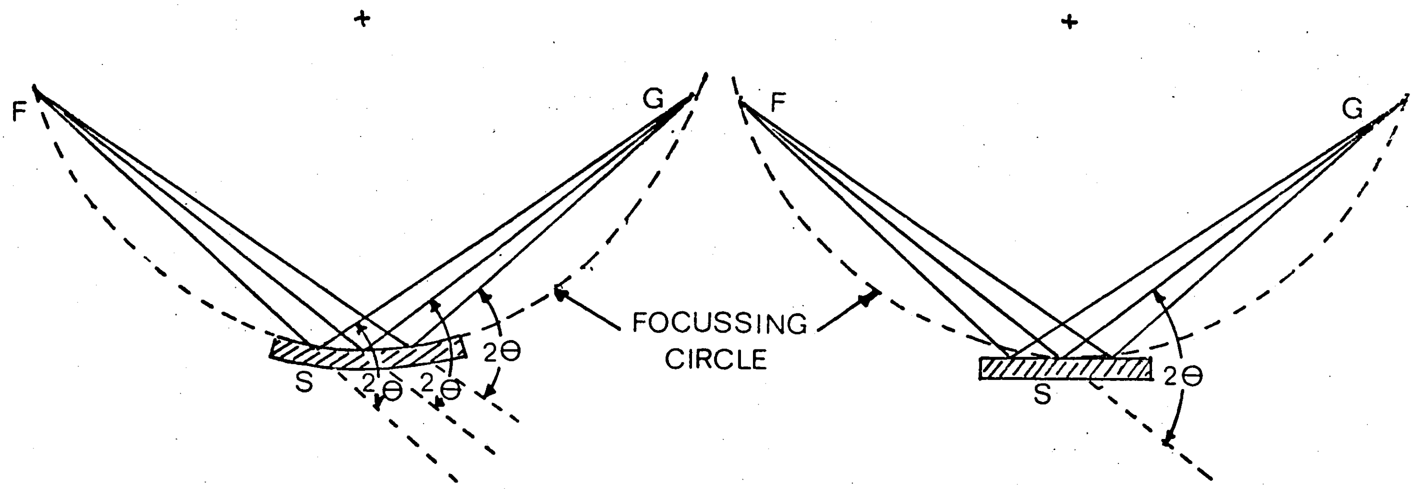

Fig.3.2 The Seeman-Bohlin parafocussing geometry.

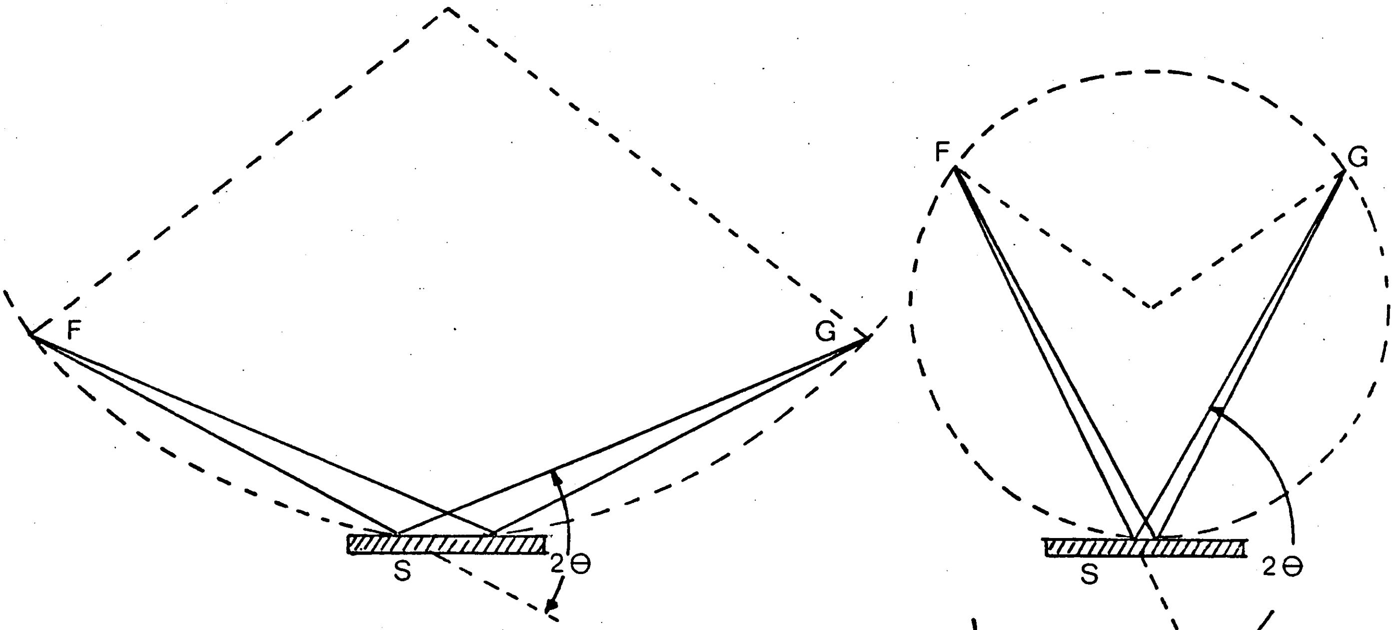

Fig.3.3 Flat sample geometry.

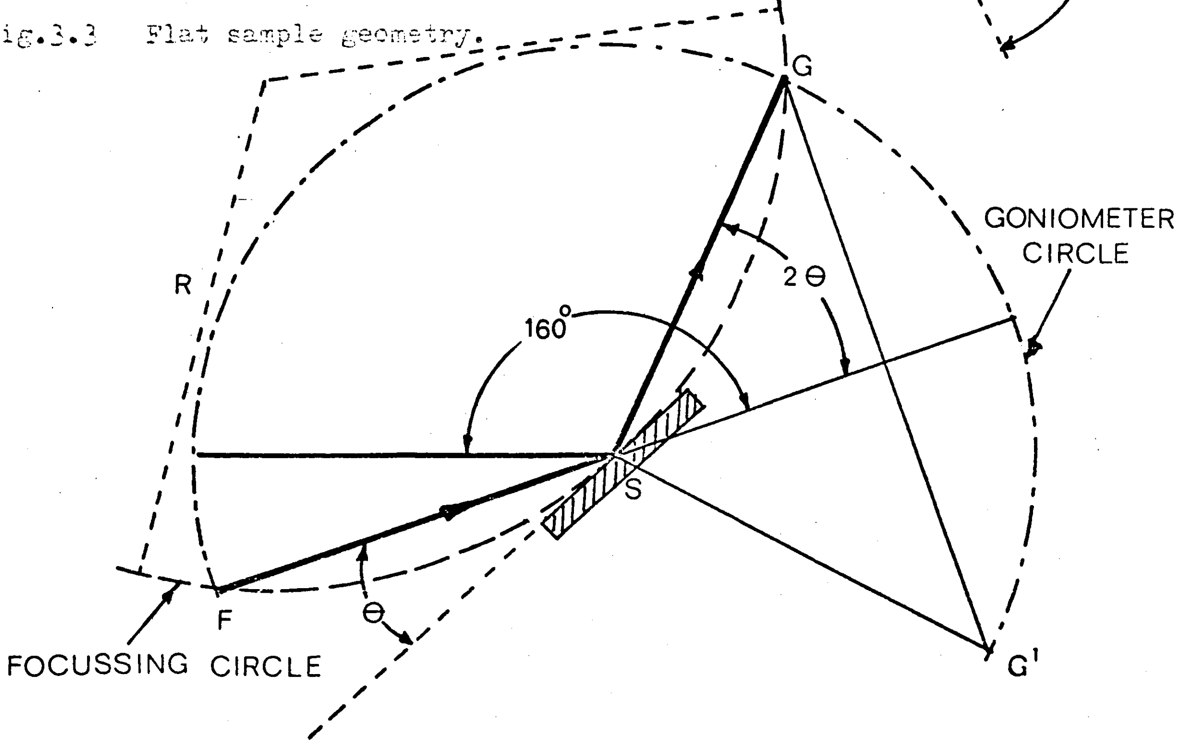

Fig.3.4 The focussing and goniometer circles.[57]

the diffraction cone which is sampled at G. Fig.3.5 shows the experimental arrangement. Divergence of the beam is limited by a soller slit and primary slit assembly so that the whole of the primary beam is incident upon the specimen surface. A receiving slit of the same size is chosen so that only the irradiated area is seen by the detector. The X-ray background is improved by a scatter slit which excludes from the counter all rays except those emanating from the specimen.

The monochromator uses the focussing principle shown in Fig.3.2. The distance B between the centre of the crystal and the detector window for a given wavelength λ is given by

$$B = \frac{R\lambda}{d} = 2R\sin\theta_m$$

where

λ = wavelength of the radiation.
R = radius of curvature of the crystal surface.
d = interplanar spacing of the (0002) graphite planes.
θ_m = glancing angle at the monochromator.

The monochromator transmits a narrow band-width of wavelengths centred about the $K\alpha$ line of the target material. This effectively eliminates the white X-ray background, the $k\beta$ line and such parasitic scattering as X-ray fluorescence. Although the band-width is small n^{th} order reflections of the $\frac{\lambda}{n}$ harmonics may still be transmitted. These higher harmonics can be suppressed by means of pulse height discrimination.

The proportional counter has a resolving time of approximately 2μs allowing a linear response up to rates of greater than 100,000 counts per second. The Quantum-counting efficiency depends on λ , the dimensions of the counter tube, the composition and thickness of the window, and the nature and pressure of the gas.

Fig.3.5 The experimental arrangement.

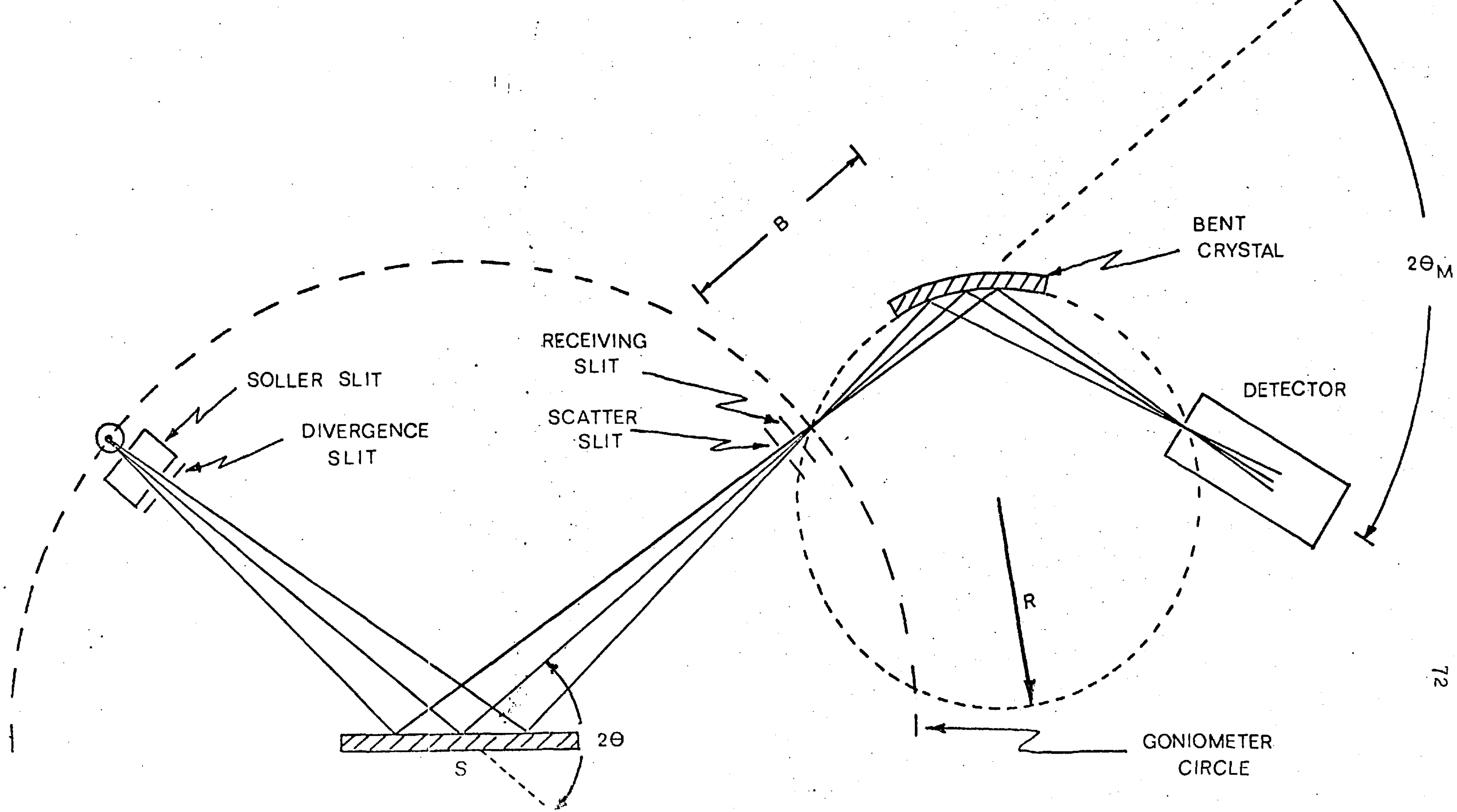

3.3 The Determination of the Absolute Intensity

In order to yield the interference function for Fourier integration the experiment and the processing of the measured data must meet the following requirements:

1. The measured intensity must be obtained as the medium's response to a monochromatic primary radiation.

2. Apart from the molecular configuration all effects which influence the angular distribution of the coherently scattered intensity must be eliminated by adequate correcting functions.

3. All kinds of extraneous scattering not characteristic of the molecular structure (Compton scattering, double scattering, fluorescence, scattering from sample holder and air scattering, etc.) must be eliminated either physically or by calculation from the total scattered intensity.

4. The intensity measured in arbitrary units (counts per second) must be put on an absolute scale (normalised to electron units).

5. The interference function must appear in the Fourier integral as a function of the variable s instead of the scattering angle 2θ .

6. The coherent and incoherent scattering functions of the independent atoms must be known as accurately as possible because of the dual role they play in the course of calculating the RDF.

The Polarisation Factor

All unpolarised electromagnetic waves are partially or totally polarised when reflected from dielectric interfaces. Although a completely satisfactory explanation of this phenomenon can only be given by Quantum theory, classical electromagnetism gives an adequate picture for our purposes. Fig.3.6 shows the experimental arrangement in which unpolarised X-rays from the anode are incident at an angle θ onto the surface of the flat specimen. Consider this incident wave as being resolved into two electric

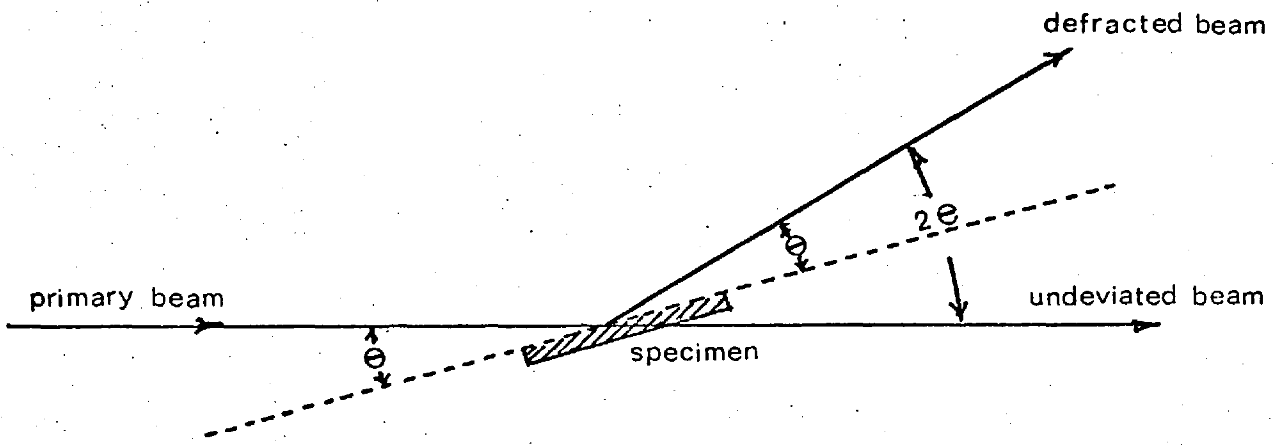

Fig.3.6 The symmetrical reflection geometry.

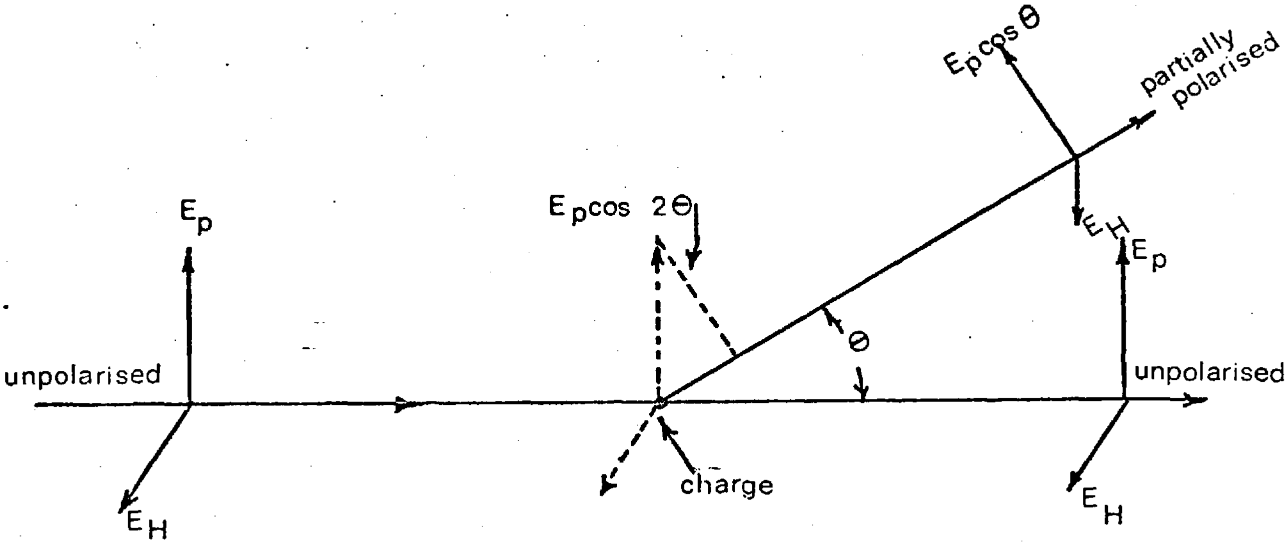

Fig.3.7 The polarisation of electric vectors on reflection from the specimen.

vector components of equal amplitude E_P and E_H. The diffracting electrons in the sample are set into forced vibrations parallel to both vectors, perpendicular to the beam, and thus radiate X-rays of the same frequency. Oscillating electric charges radiate maximum energy into directions perpendicular to their plane of motion and no energy in planes parallel to it. Fig.3.7 shows that E_H is independent of the angle θ ; whereas E_P decreases by cos2θ as θ increases, until at $2\theta = 90^{\circ}$, $E_P = 0$ and the beam is plane polarised.

Thus the diffracted intensity at an angle 2θ is proportional to:

$$E_H^{\,2} + (E_P\cos 2\theta)^2$$

or, since $I = E^2 = E_P^{\,2} + E_H^{\,2} = 2E_P^{\,2} = 2E_H^{\,2}$:

$$E^2\frac{(1 + \cos^2 2\theta)}{2}$$

Thus to obtain the true diffracted intensity, the experimental intensity must be modified by the factor

$$P(\theta) = \frac{1 + \cos^2 2\theta}{2}$$

which is independent of the diffractometer geometry.

The presence of a crystal monochromator in the diffracted beam introduces a further polarisation and modifies the correction to

$$P(\theta) = \frac{1 + \cos^2 2\theta \cos^2 2\alpha}{1 + \cos^2 2\alpha}$$

where α is the Bragg reflection angle of the monochromator.

The Absorption Factor

All X-rays are absorbed to some extent in passing through matter, the amount depending upon the absorption coefficient of the material concerned which is constant for a given wavelength of X-rays. The linear absorption coefficient μ is defined by

$$\mu = \frac{1}{t} \log_e \frac{I_o}{I} \qquad \text{cm}^{-1}$$

where I_o and I are the incident and transmitted intensities respectively and t the specimen thickness (cm), i.e.

$$\frac{I}{I_o} = e^{-\mu t}$$

The absorption factor will therefore be sensitive to wavelength and thus must be treated separately for the coherent beam (constant λ) and for the incoherent beam (λ changing with θ).

When the absorption is extremely low scattering takes place not only at the surface of the sample but also from its interior. This volume scattering results in a displacement and asymmetric broadening of the diffraction peaks and an angle dependent intensity effect[58]. Fig.3.8 represents a cross-section of the system in the plane of incidence. The incident and scattered beams are assumed to be parallel, of uniform intensity and of rectangular cross-section (breadth Z, width A and A + 2a). The beam widths A and A + 2a are determined by the slit sizes and the goniometer geometry, such that $a \gg 0$. The irradiated volume is a parallelpiped represented in the diagram by OESR. The radiation detected is scattered from a prism represented by OEKP, if the sample thickness t is greater than or equal to DP. The detected volume will be OEKNL if t is less than DP (i.e. DM). If t is less than FK (i.e. DH), the volume is OEJG and scattering from the whole volume is detected. For X-rays scattered from a volume element dV of material with linear absorption

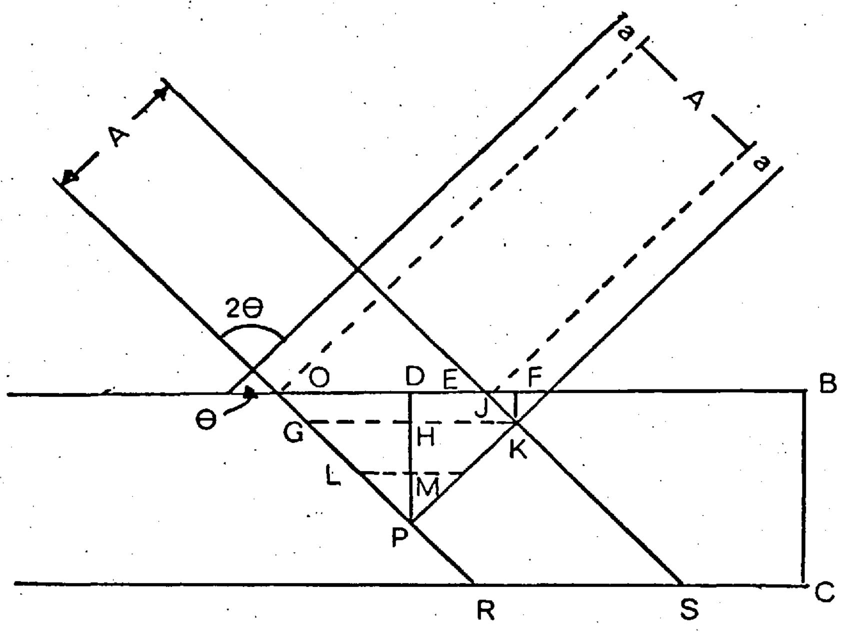

Fig.3.8 Cross-section of the system in the plane of incidence.

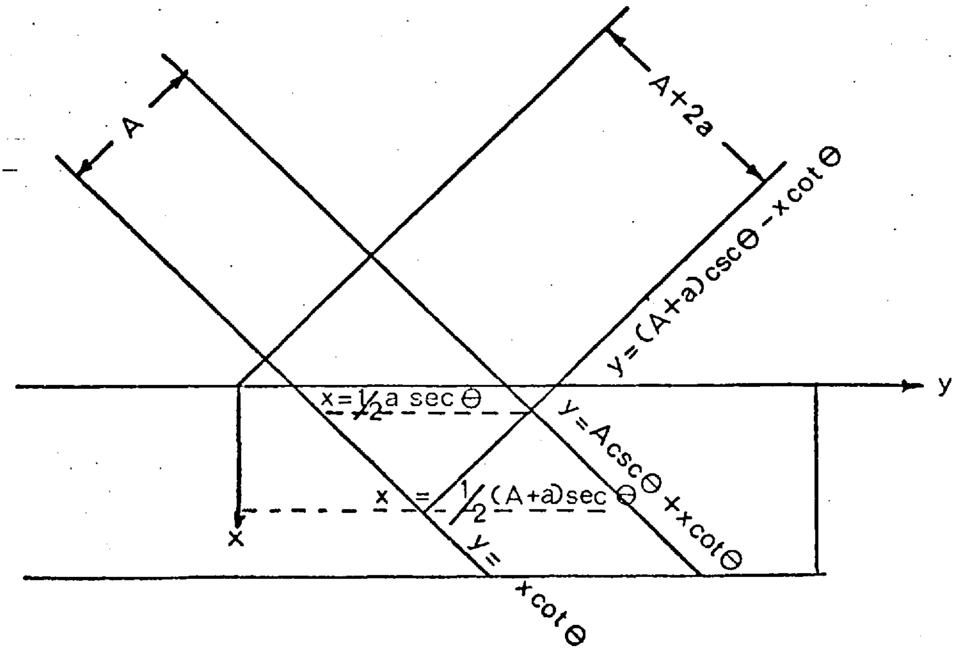

Fig.3.9 The limits of integration for the volume V.[58]

coefficient μ and total path length χ , the scattered intensity will be

$$dI = I_o e^{-\mu\chi} dV$$

Thus the total intensity scattered by V is

$$I = I_o \int_V e^{-\mu\chi} dV$$

Fig.3.9 shows the limits of integration for the volume V. For example for the volume OEJG, i.e. when $0 \leqslant t \leqslant \frac{1}{2}$ a sec

$$I = I_o \int_o^t \int_{x\cot\theta}^{A\cos\theta + x\cot\theta} \int_o^z \exp\left[-\mu(2x\csc\theta)\right] dXdYdZ$$

giving $\quad I = K(1 - e^{-2\mu t\csc\theta})$

where $\quad K = \dfrac{I_o AZ}{2\mu}$

Similarly we have for volume OEKNL i.e. $\frac{1}{2}$ a $\sec\theta \leqslant t \leqslant \frac{1}{2}(A + a)\sec\theta$

$$I = K\left[(1 - e^{-2\mu t\csc\theta}) + \left(\frac{2t\cos\theta}{A} - \frac{a}{A} + \frac{1}{\alpha}\right)e^{-2\mu t\csc\theta} \frac{-e^{-\beta}}{\alpha}\right]$$

and for volume OEKP, i.e. $t \geqslant \frac{1}{2}(A + a)\sec\theta$

$$I = K\left[1 - \frac{1}{\alpha}(1 - e^{-\alpha})e^{-\beta}\right]$$

where $\quad \alpha = 2\mu A\csc 2\theta$ and $\beta = 2\mu a\csc 2\theta$

To reduce the complexity of these equations all diffraction measurements were made using divergence and receiving slits of the same size, so that $a = 0$. As $t \rightarrow \infty$, $I \rightarrow I_\infty = I_0 AZ/2\mu$ and is independent of θ. Thus for the volume OEKP ($t \geqslant \frac{1}{2}(A + a)\sec\theta$), the absorption correction is

$$A(\theta) = \frac{I_t}{I_\infty} = 1 - \frac{1}{\alpha}(1 - e^{-\alpha})$$

Compton Modified Scattering

In 1923 Compton discovered that when a beam of X-rays of well defined wavelength λ_0 is scattered through an angle of 2θ by a metallic foil, the scattered radiation contains a component of well defined wavelength λ_1 which is longer than λ_0. This phenomenon is called the Compton effect. The wavelength λ_1 is dependent upon the angle of scattering 2θ but hardly at all on the material comprising the foil.

Compton scattering arises from collisions between a photon and a comparatively loosely bound electron. Part of the collision energy is transferred to the electron and the wavelength of the scattered photon is accordingly modified. No interference takes place between radiation scattered by different electrons of the material system (addition of intensities).

Fig.3.10 shows how such a collision might be represented, with an X-ray photon striking an electron (assumed initially at rest) and being scattered away from its original direction, while the electron receives an impulse and begins to move. In the collision the photon may be regarded as having lost an amount of energy that is the same as the kinetic energy gained by the electron, though actually separate photons are involved.

The wavelength λ_1 of the inelastically scattered photon is always greater than λ_0 since the photon has lost energy and from momentum conservation considerations it depends upon the scattering angle by

$$\lambda_1 - \lambda_0 = \frac{h}{m_0 c}(1 - \cos 2\theta)$$

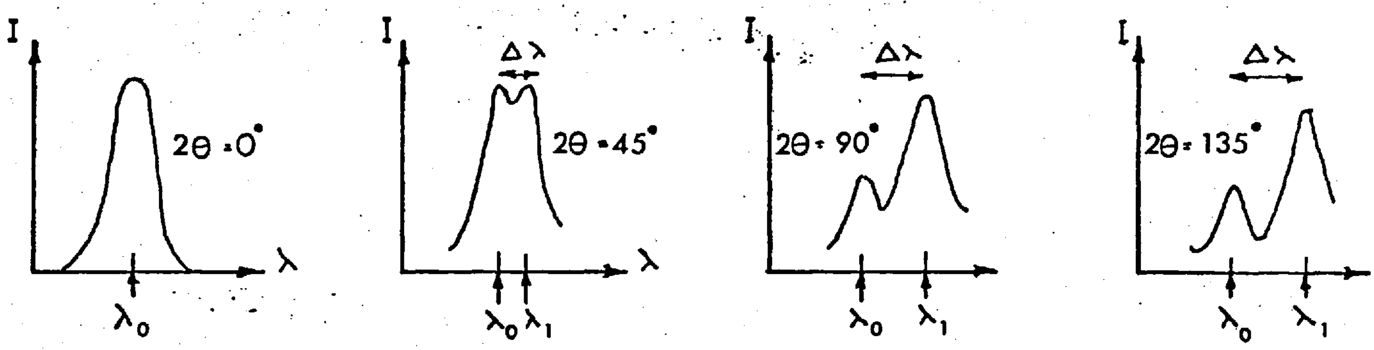

Fig.3.10a Wavelength spectra of quanta scattered at various angles from a carbon foil. From A.H. Compton, Phys. Rev. 22, 409, (1923).

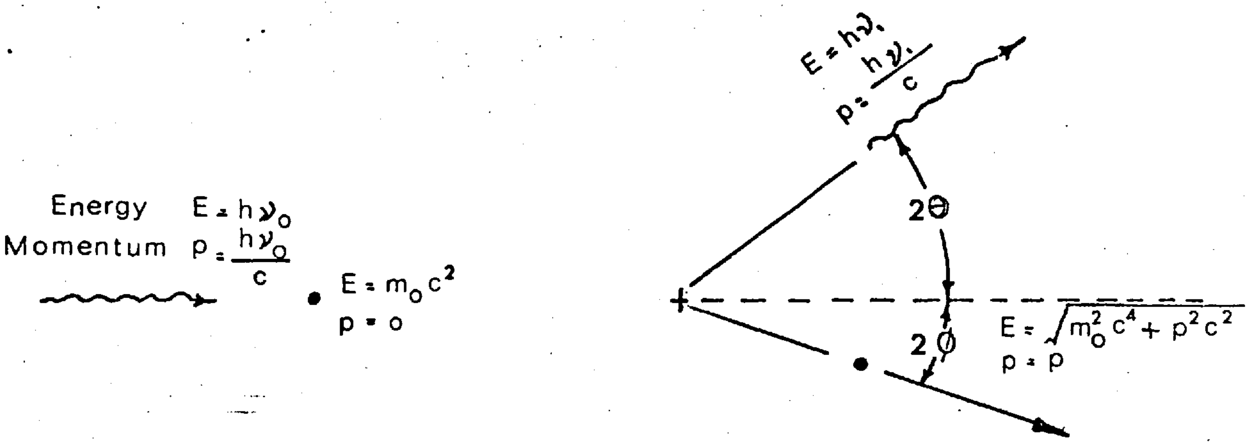

Before scattering After scattering

Fig.3.10b A collision between a quantum and a free stationary electron.

This equation gives the increase in wavelength expected for a photon that is scattered through angle 2θ by a particle of rest mass m_o; it is independent of the wavelength λ_o of the incident photon.

The quantity $\frac{h}{m_o c}$ is called the Compton wavelength of the scattering particle, which for an electron is 0.024Å. The greatest wavelength change that can occur will take place for $2\theta = 180^\circ$ when the wavelength change will be twice the Compton wavelength. Since the Compton wavelengths of other atomic particles are very much less due to their larger rest masses, the maximum wavelength change in the Compton effect is 0.048Å.

The Compton modified scattering is incoherent and takes no part in the interference phenomena characteristic of the structure. Compton scattering intensities of independent atoms have been calculated from Hartree-Fock and Thomas-Fermi-Dirac wave functions. However Hajdu[59] has recently shown that the incoherent intensities of atoms can be approximated by an analytic function of s containing three individual atomic parameters.

$$I_{inc}(s) = \left[Z - \frac{\left[f(s)\right]^2}{Z} \right] \left[1 - M\left\{ \exp(-Ks) - \exp(-Ls) \right\} \right]$$

where the coherent intensity $\left[f(s)\right]^2$ is obtained from a nine parameter fit for the atomic scattering factors

$$f(s) = \sum_{i=1}^{4} A_i \exp(-B_i s^2) + C$$

Since a crystal monochromator was employed in the diffracted beam it was found necessary to correct these tabulated incoherent intensities for the monochromator's discrimination against Compton scattering. The monochromator bandwidth was estimated experimentally by measuring the width of the 001 Gold peak when the monochromator was set on a white X-ray portion of the Mo or Cu spectrum (Fig.3.11). The Compton profile was modified in accordance with the shape of this peak as shown in Fig.3.12. It was found, however, that this correction had to be further modified (bold curve of Fig.3.12) before the experimental intensity curves could be successfully normalised.

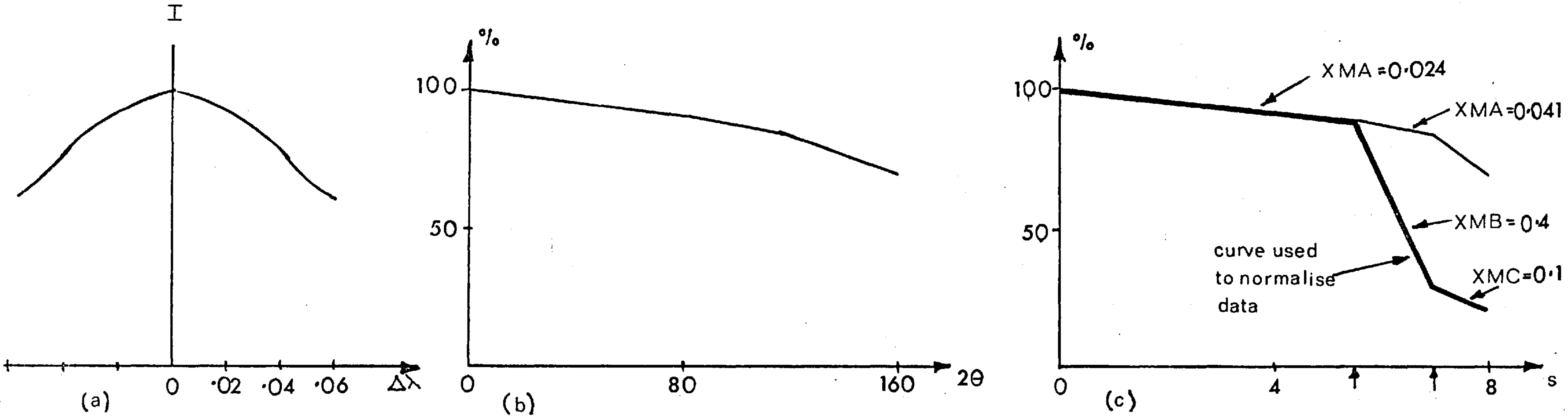

Fig.3.11 (a) The 001 gold peak obtained with a monochromator set on a white portion of the Mo X-ray spectrum. This curve was used as an approximation of the "window width" and attenuation of the monochromator (passband). (b) The shape of this peak in 2θ . (c) The shape in s. The bold curve in (c) was the actual curve needed to successfully normalise the data.

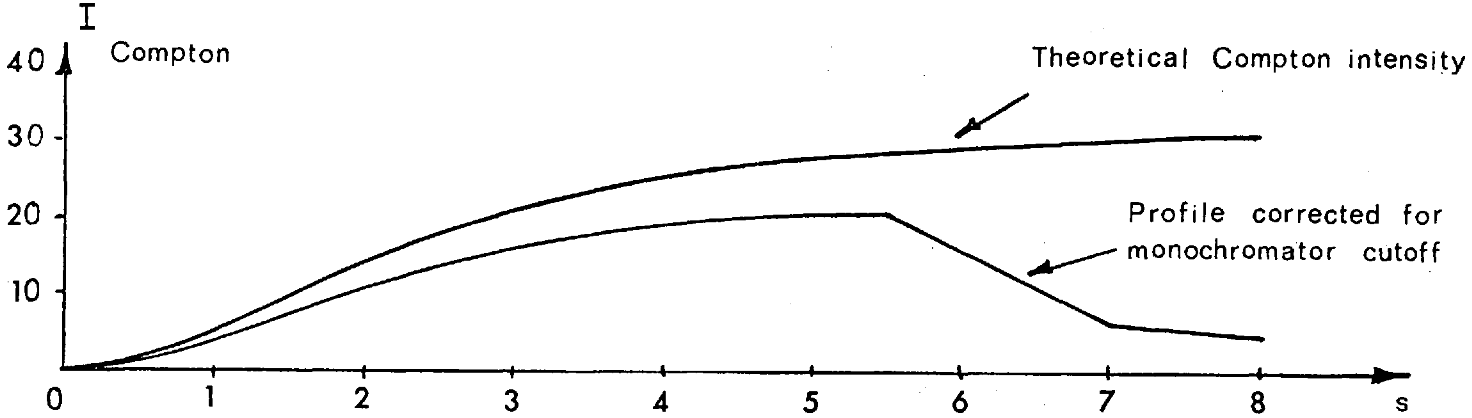

Fig.3.12 The Compton intensity for polymethyl methacrylate corrected for monochromator cut-off.

Modified Absorption Factor for the Incoherent Intensity

Various workers have pointed out that the wavelength shift of the absorption coefficient for the incoherent scattered beam must not be ignored if a relatively short primary wavelength is used and high scattering angles are involved. Hajdu and Palinkas have proposed formulae for this factor derived from[60] Victoreen's empirical formula for the mass absorption coefficient

$$\frac{d\mu}{d\lambda} = \rho(3C\lambda^2 - 4D\lambda^3) = q' \qquad \text{cm}^{-1}\ \text{Å}^{-1}$$

q' is constant for a given experiment (λ, ρ, C, D being constant). For a finite but small wavelength change $\Delta\lambda$, the increment $\Delta\mu$ of μ can be replaced by the first term of the Taylor's expansion

$$\Delta\mu = \frac{d\mu}{d\lambda}\Delta\lambda = q'\Delta\lambda \qquad \text{cm}^{-1}$$

This approximation is allowed since the Compton wavelength shift cannot exceed 0.048Å. The known Compton formula substituted into this expression yields

$$\Delta\mu = q\sin^2\theta \qquad \text{cm}^{-1}$$

$$\text{where} \qquad q = 0.048q'$$

$$= 0.048\,\rho(3C\lambda^2 - 4D\lambda^3)$$

ρ is the density of the sample (g.cm^3), λ the primary wavelength (Å), C and D are the atomic constants of Victoreen's formula.[61] For a complex system C and D are linear combinations of the corresponding constants of the constituent atoms.

The modified absorption factor A'(θ) for the incoherent beam is obtained by properly substituting $\mu' = \mu + \Delta\mu$ in the starting integral expression of the derivation of the absorption factor

$$I = I_o \int_V e^{-(\mu + \mu')x\csc\theta} \, dXdYdZ$$

Thus for the OEKP, i.e. $t \geqslant \frac{1}{2}(A + a)\sec\theta$

$$I = K'\left[1 - \frac{1}{\alpha'}(1 - e^{-\alpha'})e^{-\beta'}\right]$$

where $$K' = \frac{I_o AZ}{2\mu + \Delta\mu}$$

$$\alpha' = (2\mu + \Delta\mu)A\csc 2\theta$$

$$\beta' = (2\mu + \Delta\mu)a\csc 2\theta$$

The modified absorption coefficient for a = 0 is $A'(\theta) = 1 - \frac{1}{\alpha'}(1 - e^{-\alpha'})$

Multiple Scattering

In addition to singly scattered photons the measured diffracted intensity includes a component of multiply scattered photons whose total scattering angle in the sample is 2θ degrees. Numerical estimates of the fraction of double scattering which is the major fraction of the multiple scattering have been made by Warren and Mozi, Dwiggins and Park for unpolarised radiation. Fig.3.13 shows how this component arises in the symmetrical reflection geometry of the diffractometer. The primary X-ray beam of intensity I_o is incident upon the flat diffractometer sample at an angle θ. A fraction of the primary photons incident upon the elemental volume dV are scattered through an angle $2\theta_1$ into another part of the sample. A small fraction of this intensity $J(2\theta_1)$ is scattered by the volume element dV_2 through $2\theta_2$ degrees so that these X-rays leave the sample at the angle of incidence θ and are detected by the proportional counter.

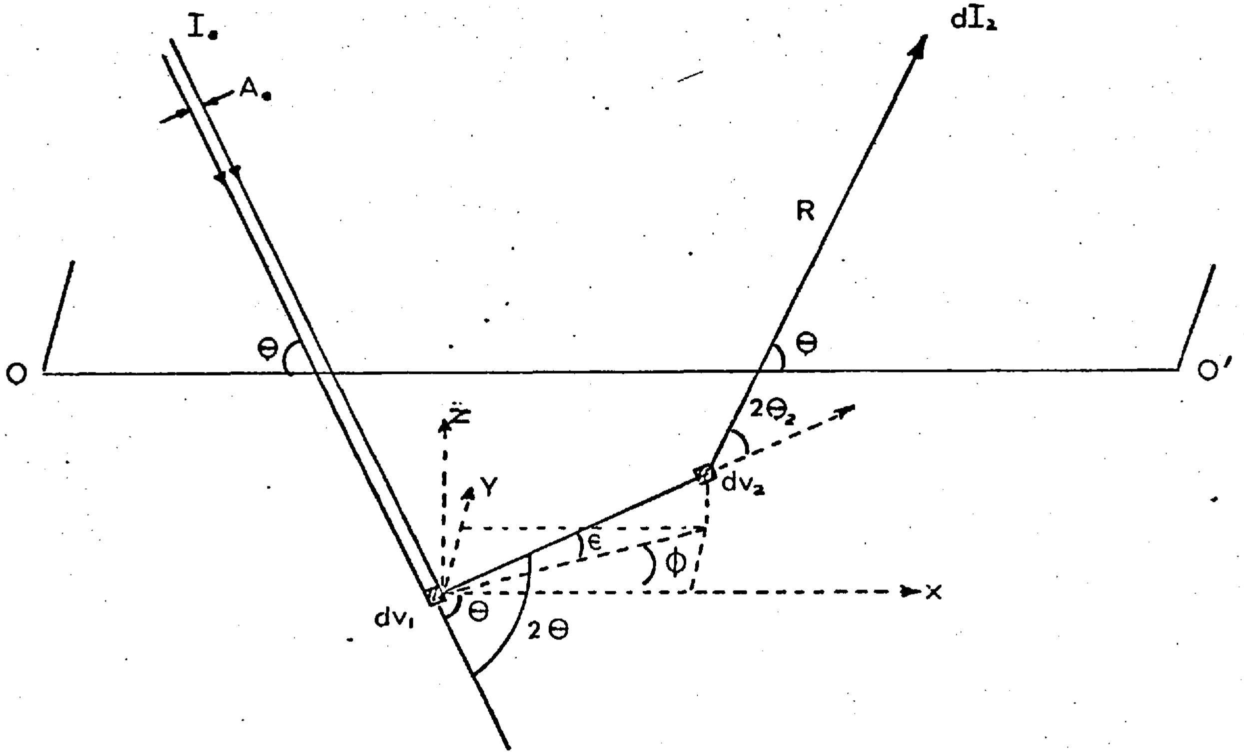

Fig.3.13 Double scattering in the symmetrical reflection diffractometer.[62]

Warren and Mozi have shown that the doubly scattered intensity I_2 at a distance R from the sample is given by[62]

$$I_2 = \frac{I_o n^2}{R^2} \int_{V_1} \int_{V_2} \frac{1}{r^2} \sigma_{e2} J(2\theta_1) J(2\theta_2) \exp(-\mu L) dV_1 dV_2$$

where n = number of units of composition per unit volume

r = distance between first and second scattering points

V_1 = volume of sample illuminated by incident X-rays

V_2 = volume of sample viewed by detector

σ_{e2} = coherent electron cross-section for double scattering

L = total distance travelled by X-ray beam in the sample

Dwiggins and Park have shown that the ratio of secondary to primary intensity can be represented by[63]

$$\frac{I_2}{I_1} = \frac{(\sum Z_j^2)^2 \, Q(b, q, \theta, \mu t)}{\sum f^2 \sum A_j \mu_j \{m\}}$$

where Z_j, A_j and $\mu_j\{m\}$ are the atomic number, atomic weight and mass absorption coefficient of the element j respectively. b and q are parameters which are used to approximate the scattering J. The function Q has been extensively tabulated so that I_2/I_1 may be determined without making lengthy calculations. Except for samples with very high absorption coefficients the correction for double scattering is too large to be neglected. Typical values of I_2/I_1 range from 1 to 10% with materials containing mainly hydrocarbons for ut values of 0.3 to 3.0.

3.4 The Normalisation Process

Two independent methods are available to us for finding the factor transforming the numerical values of the experimental intensity from arbitrary units into electron units. The first method consists of simply dividing a theoretical intensity value by the corresponding experimental one

$$\beta_i = \frac{\sum f^2 + I_{inc}}{I_{expt}} \qquad \text{for } s_i$$

where I_{inc} is the calculated incoherent scattering together with double scattering, and I_{expt} the corrected experimental intensity. At high values of s_i, β_i must converge to a single constant value, since I_{expt} tends to the scattering of independent atoms. It is obvious that the mean value of a number of such converged quotients must yield a more reliable value. The resulting quotient is used as the normalising factor

$$\beta = \frac{\sum_1^n \beta_i}{n} \qquad \text{for } s > s_{min}$$

The second method relies on the principle of the conservation of intensity, requiring that the total amount of theoretical scattering intensity $\sum f^2 + I_{inc}$ shall be exactly the total amount of experimental intensity (see Chapter II). In the case of spherical symmetry, Krogh-Moe[64] and Norman[65] have shown that the scaling factor required to equalise the intensities is given by

$$\alpha = \frac{\int_0^{s_m} s^2(\sum f^2 + I_{inc})ds - 2\pi^2 Z\rho}{\int_0^{s_m} s^2 I_{expt} ds}$$

The second term in the numerator here corresponds to the absence of the zero-angle scattering from the experimental intensity in the denominator. The fact that α and β agree is obviously a necessary condition, but does not mean that the correction process is perfect. If both the measurements and the calculations were acceptable, experience showed that the values of α and β agreed to within 1% accuracy.

Normalisation Error

Many authors have discussed normalisation procedures and the errors introduced by improper normalisation.[64,66] If I_t is the value of the correctly normalised intensity

$$I_t = \sum f^2 + I_{inc} + I_{coh}$$

then if the data is scaled to $(1 + a)I_t$ the function transformed is

$$(1 + a)I_t - (\sum f^2 + I_{inc}) = (1 + a)I_{coh} + a(\sum f^2 + I_{inc})$$

The transformation of the first term is correct (subject to termination errors), multiplied by $(1 + a)$.

If the Compton scattering is approximated to

$$I_{inc} \sim \sum_m (Z_m - \frac{f_m^2}{Z_m}) \qquad \text{then}$$

$$a(\sum f^2 + I_{inc}) = a \sum (1 - {}^1/Z_m)f_m^2 + a \sum Z_m$$

The transform of the first term is a weighted intra-atomic radial distribution function having a peak maximum near the average atomic radius and a minimum near the average atomic diameter. The transform of the second term is the function

$$\frac{2a}{r\pi} \sum Z_m(\sin(rs_{max}) - rs_{max}\cos(rs_{max}))$$

which is oscillatory in r.

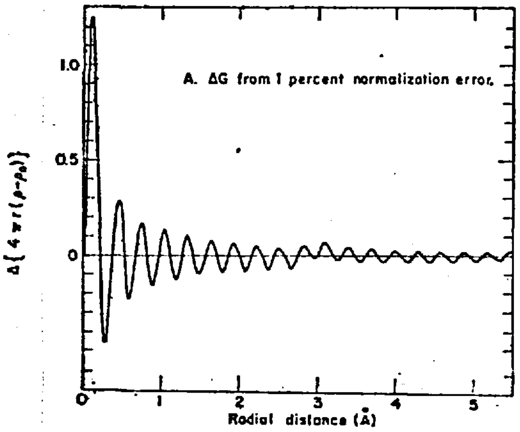

Fig.3.14 Variation in the radial distribution function G(r) arising from normalisation errors (from Kaplow et al.[67]). The large peak close to r = 0 is characteristic of such errors.

For example if $s_{max} = 12\text{Å}^{-1}$, the first few maxima will be at 0.23, 0.78 and 1.30Å, and the minima at 0.52 and 1.05Å. Scaling errors may thus change the areas under peaks and produce peak shifts. Fig.3.14 shows Kaplow, Strong and Averbach's estimate of a 1% normalisation error on their radial distribution functions of liquid mercury[67]. The characteristic large peak close to r = 0 is readily detected in all incorrectly normalised RDFs and can thus be used as a measure of the quality of the process.

3.5 The Effect of Neglecting Small Angle X-ray Diffraction (SAXD)

The Fourier transform of the scattered intensity, the reduced radial distribution function, is given by

$$G(r) = 4\pi r\left[\rho(r) - \rho_o\right] = \frac{2}{\pi}\int_0^\infty s(I_{expt} - \sum f^2)\sin rs\, ds$$

The term $-4\pi r\rho_o$ arises from the omission of "volume (zero-angle) scattering". This is the intensity scattered at extremely small angles due to the finite size of the scattering sample and is unobservable for macroscopic samples. Thus the above expression for G(r) is correct only if all the scattered intensity, except volume scattering, is included in I_{expt}. However, materials containing density fluctuations of much greater than atomic size produce scattering at angles far too small to be measured by conventional wide angle diffractometers.

Cargill[68] has considered the effect on the radial distribution function of neglecting SAXD, and has shown that if the SAXD and WAXD are well separated, an approximate expression for G(r) is

$$G_{expt}(r) = 4\pi r\left[\rho(r) - \rho_o\left\{1 + (\overline{\eta^2}(\omega)/\rho_o^2)\gamma(\omega,r)\right\}\right]$$

$\overline{\eta^2}(\omega)$ is the average square of atomic density fluctuations, $\gamma(\omega,r)$ is the density fluctuation correlation function, and ω is a volume element

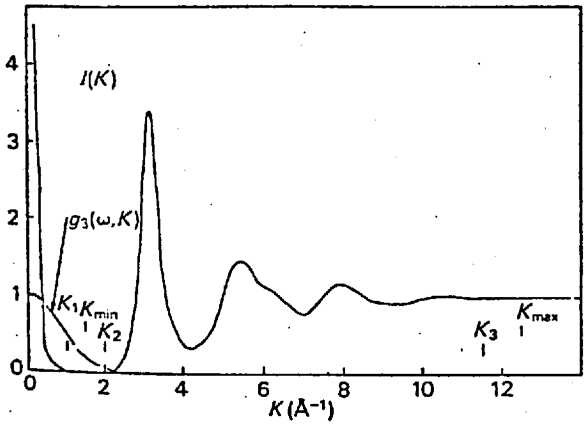

Fig.3.15a An interference function I(K) for a material in which the wide-angle and small-angle X-ray scattering are well separated. ($g_3(\omega,K)$ is the small-angle scattering intensity).

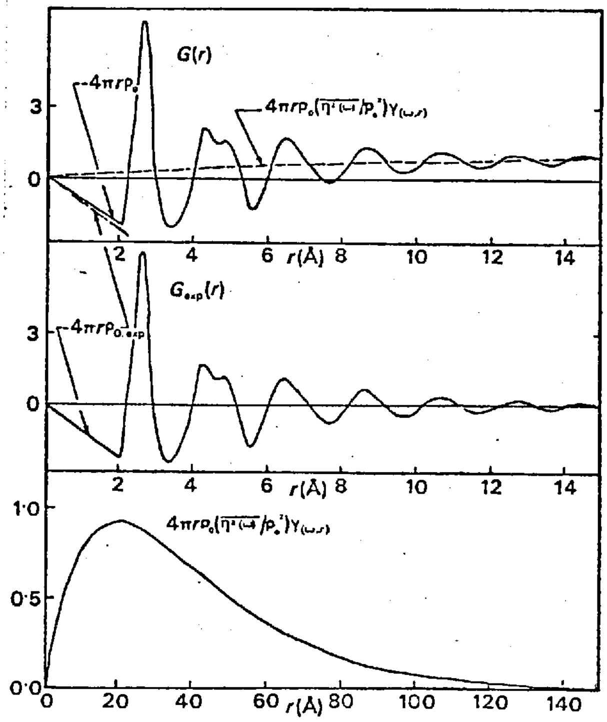

Fig.3.15b (i) Reduced radial distribution function G(r) corresponding to interference function of Fig.3.15a when small-angle scattering is included. (ii) $G_{exp}(r)$ corresponding to interference function of Fig.3.15a when small-angle scattering is neglected. (iii) $4\pi r\,\rho_o(\overline{\eta^2}(\omega)/\rho_o^2)\,\gamma(\omega,r)$ which is the difference between G(r) and $G_{exp}(r)$. Note change of vertical and horizontal scales. (from Cargill[68]).

larger than the average atomic volume but smaller than the scale of long range density fluctuations. The term $(\overline{\eta^2}(\omega)/\rho_o^2)\gamma(\omega,r)$ describes atomic density fluctuations.

Thus neglecting SAXD gives rise to a $G_{expt}(r)$ which appears to correspond to a material of greater average atomic density than that of the sample being studied.

Fig.3.15 shows the effect on the reduced radial distribution function of the inclusion and omission of small angle scattering.

In the case of amorphous polystyrene[52] it has been calculated that under the "worst possible" conditions this contribution to the results is approximately 3% at r = 10Å.

3.6 The Termination Process and Termination Error

The Fourier transformation of (58) requires that the intensity of the scattering be known from $s = 0$ to $s = \infty$. The experimental intensity curve is, however, only known between the limits $s = s_{min}$ and $s = s_{max}$. The effect of the omission of scattering between $s = 0$ and s_{min} was discussed in the previous section. The termination of data at $s_{max} < \infty$ introduces spurious detail in the resultant transform (this termination error was touched on in section 2.8 while discussing the microscope analogy). Fig.3.16 shows the reduced radial distribution function

$$4\pi r\left[\rho(r) - \rho_o\right] = \frac{2}{\pi}\int_0^{8.0} sI \sin rs \, ds$$

for polystyrene. The termination of the data at $s = 8.0$ has led to a violently distorted RDF. To overcome this effect the normalised intensity $I(s)$ must be replaced by the interference function

$$I(s) - \sum_{uc} f^2$$

where $\sum_{uc}$ is the sum over the atoms of the unit of composition of the sample.

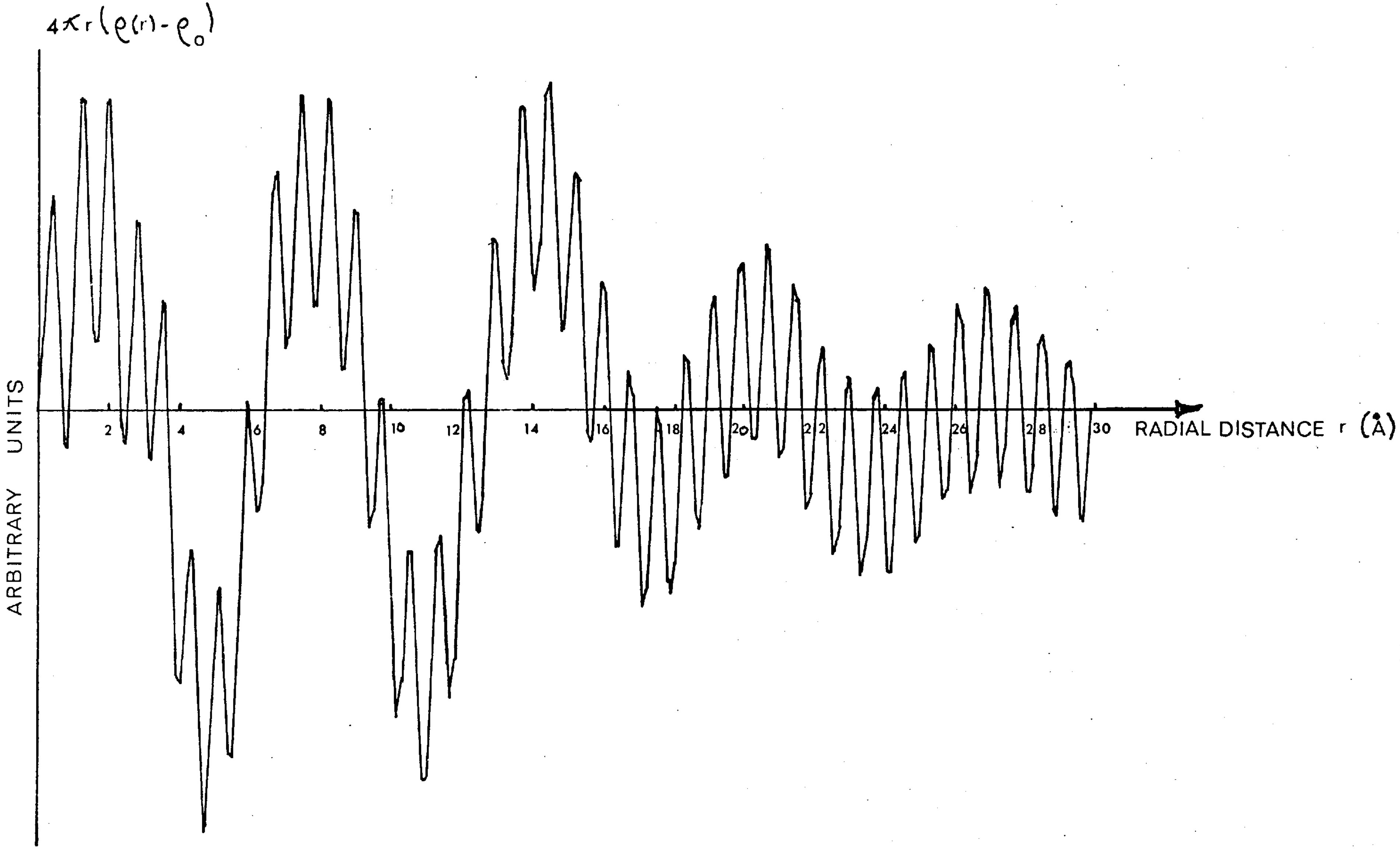

Fig.3.16 Reduced radial distribution function for polystyrene obtained without normalising the intensity. The termination of data at s = 8.0 has led to a violently distorted RDF.

If I(s) is properly normalised and extends over a sufficient range of s, the interference function will tend to zero so that

$$\int_0^\infty s(I - \sum f^2)\sin rs\, ds \quad \text{becomes} \quad \int_0^{s_{max}} s(I - \sum f^2)\sin rs\, ds$$

If the interference function $I - \sum f^2$ does not completely damp away to zero within this range a small termination ripple of approximate period $2\pi/s_{max}$ will remain. It has been demonstrated by Bragg and West that its influence may be reduced when the intensity is multiplied by a function $\exp(-ks^2)$, sometimes called an artificial temperature factor, convergence factor or damping factor. The value of the constant k is selected so as to effectively eliminate the termination ripple in the transform. Unfortunately this procedure also distorts the true peaks and results in an overall reduction of the resolving power. In Chapter IV it is shown that when our intensity data was terminated at s = 8 (Cukα) and s = 17 (Mokα) no significant changes in the transforms were seen showing that no large termination of information was occurring.

Transforming the function $I - \sum f^2$ has the effect of removing from the RDF all electron-electron vectors from within each single atom, leaving only the vectors between electrons in different atoms. Thus peaks in the RDF close to r = 0 have no physical meaning and must therefore be spurious, a fact used to ensure good normalisation.

Two additional types of errors, not considered here, may be of consequence under certain conditions. Instrumental broadening and the combined presence of $K\alpha_1$ and $K\alpha_2$ radiations can both cause a damping of the derived distribution function. These errors can be readily corrected if necessary but were not significant in these experiments.

3.7 Concluding Remarks

In this chapter I have high-lighted the problems of normalisation because it is this procedure which leads to the largest systematic error in the RDF. Unfortunately the normalisation process is necessary since without it the Fourier transform would be hopelessly distorted by termination effects. Perfect normalisation of experimental data must not be expected since correction factors such as for Compton scattering and multiple scattering are essentially approximations of the true scattering behaviour.

The interference function is in some ways more useful since it is the properties of this function which govern the resulting RDF and it has the advantage of being relatively free from error.

CHAPTER FOUR

Experimental Results

4.1 The WAXD from Amorphous Atactic Polystyrene

Flat diffractometer samples were cut from 3mm thick sheets of commercially available injection moulded atactic polystyrene (East Anglia Chemicals Ltd.). Typical specimen dimensions were 2cm x $1\frac{1}{2}$cm x 0.3cm. Fig.4.1 shows the uncorrected experimental diffracted X-ray intensity obtained for such "as received" sheets using CuKα radiation (40KV, 40mA, $\frac{1^{\circ}}{6}$ divergence and receiving slits). All subsequent data collected using CuKα was obtained using these machine settings. Two very distinct halos were detected at $2\theta \sim 10^{\circ}$ and $2\theta \sim 19^{\circ}$ while very much weaker ones were found at $2\theta \sim 41^{\circ}$ and $2\theta \sim 80^{\circ}$. The Bragg spacings corresponding to the maxima of these peaks were as follows:

2θ	10°	19°	41°	80°
d-spacing (Å)	8.85	4.67	2.20	1.20

Table 4.1 The Bragg spacings for atactic polystyrene.

Fig.4.2 shows the normalised corrected intensity together with the theoretical independent scattering curve. As required these two intensities converged at large diffraction angles where no interference effects were present. The resulting interference function that was obtained is shown in Fig.4.3.

It was explained in Chapter III that the incoherent Compton scattering emitted by the specimen was modified by the graphite monochromator in the diffracted beam. The correction required to the theoretical Compton scattering was estimated from the shape of the 001 Gold peak when the monochromator was set on a white portion of the X-ray spectrum. It was found that after

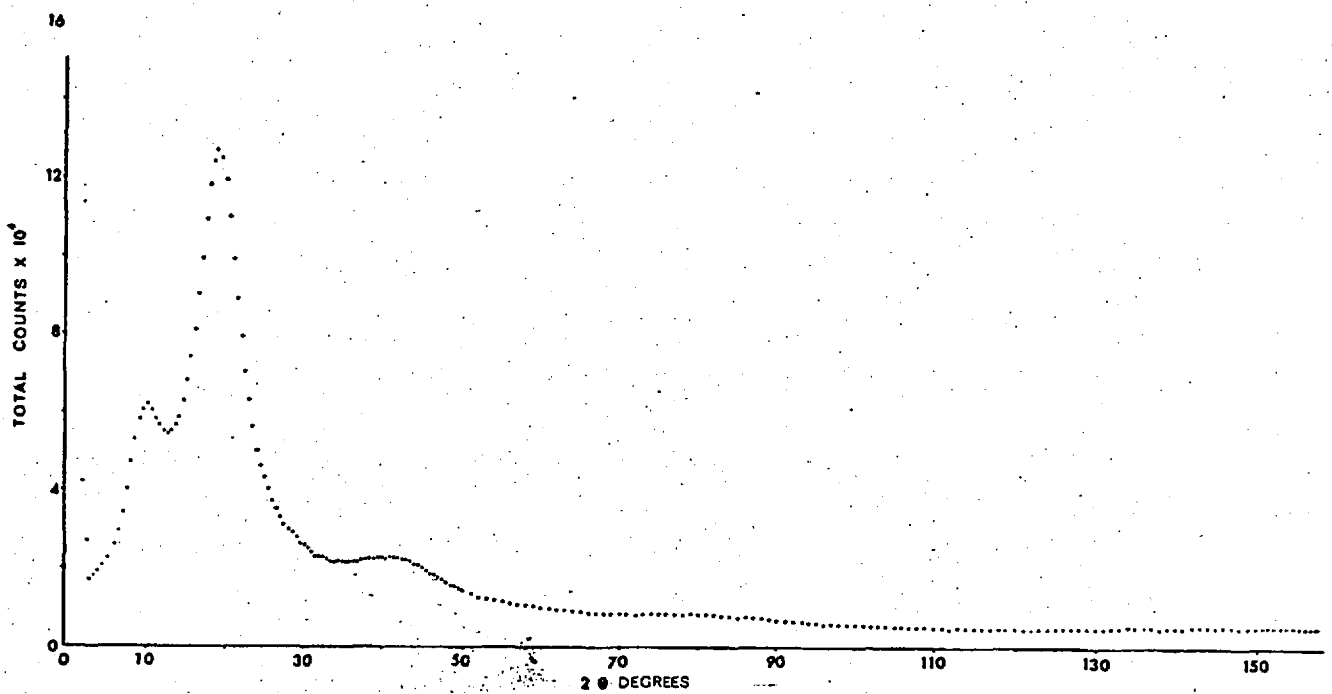

Fig.4.1 The uncorrected experimental diffracted X-ray intensity for an "as received" sheet of atactic polystyrene (CuKα radiation).

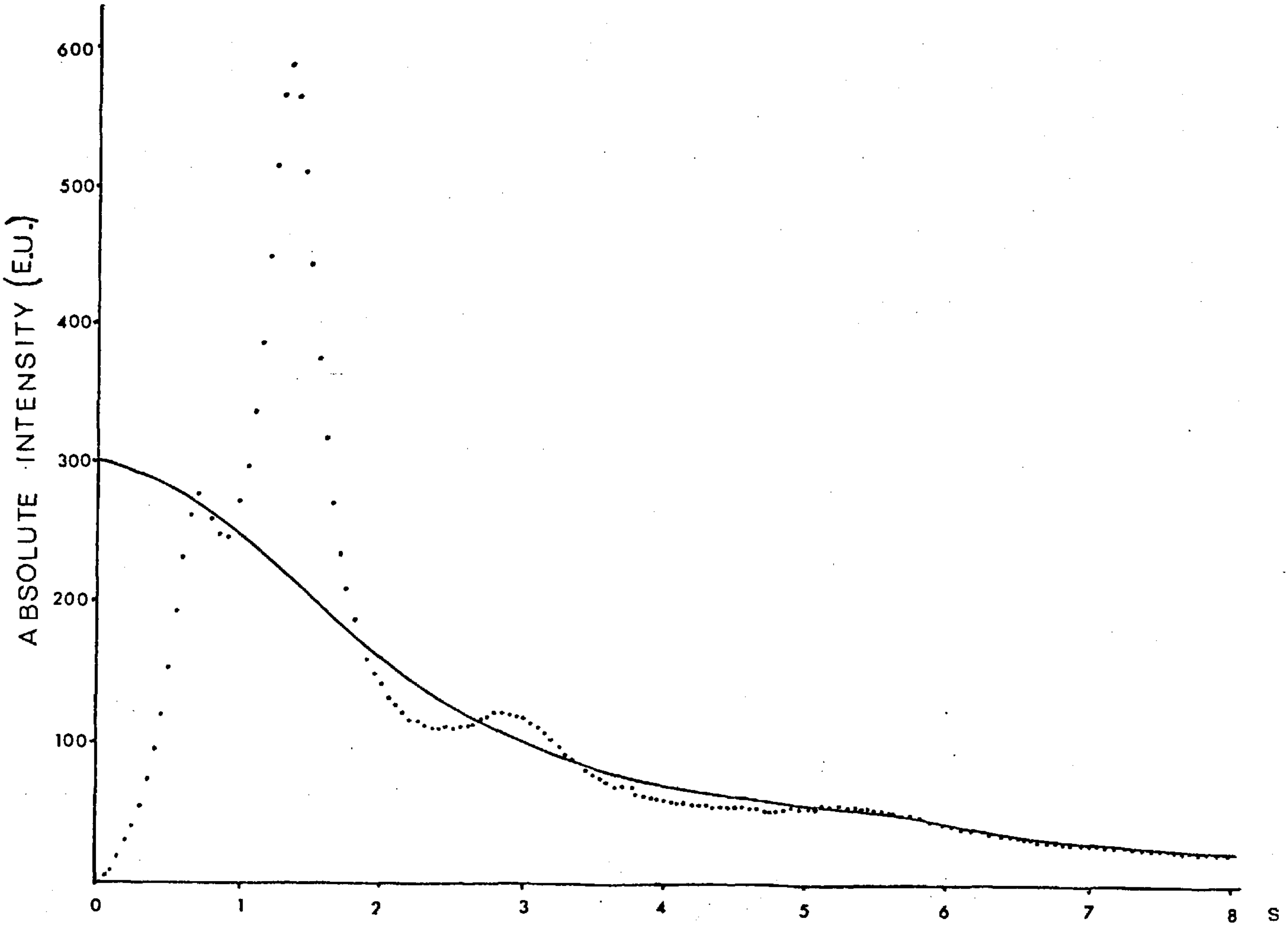

Fig.4.2 The normalised intensity corrected for absorption and polarisation together total theoretical independent scattering curve (includes double scattering and Compton intensities).

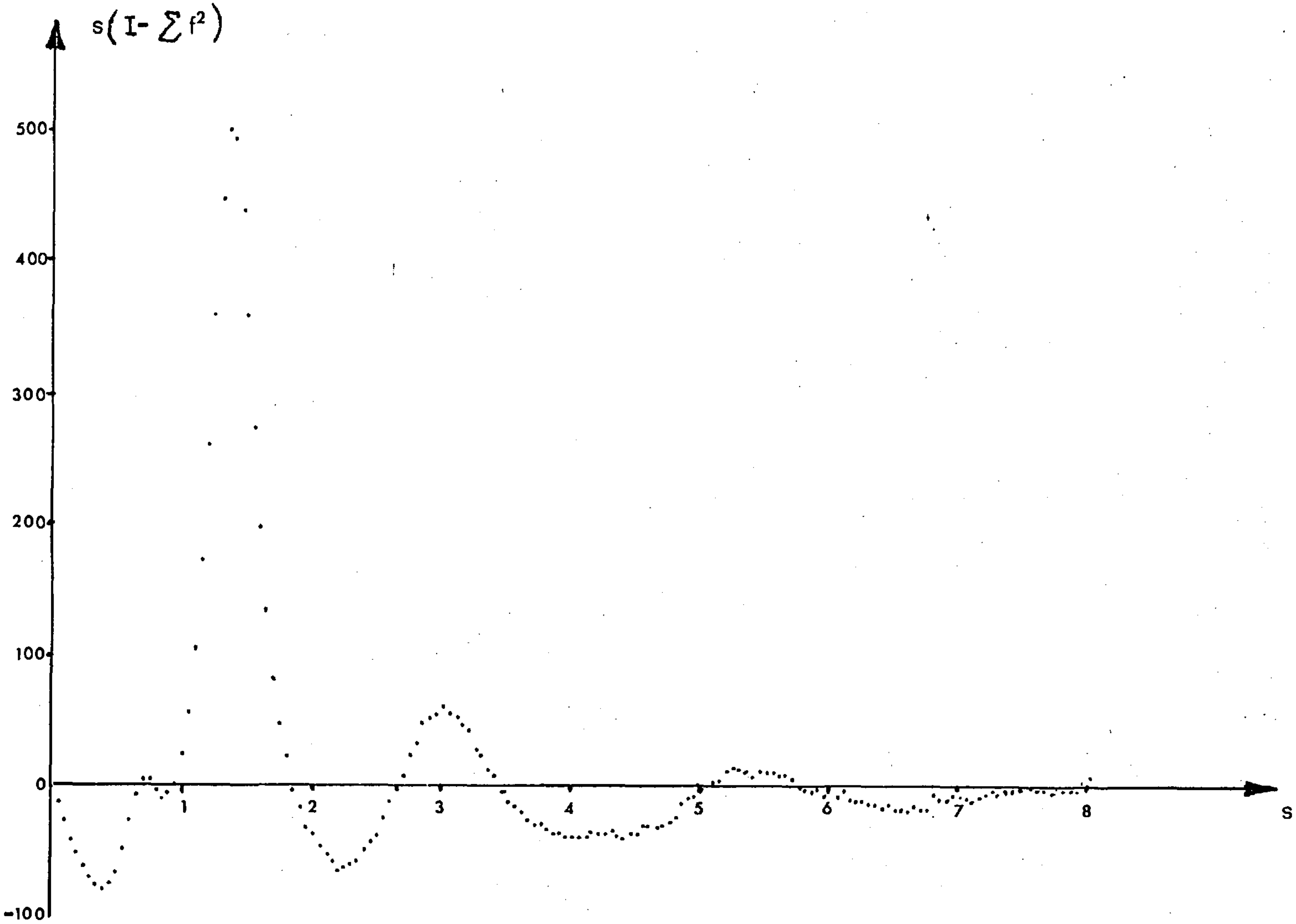

Fig.4.3 The interference function for "as received" atactic polystyrene.

this correction was applied, only slight modification to the tail of the Compton curve was necessary to successfully normalise all subsequent data. Thus all the interference functions presented in this chapter were effectively obtained using the same Compton correction.

Table 4.2 gives the details of the interference function for atactic polystyrene:

Peak	1	2	3	4
s (Å^{-1})	0.7	1.35	3.0	5.35
Intensity (e.u.)	2	497	55	11
d-spacing (Å)	9.0	4.65	2.10	1.18

Table 4.2 Details of the interference function for atactic polystyrene (CuKα).

The peaks in the interference function were measured at the centre of a line drawn horizontally through each peak at half its maximum height.

Fig.4.4 shows the reduced electronic radial distribution function obtained for atactic polystyrene. The peaks in the RDF appeared considerably distorted suggesting that they were composed of two or more single peaks. The radial density function (Fig.4.5) emphasised this distortion:

Peak	r (Å)	$4\pi r(\rho(r) - \rho_o)$	r (Å)	$4\pi r^2(\rho(r) - \rho_o)$
1	1.0	117	1.4	140
2	~2.3	~40	~2.3	~25
3	5.5	66	5.6	350
4	10.3	35	10.35	365
5	14.9	7	14.85	110
6	19.6	4	19.6	90

Table 4.3 Details of the radial distribution and radial density functions of atactic polystyrene (CuKα).

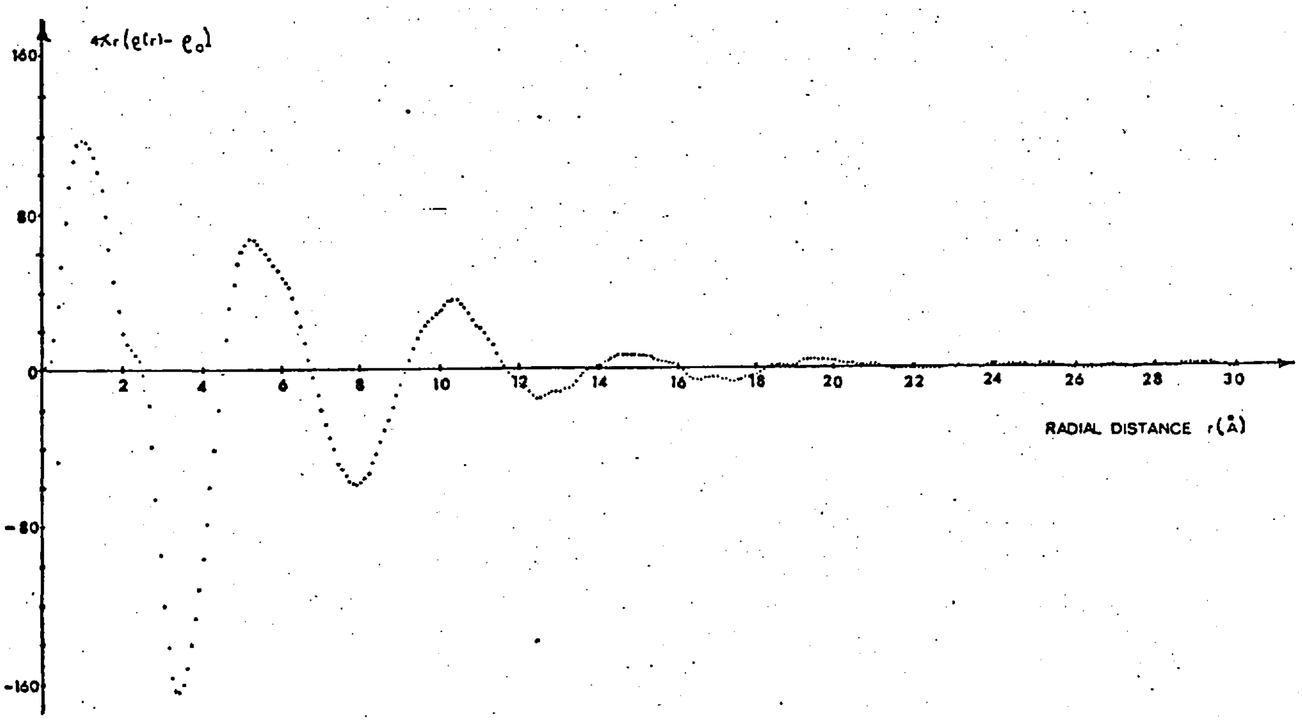

Fig.4.4 Reduced electronic radial distribution function for atactic polystyrene.

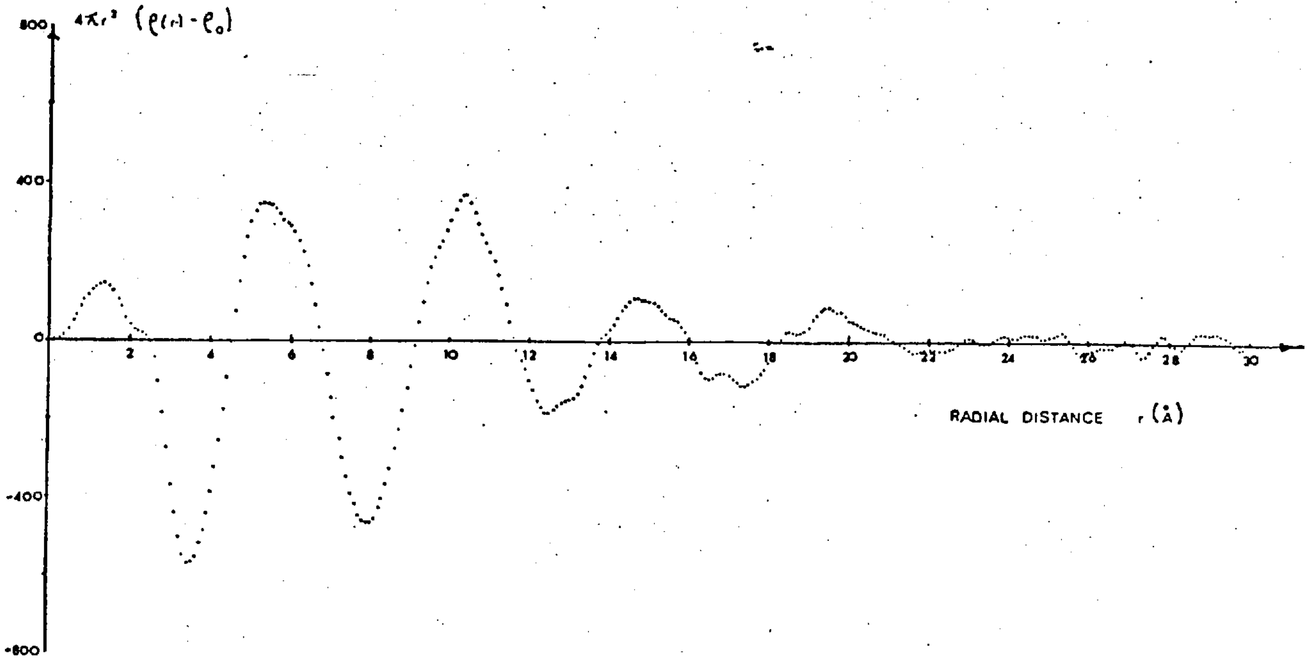

Fig.4.5 Radial density function for atactic polystyrene.

It is to be expected that the first two peaks in the RDF of this polymer would be of approximately the same size and occur at ~ 1.5Å (spacing between carbon atoms chemically bonded to nearest neighbours) and at ~2.5Å (spacing between second nearest neighbour carbon atoms). However Fig.4.4 shows the first peak at 1.0Å with only a small contribution at ~ 2.3Å for the second. As explained above, the $r \leqslant 3$Å region of the RDF is extremely sensitive to normalisation error and is dependent on the quality of the diffraction data at high s (which is poor). Fig.4.6 shows the interference function for the same polystyrene diffraction data which has been purposely incorrectly normalised. In the RDF (Fig.4.7) a large peak at r = 0.7Å was found together with sharp peaks at r = 1.4Å and r = 2.3Å. The peak at r = 0.7Å was obviously spurious and typical of faulty normalisation. In Fig.4.8 the RDF for the purposely incorrect normalisation is compared with that for the best normalisation which was obtained. Apart from a distinct ripple which extended throughout the transform, the two functions were remarkably similar. It was concluded therefore that although the RDF in the range $r \leqslant 3$Å was extremely sensitive to normalisation error and could be badly distorted in this region, the range $r \geqslant 3$Å which contained all the structural information was remarkably insensitive and considerable confidence could thus be placed in the transform in this region.

To assist in comparing these distribution functions with those of other workers, the reduced atomic distribution function for atactic polystyrene was also generated. Fig.4.9 shows that the interference function $s(I/\sum f^2 - 1)$ required here is far more sensitive to the normalisation process than the electronic form. In Chapter II it was stated that division of the interference function by $\sum f^2$ meant that the RDF was deconvoluted with the distribution function of an average atom. The atomic distribution function obtained in this way (Fig.4.10) has peaks corresponding to vectors between atom centres. Fig.4.10 clearly shows that all peaks have been drastically "sharpened" including the spurious normalisation ripple that is present. The accentuation of this ripple effectively obliterated the RDF at $r \geqslant 14$Å. However the function clearly shows the required peaks at 1.5Å and 2.5Å. Table 4.4 compares the peaks at Fig.4.10 with those of the RDF for quenched atactic polystyrene obtained by Wecker, Davidson and Cohen[52].

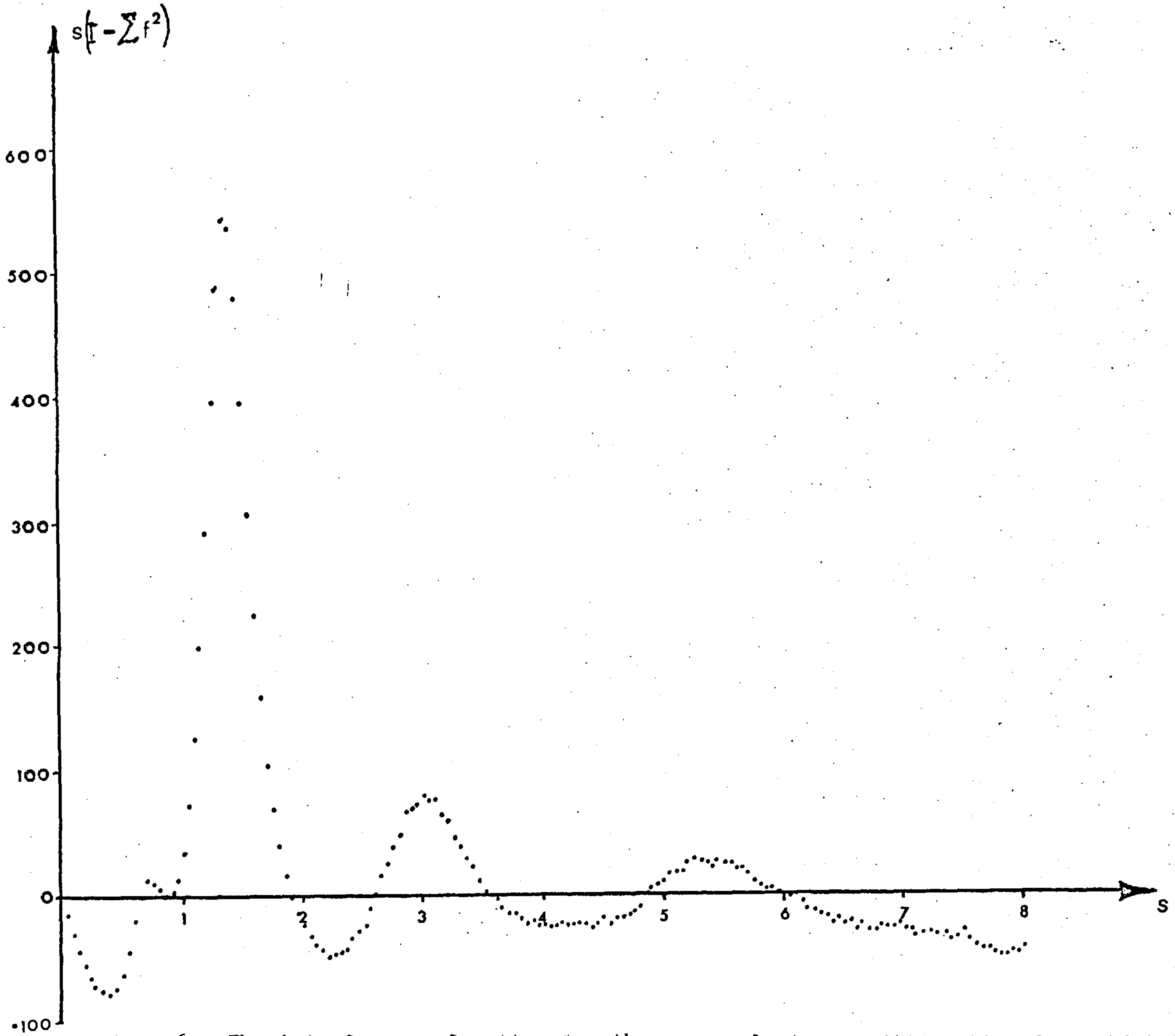

Fig.4.6 The interference function for the same polystyrene diffraction data which has been incorrectly normalised (incorrect cut off applied to the Compton scattering profile).

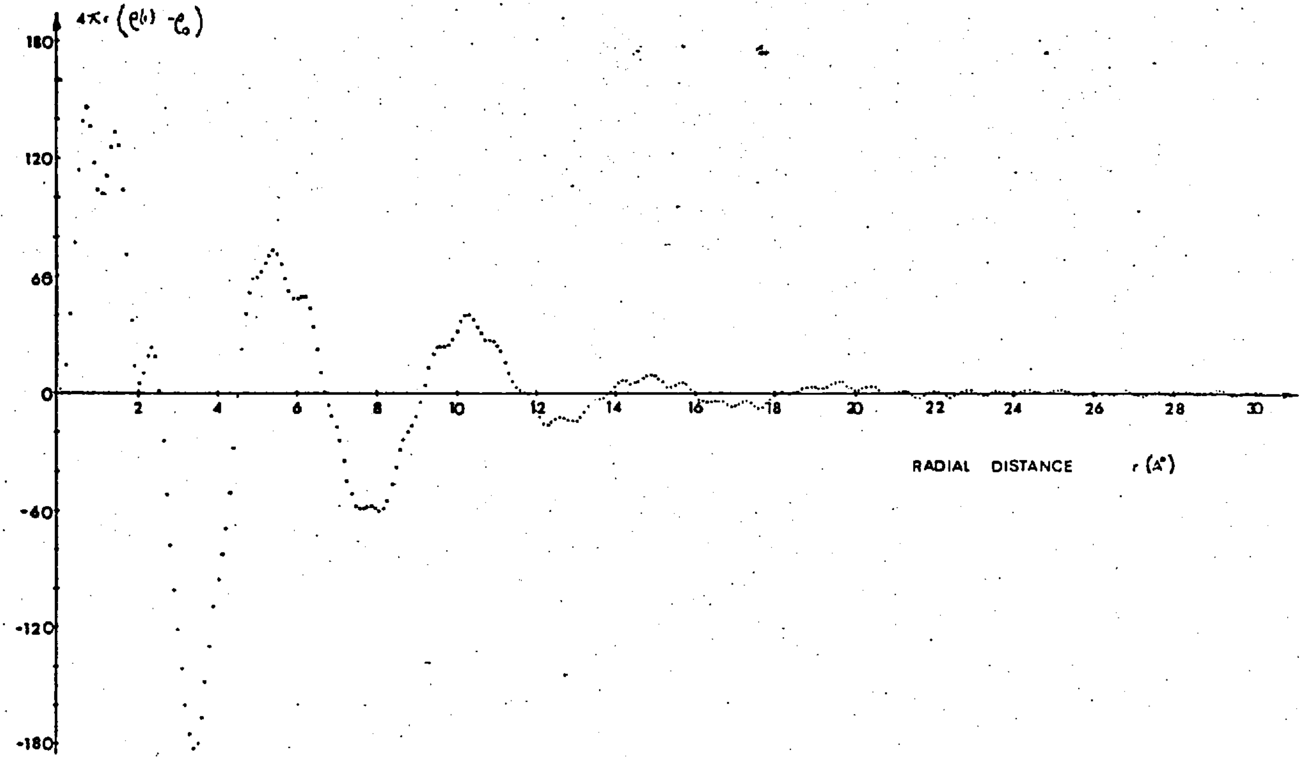

Fig.4.7 Reduced electronic radial distribution function for incorrectly normalised atactic polystyrene.

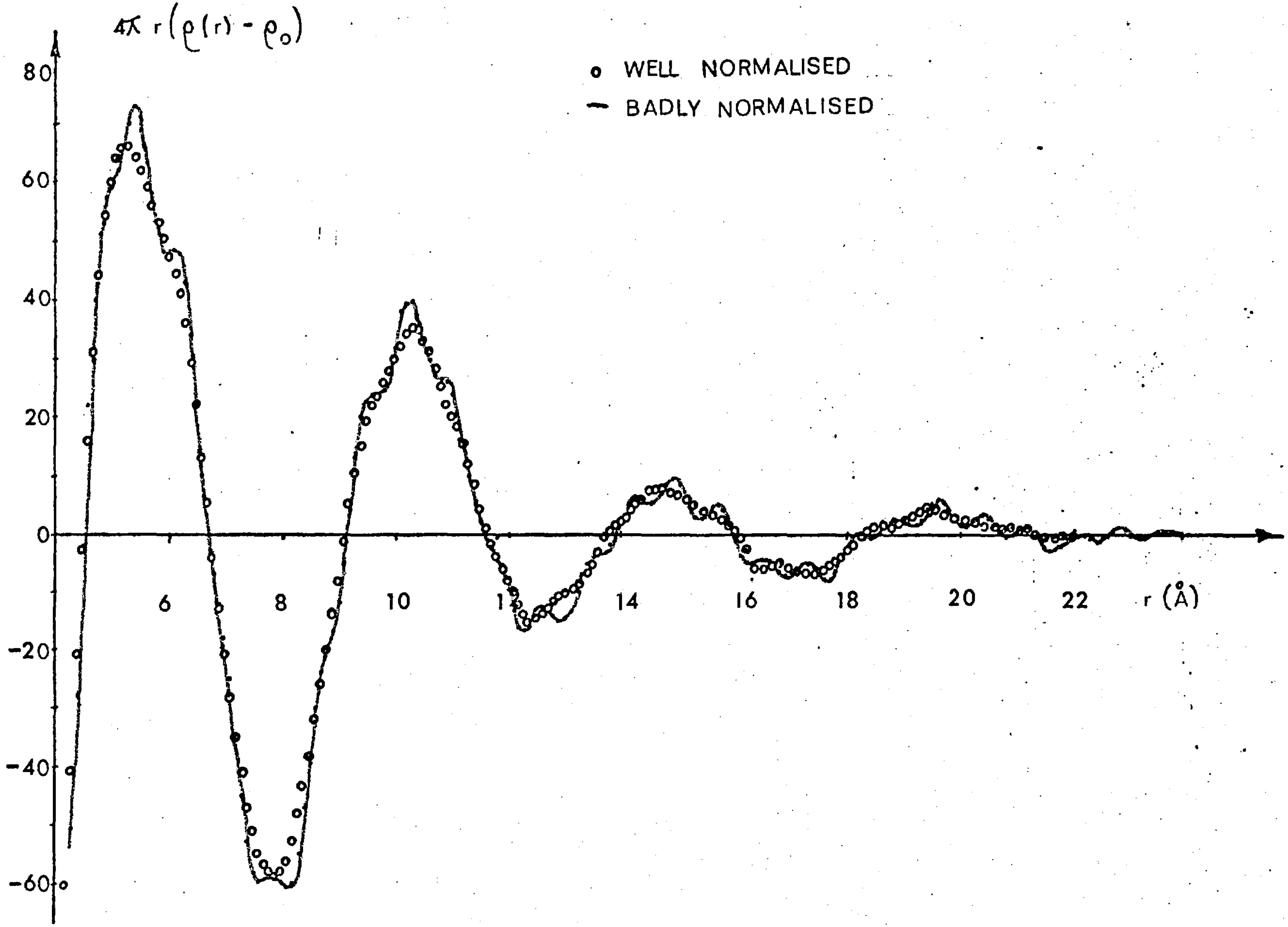

Fig.4.8 Comparison of the RDFs of the correctly and incorrectly normalised data for atactic polystyrene.

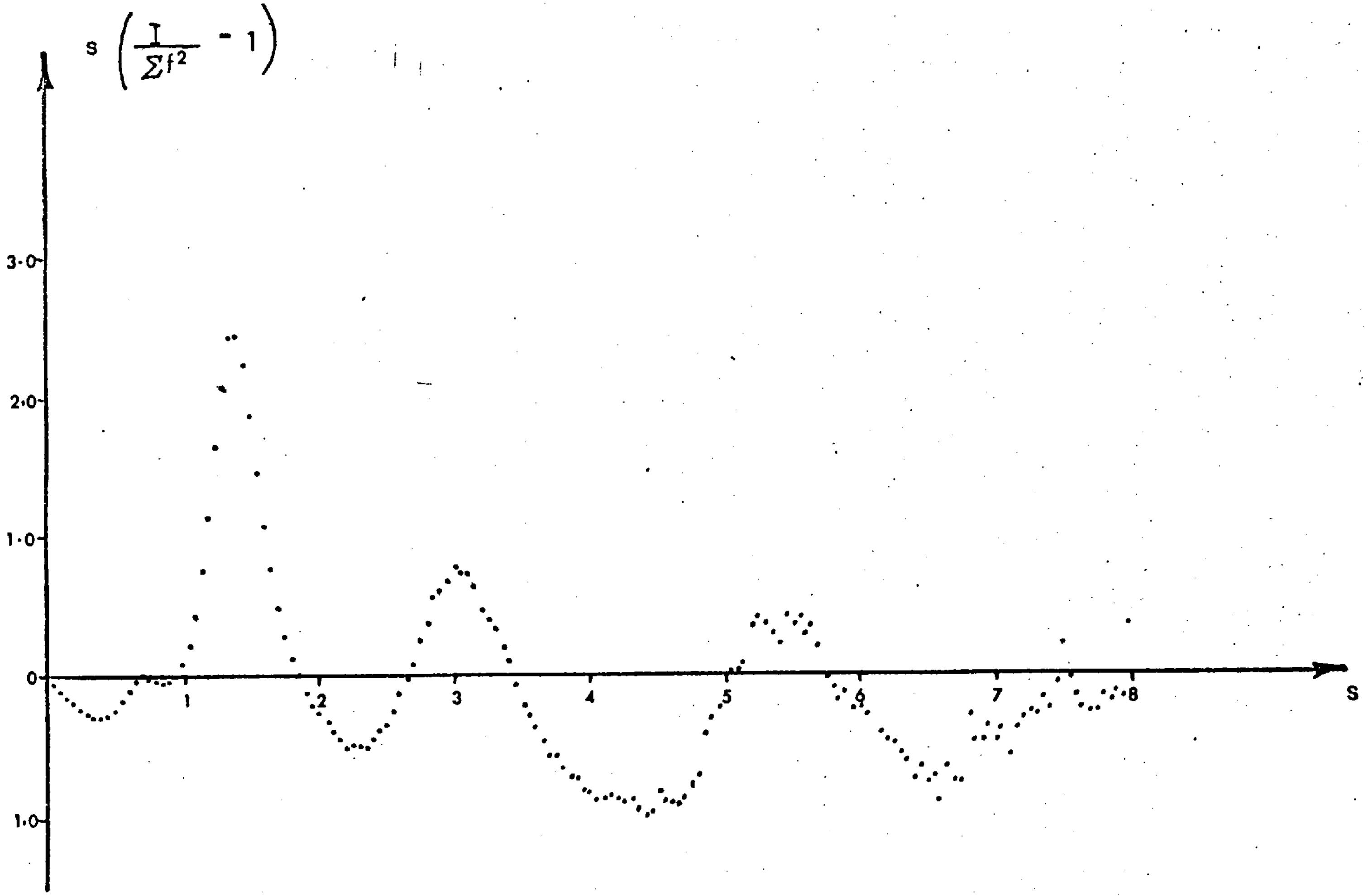

Fig.4.9 The interference function $s(I/\sum f^2 - 1)$ used to generate the atomic radial distribution function for atactic polystyrene.

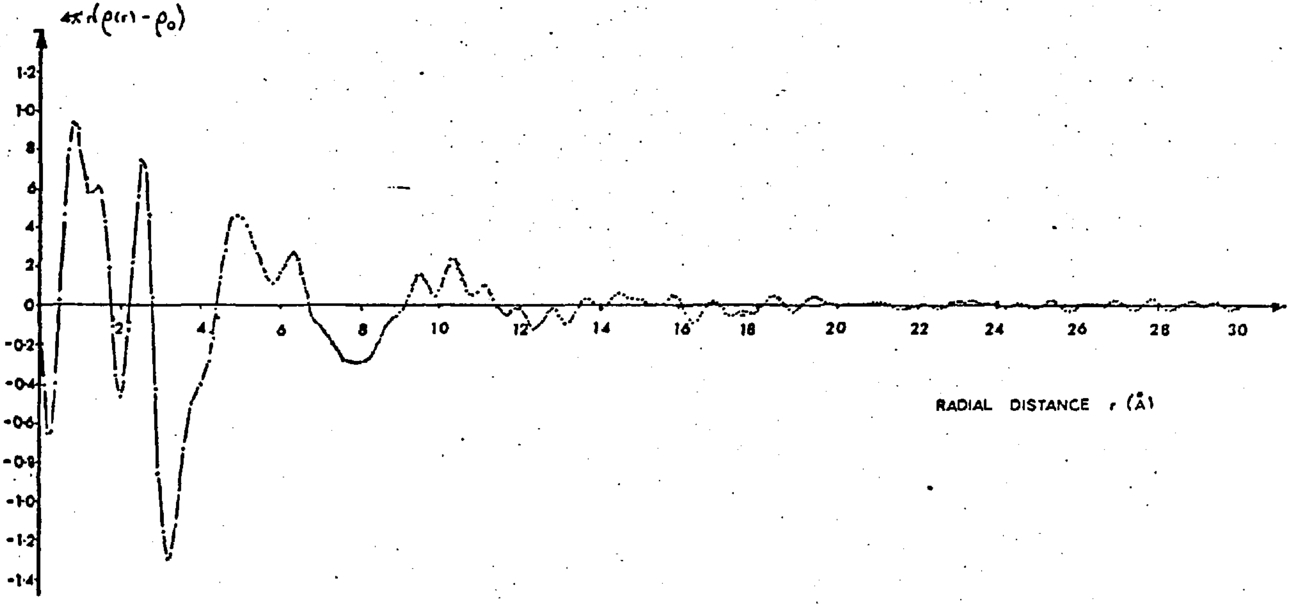

Fig.4.10 Reduced atomic radial distribution function for "as received" atactic polystyrene. This function has been deconvoluted by the electronic distribution function for an "average" atom.

	Fig.4.10		Wecker et al.[52]	
Peak	r (Å)	$4\pi r(\rho(r) - \rho_o)$	r (Å)	$4\pi r(\rho(r) - \rho_o)$
1	1.45	0.60	1.51	2.10
2	2.50	0.74	2.53	1.68
3	5.00	0.46	5.05	0.657
4	6.25	0.26	6.11	0.265
5	~10.25	~0.24	10.1	0.175
6	~14.7	~0.06	14.7	0.0393

Table 4.4 Comparison of the atomic distribution functions for atactic polystyrene of Fig.4.10 with that of Wecker, Davidson and Cohen[52].

The close agreement obtained between these two sets of independently obtained data demonstrated the accuracy of this analysis and the reliability of the derived functions.

4.2 The WAXD from Amorphous Isotactic Polystyrene

A specimen of amorphous isotactic polystyrene prepared by rapidly quenching the material from above its crystal melting temperature was also investigated. The Bragg spacings corresponding to the intensity maxima of the uncorrected experimental scattering were as follows:

2θ	9°	18°	43°	83°
d-spacing (Å)	9.83	4.93	2.10	1.16

Table 4.5 The Bragg spacings for amorphous isotactic polystyrene (CuKα).

The interference function for isotactic polystyrene (Fig.4.11) differed from that of the atactic material in that the peaks were of different inten-

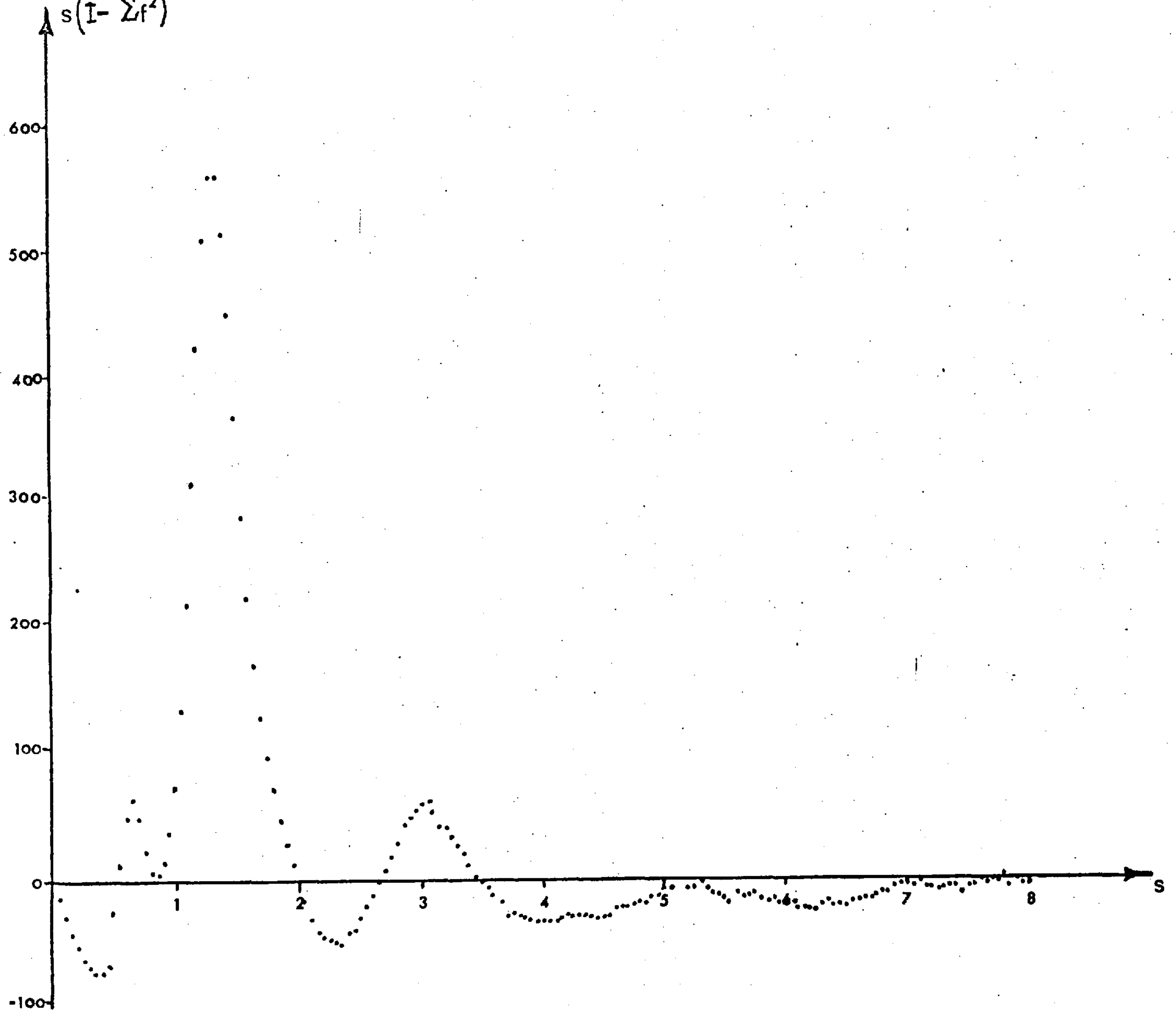

Fig.4.11 The interference function for amorphous isotactic polystyrene.

sities and had slightly different s values:

Peak	1	2	3	4
s (Å^{-1})	0.65	1.33	3.05	~5.3
Intensity (e.u.)	65	560	60	-2
d-spacing (Å)	9.67	4.72	2.06	1.19

Table 4.6 Details of the interference function for amorphous isotactic polystyrene (CuKα).

The normalisation achieved here was poorer than for atactic polystyrene and this was reflected in the RDF below 3Å. The RDF for the isotactic sample exhibited consistently longer spacings than the atactic material.

Peak	r (Å)	$4\pi r(\rho(r) - \rho_o)$	$\Delta r = r_i - r_a$
1	1.15	174	0.15
2	5.65	60	0.15
3	10.80	34	0.5
4	15.2	5	0.3
5	22.0	3	2.4

Table 4.7 Details of the radial distribution function of amorphous isotactic polystyrene (CuKα). The difference Δr in the peak positions between isotactic and atactic polystyrene is also shown.

It is likely that each peak in the RDF is composed of both intra- and inter-molecular spacings. A shift in either or both of these contributions could produce an overall shift in the position of the observed peaks. Longer intra-spacings may be expected here if, for example, the isotactic chains were straighter or they had a very different molecular conformation to that of the atactic material. Similarly longer inter-spacing may also arise due to a different chain conformation (cross-section).

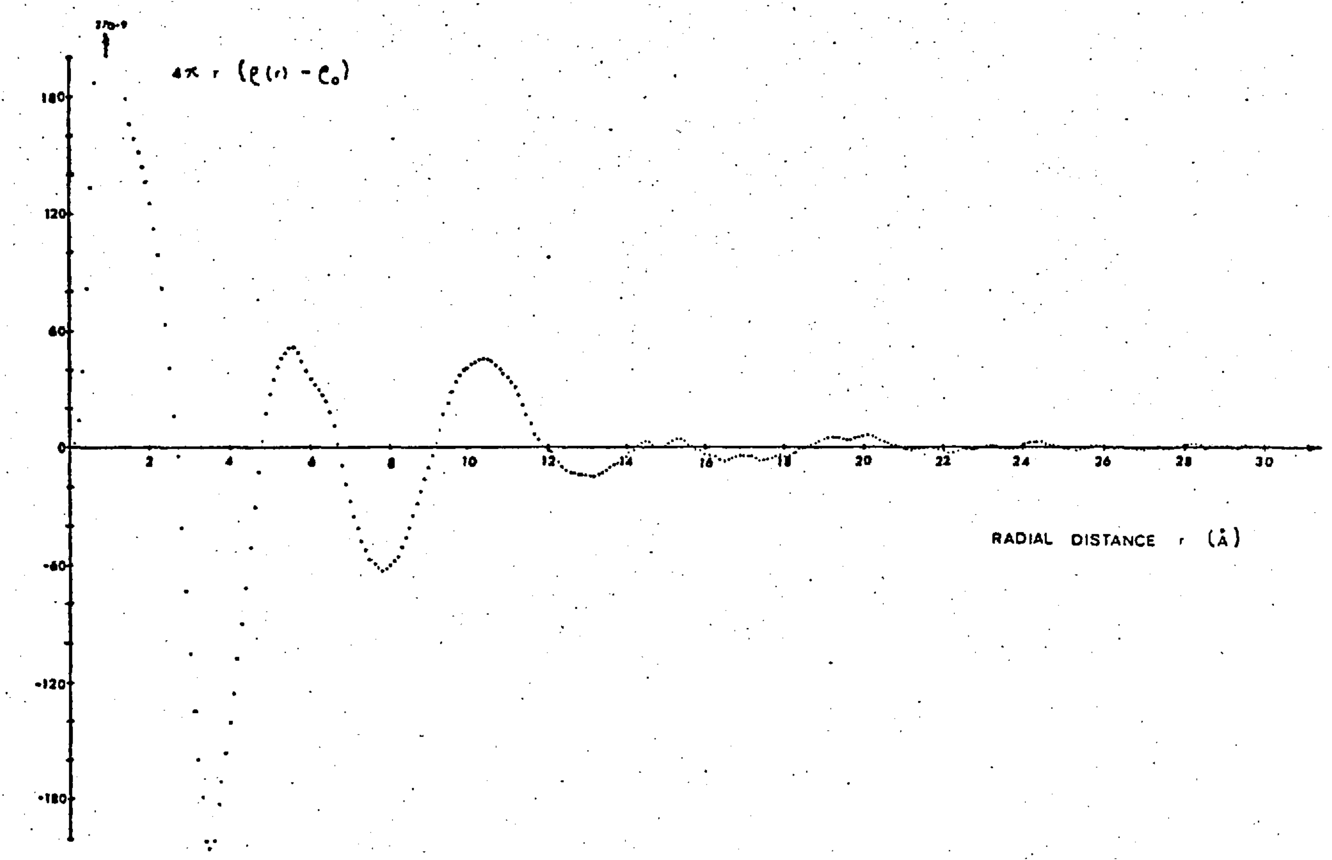

Fig.4.12 Reduced electronic radial distribution function for amorphous isotactic polystyrene.

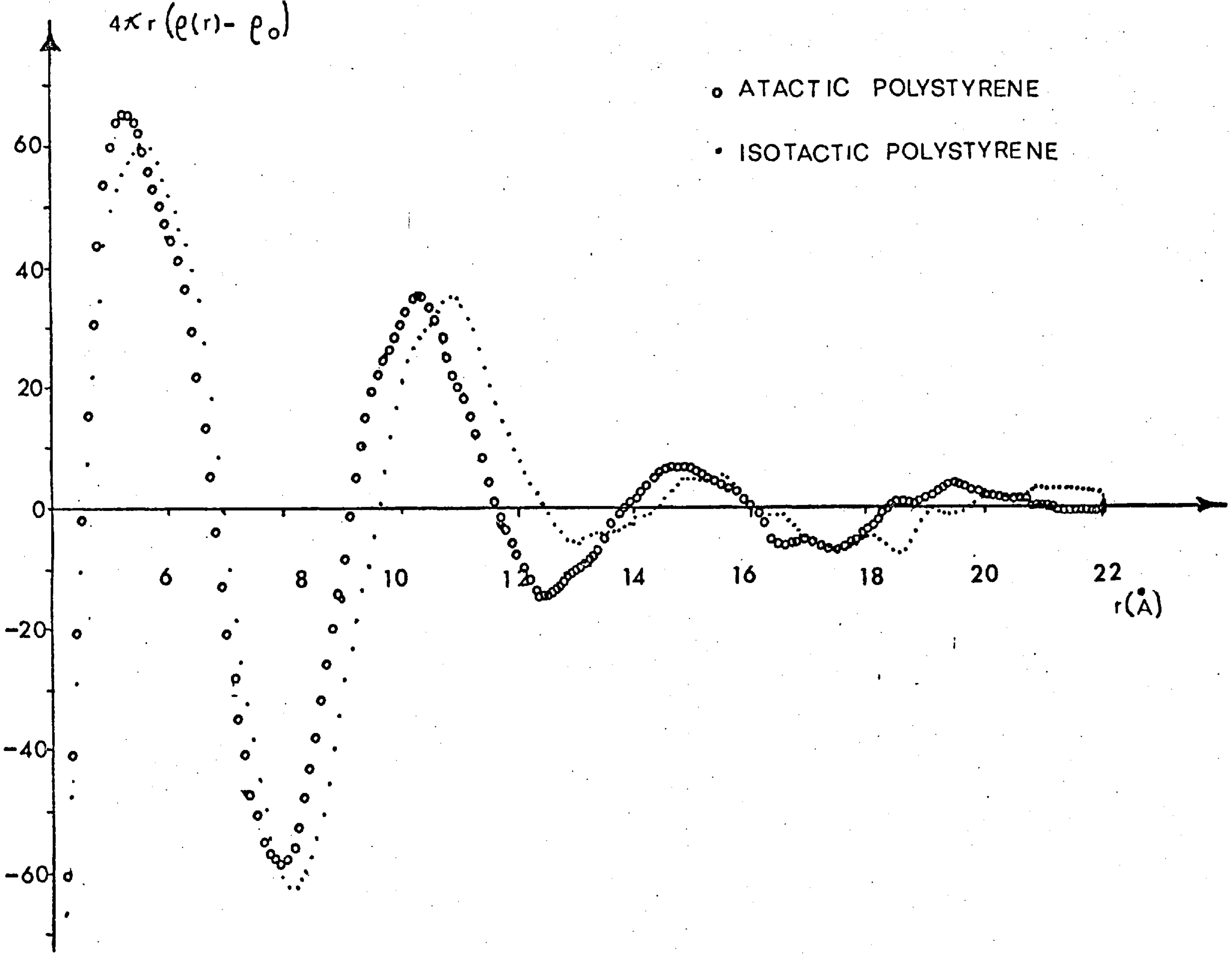

Fig.4.13 Comparison of the RDFs for atactic and amorphous isotactic polystyrene.

4.3 The WAXD from Atactic Polymethyl Methacrylate

Flat diffractometer samples were cut from 2mm thick sheets of commercially available polymethyl methacrylate PMMA ("Perspex", I.C.I. Ltd.). Fig.4.14 shows the uncorrected scattering intensity obtained for such "as received" sheets using CuKα radiation. Distinct halos were observed at $2\theta \sim 13.5^\circ$, $2\theta \sim 30^\circ$ and $2\theta \sim 41.5^\circ$ together with a very weak halo at $2\theta \sim 88^\circ$. The Bragg spacings corresponding to these halos were as follows:

2θ	13.5°	30°	41.5°	88°
d-spacing (Å)	6.56	2.98	2.18	1.11

Table 4.8 The Bragg spacings for atactic polymethyl methacrylate (CuKα).

Fig.4.15 shows the normalised corrected intensity together with the theoretical independent intensity. The interference function (Fig.4.16) had the following properties:

Peak	1	2	3	4
s (Å^{-1})	1.0	2.2	2.95	5.7
Intensity (e.u.)	261	83	70	25
d-spacing (Å)	6.29	2.85	2.14	1.10

Table 4.9 Details of the interference function for atactic polymethyl methacrylate (CuKα).

Fig.4.17 shows the reduced electronic radial distribution function for atactic PMMA. Unlike the distribution functions for amorphous polystyrene, the peaks here appeared to be constructed of single components and the region $r \leqslant 3$Å was relatively free of spurious normalisation effects. The radial density function is reproduced in Fig.4.18.

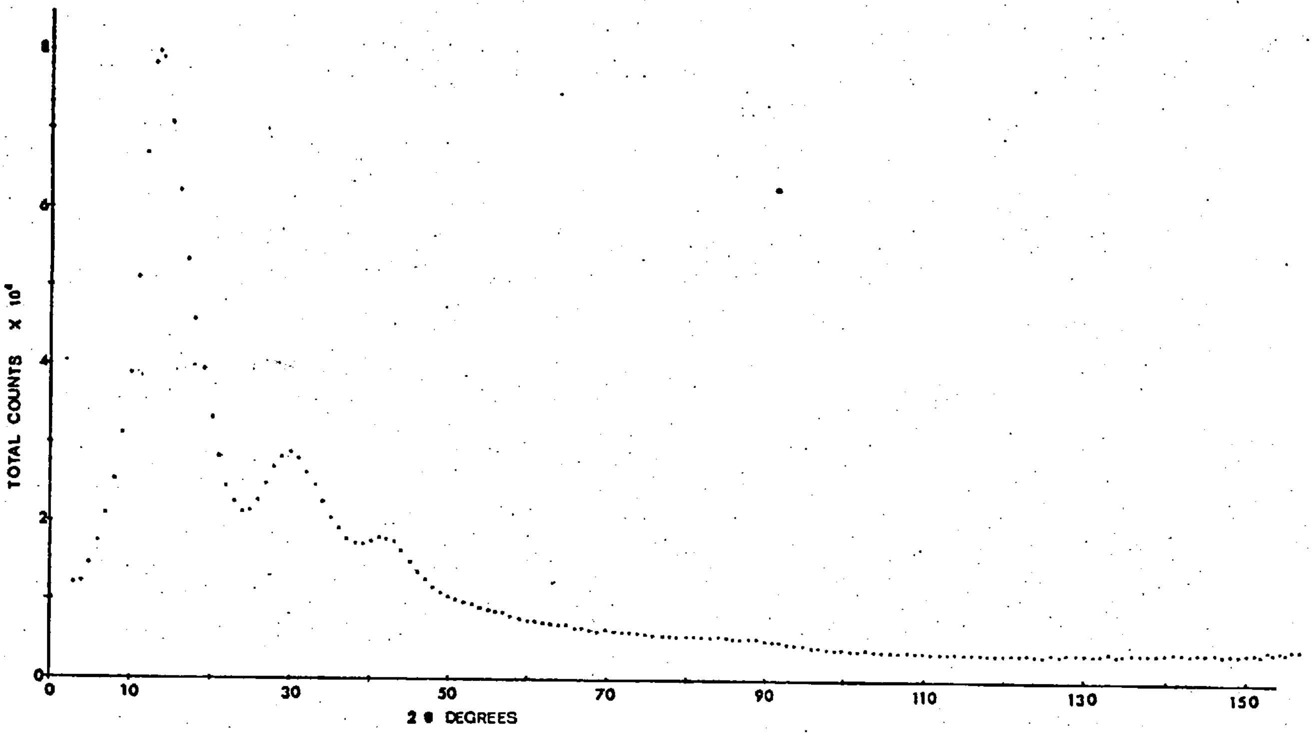

Fig.4.14 Uncorrected experimental scattering intensity for "as received" atactic polymethyl methacrylate (CuKα radiation).

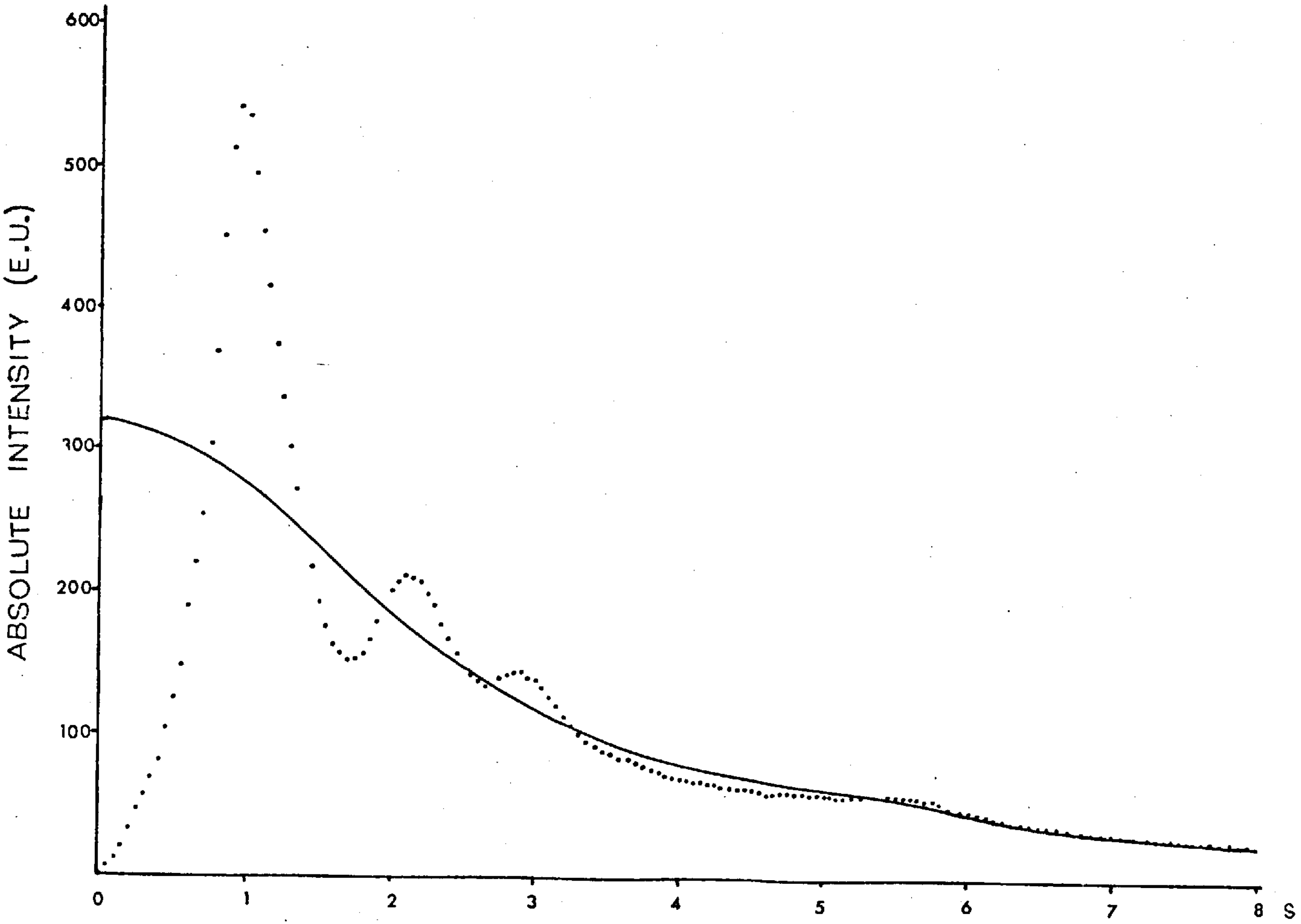

Fig.4.15 The normalised intensity corrected for absorption and polarisation together with the total theoretical independent scattering curve.

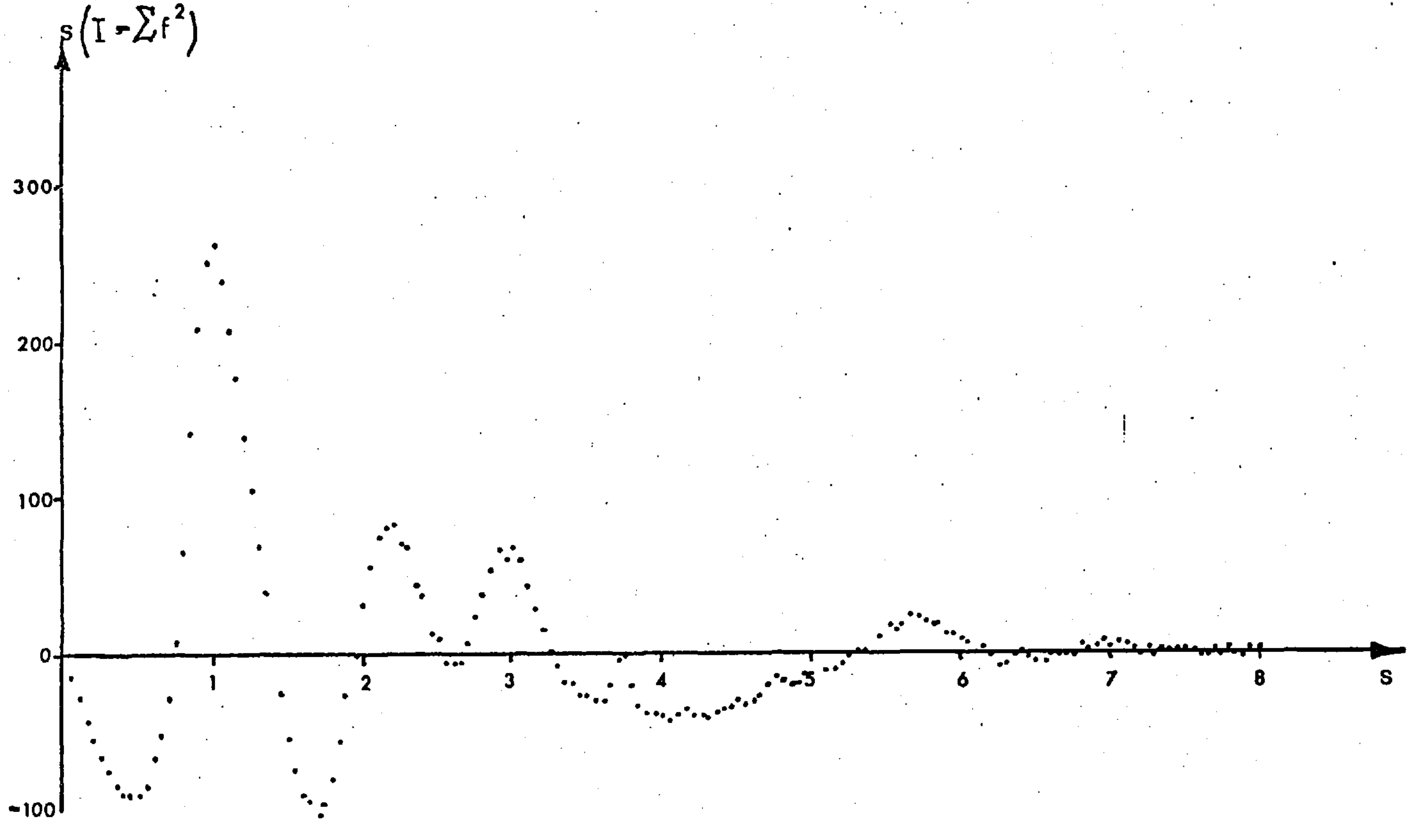

Fig.4.16 The interference function for "as received" atactic polymethyl methacrylate.

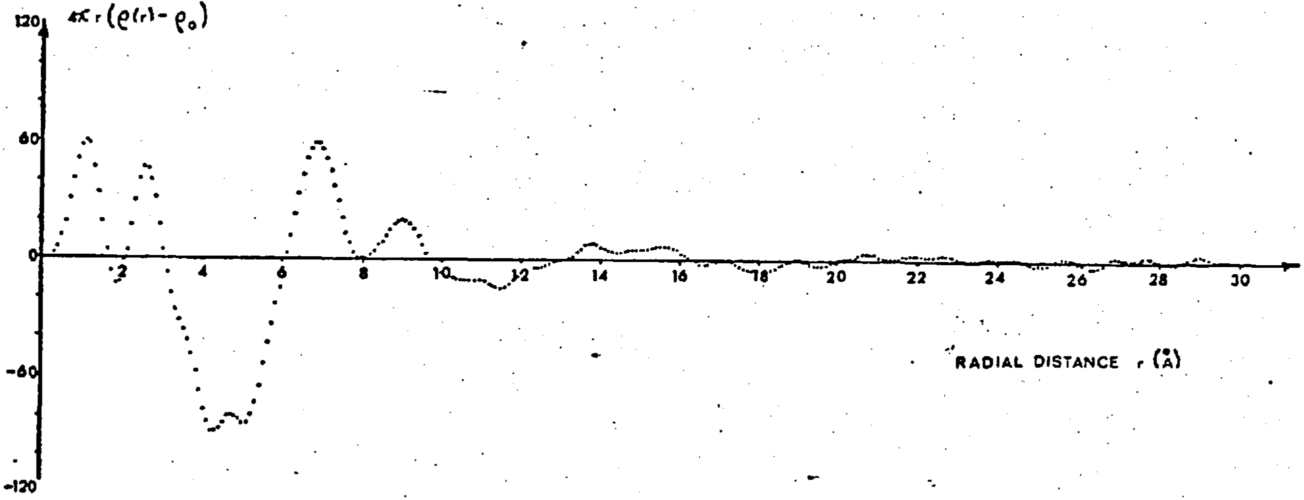

Fig.4.17 Reduced electronic radial distribution function for "as received" atactic polymethyl methacrylate.

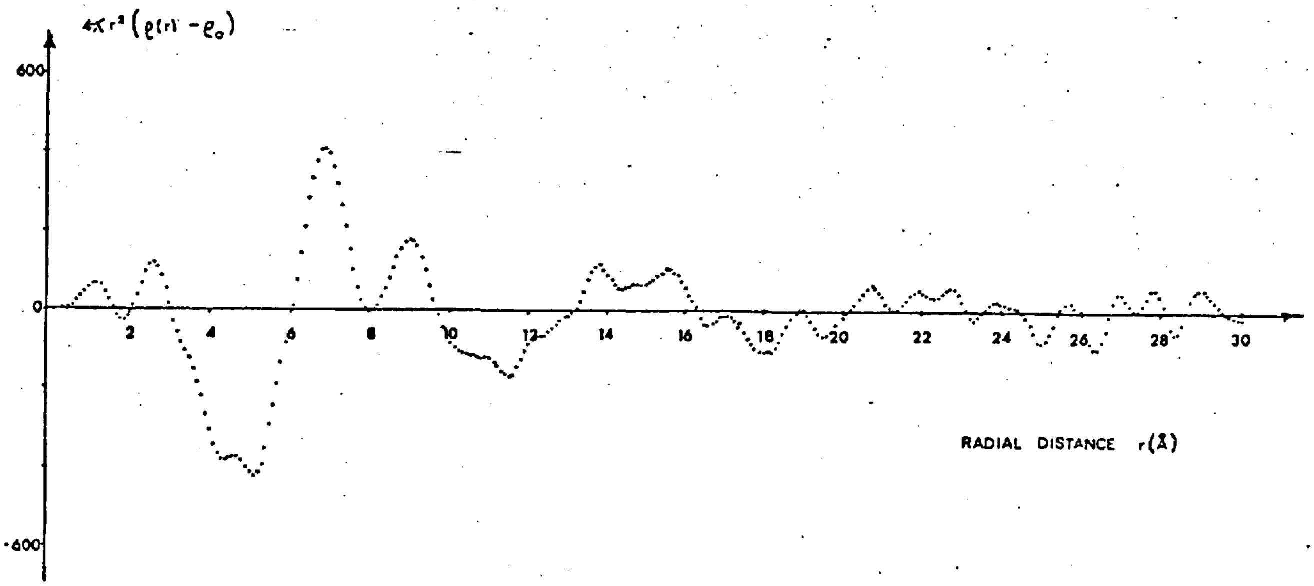

Fig.4.18 Reduced radial density function for "as received" atactic polymethyl methacrylate.

Peak	r (Å)	$4\pi r(\rho(r) - \rho_o)$	r (Å)	$4\pi r^2(\rho(r) - \rho_o)$
1	1.1	60	1.2	70
2	2.55	46	2.6	120
3	6.9	59	6.9	410
4	9.0	20	9.0	180
5	14.7	6	14.8	~90
6	~21.6	4	~21.6	~30

Table 4.10 Details of the radial distribution and radial density functions of atactic polymethyl methacrylate (CuKα).

The effect on the RDF of changing the X-ray wavelength was also investigated. Fig.4.19 shows the reduced electronic radial distribution for atactic PMMA using MoKα radiation (λ = 0.7107Å). By using MoKα radiation the

Peak	r (Å)	$4\pi r(\rho(r) - \rho_o)$
1	1.4	60
2	2.6	61
3	7.0	44
4	9.2	22
5	~15.7	~4
6	~21.2	~1

Table 4.11 Details of the radial distribution function of atactic polymethyl methacrylate (MoKα).

s range was doubled ($s_{max} \approx 17$) and any omission of structural information would be clearly seen. No significant differences were observed between the RDFs for these two radiations and it was therefore concluded that termination errors were small and that the majority of systematic errors occurring in the distribution functions arose from faulty normalisation.

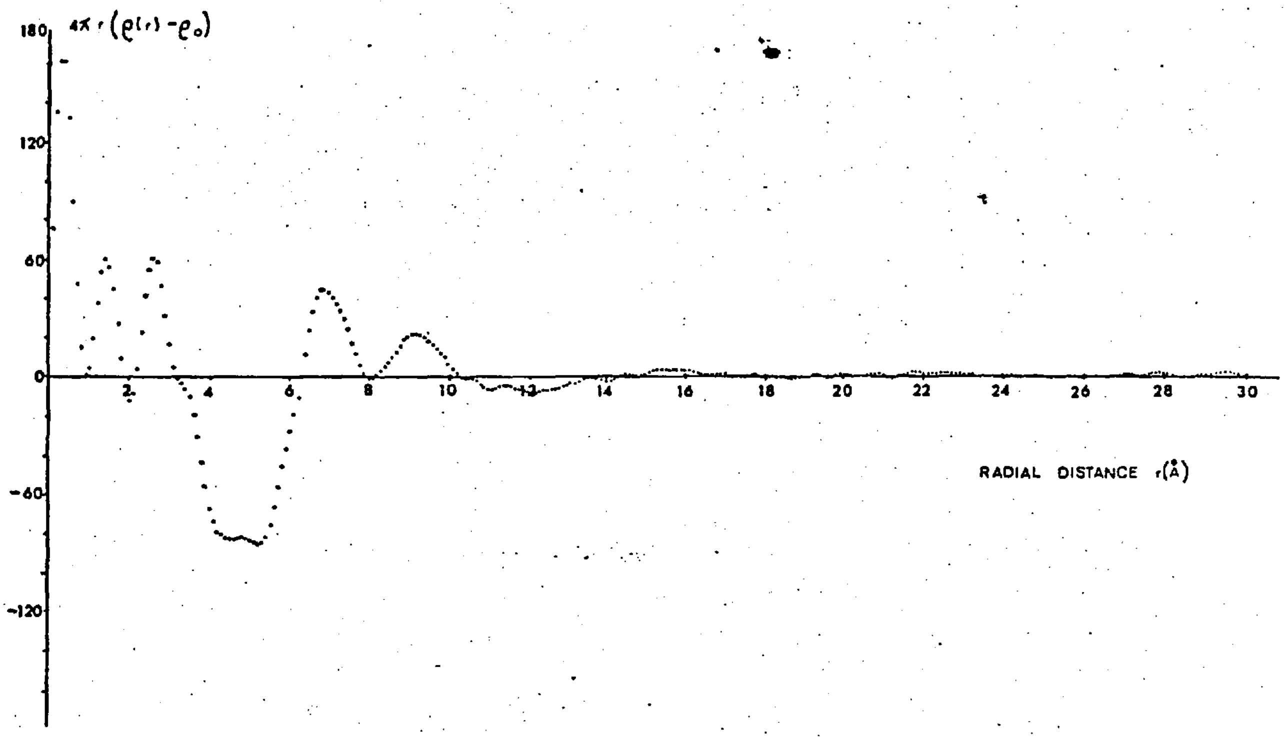

Fig.4.19 Reduced electronic radial distribution function for atactic polymethyl methacrylate obtained using MoKα radiation.

A copper target was preferred to facilitate computing and to reduce the size of the detected X-ray background due to inefficient shielding.

4.4 The Effect of Temperature and Annealing Time on the WAXD from Atactic PMMA

The WAXD from atactic PMMA was investigated as a function of temperature in the range 20°C to 200°C. The two strongest diffraction halos at 6.3Å and 2.9Å were monitored as the specimen was heated in vacuo from room temperature, through the glass transition temperature T_g to 200°C. The specimen was then gradually cooled back to room temperature. Bowing of the specimen as it expanded was prevented by clamping it at one end only and allowing it to move over a flat copper block. It is well known from dilatometry experiments that the volume expansion of a glassy polymer such as PMMA exhibits a sharp discontinuity at the characteristic temperature T_g. Fig.4.20 shows how the Bragg spacings of the two halos varied as the temperature was cycled. T_g for the commercial PMMA (I.C.I. Ltd.) used in this investigation was between 100 and 105°C and at about this temperature the d spacing of the first halo began to increase steadily. The second peak however appeared to exhibit no such variation (note however that the accuracy in measuring $d = \lambda/(2\sin\theta)$ decreased as θ increased). Thus it was concluded that the first halo (~6.3Å) in atactic PMMA was at least in part intermolecular in origin while the second peak (2.9Å) was predominantly intramolecular.

When atactic PMMA was annealed for long periods at a constant temperature just below T_g a significant increase in the intensity of the first two peaks was obtained. Fig.4.21 shows the interference function obtained for an atactic PMMA sample which had been annealed for 16 weeks at 90°C:

Peak	1	2	3	4
s	0.98	2.18	2.95	5.7
Intensity	345	100	68	24
d-spacing	6.41	2.88	2.14	1.10
$\frac{I_{annealed}}{I_{unannealed}}$	1.32	1.21	0.97	0.96

Table 4.12 The interference function for annealed atactic PMMA.

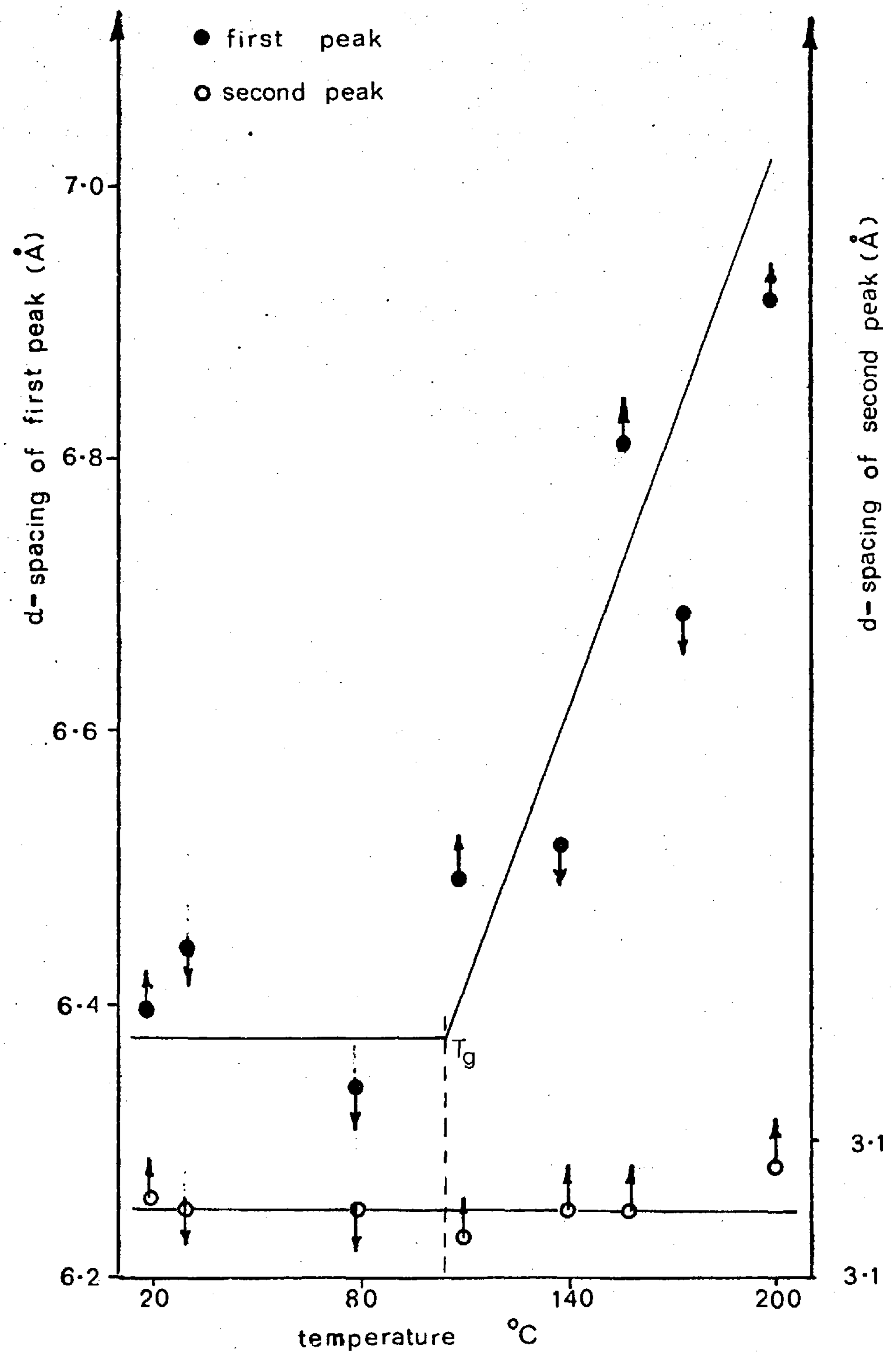

Fig.4.20 The variation in the Bragg spacings of the first two halos of atactic PMMA as the temperature was first increased (↑) to 200°C and then decreased (↓) again to room temperature.

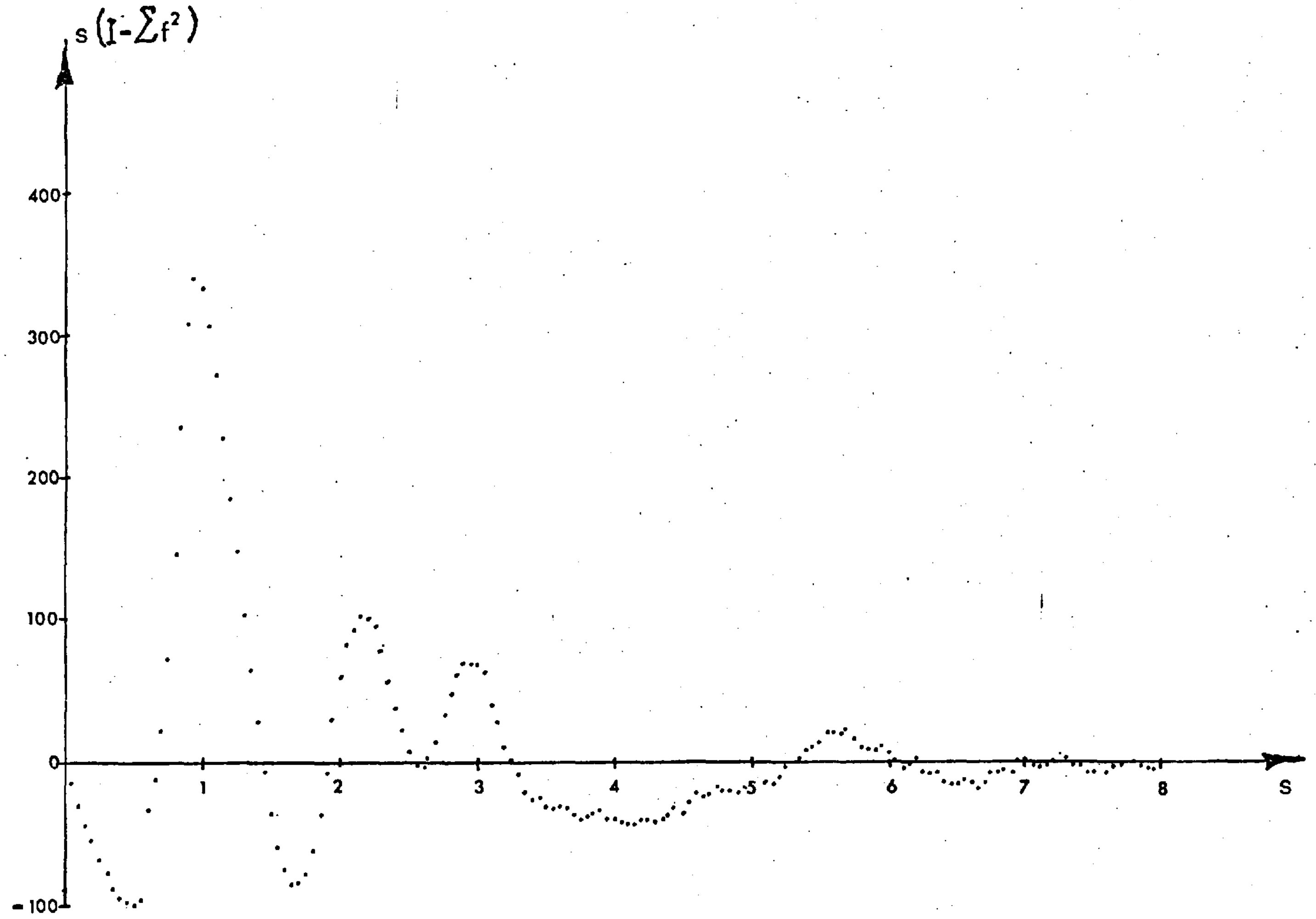

Fig.4.21 The interference function for an atactic PMMA sample which had been annealed for 16 weeks at 90°C.

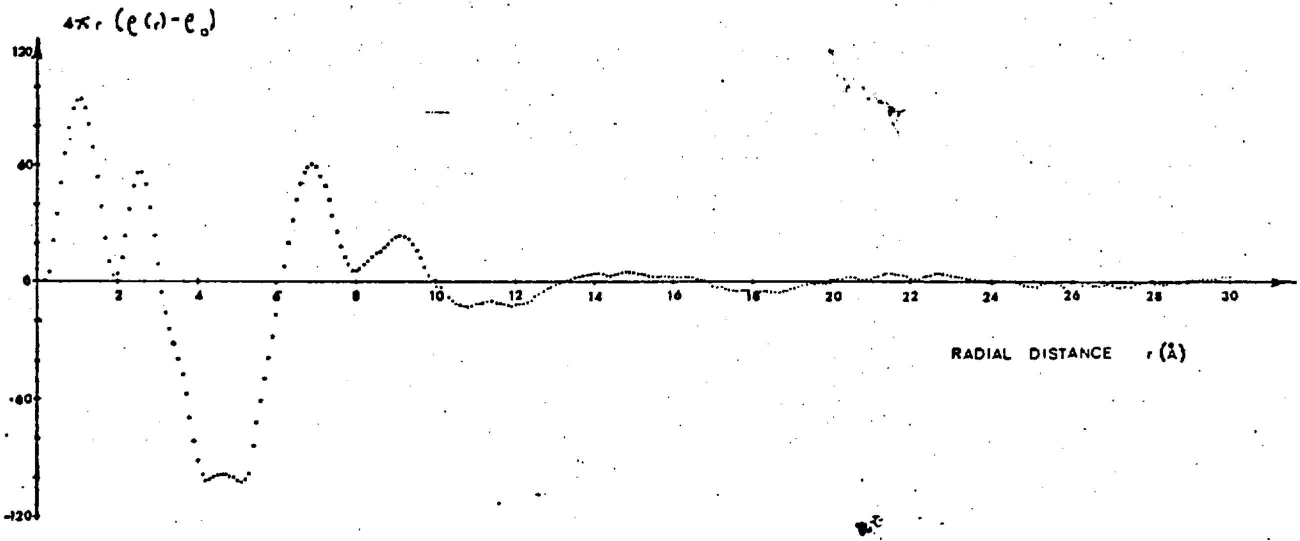

Fig.4.22 Reduced electronic radial distribution function for an atactic PMMA sample annealed for 16 weeks at 90°C.

Several workers have shown that the annealing of some glassy polymers including PMMA at temperatures close to T_g has produced slight (0.05%) density increases in these polymers.[69] The large percentage increase in the intensities of the first two peaks of the interference function could arise from an improvement in chain alignment on a microscale (intermolecular contributions) and/or a straightening of chains or perhaps a more regular atomic arrangement along the chains (intramolecular contribution). Thus the WAXD from annealed atactic PMMA was consistent with the suggestion that annealing glassy polymers close to T_g leads to an improvement in local segmental ordering. Fig.4.22 shows the reduced radial distribution function for the annealed atactic PMMA:

Peak	r (Å)	$4\pi r(\rho(r) - \rho_0)$	
1	1.1	94	
2	2.55	56	
3	6.93	60	
4	9.0	24	(2 components)
5	15.0	5	
6	21.9	4	

Table 4.13 Details of the reduced radial distribution function for atactic PMMA annealed for 16 weeks at 90°C.

The RDF was remarkably similar to that for the "as received" material except that the fourth peak was now clearly composed of two components : one centred at $\sim$8.6Å, the other at $\sim$9.1Å.

4.5 The WAXD from Orientated Atactic Polystyrene

Preferential molecular orientation as revealed by X-ray diffraction was induced in atactic polystyrene by extruding the polymer from a dye under load at 85°C. Fig.4.23 summarises the experimental details while Plate 4.2 shows a typical X-ray pinhole transmission pattern obtained for the orientated material. Flat sheets of the extruded polymer were mounted

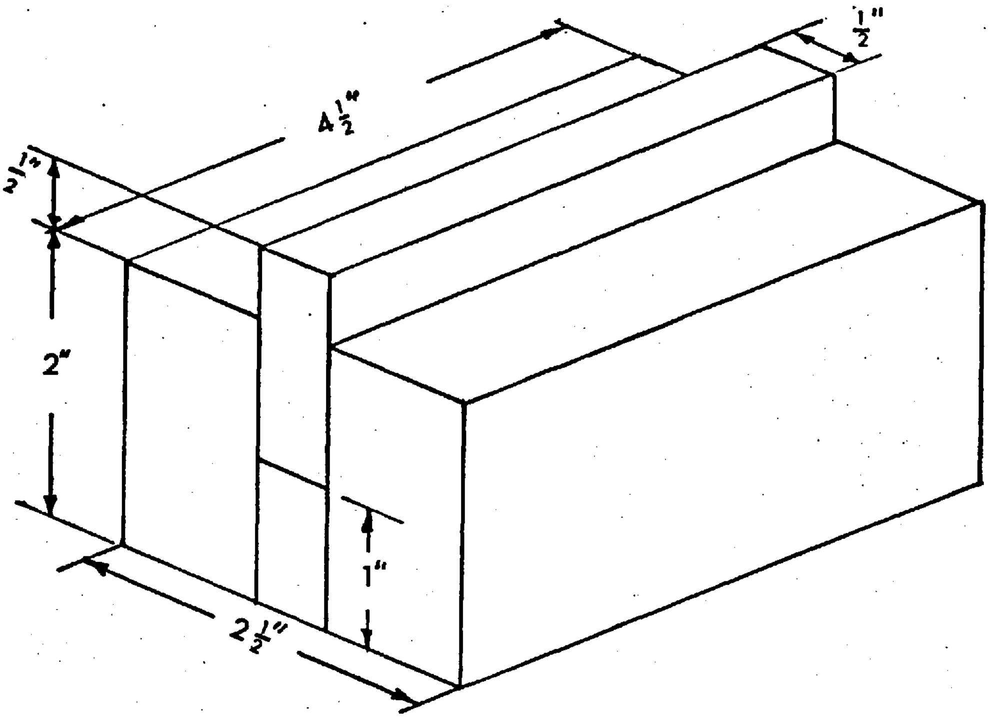

Fig.4.23a Extrusion dye used to orientate atactic polystyrene sheet.

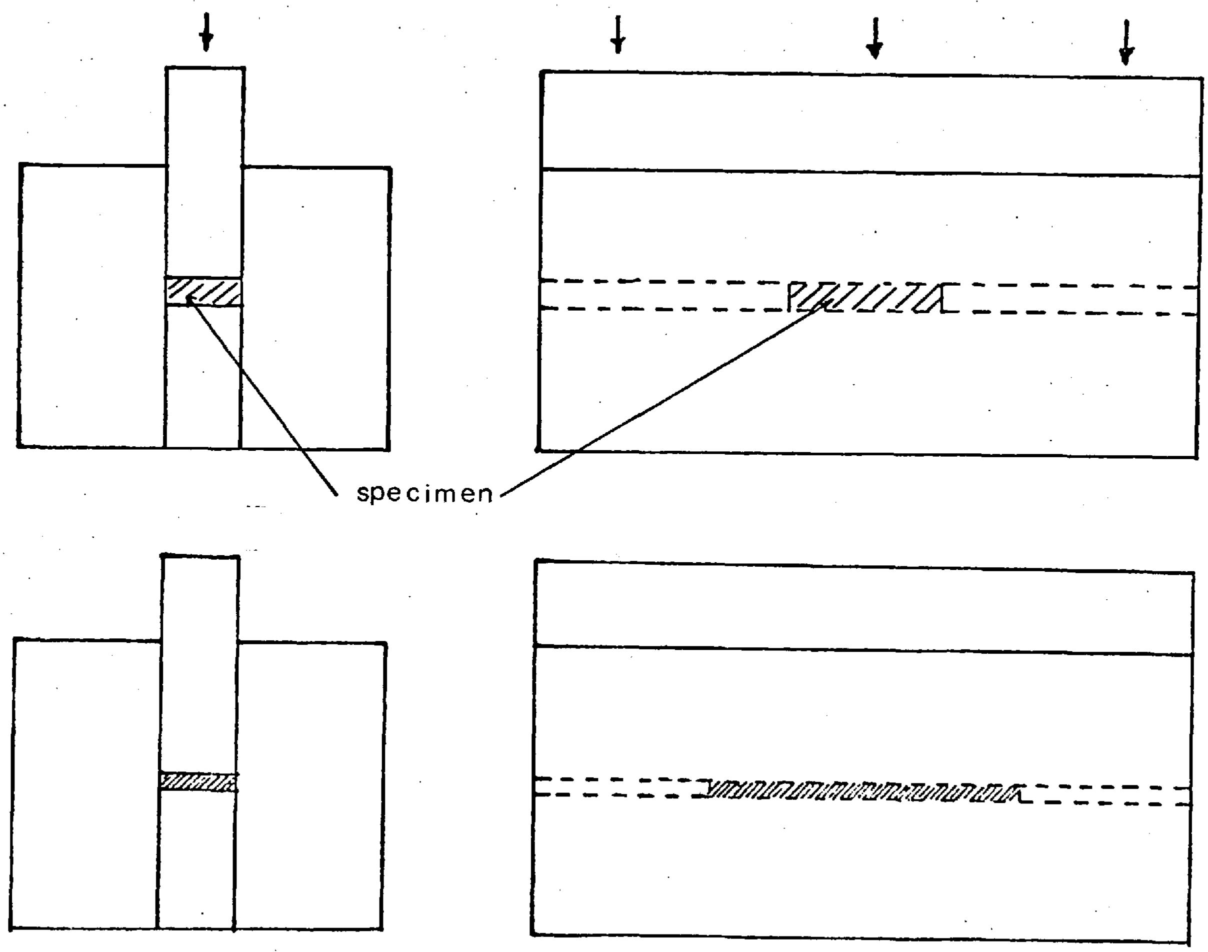

Fig.4.23b Side and end elevations of the dye during the extrusion of a sheet specimen.

into the diffractometer in the conventional manner and the intensity profile along the equator (zero layer line) was recorded. To obtain the intensity profile along the meridian the extruded sheets were cut into strips perpendicular to the flow direction and reformed into a block so that the fibre axis of each strip was vertical. Fig.4.24 shows this specimen procedure. The intensity curves were corrected for polarisation and absorption and then normalised to the total theoretical independent scattering. In the case of the equatorial scattering the Krogh-Moe[64] scaling factor had to be modified to

$$\alpha = \frac{\int_0^{R_{max}} R\left(\sum f^2 + I_{inc}\right)dR}{\int_0^{R_{max}} R\ I(R,0)dR}$$

to account for statistical cylindrical symmetry.

In the diffraction from a well orientated fibre the intensity distribution along the meridian usually contains information largely about the internal structure of the molecules whereas the distribution along the equator contains information largely regarding the mutual disposition of these molecules. Thus studying how the diffraction pattern changes when the polymer is orientated should give valuable clues as to how the diffracted intensity from the unorientated material is formed. In particular it should be possible to estimate the relative importance of intra- and inter-molecular contributions to the pattern.

Plate 4.1 shows the pinhole X-ray pattern obtained for atactic polystyrene while Plate 4.2 shows the pattern after the polymer had been orientated. Considerable equatorial and meridional arcing occurred for the orientated material. These photographs supported Kilian and Boueke's[51] conclusion that the inner halo of unorientated polystyrene (8.85Å) arises due to intermolecular interferences. Also the outer halo in Plate 4.2 appeared quite oval in shape suggesting that it may be composed of both inter- and intra-molecular components. This

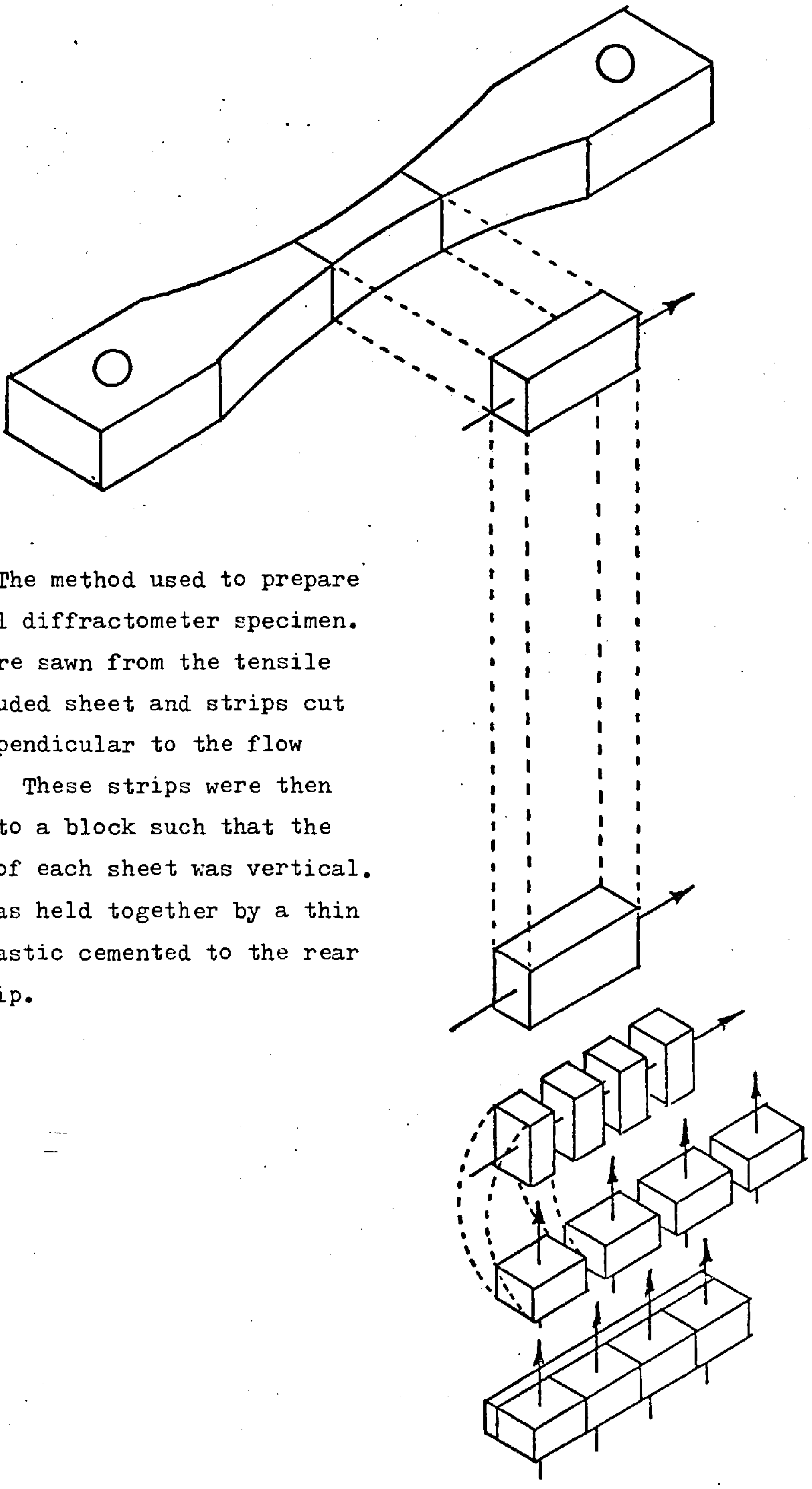

Fig.4.24 The method used to prepare a meridional diffractometer specimen. Sections were sawn from the tensile bar or extruded sheet and strips cut in this perpendicular to the flow direction. These strips were then reformed into a block such that the fibre axis of each sheet was vertical. The block was held together by a thin sheet of plastic cemented to the rear of each strip.

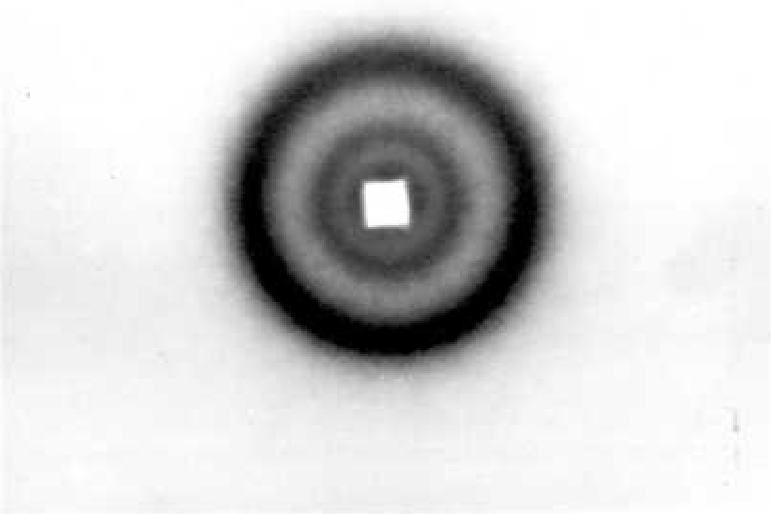

Plate 4.1 Pinhole transmission X-ray pattern from unorientated atactic polystyrene. Nickel-filtered Cukα radiation.

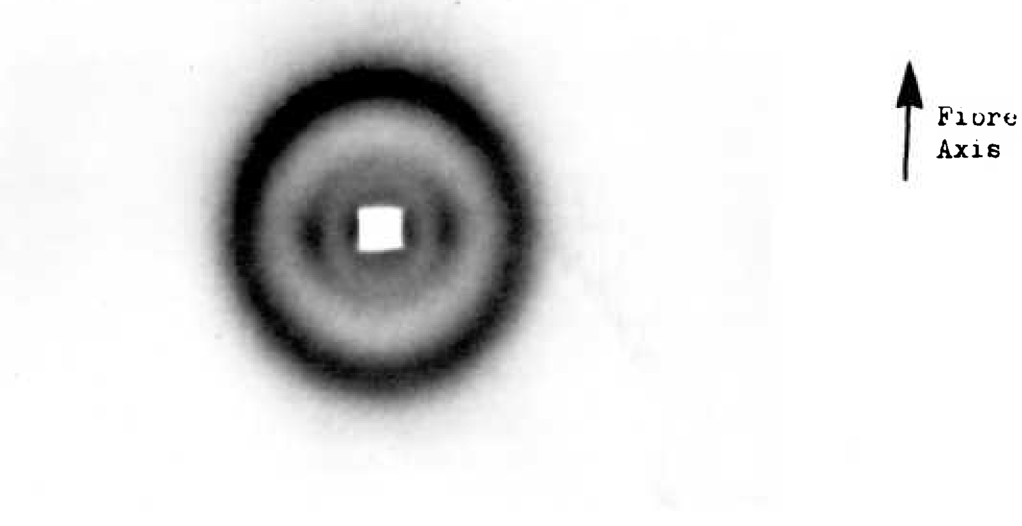

Plate 4.2 Pinhole transmission X-ray pattern from orientated atactic polystyrene. The sample was orientated by extrusion from a dye at $85^{\circ}C$ ($< T_g$) resulting in a draw ratio of 4 : 1.

was confirmed when quantitative measurements were performed on the diffractometer. The diffracted intensity measured along the meridian is shown in Fig.4.25. The Bragg spacings corresponding to the peak maxima were as follows:

2θ	10°	20°	40.5°	80°
d-spacing	8.85	4.44	2.23	1.20

Table 4.14 The Bragg spacings for the meridional scattering from orientated polystyrene (CuKα).

Fig.4.26 shows the meridianal interference function for orientated atactic polystyrene:

Peak	1	2	3	4
s (Å^{-1})	~ 0.65	1.43	3.0	~ 5.25
Intensity (e.u.)	-90	320	20	5
d-spacing (Å)	9.66	4.40	2.10	1.20
$\frac{I_{\text{orientated}}}{I_{\text{unorientated}}}$	-45	0.64	0.36	0.45

Table 4.15 The interference function for the meridional scattering from orientated atactic polystyrene.

The intensity of each peak in the interference function had been considerably reduced, in particular the first peak was hardly detectable and the second peak had shifted to s = 1.43.

Fig.4.27 shows the scattering that was detected along the equator (zero order layer line). The Bragg spacings corresponding to the intensity maxima were as follows:

2θ	10°	18.5°	40°
d-spacings (Å)	8.85	4.80	2.25

Table 4.16 The Bragg spacings for the equatorial scattering from orientated polystyrene (CuKα).

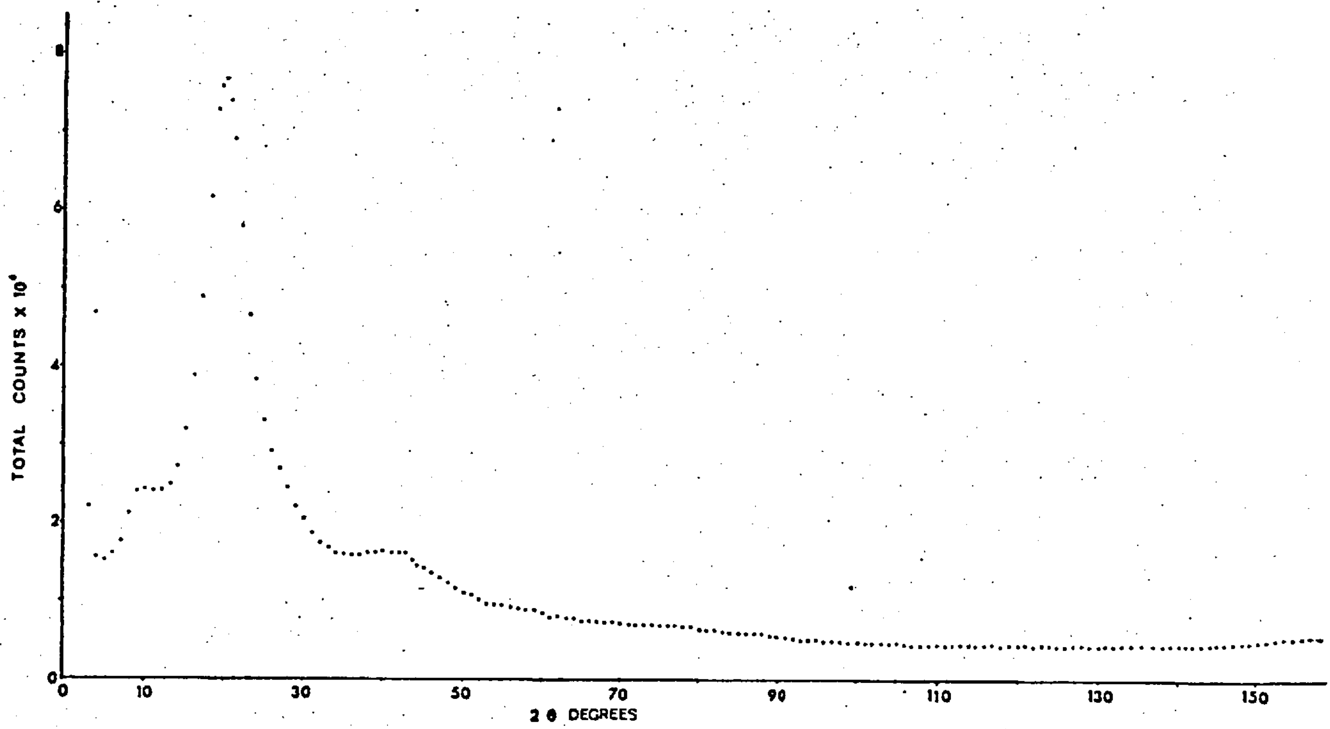

Fig.4.25 The uncorrected experimental scattering intensity measured along the meridian of an orientated atactic polystyrene sample (CuKα).

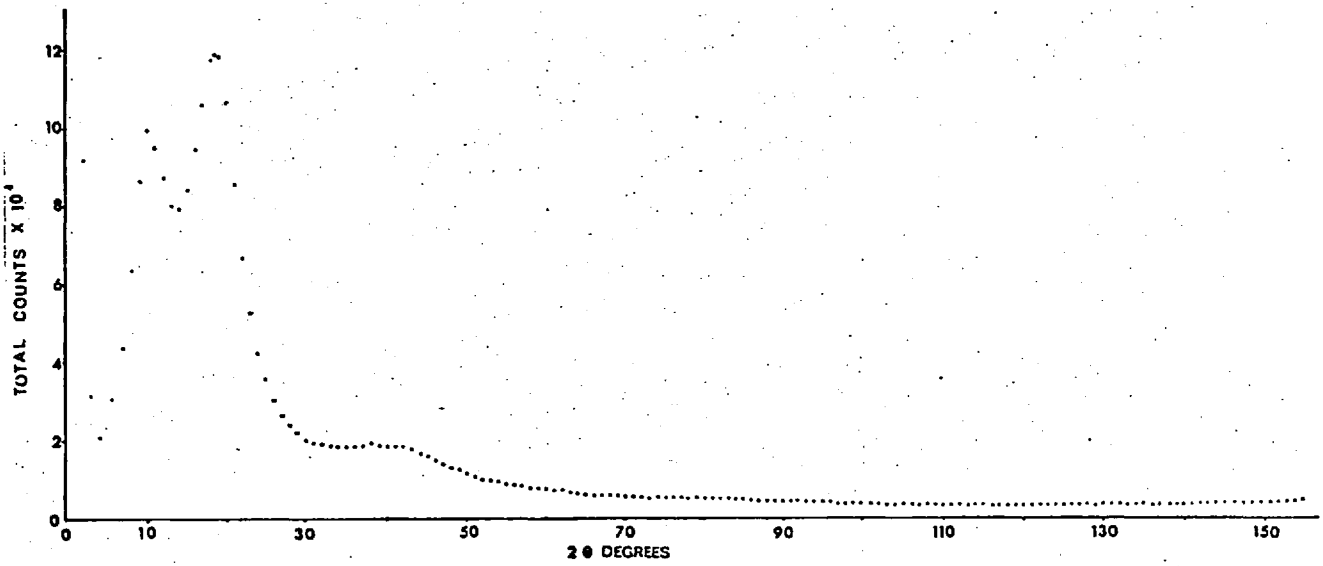

Fig.4.27 The uncorrected experimental scattering intensity measured along the equator of an orientated atactic polystyrene sample (CuKα).

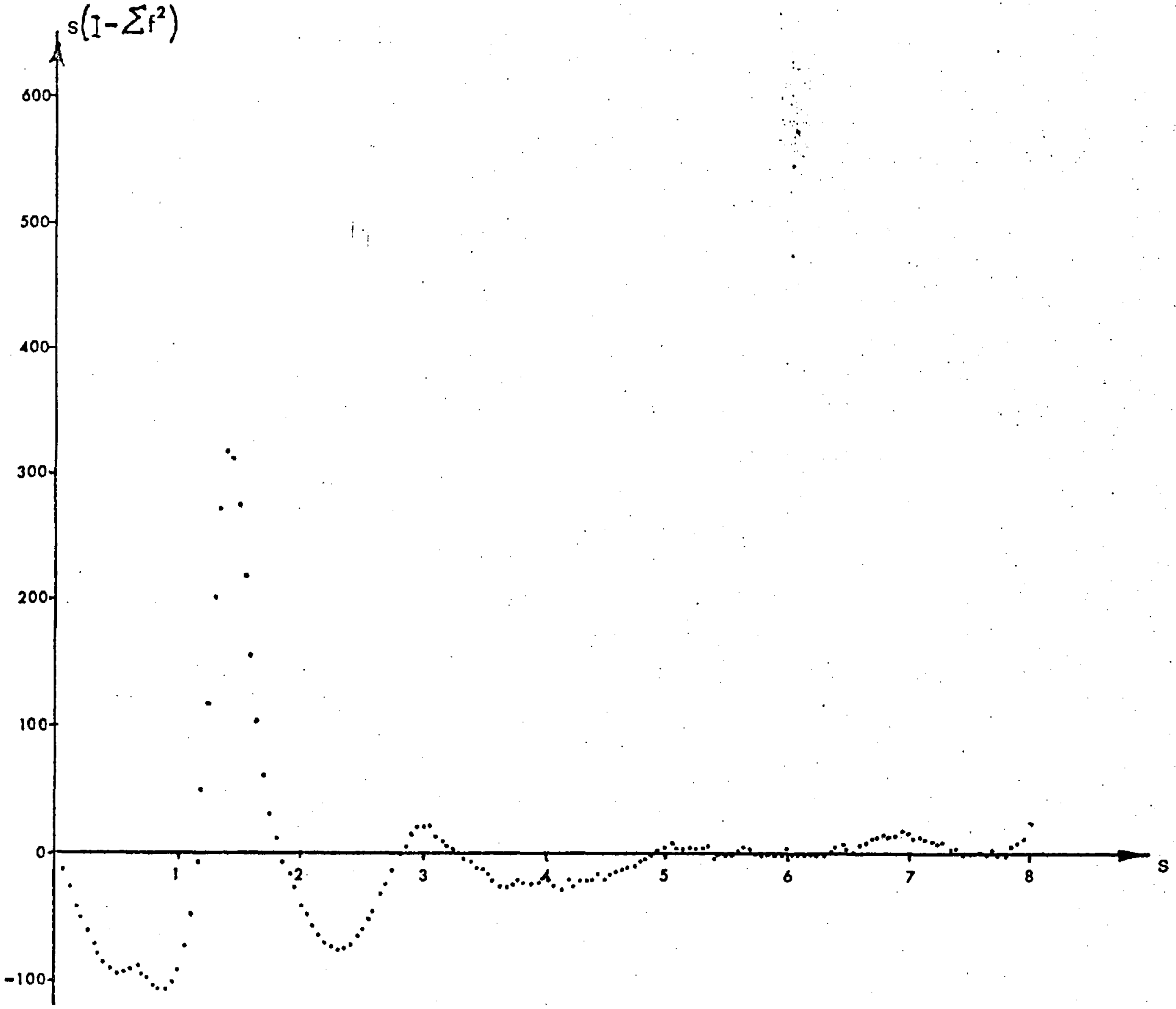

Fig.4.26 The meridional interference function for orientated atactic polystyrene.

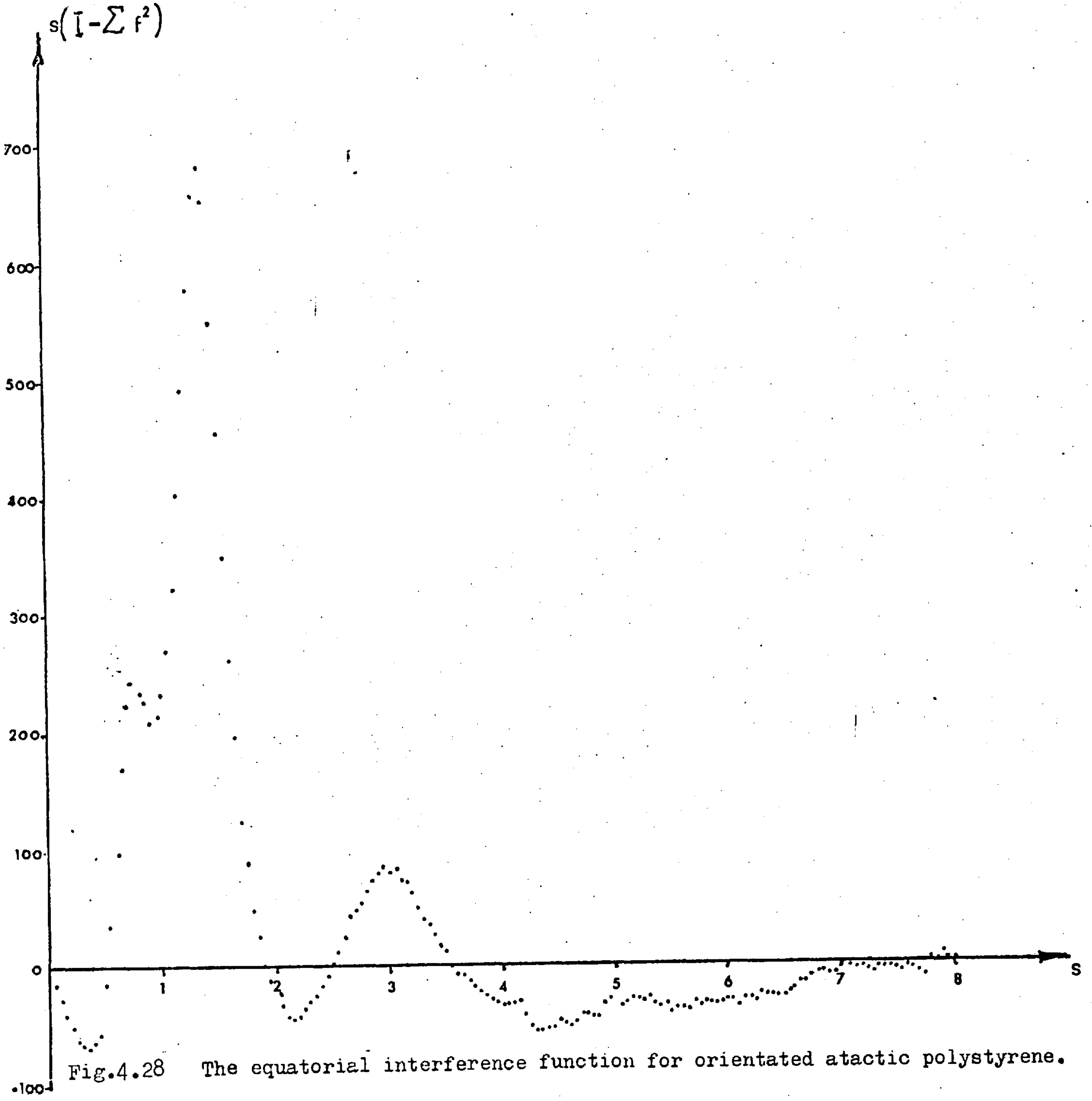

Fig.4.28 The equatorial interference function for orientated atactic polystyrene.

Fig.4.28 shows the interference function obtained for the equatorial scattering:

Peak	1	2	3	4
s (Å^{-1})	0.75	1.35	3.0	~5.0
Intensity (e.u.)	240	682	83	-30
d-spacing (Å)	8.38	4.65	2.10	1.26
$\frac{I_{\text{orientated}}}{I_{\text{unorientated}}}$	120	1.37	1.5	-2.73

Table 4.17 The interference function for the equatorial scattering from orientated polystyrene.

The first peak in the interference function had shifted to s = 0.75 and increased in intensity one hundredfold, confirming that it was exclusively intermolecular in nature. The second and third peaks in the function had also increased in intensity but had not shifted noticeably in s.

Thus it would appear from a simple comparison of the interference functions that intermolecular effects dominate the diffraction from amorphous polystyrene. However, the cross-section of the polystyrene molecule could be sufficient to allow significant intramolecular effects to be present even in the equatorial scattering from a perfectly orientated fibre.

Fig.4.29 shows the distribution function $H_3(z) - H_{3(o)}$ for the meridional scattering. In a perfectly orientated fibre this one dimensional function represents the distribution of atoms within the polymer molecules, projected onto the principal axis z.

Peak	r (Å)	$H_3(z) - H_{3(o)}$	$\Delta r = \bar{c}$
1	0.80	-45	3.53
2	4.33	25	4.67
3	9.00	13	4.40
4	13.40	3	4.65
5	18.05	2	4.50
6	22.55	0.5	

Table 4.18 Details of the distribution function $H_3(z)$ for orientated atactic polystyrene. $H_3(z)$ is a line distribution of the atoms within the polymer molecule in projection on the principal axis (assuming perfect orientation).

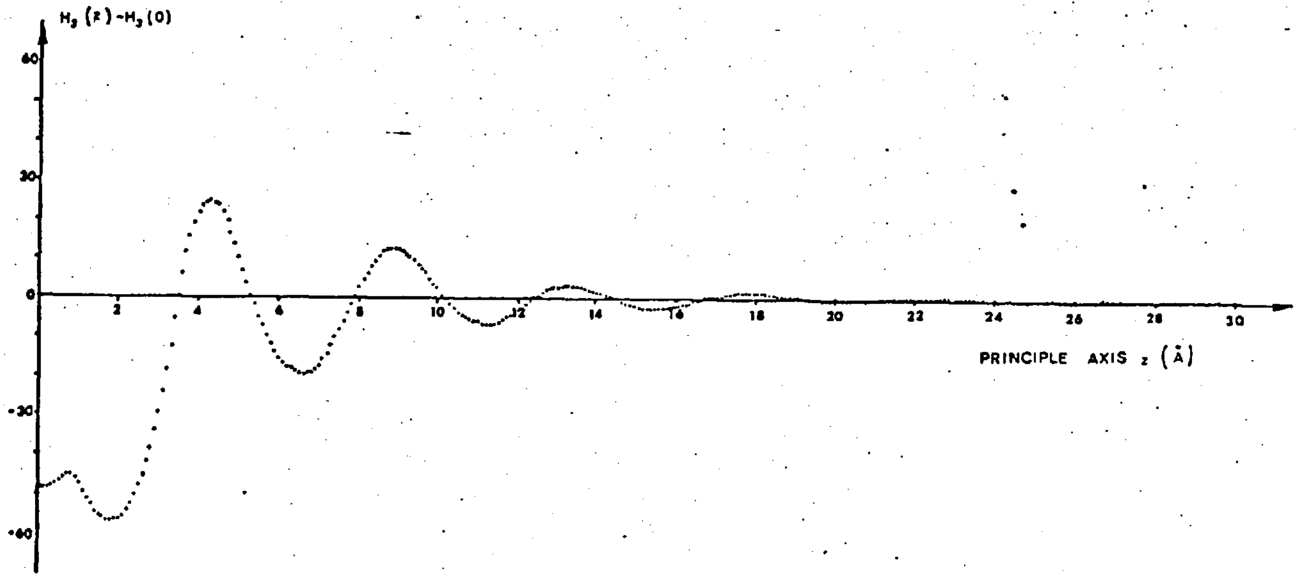

Fig.4.29 The distribution function $H_3(z) - H_{3(o)}$ for the meridional scattering from orientated atactic polystyrene.

$H_3(z)$ had the characteristics of a distribution function for a one dimensional lattice with distortions of the second kind. The peaks were approximately equally spaced with an average separation of 4.56Å, and damped away uniformly to zero within the distance $r_m \approx 24$Å, after which all distances became equally probable.

Fig.4.30 shows the one dimensional cylindrical distribution function $z_c(r) - z_{av}$ for the equatorial scattering. This function represents the electron density projection in the basal plane of an array with statistical cylindrical symmetry.

Peak	r (Å)	$z_c(r) - z_{av}$	Δr
1	5.20	32	4.65
2	9.85	45	4.65
3	~14.5	~-10	5.5
4	~20	~-5	

Table 4.19 Details of the cylindrical distribution function $z_c(r) - z_{av}$ for orientated atactic polystyrene.

A long wavelength component was clearly evident in this function. It was not certain whether this wave was spurious or not; if it were not it should be possible to detect in the interference function the intensity component giving rise to it. The two waves are connected by the zero order Bessel function $J_0(rs)$, which peaks at rs values of 0, 7.02, 13.32, 19.70, etc. The long wavelength component in $z_c(r)$ peaked at $r \approx 0$, 10.5 and ~24Å. This would mean that a component peaking at $s \approx 0.6$ should be seen in the interference function. Although this is not evident in Fig.4.28 it will be shown in Chapter V that such a component may well be present.

However Fig.4.31 shows the radial distribution function that was obtained by using the equatorial interference function of Fig.4.28. In using this function we have assumed that the interference function had spherical symmetry (interatomic vectors averaged over all possible orientations).

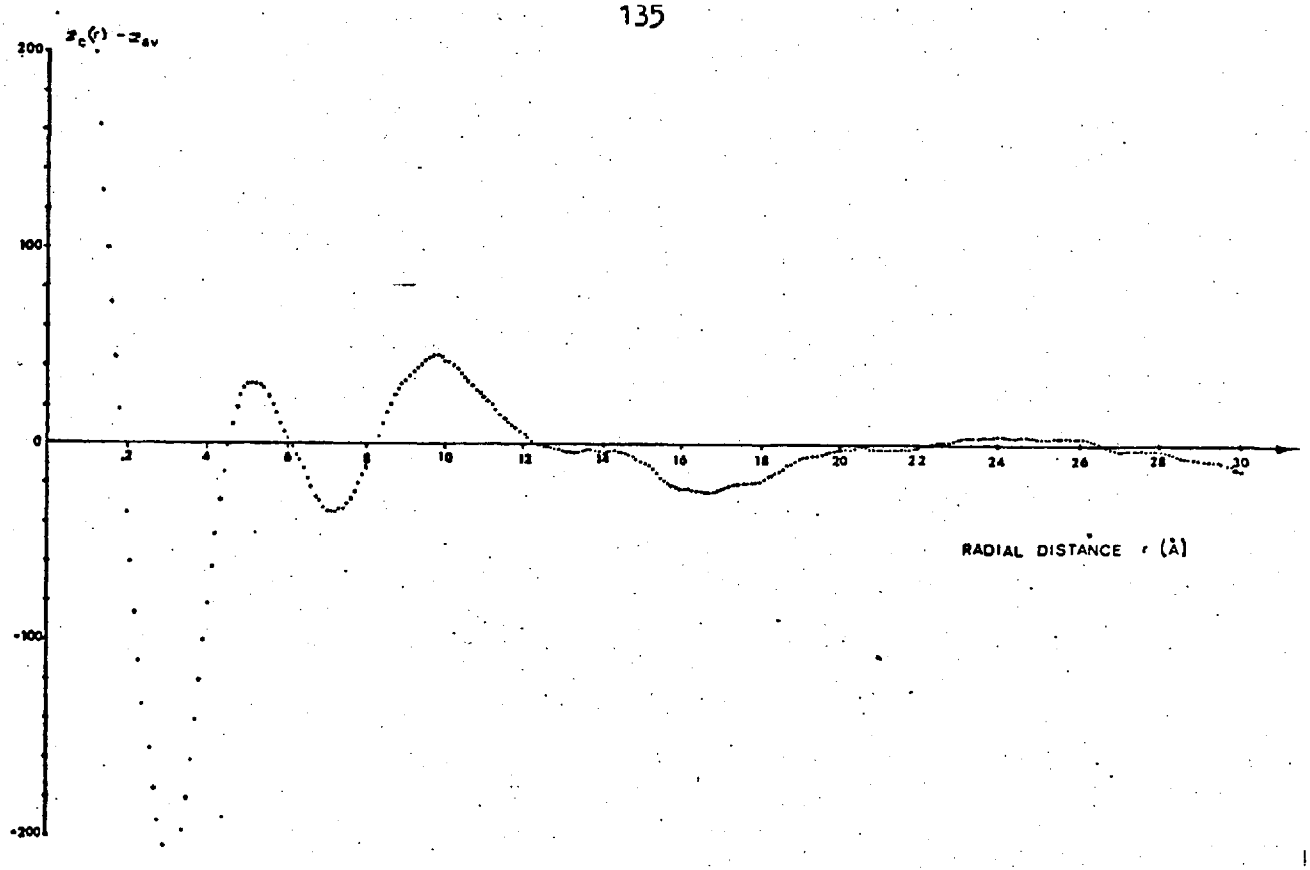

Fig.4.30 Cylindrical distribution function $z_c(r) - z_{av}$ for the equatorial scattering from orientated atactic polystyrene.

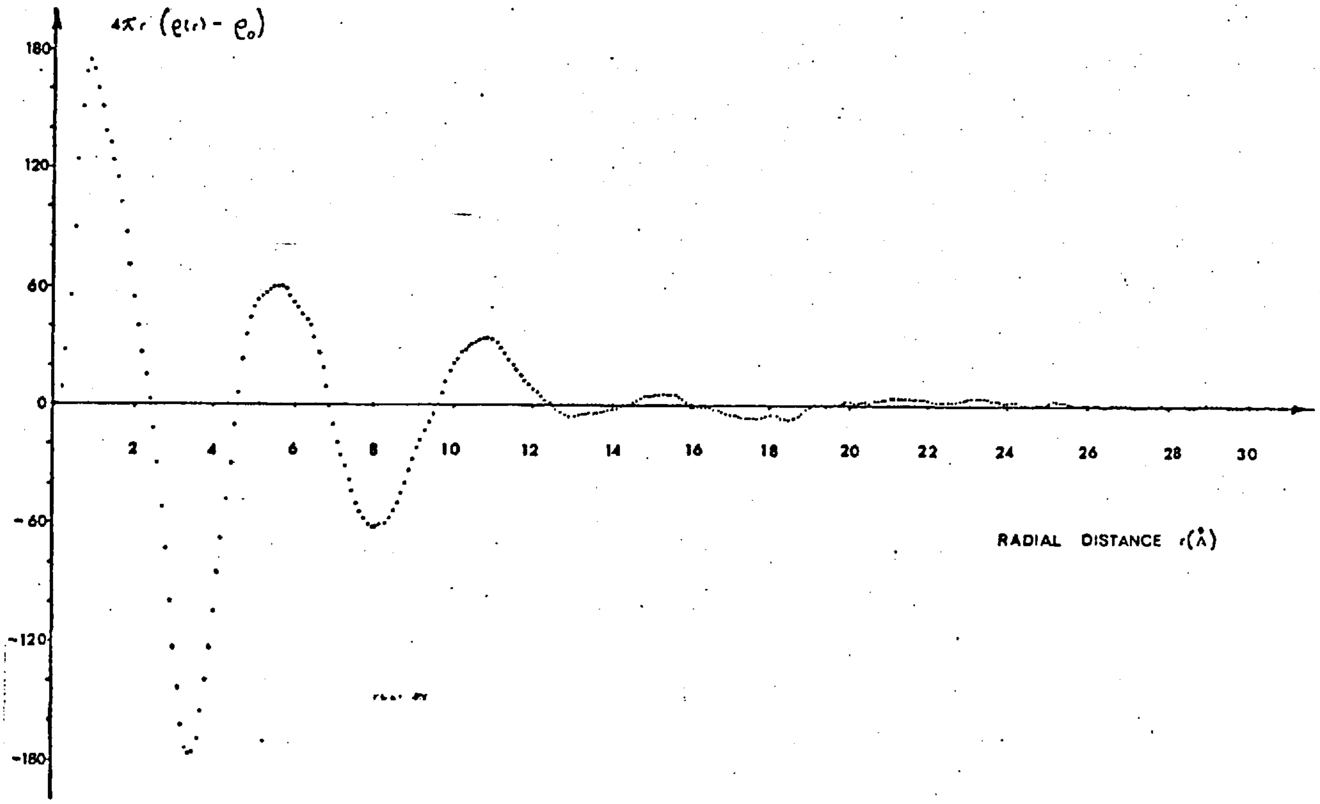

Fig.4.31 Radial distribution function obtained for the equatorial scattering from orientated atactic polystyrene. (Spherical symmetry has been assumed).

Peak	r (Å)	$4\pi r(\rho(r) - \rho_o)$
1	0.9	271
2	5.7	50
3	10.45	46
4	15.0	~4
5	19.8	~4
6	~24.6	~1

Table 4.20 Details of radial distribution function for the equatorial scattering from orientated atactic polystyrene. (Spherical symmetry has been assumed).

The general features of the cylindrical distribution $z_c(r)$ were also evident in the RDF, but no corresponding long wave component was present.

The long wavelength component may have arisen from the numerical transformation process and it was therefore considered safest not to interpret this component in terms of physical effects.

4.6 The WAXD from Orientated Atactic Polymethyl Methacrylate

Preferential molecular orientation was induced in atactic PMMA by cold drawing tensile specimens at 85°C. At 85°C it was found that PMMA could be drawn fairly easily 2 : 1. Plate 4.4 shows the typical orientation that was obtained. Equatorial and meridional diffractometer samples were prepared in identical fashion to those of polystyrene (Fig.4.24). The orientation obtained was inferior to that of the polystyrene samples but considerable arcing was produced. The inner halo at ~ 6.29Å was clearly oval in shape indicating the presence of both equatorial and meridional components. The very much fainter ring at 2.85Å showed slight meridional arcing.

These observations were confirmed quantitatively using the diffractometer. Fig.4.32 shows the X-ray scattering detected along the meridian

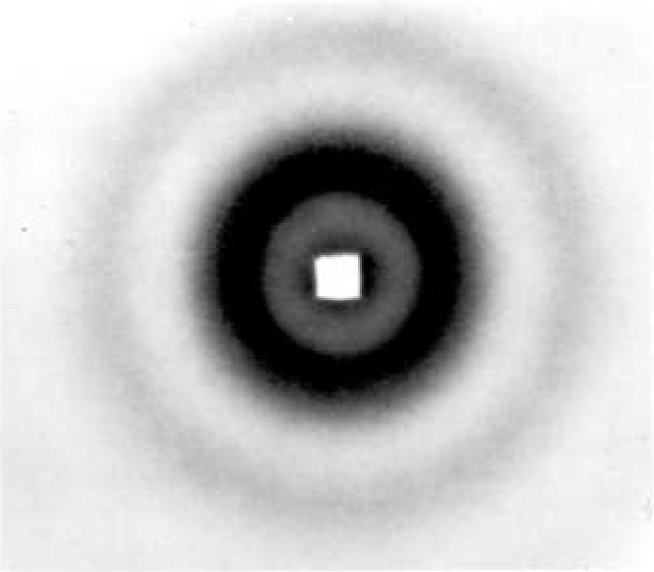

Plate 4.3 Pinhole transmission X-ray pattern from unorientated atactic poly(methyl methacrylate). Nickel-filtered CuKα radiation.

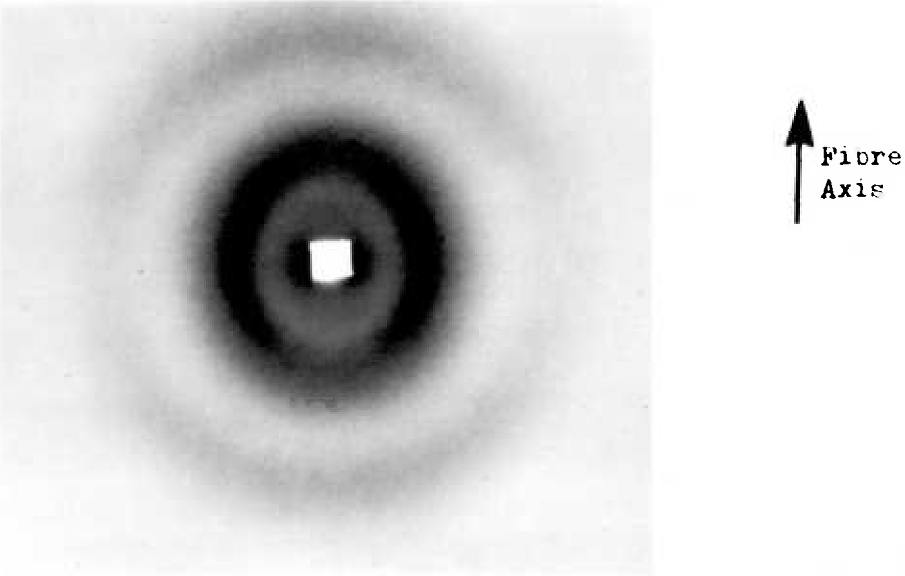

Plate 4.4 Pinhole transmission X-ray pattern from orientated atactic poly(methyl methacrylate). The sample was orientated by stretching 2 : 1 at 85°C ($< T_g$).

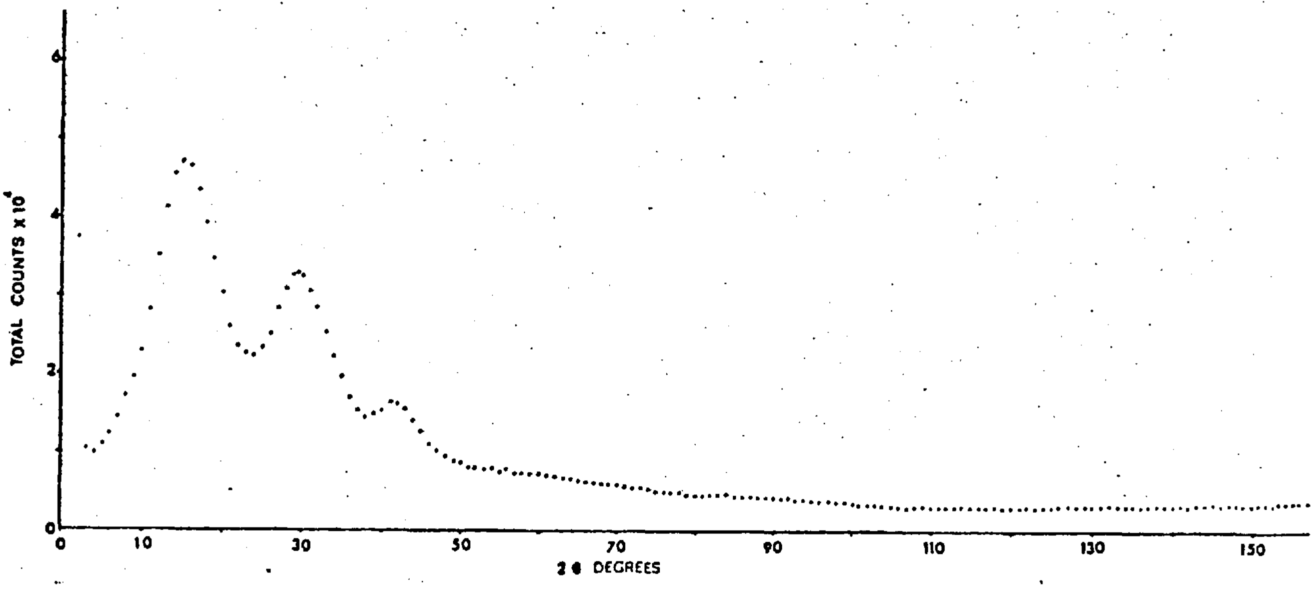

Fig.4.32 The uncorrected experimental scattering intensity measured along the meridian for orientated atactic PMMA (CuKα).

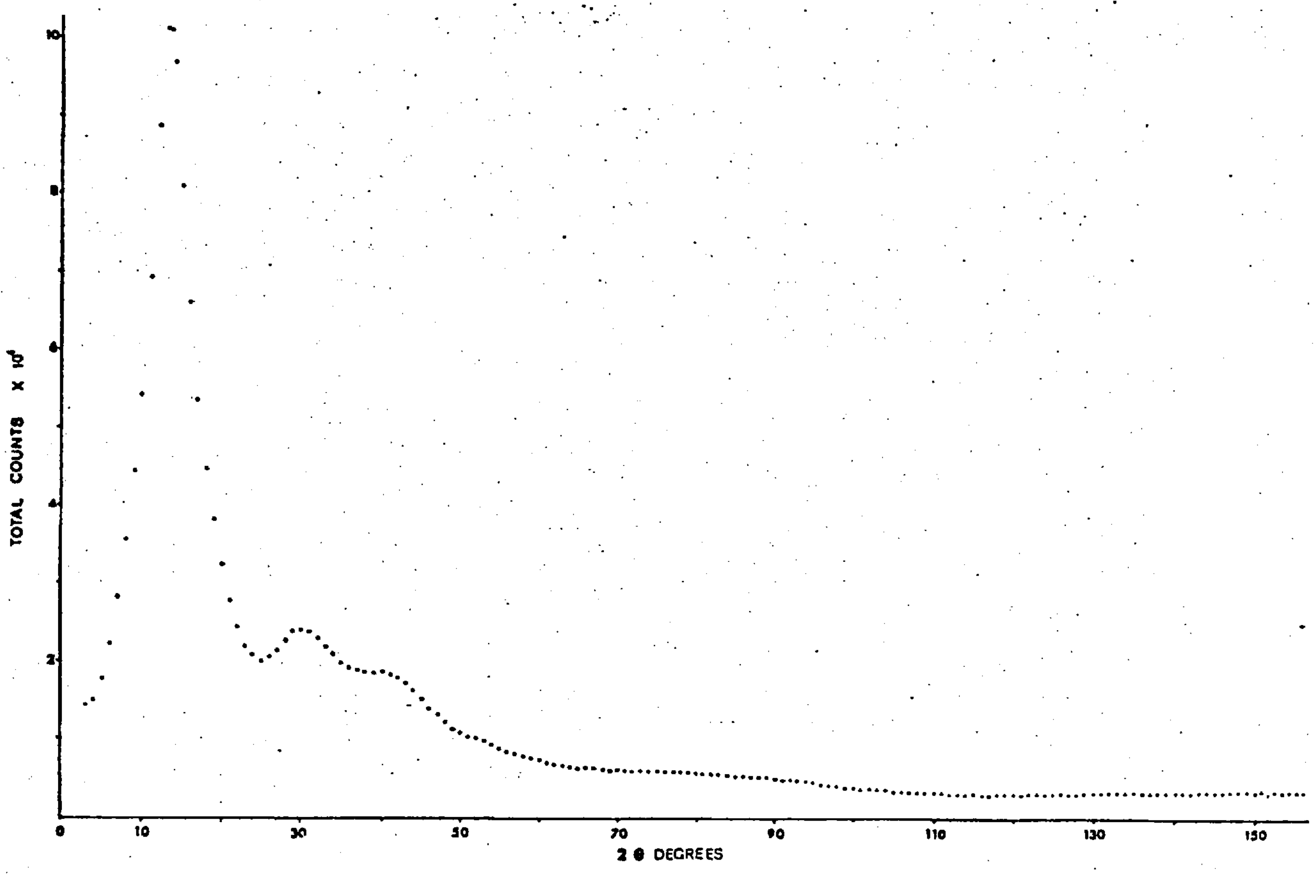

Fig.4.34a The uncorrected experimental scattering intensity measured along the equator of an orientated atactic PMMA specimen (CuKα).

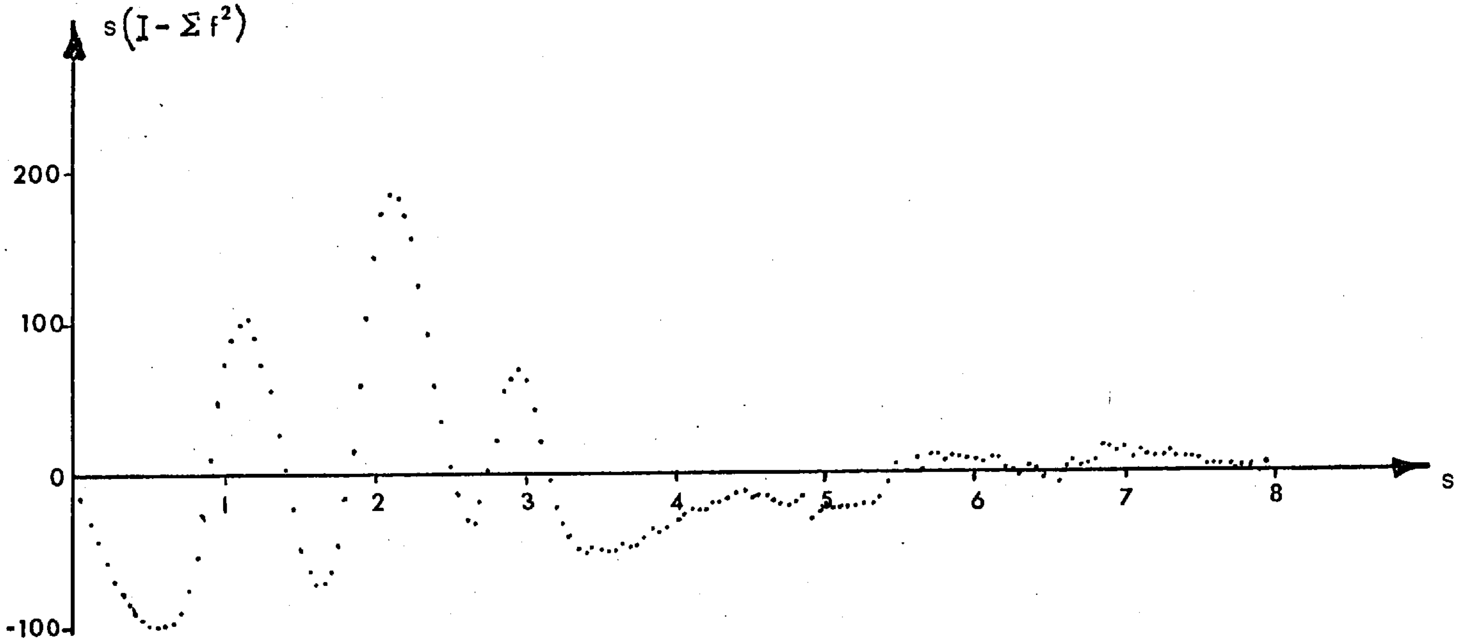

Fig.4.33 The meridional interference function for orientated atactic PMMA.

of an orientated PMMA specimen. The Bragg spacings corresponding to the intensity maxima were as follows:

2θ	15°	29.5°	41.5°	90°
d-spacing (Å)	5.91	3.03	2.18	1.09

Table 4.21 The Bragg spacings for the meridional scattering from orientated atactic PMMA (CuKα).

Fig.4.33 shows the meridional interference function for orientated atactic PMMA:

Peak	1	2	3	4	5
s (Å^{-1})	1.15	2.13	2.95	~4.45	~5.75
Intensity (e.u.)	100	185	69	-15	10
d-spacing (Å)	5.46	2.95	2.14	1.41	1.09
$\frac{I_{orientated}}{I_{unorientated}}$	0.38	2.23	0.99	-	0.40

Table 4.22 Details of the interference function for the meridional scattering from orientated atactic PMMA.

The second peak (2.95Å) had more than doubled in intensity whilst a peak at ~1.41Å was detected which was absent from the interference functions of all other samples.

Fig.4.34 shows the interference function for the equatorial scattering:

Peak	1	2	3	4
s (Å^{-1})	0.98	2.25	2.95	5.75
Intensity (e.u.)	395	15	70	30
d-spacing (Å)	6.40	2.79	2.15	1.09
$\frac{I_{orientated}}{I_{unorientated}}$	1.51	0.18	1.00	0.60

Table 4.23 Details of the interference function for the equatorial scattering from orientated atactic PMMA.

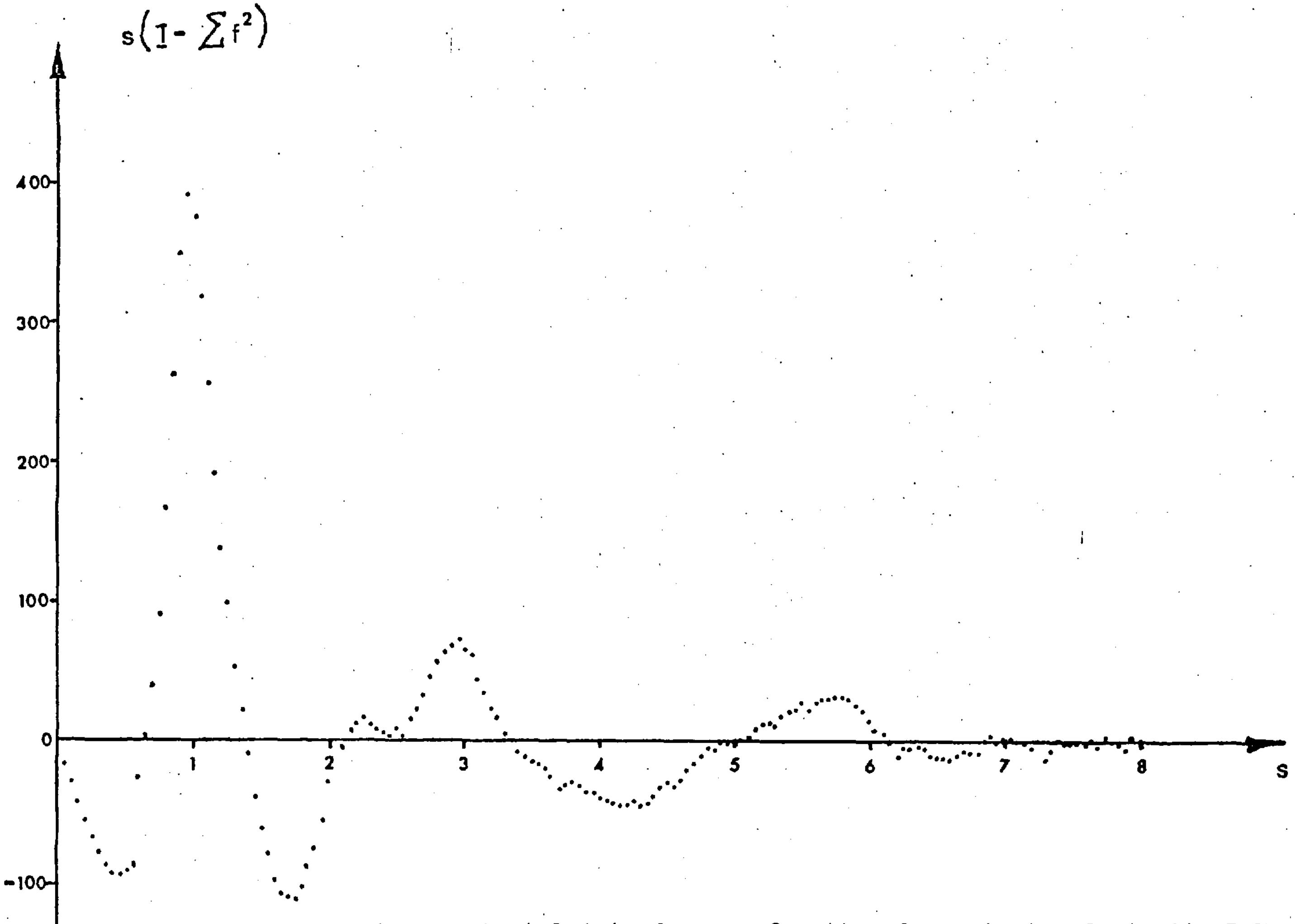

Fig.4.34 The equatorial interference function for orientated atactic PMMA.

Thus it was concluded that the first peak in unorientated PMMA (6.29Å) was constructed of two components: an intramolecular peak centred at ~5.46Å and a more intense intermolecular peak centred at ~6.40Å. The second peak in unorientated PMMA (2.85Å) was constructed predominantly of an intramolecular peak at ~2.95Å in the orientated material and the third peak (~2.14Å in unorientated PMMA) was composed of equal amounts of intra- and inter-molecular effects.

Fig.4.35 shows the distribution function $H_3(z) - H_{3(o)}$ for the meridional scattering of orientated PMMA:

Peak	r (Å)	$H_3(z) - H_{3(o)}$	$\Delta r = \bar{c}$
1	0.70	-44	2.40
2	3.10	-25	2.85
3	5.95	23	2.90
4	8.85	-1	2.25
5	11.10	1	1.65
6	12.75	2.5	2.35
7	15.10	1	

Table 4.24 Details of the distribution function $H_3(z)$ for orientated atactic PMMA.

Unlike the case of atactic polystyrene, $H_3(z)$ for PMMA did not resemble the kind of distribution function obtained for pure paracrystalline distortions. The main feature of $H_3(z)$ was a large peak at 5.95Å. All oscillations damped away within the range $r_m \approx 18$Å.

The one dimensional cylindrical distribution $z_c(r)$ was also calculated and is reproduced in Fig.4.36.

Peak	r (Å)	$z_c(r) - z_{av}$
1	0.7	100
2	2.35	26
3	6.8	38
4	~8	~12
5	11	4
6	21.4	14

Table 4.25 Details of the cylindrical distribution function $z_c(r)$ for orientated atactic PMMA.

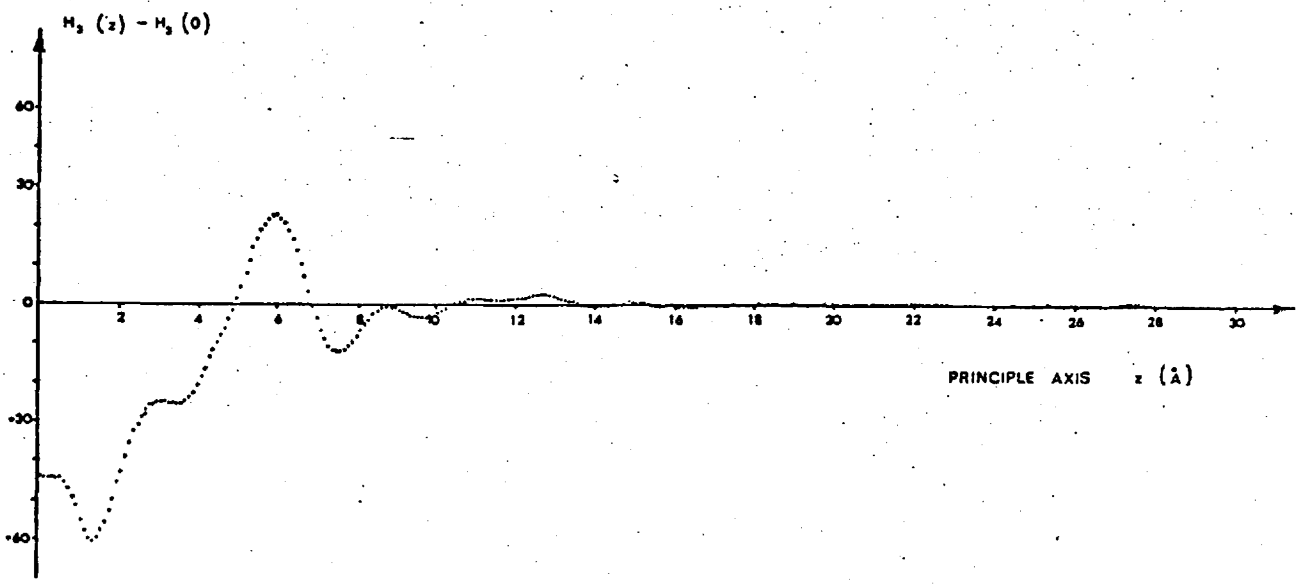

Fig.4.35 The distribution function $H_3(z) - H_{3(o)}$ for the meridional scattering from orientated atactic PMMA.

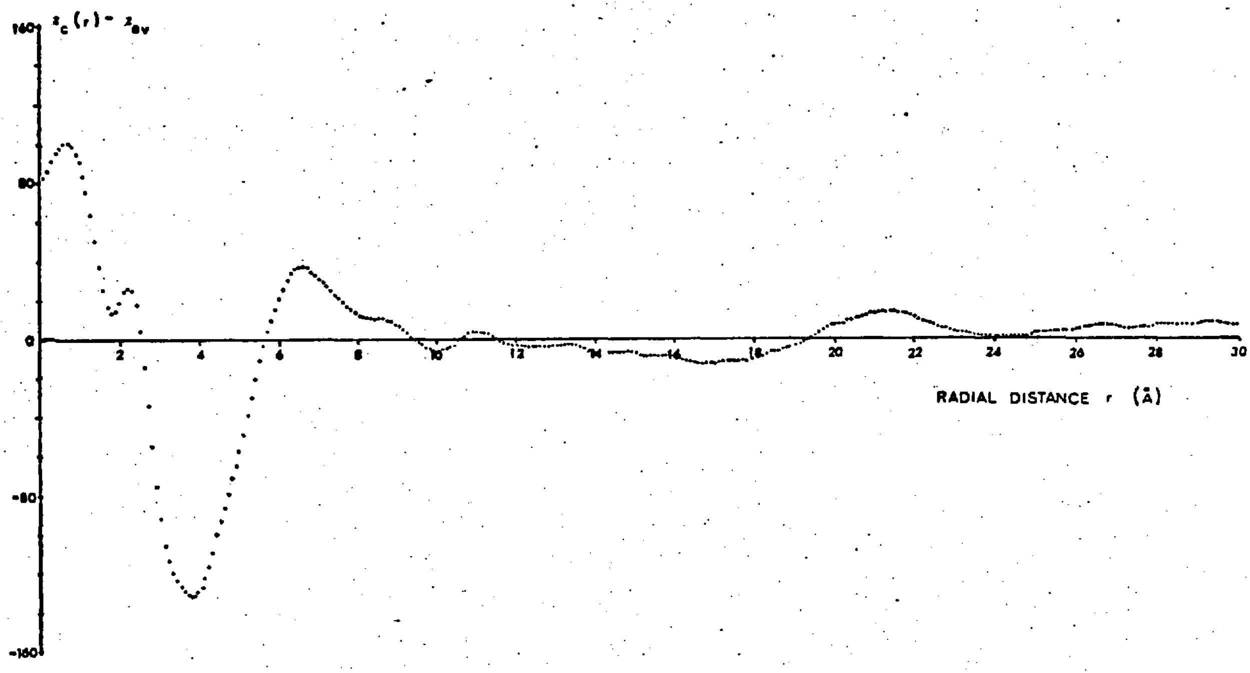

Fig.4.36 Cylindrical distribution function $z_c(r) - z_{av}$ for the equatorial scattering from orientated atactic PMMA.

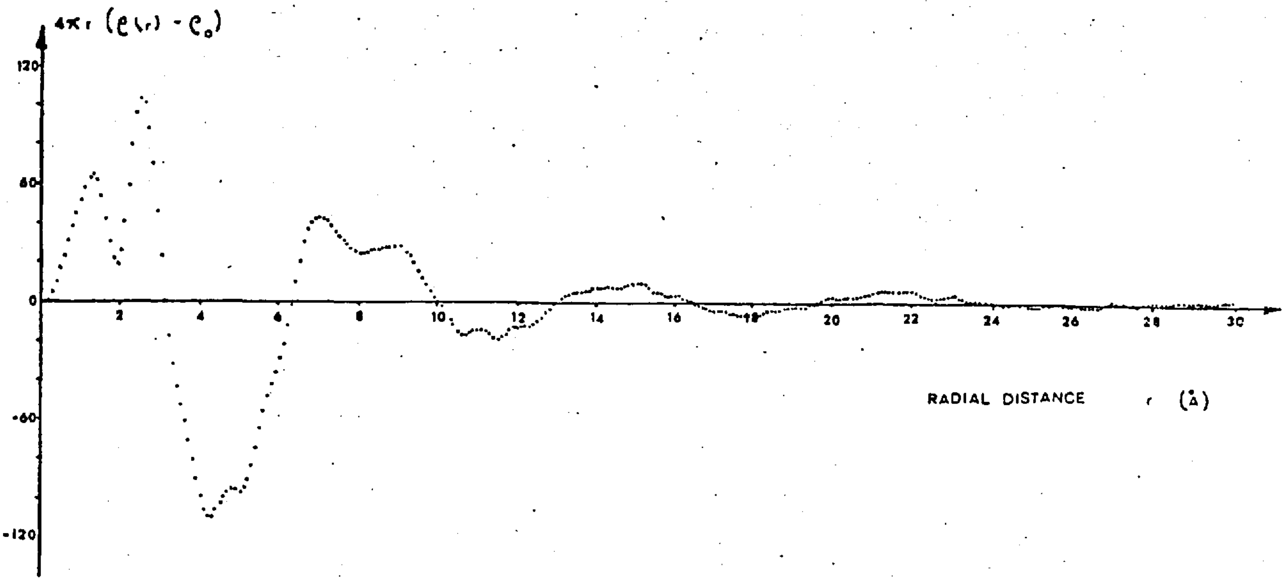

Fig.4.37 Radial distribution function obtained for the equatorial scattering from orientated atactic PMMA. (Spherical symmetry has been assumed).

As with polystyrene, this function may contain spurious details so a radial distribution function was also generated from the equatorial interference function (Fig.4.37).

Peak	r (Å)	$4\pi r(\rho(r) - \rho_o)$
1	1.3	64
2	2.5	102
3	7.0	42
4	~8.7	28
5	14.7	9
6	~21.8	5

Table 4.26 Details of the radial distribution function generated from the equatorial interference function for orientated PMMA (spherical symmetry assumed).

4.7 The Equilibrium Swelling of PMMA by Methyl Alcohol

Initial test specimens were cut from 1.5mm PMMA sheet, cleaned and weighed on a microbalance and then placed in flasks containing methyl alcohol. The specimens were kept at constant temperature (20°C or 60°C) for between two days and six months. Periodically the specimens were removed from their flasks, dried with tissue paper and weighed on a microbalance. The volume fraction V_P of the polymer in the PMMA/alcohol mixture was calculated as

$$V_P = (W_P/\rho_P) / (W_A/\rho_A + W_P/\rho_P)$$

where W_A and W_P are the weight of alcohol in the swollen mixture and the original weight of the PMMA respectively. ρ_A and ρ_P are the density of the alcohol at the test temperature and the density of the PMMA.

Equilibrium Swelling at 60°C

From the weight measurements it was found that equilibrium swelling occurred in the PMMA/methanol system in about two days. Equilibrium volume fractions of between 0.60 and 0.64 were obtained and after equilibrium swelling had been achieved the PMMA specimens were found to be quite rubbery. Andrews et al.[70] have observed that for all the alcohols, T_g was increasingly depressed with increased swelling, and have estimated that for PMMA/methanol with $V_p = 0.6$, T_g was approximately 15°C.

At this point the specimens were removed from their flasks, dried and then placed in stoppered containers at room temperature. The weight of each specimen was then monitored at regular intervals. Fig.4.38 shows the typical desorption isotherm obtained. After an initial rapid rate of weight loss (from $V_p = 0.61$ to $V_p = 0.72$ in three hours) the rate decreased so that after fifty hours the specimen still contained 10% by weight of methanol ($V_p \sim 0.86$). The decrease in the rate could be attributed to

a) classical diffusion behaviour (Fick's Law: Particle flux proportional to concentration gradient).

b) a "skin" of glassy unswollen polymer that formed on the specimen's surfaces after a period of a couple of hours (for $V_p = 0.7$; $T_g \sim 30°C$).

Volume and density measurements were performed on a carefully machined PMMA block whose surface dimensions were accurately known. Table 4.27 shows the results before and after equilibrium swelling in methanol. Upon removal from methanol at 60°C the specimen was found to have increased in volume by approximately 52% while only increasing in weight by 38%. This represented a density decrease of approximately 10%. The swollen sample had only slightly inferior optical properties to the original unswollen polymer suggesting that the observed density decrease was not due to the presence of small voids in the material.

	Mean Volume cm^3 (± 0.005)	Mean Weight gm (± 0.0005)	Density gm/cm^3 (± 0.01)	V_p	Ratio of surface dimensions
Before swelling	2.976	3.5444	1.19	1.00	1 : 1.34 : 2.76
Immediately after swelling	4.537	4.8850	1.08	0.64	1 : 1.25 : 2.51
After 4 days at room temp.	3.605	4.1602	1.15	0.80	1 : 1.25 : 2.54

Table 4.27 Estimates of the density of a PMMA specimen before and after swelling to equilibrium in Methyl Alcohol at 60°C (Average of five readings).

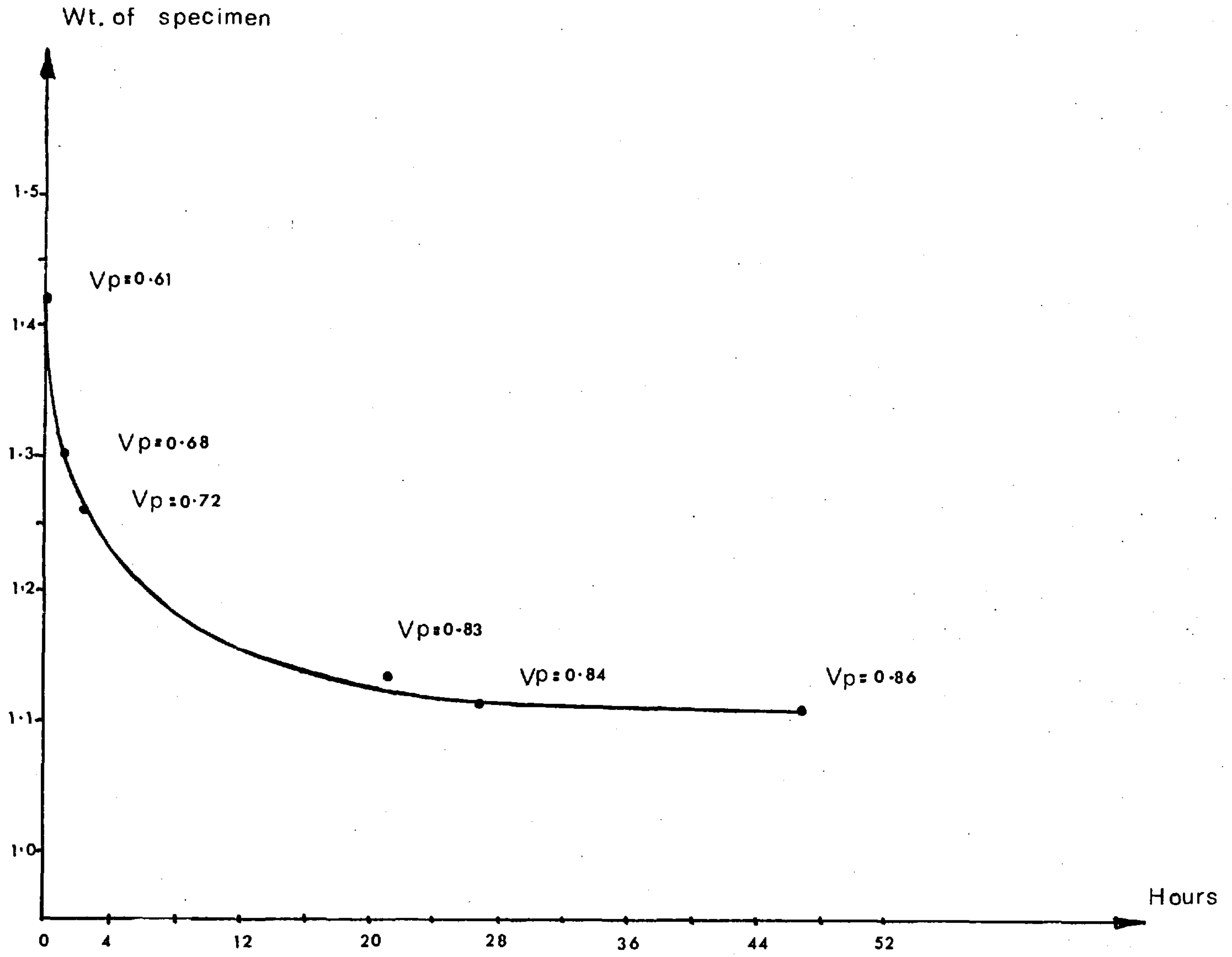

Fig.4.38 Desorption isotherm for a 0.15cm sheet of atactic PMMA after swelling in methanol at 60°C.

The ratios of the surface dimensions showed that strains induced in the formation of the sheet from which the block was cut were relaxed upon swelling (the percentage increase in the dimension corresponding to the sheet thickness was the largest). Strain relaxation was also observed in PMMA specimens which had been previously orientated by stretching 2 : 1 at 85°C. Identical swelling characteristics to those described above were observed with the polymer fully recovering its pre-stretched dimensions.

Fig.4.39 shows the uncorrected WAXD pattern observed for a 0.35cm sheet of PMMA swollen to equilibrium in methanol at 60°C. Upon removal from the methanol the specimen was immediately mounted in the diffractometer at room temperature. The scan time required was approximately 35 hours. The Bragg spacings corresponding to the observed halos were as follows:

2θ	14.5°	30°	41°	89°
d-spacing (Å)	6.11	2.98	2.20	1.10

Table 4.28 The Bragg spacings for PMMA swollen in methanol at 60°C.

The most striking feature of this pattern was the reduction in the intensity of the first halo and its shift to a smaller d-spacing. The experimental intensity was normalised in the usual manner with due regard for the inclusion of methanol molecules (38% by weight) in the calculation of $\sum f^2$ for the sample. No attempt was made to remove the intensity arising from interference effects between the atoms in each methanol molecule. The interference function (Fig.4.40) had the following properties:

Peak	1	2	3	4
s (Å^{-1})	1.1	2.18	2.95	5.70
Intensity (e.u.)	63	72	50	43
d-spacing (Å)	5.71	2.88	2.14	1.10
$\frac{I_{swollen}}{I_{unswollen}}$	0.24	0.87	0.72	1.72

Table 4.29 The interference function for atactic PMMA swollen to equilibrium in methanol at 60°C then examined in air at room temperature.

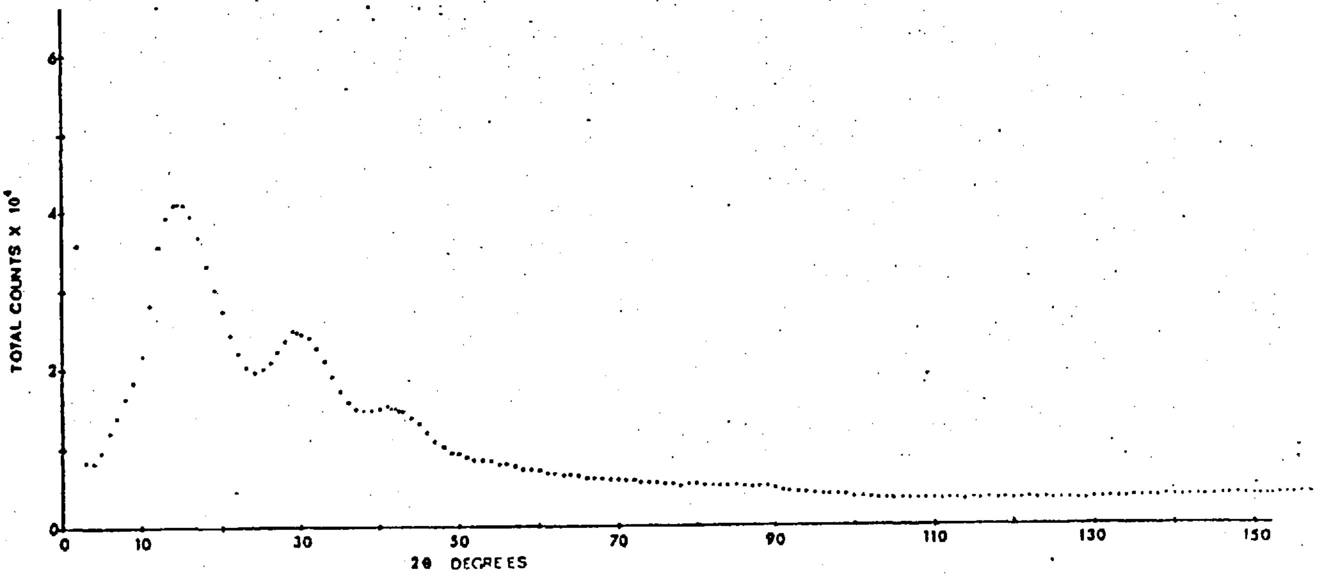

Fig.4.39 The uncorrected experimental scattering intensity for an atactic PMMA sample swollen to equilibrium in methanol at 60°C and then examined in the diffractometer at room temperature in air.

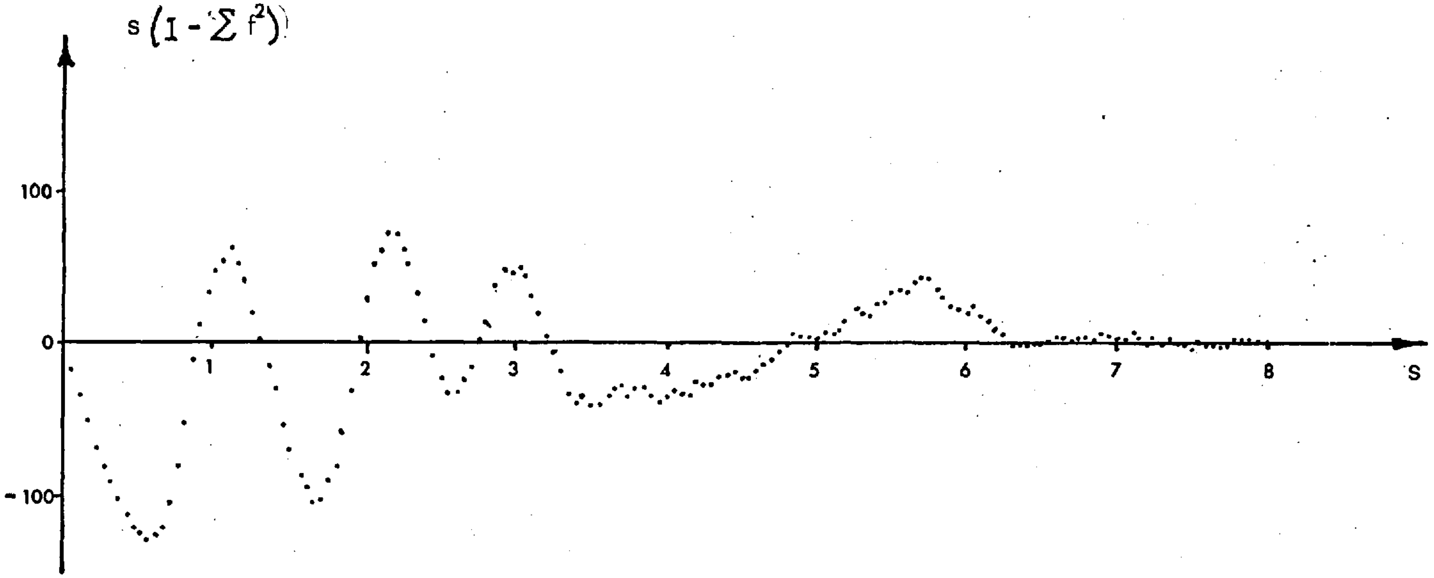

Fig.4.40 The interference function for atactic PMMA swollen to equilibrium in methanol at 60°C then examined in air at room temperature.

Comparison of these peaks with those of "as received", and orientated atactic PMMA (Fig.4.41 and 4.42) suggested that the scattering from swollen PMMA was predominantly intramolecular in nature.

Fig.4.43 shows the reduced electronic radial distribution function for the PMMA/methanol system

Peak	r (Å)	$4\pi r(\rho(r) - \rho_o)$
1	1.25	-1
2	2.65	8
3	3.5	-27
4	4.70	-41
5	6.73	53
6	9.15	14
7	~15.2	3

Table 4.30 Details of the radial distribution function for atactic PMMA swollen to equilibrium in methanol at 60°C.

When the swollen PMMA was removed from the diffractometer and baked for several days in an oven at $\leqslant$ 100°C it was found that the sample regained its original weight and that the WAXD pattern was identical to that of the pre-swollen polymer.

Swelling at Room Temperature

At this lower temperature it was found that the time for sorption was considerably increased: equilibrium swelling by methanol took approximately one month (V_P = 0.77). This volume fraction depressed T_g to approximately 35°C and thus the specimens were not rubbery at room temperature. Accurate measurements of weight and volume of the PMMA/methanol system yielded a density of 1.16 (weight increase ~ 8%, volume increase ~ 12%). When the PMMA/methanol sample was removed finally from its flask and dried, it initially lost weight rapidly (V_P = 0.77 to V_P = 0.80 within one hour). However as with PMMA/methanol at 60°C the rate decreased and after 50 hours V_P was of the order of 0.87. Fig.4.44 shows the uncorrected experimental intensity observed.

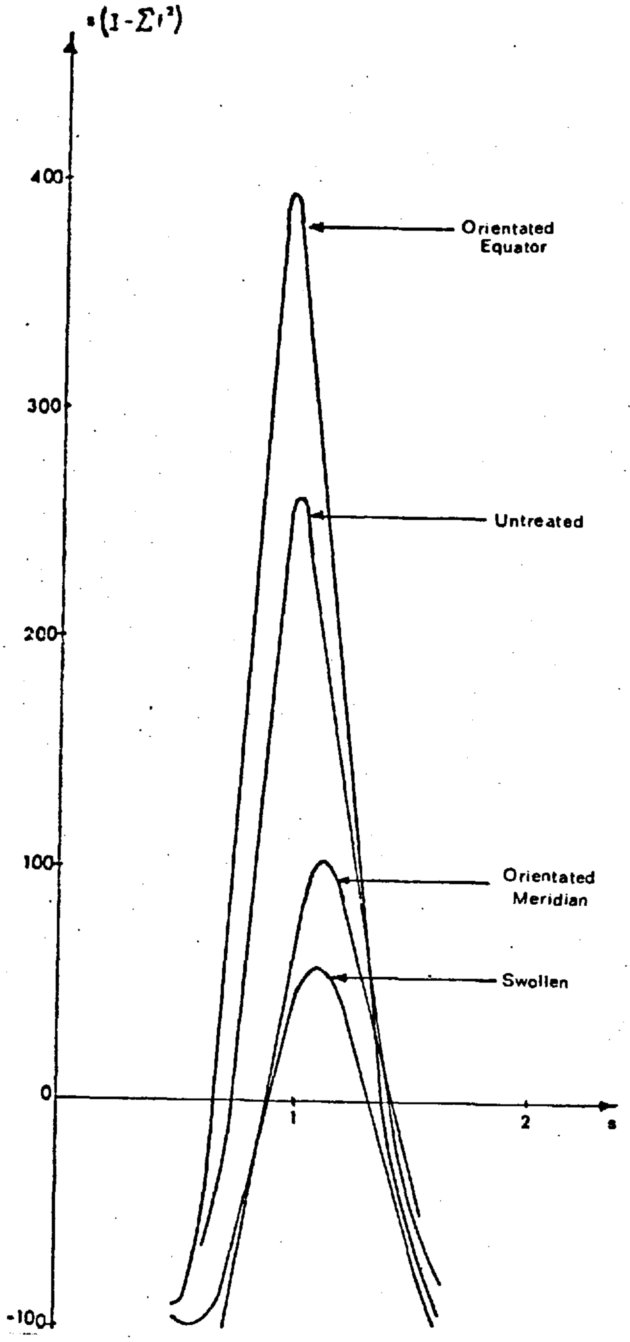

Fig.4.41 Comparison of the first peak in the interference functions of untreated, swollen and orientated atactic PMMA.

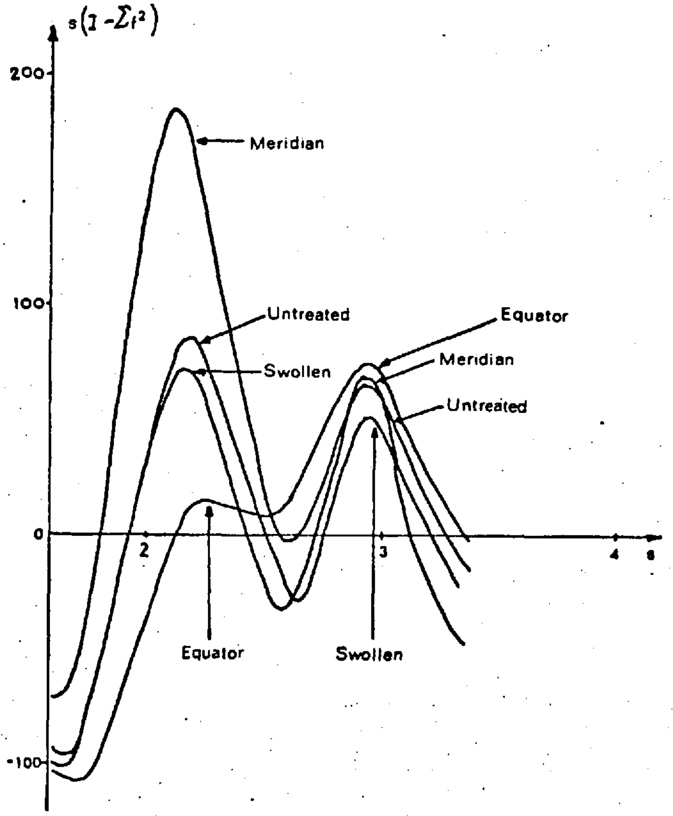

Fig.4.42 Comparison of the second and third peaks in the interference functions of untreated, swollen and orientated atactic PMMA.

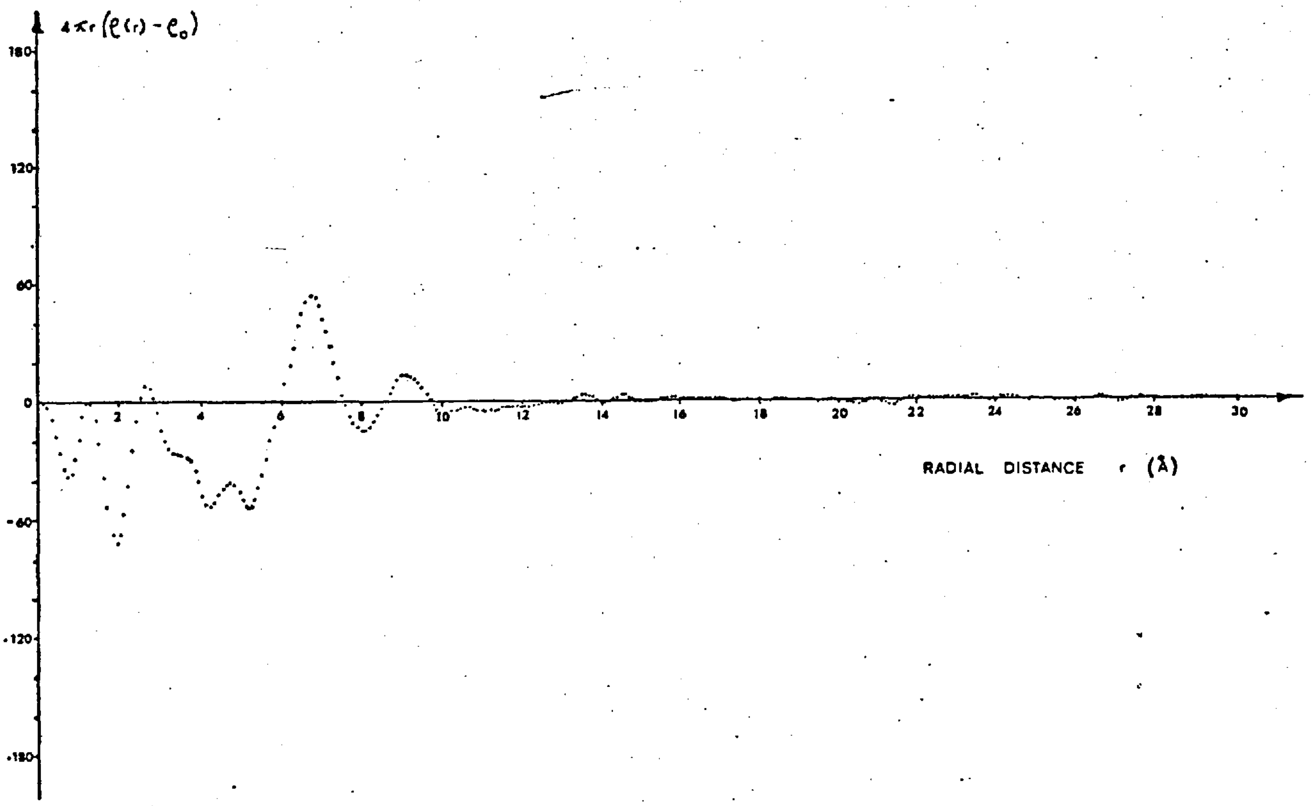

Fig.4.43 Reduced electronic radial distribution function for an atactic PMMA sample swollen to equilibrium in methanol at 60°C and examined in air at room temperature.

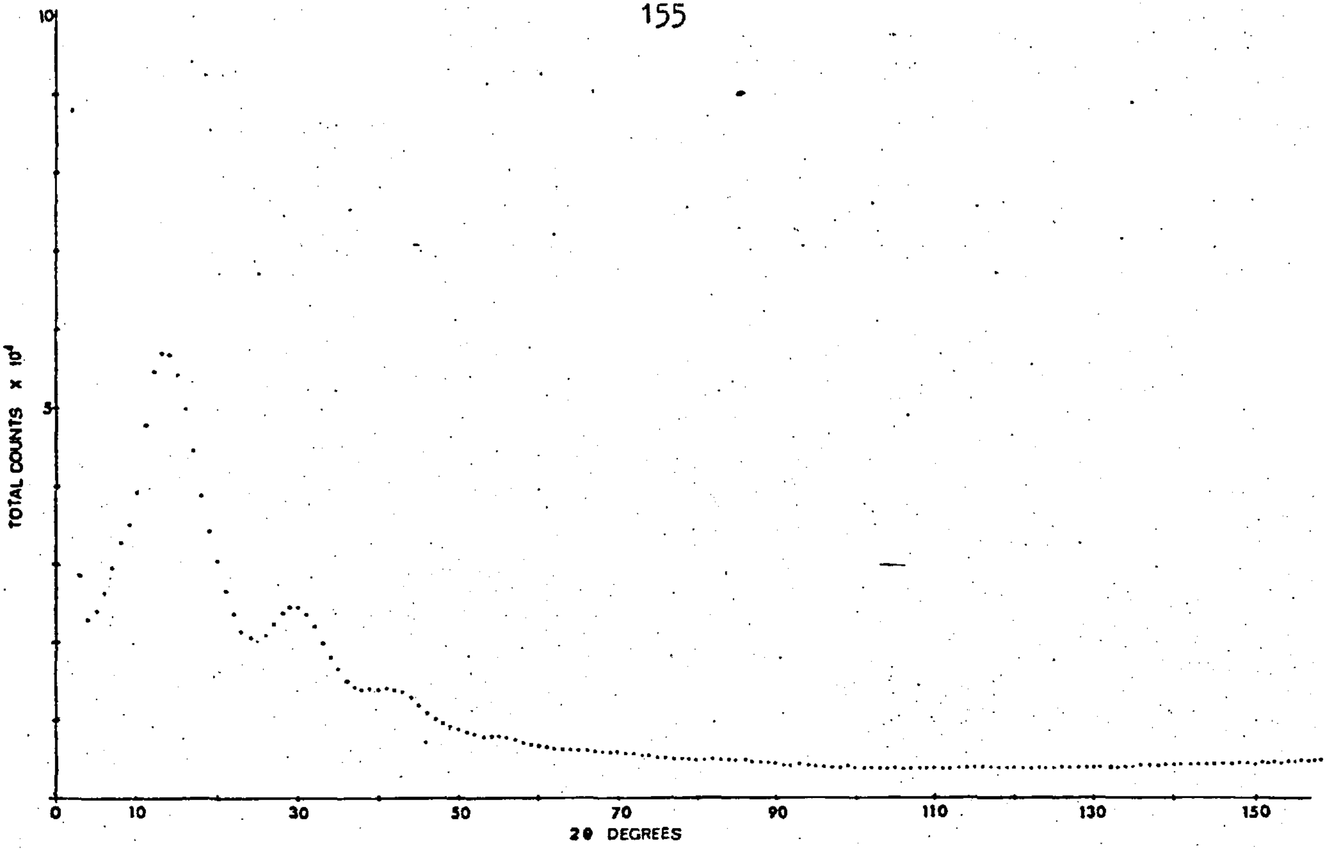

Fig.4.44 The uncorrected experimental scattering intensity for an atactic PMMA sample swollen in methanol at room temperature and then examined in air (CuKα).

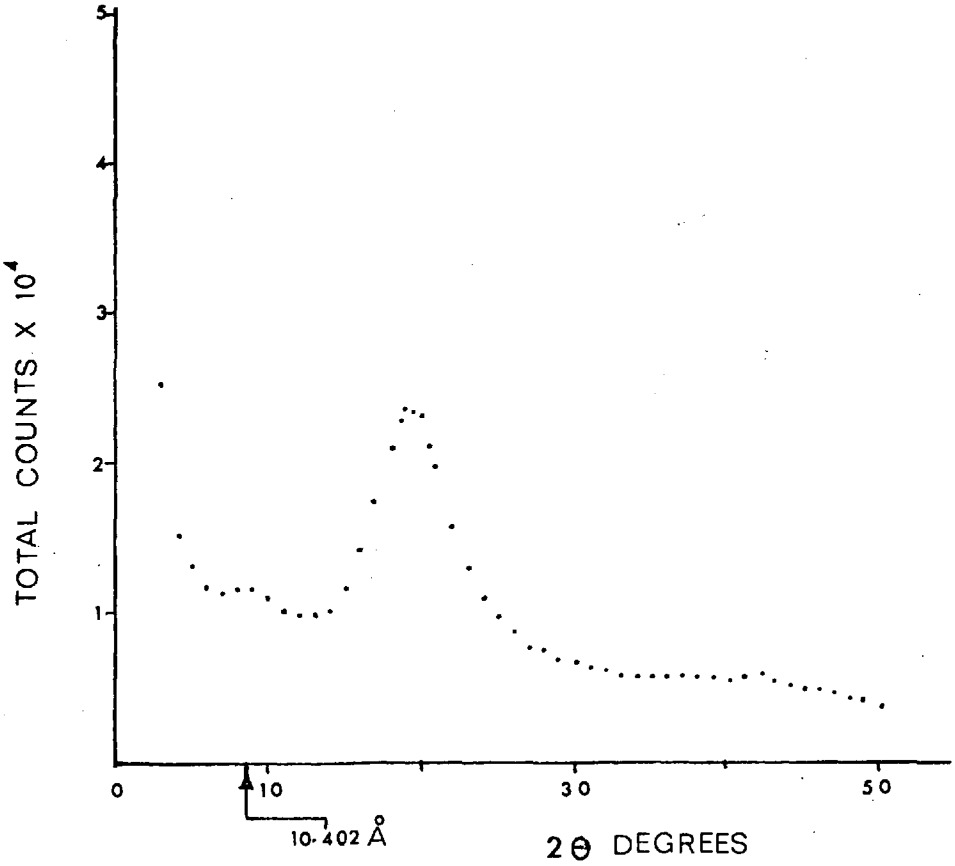

Fig.4.45 A typical experimental scattering curve for an atactic polystyrene/acetone gum.

2θ	13.5°	30°	41°	87°
d-spacing (Å)	6.56	2.98	2.20	1.12
$\frac{I_{swollen}}{I_{unswollen}}$	0.72	0.63	0.78	~1

Table 4.31 The Bragg spacings for atactic PMMA swollen in methanol at room temperature.

The first three peaks were reduced in intensity but no significant shifting in s was observed.

4.8 The WAXD from Atactic Polystyrene Dissolved in Acetone

No suitable organic liquid was found that would swell uncrosslinked polystyrene to the extent that alcohol swelled PMMA. However acetone was found to dissolve the polymer into a sticky gum and this was used to investigate the effect of solvent on the 8.85Å intermolecular peak of atactic polystyrene.

Three millimetre thick sheets of atactic polystyrene were immersed in a flask containing excess amounts of acetone at room temperature. After a period of about 30 minutes the swollen gum was removed from the flask and stretched over a rectangular wire frame and mounted into the diffractometer. Fig.4.45 shows the typical WAXD pattern observed. The intensity quite closely resembled that of the uncorrected meridional scattering of orientated polystyrene. Unfortunately the specimen quickly (~60 sec) developed a skin of dry polymer over its surfaces which rendered it quite rubbery and tended to pull it into a ball. Thus these results were not considered suitable for detailed analysis.

Fig.4.46 shows how the profile of the 8.85Å peak changed with the time for which the specimen was out of the solvent. These plots show clearly that the intermolecular peak was all but absent from the scattering when the gum was first removed, but within a few minutes this quickly returned as the dry skin formed. The residue of the peak was shifted to a longer Bragg spacing (8.85Å → 10.40Å) but this was difficult to interpret since the peak must be superimposed on the tails of others.

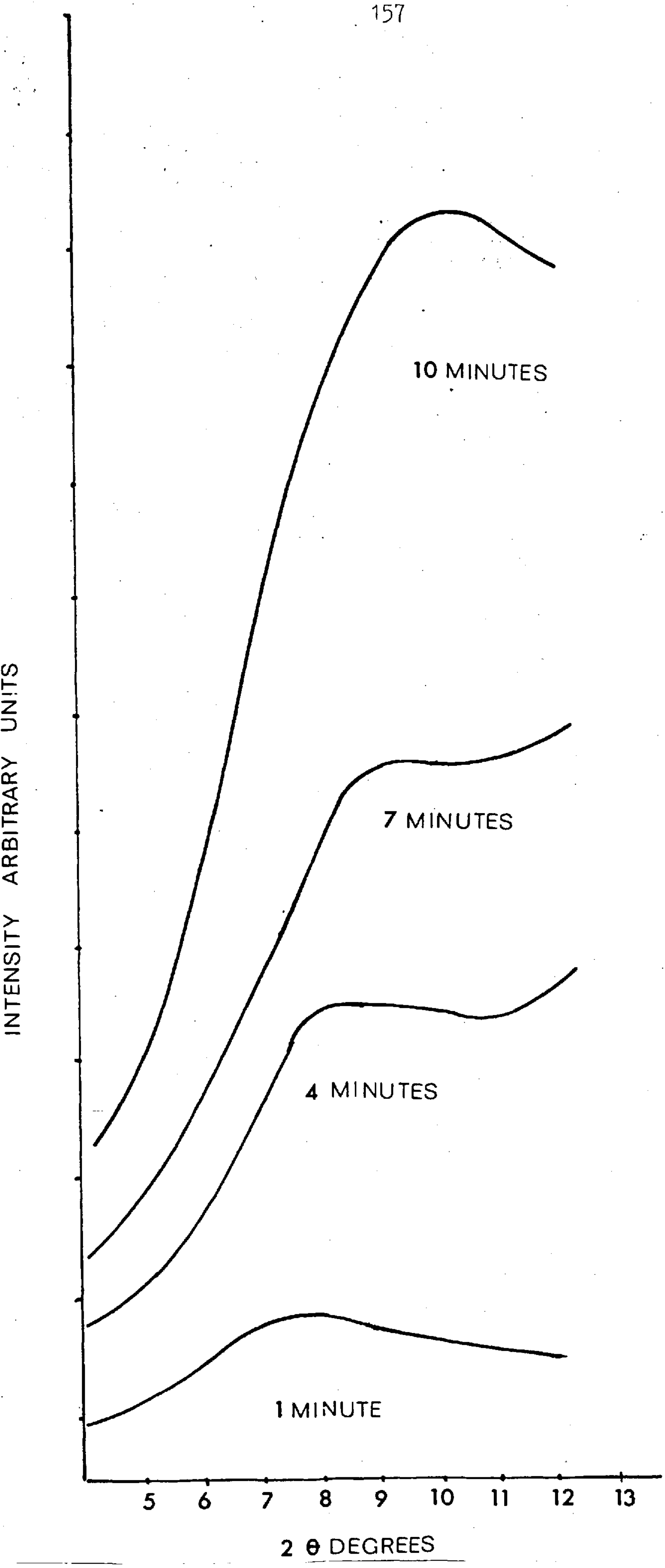

Fig.4.46 Variation in the profile of the 8.85Å peak of the atactic polystyrene/acetone gum with time out of the solvent.

4.9 Concluding Remarks

One dimensional radial and cylindrical distribution functions have been generated from the wide-angle X-ray diffraction detected from atactic polystyrene and atactic polymethyl methacrylate. With the exception of $H_3(z)$ for orientated polystyrene none of these distribution functions exhibited the characteristics described in Chapter 2 for arrays with paracrystalline distortion. However, in the remaining chapter an attempt is made to demonstrate that the diffraction effects observed do not preclude the presence of paracrystalline order, and that not all of these paracrystalline effects could be explained by the periodicity inherent in each chain. On this basis it is suggested that the swelling of PMMA by methanol results in the destruction of interchain ordering. The discussion centres on the separation of the interference functions into intra- and intermolecular scattering contributions.

CHAPTER FIVE

DISCUSSION OF THE RESULTS

5.1 Radial Distribution Functions

This work has high-lighted the problems associated with the generation of radial distribution functions. In particular the effects of data termination and normalisation have been investigated and the latter has been shown to be of paramount importance in obtaining error free RDFs. The close similarity between the atomic RDFs for quenched atactic polystyrene obtained by Wecker, Davidson and Cohen[52] (Fig.1.14) and Fig.4.10 for a different commercial sample of the same polymer demonstrated the reliability of the method and the similarity of the two samples on a microscale.

The electronic radial density function obtained for "as received" atactic PMMA (Fig.4.18) was also remarkably similar to that obtained by Bjornhaug et al.[50] (Fig.1.10) using X-ray films. It appears that the electronic form of the RDF is to be preferred since the atomic RDF emphasises the presence of residual normalisation ripple which can lead to a seriously distorted transform. It is felt that this is what occurred in the atomic RDFs of polycarbonate obtained by Wignall and Longmann[54].

The RDF of atactic polystyrene (Fig.4.4) differed significantly from that of amorphous isotactic polystyrene (Fig.4.12) in that the spacings in the isotactic material were consistently longer. Wecker, Davidson and Cohen[52] observed similar differences in their atomic RDFs of quenched atactic and quenched isotactic polystyrene, although the shifts in the peak positions were smaller and the peak at $r \approx 5\text{Å}$ shifted to a shorter spacing in the isotactic sample (see Table 1.4). An exactly similar effect was observed when amorphous isotactic polystyrene was annealed below T_g (Table 1.4). Wecker, Davidson and Cohen showed that annealing isotactic polystyrene below T_g resulted in ~ 1% increase in the sample density. Thus to explain the effects described, the RDFs of polystyrene must be dominated by intramolecular effects, and from the results of Wecker, Davidson and Cohen it appears that their peak at r ~ 5Å was predominantly intermolecular in nature. In the electronic RDF we obtained for amorphous isotactic polystyrene no shift to a shorter spacing was observed in the third peak (r ~ 6Å) corresponding to their 5Å peak. This may be due to the increased breadth of the peaks in the electronic form of the RDF which could mask small changes in peak positions.

Similar annealing effects were observed in the atactic PMMA sample: annealing produced 0.3Å shifts to longer spacings for the fifth and sixth peaks in the RDF. However the effect of annealing was most marked in the interference function (Fig.4.21).

To obtain much more information from the interference and radial distribution functions, we must estimate more clearly the nature of the peaks in these functions i.e. distinguish between intra- and inter-molecular contributions. To do this we have investigated two effects:

1) the effect of temperature on the WAXD

2) the effect of molecular orientation on the WAXD

The combined knowledge of these two effects is a powerful tool which enables us to separate intra- and inter-molecular components. Pure intra-diffraction should yield direct information about any preferred chain conformation of the polymer molecules in the amorphous state. Pure inter-diffraction should yield information about any preferred arrangement of chain packing in the orientated state. The minute increases in density (~ 0.05%) which[71,72] have been reported for these polymers after orientation suggest that any packing arrangement that is present in the orientated material is in fact also present in unorientated material. The extruding and drawing processes may have the effect of only aligning any ordered regions so that the scattering is concentrated at the meridian or the equator.

5.2 Atactic Polystyrene

Table 5.1 summarises the relevant results of past work on the character of the diffraction halos of atactic polystyrene:

Author	First Halo	Remarks	Second Halo	Remarks
Katz[42] (X-ray)	10Å	Polymerisation ring. Suggested as interchain	4.8Å	-
Krimm[46] (X-ray)	8.84Å	-	4.67Å	Ratio of intensity of second to first decreased with increased temp.
Kilian & Boueke[51] (X-ray)	8.8Å	Temperature dependent	4.6Å	Temperature independent
Yeh[14] (Electron)	9Å	-	4.78Å	Increased to 6.38Å on cross-linking

Table 5.1 Summary of the past work on the diffraction halos of atactic polystyrene.

That the first halo of atactic polystyrene arises from intermolecular effects has been clearly demonstrated by its strong equatorial arcing and temperature dependence. The origin of the second halo has not been so clearly demonstrated. Clues as to the origin of the remaining halos may be obtained from a study of the orientated polymer.

5.3 Orientated Atactic Polystyrene

Meridional Scattering

In an orientated polymer whose molecules have a perfectly periodic internal structure (i.e. isotactic or syndiotactic molecules) the X-ray diffraction

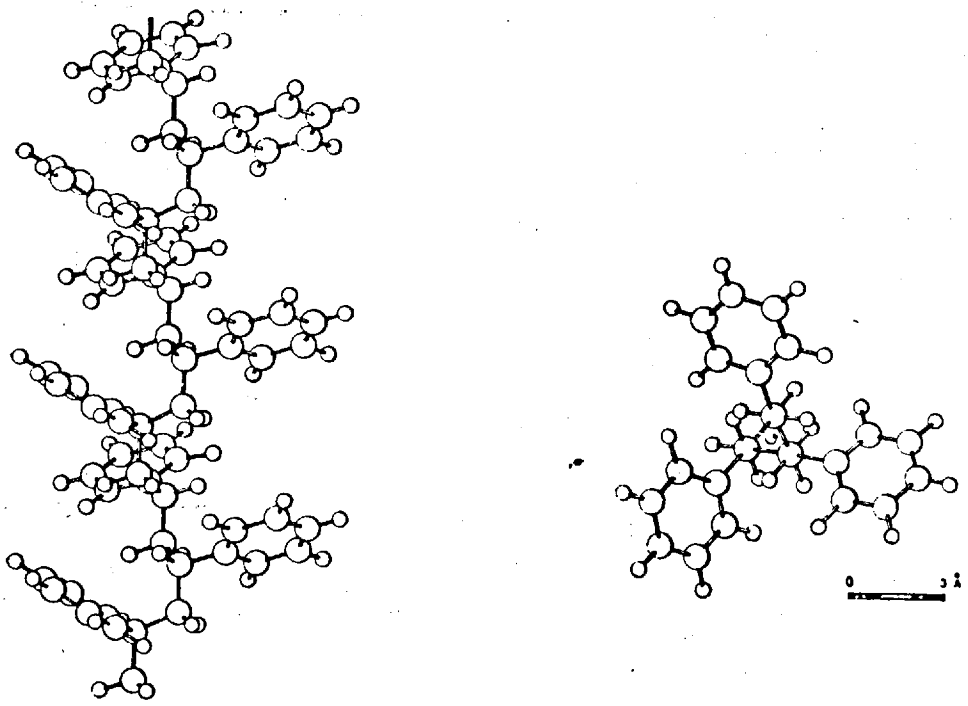

Fig.5.1 The conformation of the isotactic polystyrene macromolecule in the crystalline state (side and end views).[55]

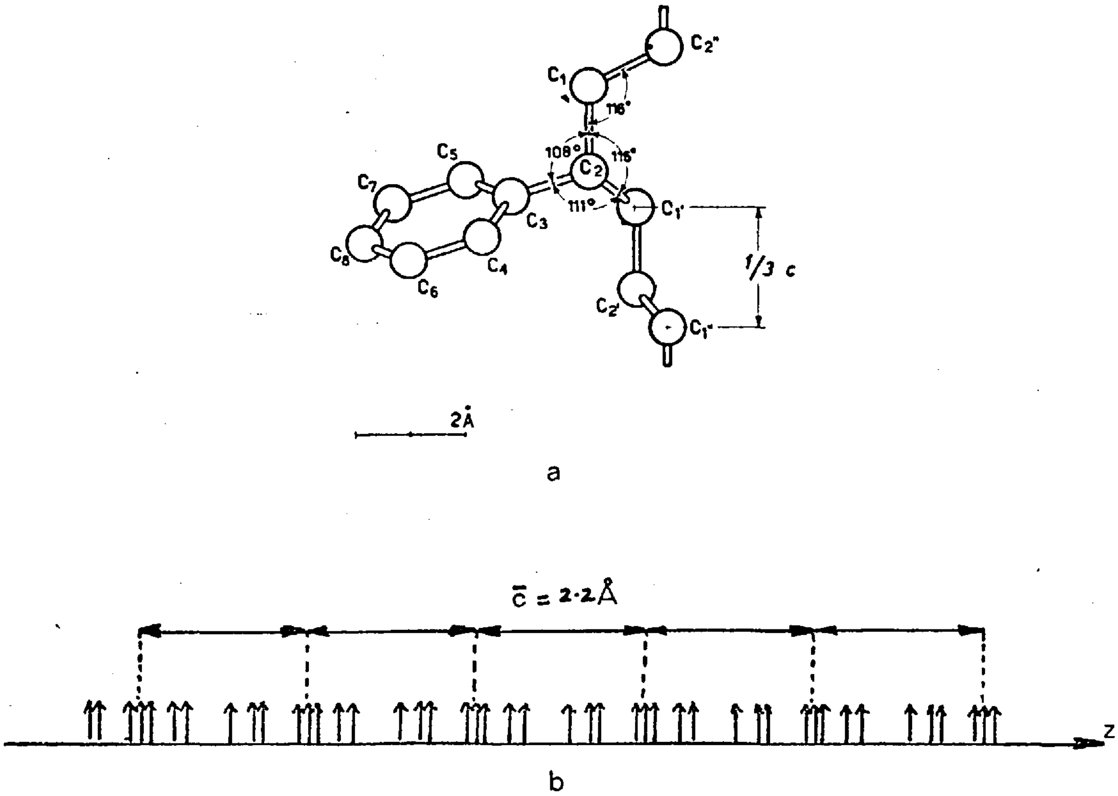

Fig.5.2 a) The conformation of the independent structural unit of isotactic polystyrene[55] b) arrow diagram of the projection of atom density on the principal axis calculated using a).

pattern contains a system of layer lines arising from interferences between the scattering elements regularly spaced along the chain. If the orientated chains possess paracrystalline distortions the whole molecule still scatters X-rays but mutual interference effects occur only between a few nearest-neighbour groups at each point in the chain. Disorder inherent in the chain (e.g. atactic chains) or flexures in the molecules about the principal axis are the kinds of distortion which result in the loss of meridional reflections.

The meridional interference function for orientated atactic polystyrene (Fig.4.26) resembled quite closely the type of interference function expected for a one dimensional lattice with distortions of the second kind. The distribution function $H_3(z)$ (Fig.4.29) was also characteristic of such an array and had a period $\bar{c}$ = 4.4Å and a radius of interaction r_M = 25Å. This would mean that the number of nearest neighbours in the lattice contributing to give mutual interference effects would be of the order of

$$M = \frac{25}{4.4} \qquad \text{i.e. } 5 \text{ or } 6 \text{ lattice points}$$

It is likely that the atactic polystyrene molecules have some form of distorted helical conformation which may be similar to that of isotactic polystyrene in its crystalline state (Fig.5.1). The phenyl ring predominates in the structure of the isotactic polystyrene repeat unit. The size of the phenyl rings prevents the isotactic chain from adopting a planar zig-zag conformation since this would produce too little separation between them. The spacings between the rings are increased by rotations about chain bonds resulting in a helix with three monomer units in each turn and 6.65Å between equivalent phenyls (this is called a 3/1 helix).

Fig.5.2 shows an arrow diagram of the projection of the atom density of such a chain on the principal axis z. This projection has a strong period of approximately 2.2Å and arises from the regular spacings of the C_1, C_3 and C_7 atoms along the chain. The syndiotactic molecule (Fig.5.3) which has a planar zig-zag conformation has a very similar z-axis projection with a phenyl repeat of 5.2Å. Atactic molecules could be considered as isotactic molecules which have a number of syndiotactic linkages occurring throughout their length which would disrupt the periodicity of the helix.

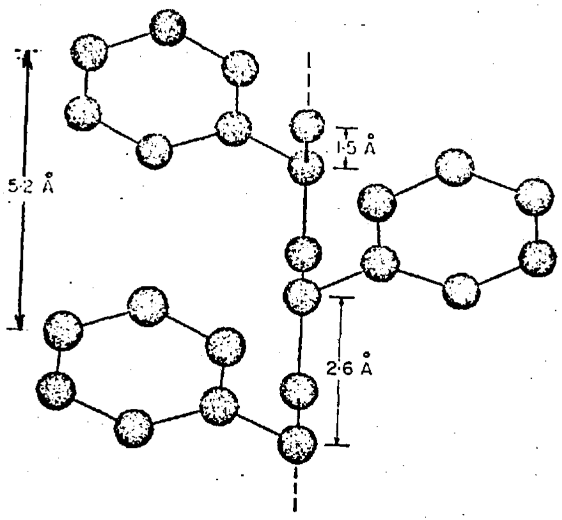

Fig.5.3 A syndiotactic polystyrene sequence[52].

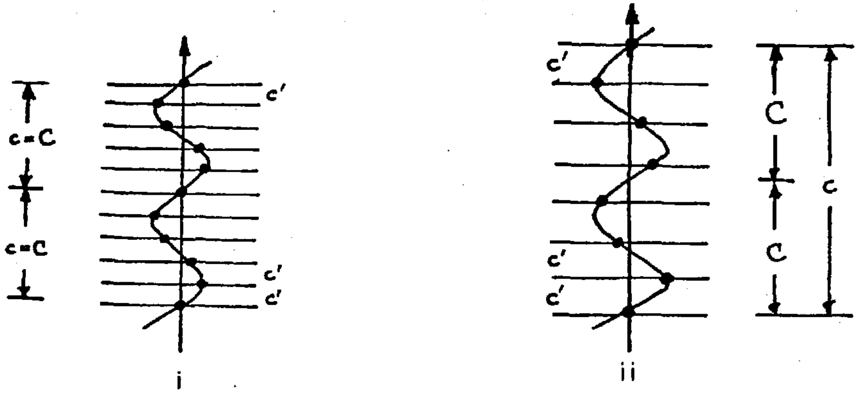

Fig.5.4a Chain molecules with their scattering units arranged on continuous helices: i) 5/1; ii) 7/2.

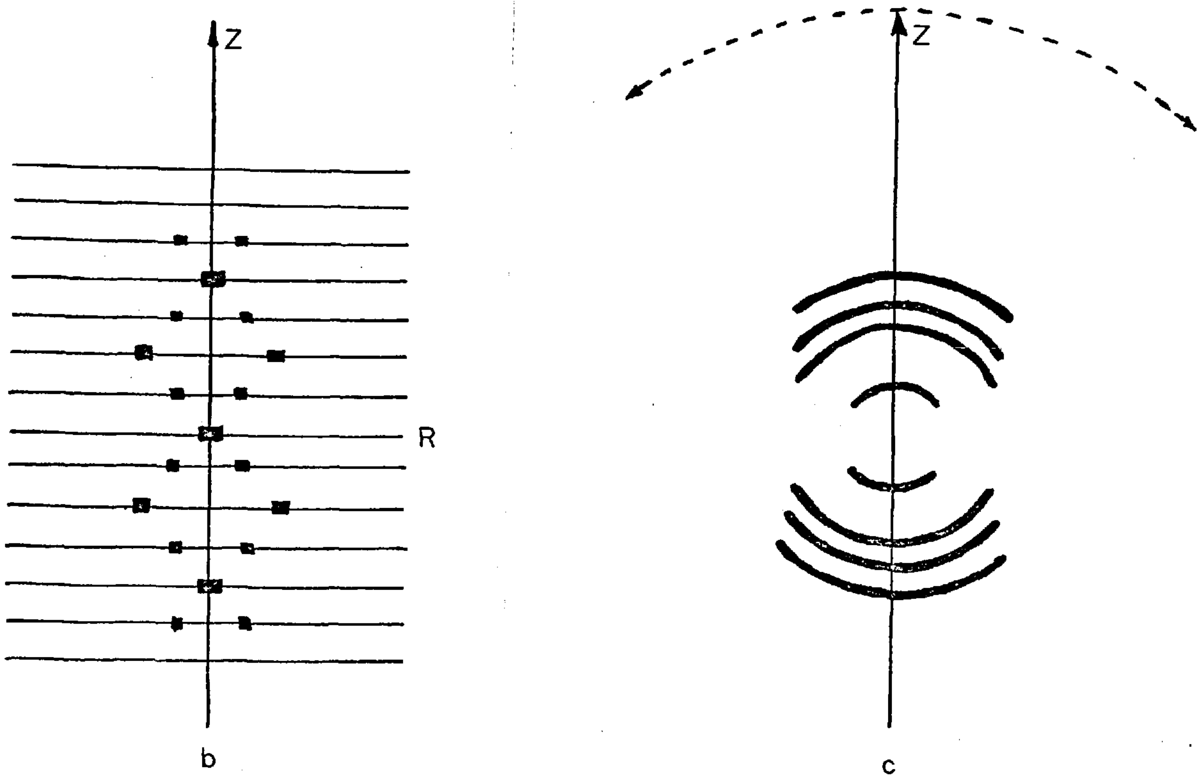

Fig.5.4b Diffraction pattern from perfectly orientated helical polymer molecules. Reflections on the meridian z, arise from the c' projections; c) if the molecules are imperfectly orientated other reflections which arise from c and C may be brought onto the meridian and thus detected in $H_3(z)$.

Therefore we might clearly expect $H_3(z)$ which is a distribution function of the atoms in a molecule projected onto the z-axis, to have a distinct period of ~2.2Å even in an atactic polystyrene molecule. However, if the molecules are not perfectly orientated, $H_3(z)$ will probably contain the true repeat distances as well as the projected ones. This is shown schematically in Fig.5.4. Fig.5.4a shows a chain molecule as a set of discrete points arranged on a continuous helix. Such a system can be specified by the following periodic components along the principal axis z: the projection c' on the axis of the distance between adjacent points (2.2Å here), the pitch C of the continuous helix and the true repeat distance c of the discontinuous one. A discontinuous helix gives layer lines having indices n whose repeat distance is $C^* = 1/C$ and also additional ones of repeat distance $c^* = 1/C$. The intensity along each layer line is governed by one or more Bessel functions which gives the diffraction pattern its characteristic cross shape (Fig.5.4b). Only J_o is finite at the origin and this occurs on layer lines which correspond to the repeat distance c' (i.e. ~ 2.2Å in our case). If the molecules are not perfectly orientated, Fig.5.4c shows that other "reflections" may be detected along the meridian. Thus the measured period of 4.4Å found in $H_3(z)$ may arise from a helix repeat such as c or C. Calculation has shown that the first peak in J_1 for the first layer line is very close to the meridian so that only slight misorientation would be required to produce the effect described in Fig.5.4c.

The 4.4Å period of $H_3(z)$ appears to exclude the 3/1 helical conformation of crystalline isotactic polystyrene and the planar zig-zag conformation of syndiotactic polystyrene. Bunn[73] has shown that on the basis of idealised bond distances and angles we may expect characteristic identity periods to be observed for a number of single-bonded carbon-chain conformations. Five of these conformations are shown in Fig.5.5. The $TGT\bar{G}$ conformation (2/1 helix) has the required identity repeat of 4.4Å and would therefore appear to be the most likely candidate for the overall chain conformation of atactic polystyrene.

Thus it was concluded that the observed meridional scattering from orientated atactic polystyrene contained a large paracrystalline component

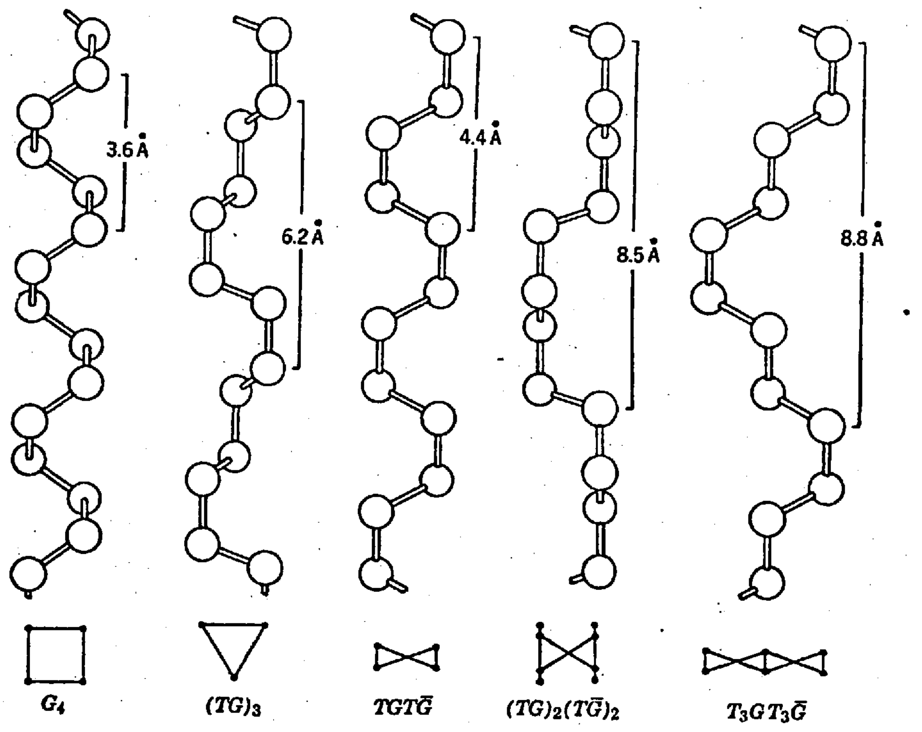

Fig.5.5 Five chain conformations based on the T (trans), G (left gauche), and Ḡ (right gauche) staggered bond orientations. The three basic bond sequences T, G and Ḡ, are the only ones permitted by the principle of staggered bonds for single-bonded carbon chains[73].

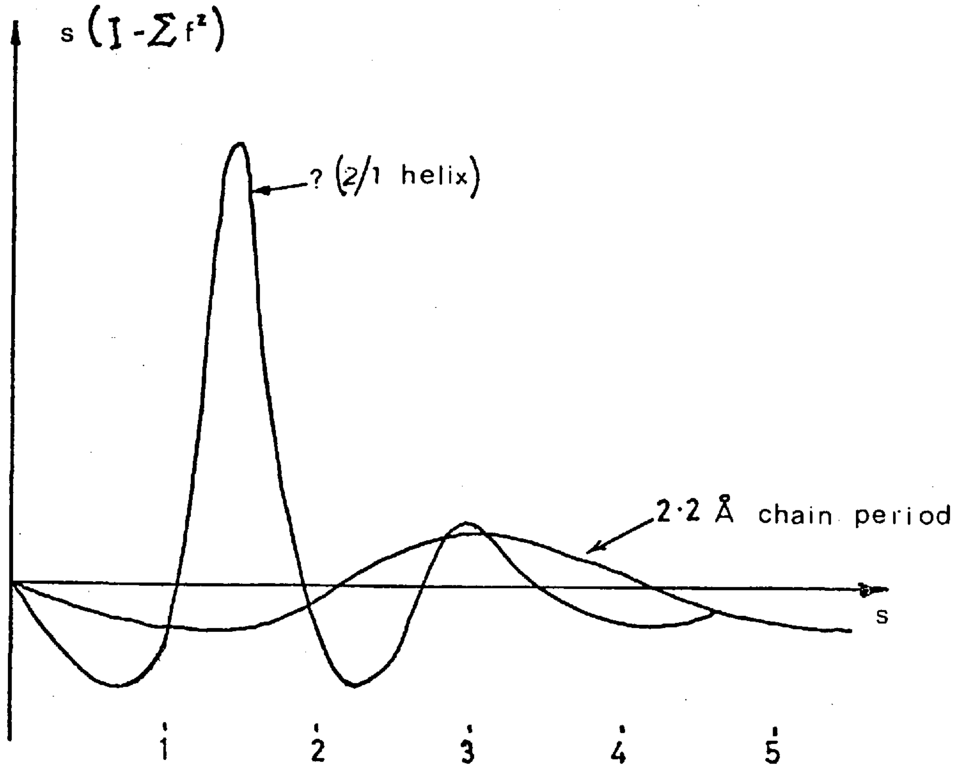

Fig.5.6 The possible composition of the meridional interference function for orientated atactic polystyrene. The long wave component arises from the 2.2Å period inherent in each chain. The other component arises due to imperfect orientation of the molecules and contains information about true repeat distances.

due to the true repeat distances along the chains which concealed the presence of the projected 2.2Å period. This is shown schematically in Fig.5.6. It is suggested that the molecules have predominantly a 2/1 helical conformation which gives rise to the observed 4.4Å repeat.

The Equatorial Scattering

The interference function for the equatorial scattering from orientated polystyrene (Fig.4.28) unlike the meridional scattering did not resemble the type expected for an array with paracrystalline distortions. Fig.5.7 shows however that this function can be separated into two components. The high frequency component peaks at $s = 0.6, 1.2, 1.8, 2.4, 3.0$, etc. and corresponds to the 8.85Å ring which has been shown to be intermolecular in nature. The low frequency component is of greater intensity and peaks at $s = 1.5, 3.0$, etc. and corresponds to part of the second halo. Kilian and Boueke[51] have shown that the second halo of the <u>unorientated</u> material (4.6Å) is roughly independent of temperature (Fig.1.7). These studies have shown that this halo is composed of two elements which upon orientation concentrate at the meridian (4.4Å) or at the equator (4.65Å). Thus it is concluded that the low frequency component of the equatorial scattering is intramolecular and must arise from electron-electron vectors across one molecule since the equatorial scattering describes the electron density projected onto the basal plane. Fig.5.8 shows the projection on the basal (001) plane of the electron density of a single repeat of the 3/1 isotactic molecule. Possible vectors which could give rise to the intramolecular scattering observed are also shown. It is highly likely that very similar vectors would be found in the projections of other molecular conformations of polystyrene.

Thus the interference function of the equatorial scattering from orientated atactic polystyrene appears to contain two components: one intra-component which arises not because the material is imperfectly orientated but because the molecules are sufficiently large in cross-section to allow intra-spacing to occur in the basal projection; and an inter-component which alone contains the information regarding the molecular packing in the material. This inter-component may well exhibit paracrystalline characteristics and Fig.5.7 shows that it may have a period of $\bar{a}^{*} \sim 0.6\,\text{Å}^{-1}$ which requires

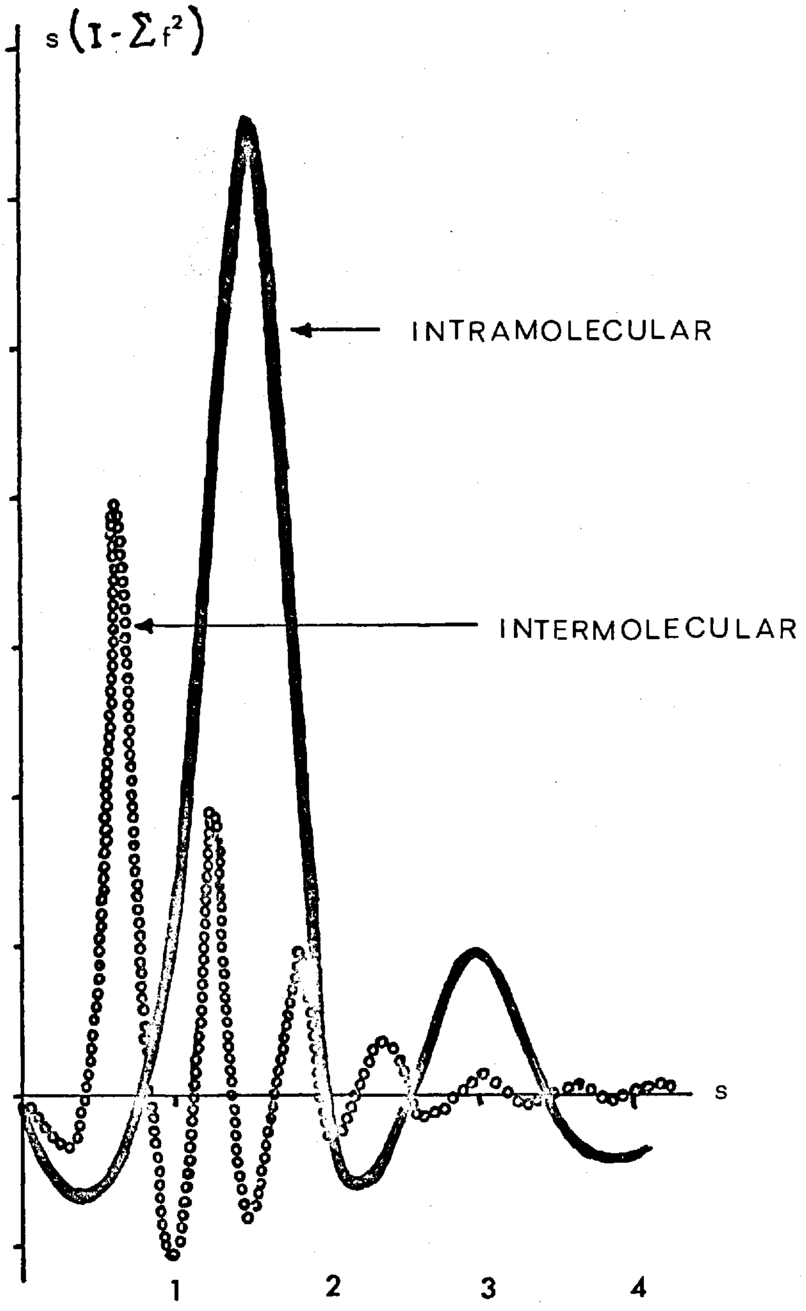

Fig.5.7 Possible composition of the equatorial interference function for orientated atactic polystyrene. The long wave component is intramolecular and arises not because the material is imperfectly orientated but because the molecules are sufficiently large in cross-section to allow intra-spacings to occur in the basal projection. The other component is intermolecular and contains information regarding the molecular packing.

that the distribution function for such distortions has a period of $\bar{a} \sim 10.5$Å. Table 5.3 shows the Bragg spacings which correspond to the peaks in this function.

s (Å^{-1})	0.6	1.2	1.8	2.4	3.0
d-spacing (Å)	10.5	5.2	3.5	2.6	2.1

Table 5.2 The Bragg spacings of the peaks in the proposed pure intermolecular interference function of orientated polystyrene (Fig.5.7).

The molecular conformation is also important in considering the equatorial scattering since each conformation has a different cross-section (Fig.5.5). The crystal structure of isotactic polystyrene is well known so let us start by assuming that the atactic or amorphous isotactic molecules have the 3/1 helix conformation of this structure (Fig.5.9). From Fig.5.8 it can be seen that the electron projection on the basal plane of the isotactic molecule has greatest density at its centre due to the carbon backbone. It is to be expected therefore that the most prominent interatomic vectors in the material would arise from the regular packing of the backbones.

An important feature of the molecular packing in the isotactic crystal is the presence of enantiamorphic pairs. Such pairing requires that the molecules have longitudinal register (hydrogen bonding) and separates the backbones by distances of ~7.4Å. This ensures that in the crystal the 110 planes are ~10.9Å apart. We have to ask whether the molecules in orientated atactic polystyrene have highly developed enantiamorphic pairs so that the packing approximates to a distorted isotactic polystyrene crystal lattice which then produces psuedo 110 "reflections". Or are the molecules not in pairs but packed so that the carbon backbones are spaced at ~10.5Å?

In a polymer in which the molecules are totally aperiodic, the chains are highly unlikely to have longitudinal register and may exhibit continuous shift with respect to each other. Here the mutual disposition of

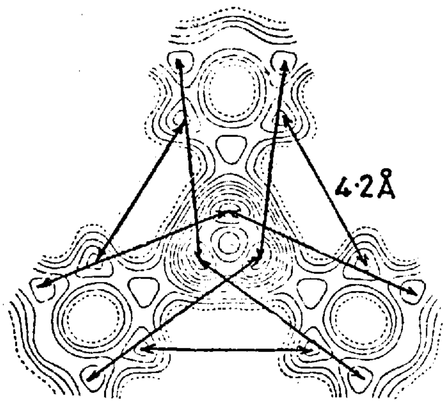

Fig.5.8 Projection on (001) of the electron density of a single repeat of the isotactic molecule. Contours are drawn at 0.5e/Å^2, the broken line is the 2e/Å^2 level (from Natta, Corradini and Bassi[55]). Possible vectors giving rise to the intramolecular scattering are shown.

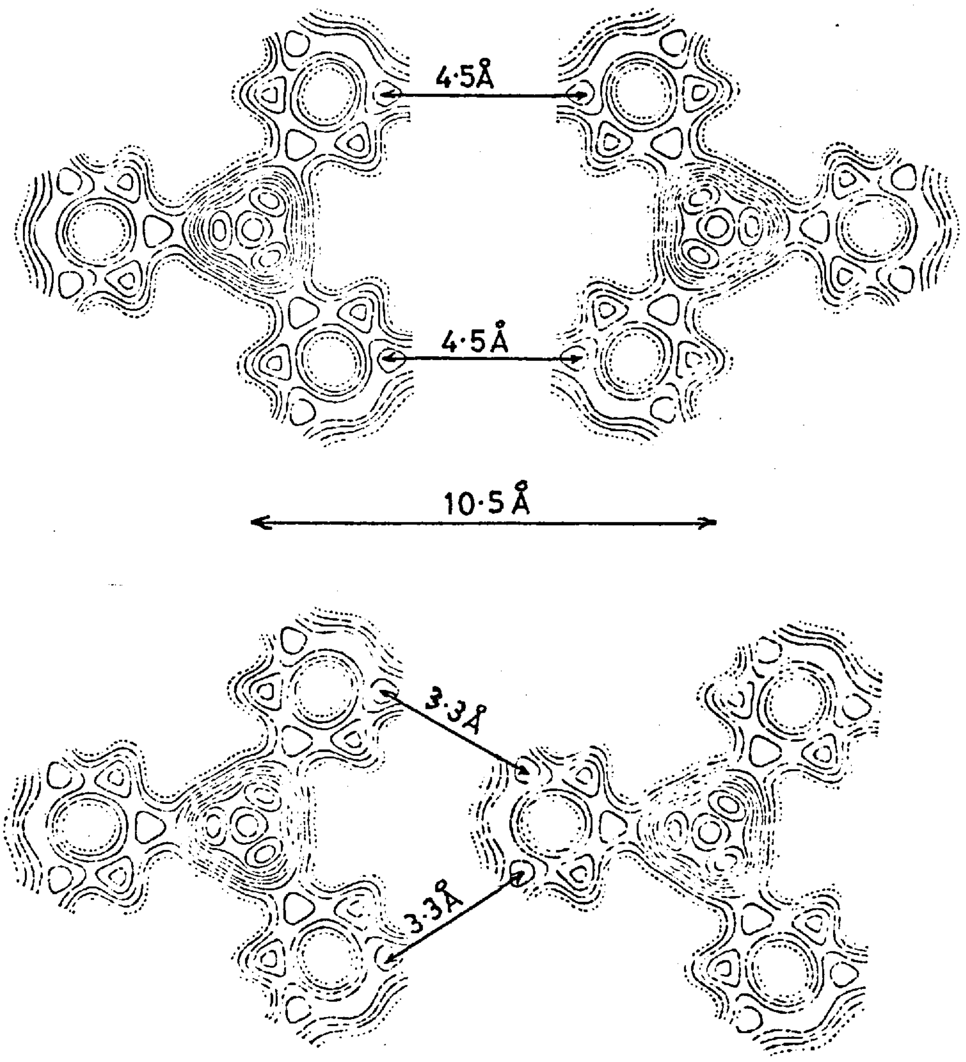

Fig.5.10 shows the molecules in the (001) projection spaced so that their carbon backbones are 10.5Å apart. Rotation of one molecule with respect to the other is required to bring the molecules to their approximate van der Waals spacings.

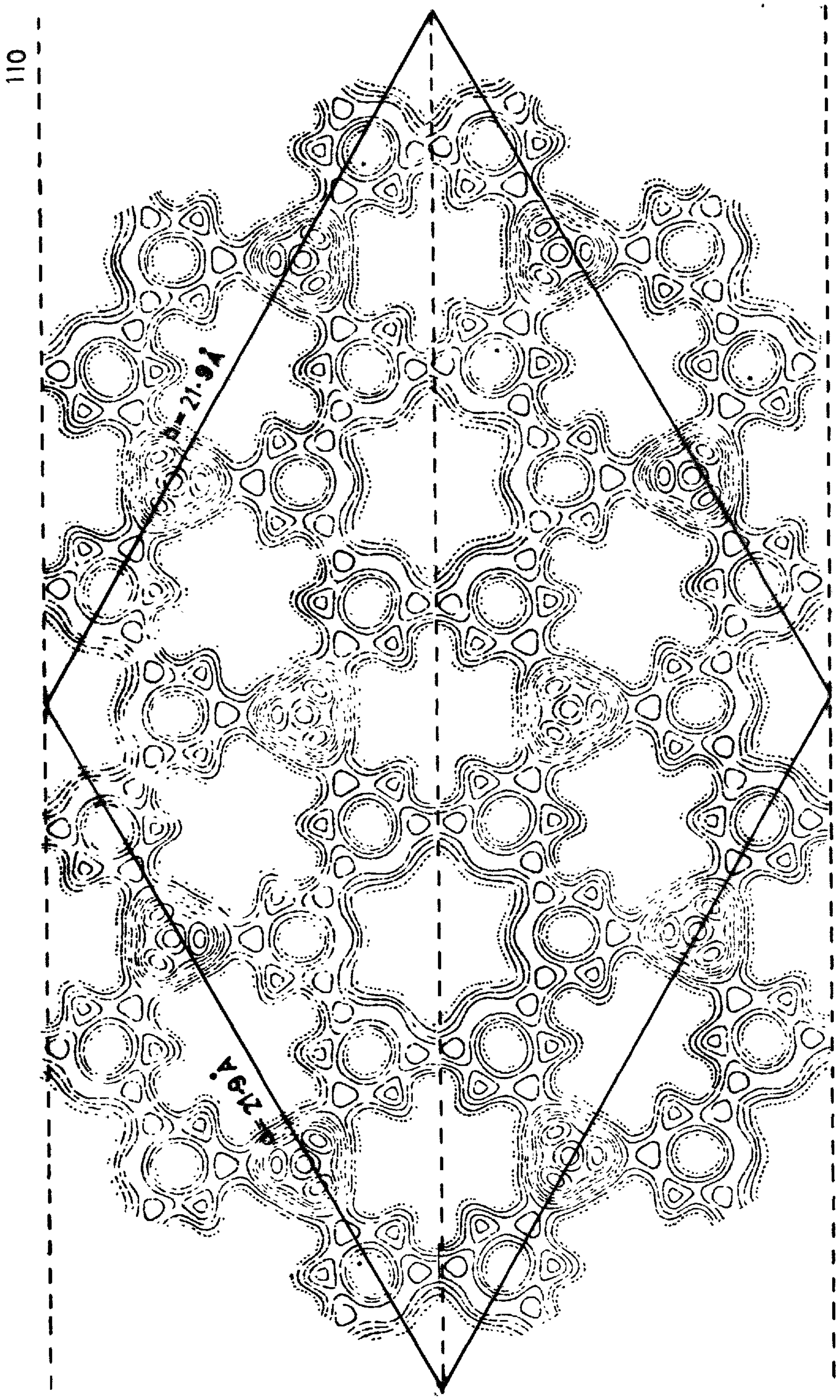

Fig.5.9 Projection on (001) of the structure of isotactic polystyrene for the R3c space group (from Natta, Corradini and Bassi[55]).

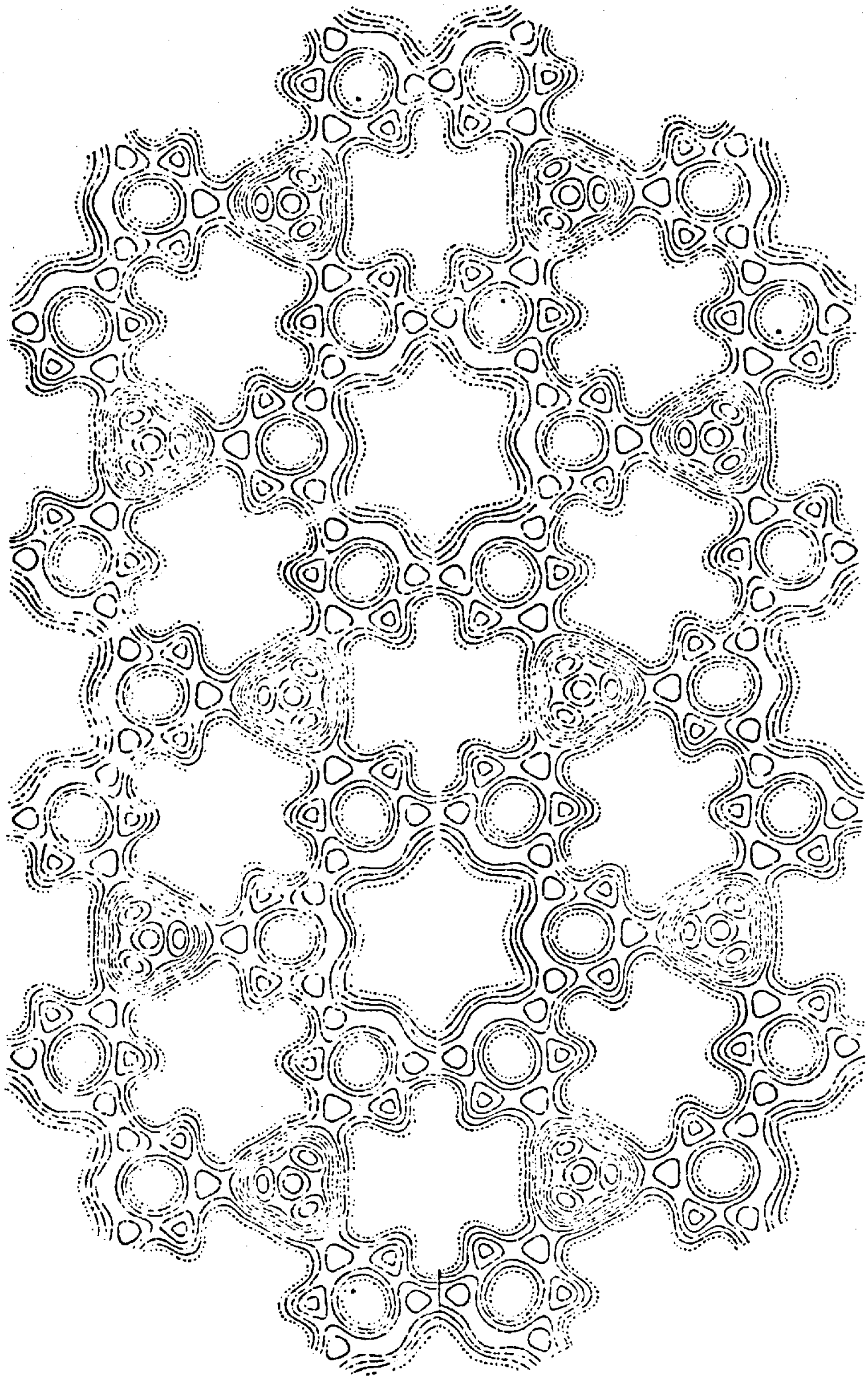

Fig.5.9 Projection on (001) of the structure of isotactic polystyrene for the R3c space group (from Natta, Corradini and Bassi[55]).

these molecules is most probably governed by the weak van der Waals forces. Fig.5.10 shows that if the molecules in the 001 projection of the isotactic crystal are spaced so that their backbones are ~10.5Å apart, then they are further apart than their van der Waals radii would allow. If, however, the molecules were rotated so that a phenyl group directly separates the backbones then the carbon atoms in adjacent phenyl groups would be correctly spaced. Fig.5.11 shows a packing model which has this interlocking arrangement. That the paracrystalline lattice (see overlay of Fig.5.11) has an average translation vector of ~10.5Å ensures that the distribution function or self-convolution of this lattice has a period of ~10.5Å also.

A very important requirement of any model of the amorphous state of a polymer is that it should predict its density correctly. It is shown in Table 1.1 that the density of amorphous isotactic polystyrene is ~ 95% that of the crystalline material. From the unit cell of isotactic polystyrene we have for the density of lattice points:

$$\rho = \frac{6}{21.9^2 \sin 60^\circ} = 0.0144 \text{ lattice points per square Angstrom}$$

From the primitive unit cell of the interlocking model of Fig.5.9

$$\rho = \frac{1}{10.5^2 \sin 60^\circ} = 0.0105 \text{ lattice points per square Angstrom}$$

i.e. only 73% of the crystalline density.

Therefore this "interlocking" model with the chains behaving like solid rods (continuous shift) held together by van der Waals attraction at an average spacing of 10.5Å, appears too inefficient a packing scheme to predict the macroscopic density observed.

If however the molecules were to have a 2/1 helical conformation in the glassy state, the chain cross-section may have the general form shown in Fig.5.12. Such a shape may allow the molecules to pack in the manner shown in Fig.5.13. Such packing could well produce two average transla-

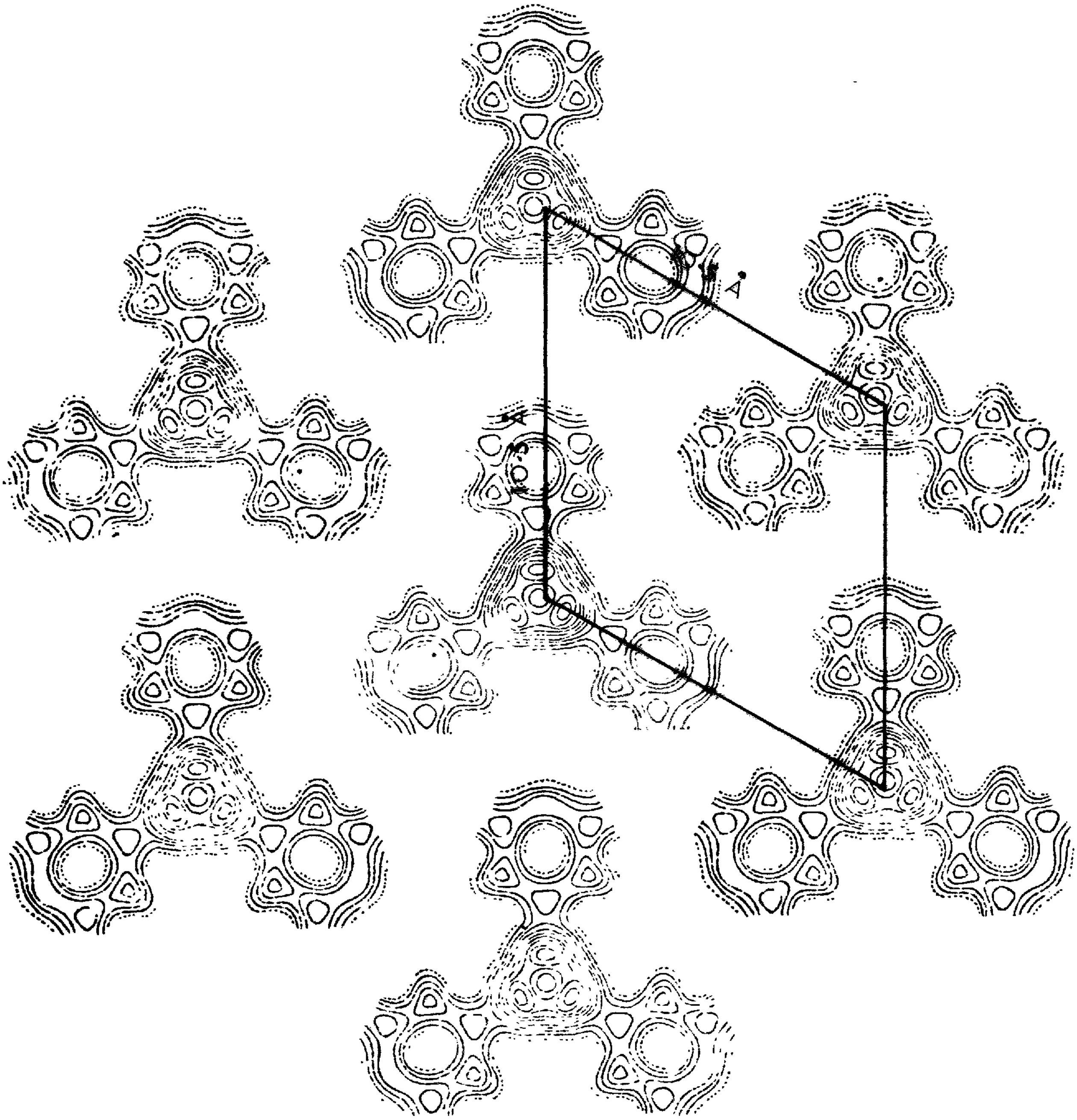

Fig.5.11 Hexagonal packing model for polystyrene molecules spaced at the approximate van der Waals distances.

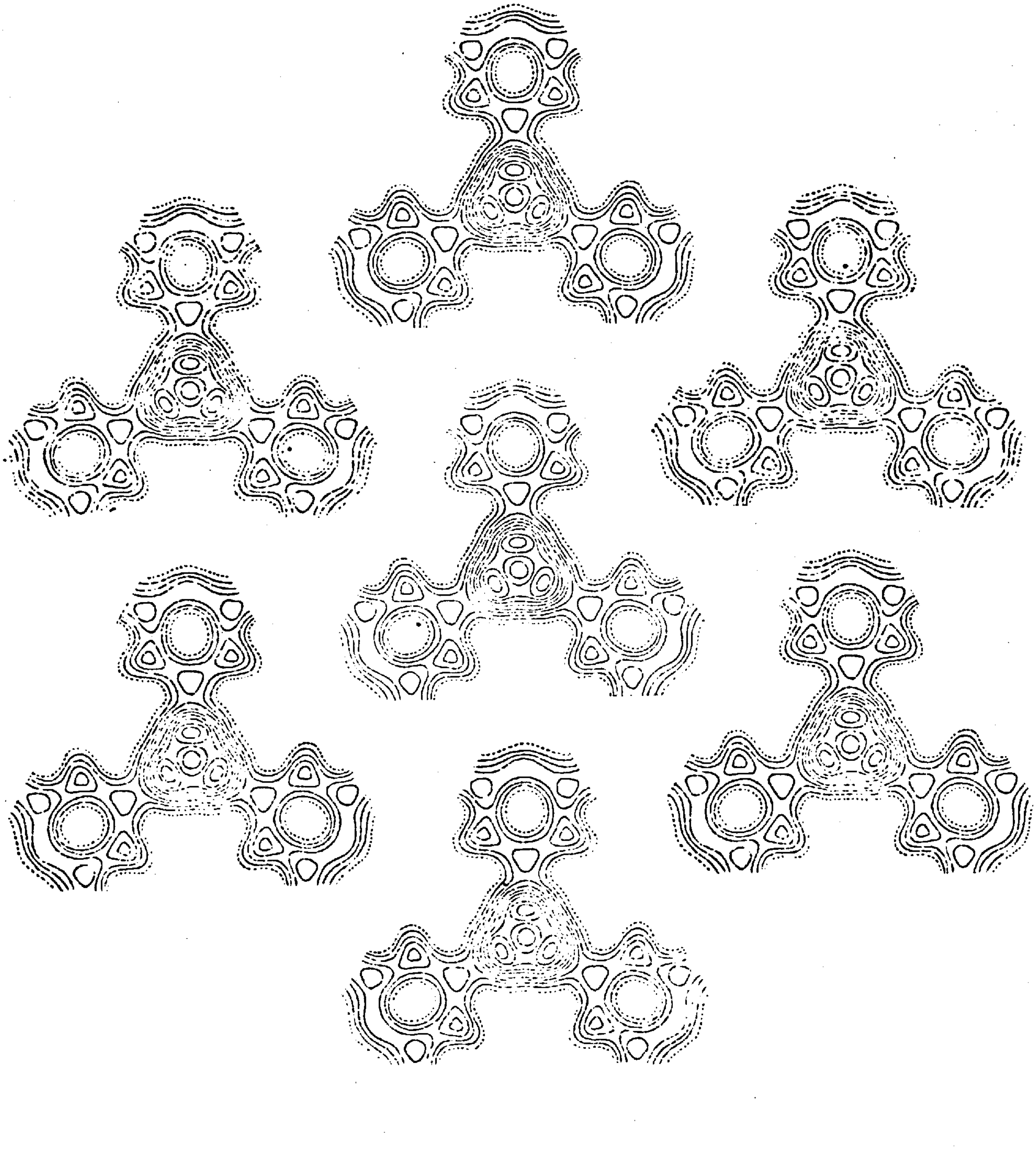

Fig.5.11 Hexagonal packing model for polystyrene molecules spaced at the approximate van der Waals distances.

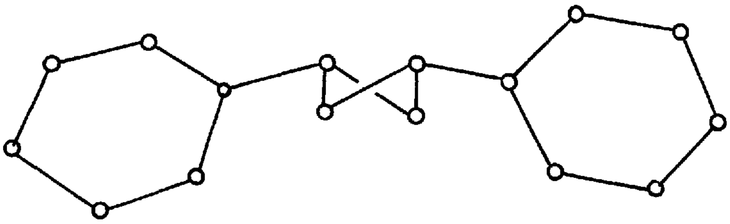

Fig.5.12 A sketch of the probable average cross-section of an atactic polystyrene molecule in a distorted 2/1 helix conformation.

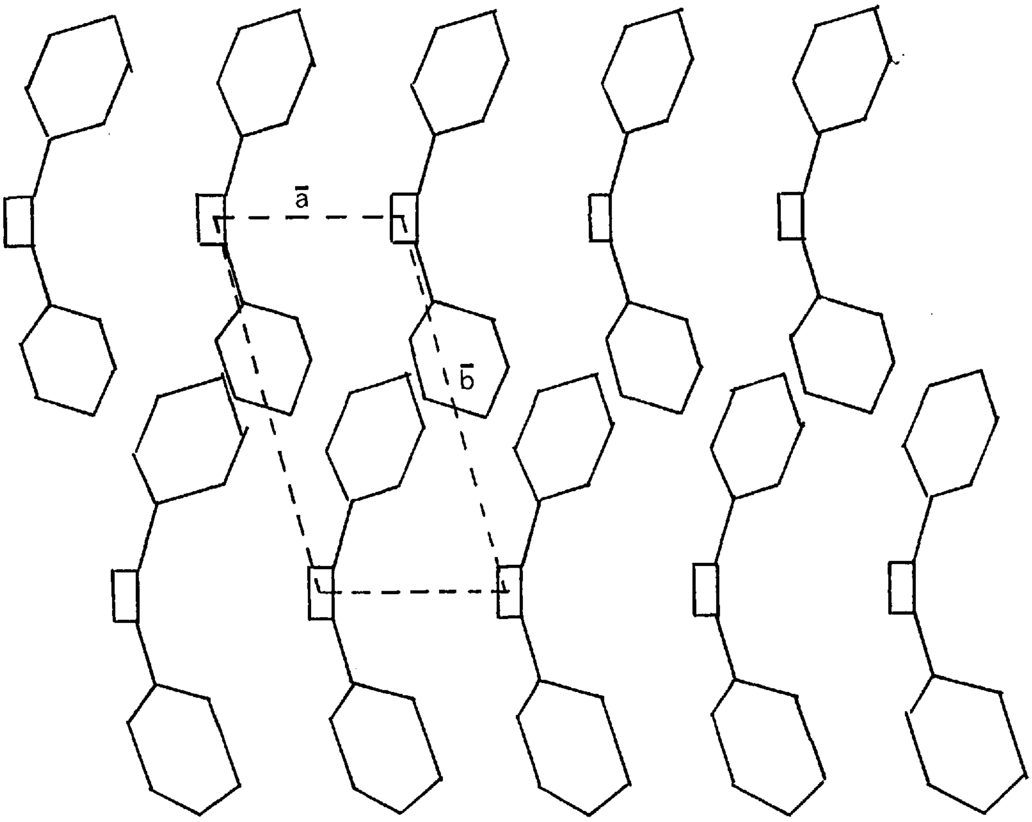

Fig.5.13 A sketch of a possible packing model for polystyrene molecules in 2/1 helices. This packing arrangement has two average translations $\bar{a}$ and $\bar{b}$ which could easily be ~5Å and ~10Å. In the X-ray diffraction pattern a 5Å peak would be masked by considerable intramolecular scattering (see. Fig.5.7).

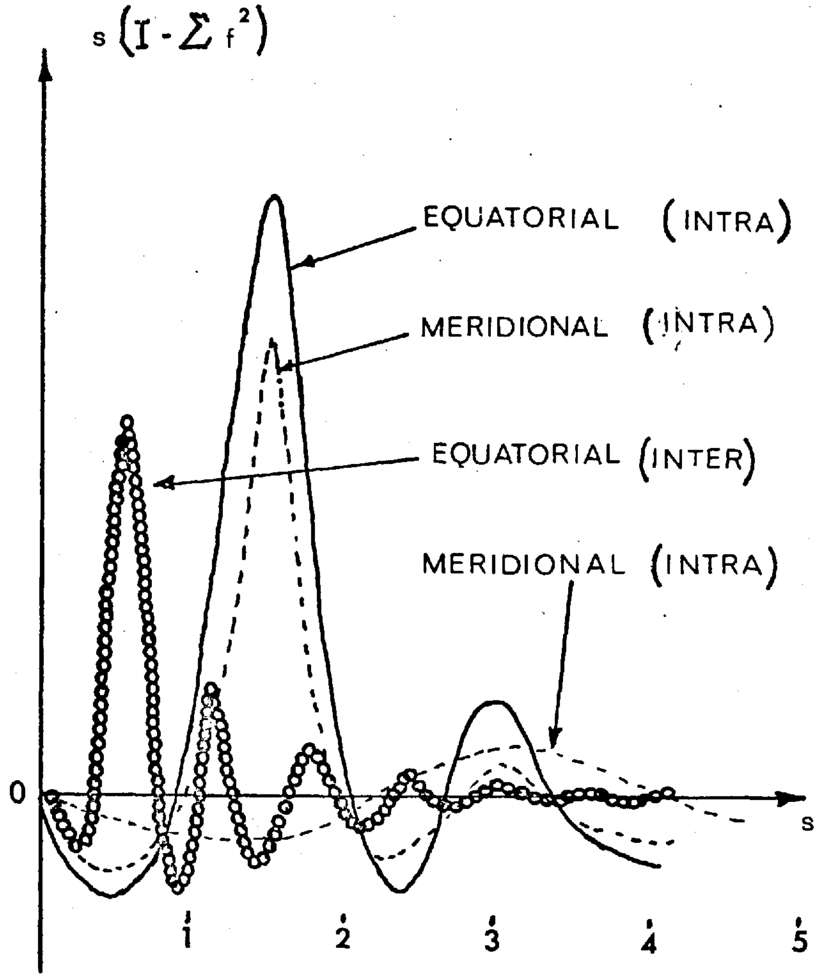

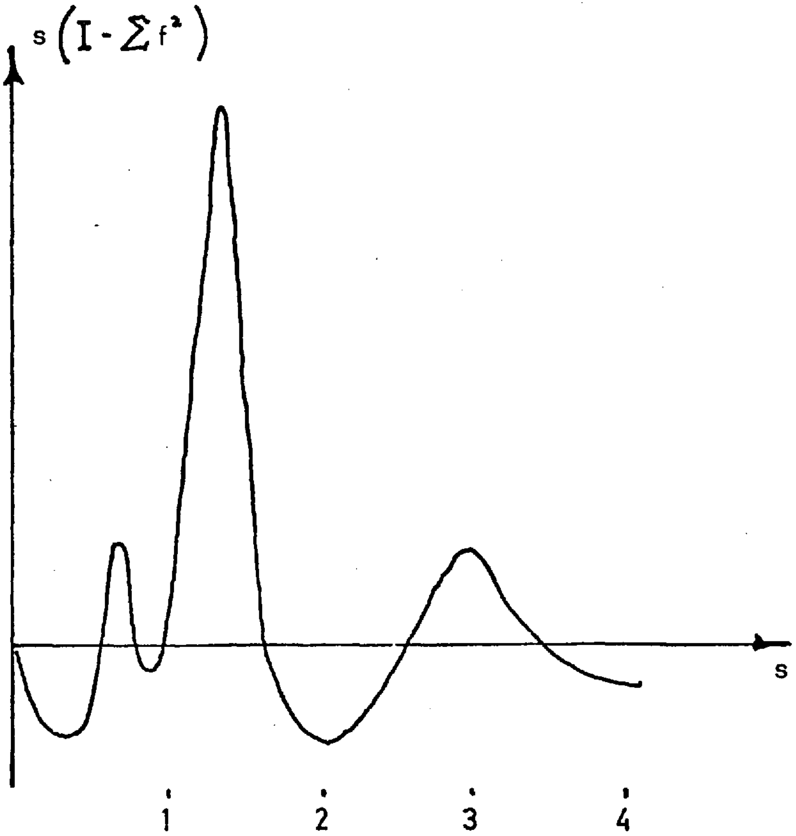

Fig.5.14 Possible composition of the diffraction halos of unorientated atactic polystyrene.

tion vectors of ~5Å and ~10Å. Such a lattice could also yield a density as high as that of the isotactic crystal.

Further work is obviously required on this point but the results discussed here appear to be consistent with the proposal that atactic polystyrene molecules in the orientated state at least, are packed together in such a manner as to produce an array which possesses a fair degree of paracrystalline order.

5.4 Unorientated Polystyrene

On the assumption outlined in section 5.1 that the extrusion process did not drastically alter the microstructure of the unorientated atactic polystyrene, the following scheme for the construction of the diffraction halos is proposed:

1) First halo (9Å) : pure equatorial (interchain)

2) Second halo (4.65Å) : two separate equatorial components (one inter- and the other intra-molecular) plus a meridional contribution (intra-molecular)

3) Third halo (2.1Å) : similar to second halo

This is shown schematically in Fig.5.14.

5.5 Atactic Polymethyl Methacrylate

The temperature experiments described in section 4.4 have shown that the first peak in the WAXD from unorientated PMMA (6.56Å) is at least in part intermolecular in nature whilst the second peak (2.98Å) must be predominantly intramolecular.

Meridional Scattering

Stereo-regular PMMA has been prepared in both isotactic and syndiotactic forms but to date the molecular conformation or crystal structure of either has yet to be settled. Fig.5.15 shows the 5/1 helical conformation which has recently been proposed for crystalline isotactic PMMA. An approximate period of ~2.2Å would be seen in the projection of this molecule on the

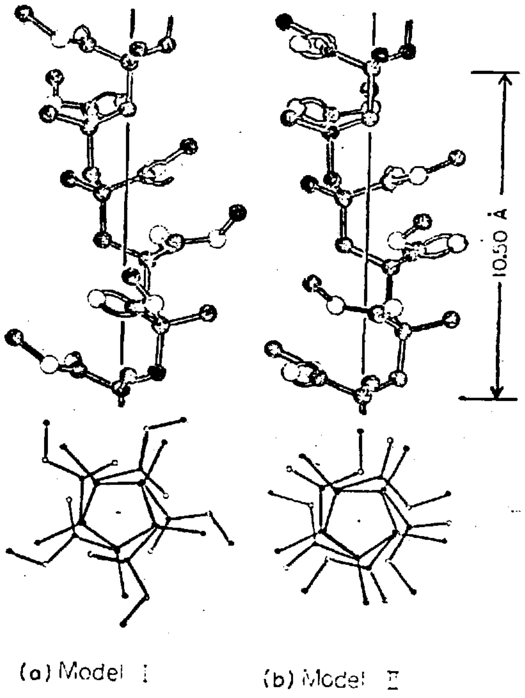

Fig.5.15 Two possible models for the molecular conformation of isotactic PMMA. Model 1 has been found to be more reasonable from far infra-red spectroscopy measurements (Tadokoro et al.)[74].

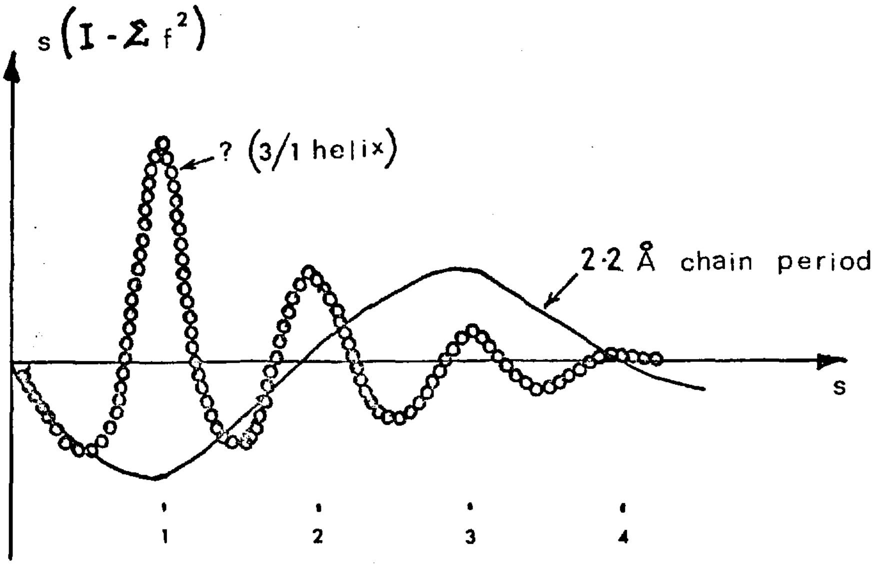

Fig.5.16 Possible composition of the meridional interference function for orientated atactic PMMA.

principal axis due to the repetition of the ester side groups. A similar period would probably be expected in the syndiotactic molecule. Fig.5.16 shows how using this repeat the observed interference function could be constructed. The second component has a period of $\bar{a}^* \sim 1.0$ ($\bar{a} \sim 6.3$Å) and may have paracrystalline characteristics, although $H_3(z)$ for this polymer (Fig.4.35) did not resemble a paracrystalline lattice so clearly as did polystyrene. The orientation obtained here was inferior to that obtained for polystyrene and would therefore probably contain information about true identity repeats in the molecule. The 5/1 conformation of crystalline isotactic PMMA would appear to be excluded on this basis. Fig.5.5 shows that the simpler 3/1 helix could give an identity period very close to 6.3Å.

Equatorial Scattering

From our experience with polystyrene, it is to be expected that the equatorial scattering from PMMA contains a component due to intramolecular effects within the projected cross-section of each molecule on the basal plane. Fig.5.17 shows how the equatorial interference function may be constructed of two components: one intramolecular which peaks at s = 1, 2, 3, etc. and the other intermolecular which has a period of $\bar{a}^* \sim 0.8$ ($\bar{a} \sim 7.8$Å).

5.6 Unorientated PMMA

If it is assumed that no change in the microstructure of the polymer occurs on orientation the following scheme for construction of the diffraction halos in unorientated PMMA may be obtained:

1) First halo (6.29Å)	: three components: one intermolecular (equator), one intramolecular (meridian) and the other probably intramolecular (equator).
2) Second halo (2.85Å)	: two main contributions: one meridional (intramolecular), the other equatorial (probably intramolecular).
3) Third halo (2.14Å)	: all four components.

This is shown schematically in Fig.5.18. It has been assumed in this construction that the larger component of the equatorial scattering is intramolecular since experiment has shown that the second halo is roughly independent of temperature. This construction is consistent with the temperature observations of section 4.4. The effects of annealing PMMA below T_g and of swelling PMMA in methanol are now discussed in terms of Fig.5.18.

5.7 The Effect of Annealing Atactic PMMA Below T_g

Increases of ~ 0.5% in the macroscopic density of PMMA have been reported for this polymer when samples have been annealed below T_g for long periods[69]. When our atactic samples were annealed at ~ 90°C for sixteen weeks the intensities of the first and second halos were seen to increase and both shifted to longer d-spacings. The increase in macroscopic density must reflect an increase and/or improvement in the existing order within the sample. This leads to an increase and possible shift in the intermolecular scattering which has the effect of shifting the observed halos to longer d-spacings. To investigate whether the intermolecular scattering in fact shifts to shorter d-spacings upon annealing (possible improvement of existing ordering), experiments must be performed on previously orientated specimens which are constrained from recovering or by annealing specimens which are then drawn.

5.8 The Effect of Swelling Atactic PMMA in Methanol

The swelling of atactic PMMA in methanol at an elevated temperature has been shown to result in a substantial decrease in the sample density. The scattered intensity from such a sample closely resembled that of the meridional scattering from the orientated material which appears to be pure intramolecular in nature. Thus it is suggested that in swelling PMMA in methanol at 60°C, the intermolecular ordering is largely destroyed. It is envisaged that methanol molecules force their way between parallel packed polymer segments and "lubricate" the chains. This has the effect of lowering the macroscopic density and depressing T_g below the swelling

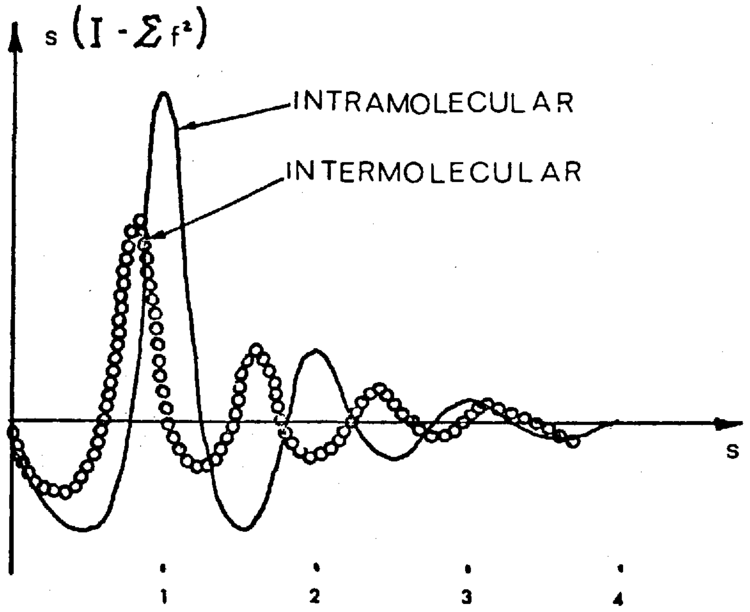

Fig.5.17 Possible composition for the equatorial interference function for orientated atactic PMMA.

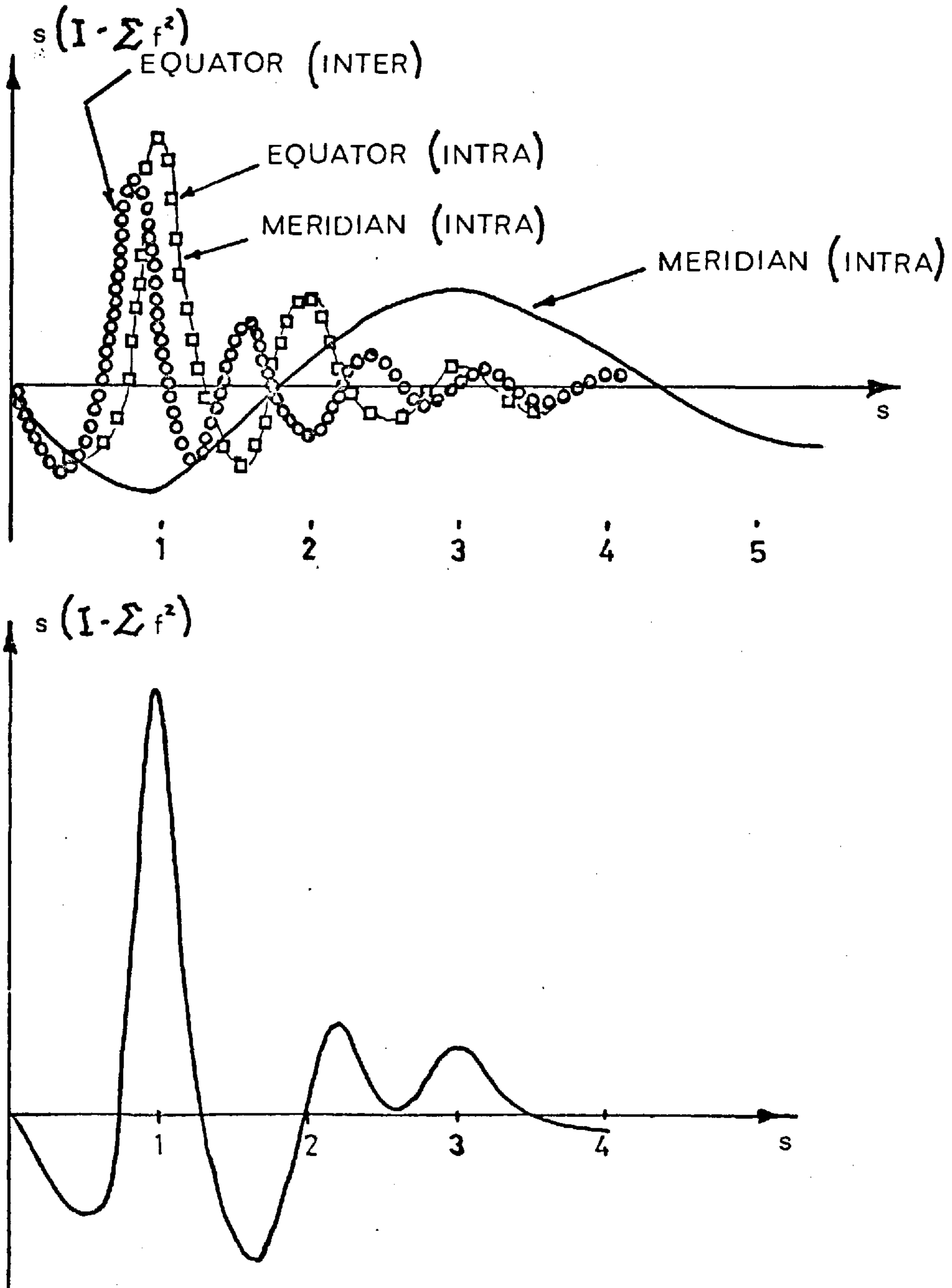

Fig.5.18 Possible composition of the diffraction halos of unorientated PMMA.

temperature. In swelling PMMA at room temperature the samples were not rubbery and although the halos were decreased in intensity no significant peak shift was observed. This suggests that swelling at this temperature does not result in the total destruction of interchain ordering.

The observation that the density decreases on swelling contradicts the suggestion that the solvent molecules swell only disordered regions and leave ordered ones intact since this should lead to an increase in the macroscopic density.

Thus we conclude that swelling PMMA in methanol at 60°C results in the destruction of some or all of the interchain ordering present in the unswollen state and since the swollen polymer has the physical characteristics of a rubber its chain molecules may well closely resemble the statistical random coil of the high elasticity theory.

5.9 Concluding Remarks

This work has revealed the complexity of the diffraction effects which are obtained from two common non-crystallisable synthetic polymers. Both have been shown to possess considerable intramolecular ordering in their orientated states as well as at least one component which undoubtedly arises from interchain ordering.

The equatorial and meridional interference functions have been shown to be consistent with a scheme in which the functions can be constructed from a number of paracrystalline components of both intra and intermolecular effects. That the interference functions are so composed has in the main prevented detailed use of the radial and cylindrical distribution functions which have been generated. It was hoped that orientation of the samples would separate the scattering into purely intramolecular scattering on the meridian and purely intermolecular scattering on the equator so that the peaks in the distribution functions could be unambiguously identified. However, it has been shown that even perfect orientation of the polymers in question would not eliminate intra-effects from the equator.

The distribution functions $H_3(z)$ for orientated polystyrene and polymethyl methacrylate are probably the first of their kind to be generated for polymer molecules in their amorphous state. In the case of polystyrene, this function has shown that the chains have a highly developed paracrystalline nature which appears to require that they are arranged in simple 2/1 helices. This would have interesting implications for amorphous isotactic polystyrene which crystallises by forming enantiamorphic pairs. Are the molecules in the amorphous state in 3/1 helices which have to diffuse through the material in search of an anti-parallel partner, or are they packed in 2/1 helices which upon crystallisation unwind to 3/1 conformations and find partners with relatively little diffusion?

5.10 Suggestions for Future Work

A few immediate areas of interest are:-

1) Improved molecular orientation would obviously be useful particularly in the case of the intramolecular scattering. The determination of the correct preferred molecular conformation is central to these structure studies. Also orientation experiments would be useful in studying annealing and possibly swelling since the meridional and equatorial scattering could be investigated separately.

2) Three dimensional molecular building kits should be used to construct probable structures so that these can be discussed more critically.

3) Annealing and swelling experiments should be performed on polystyrene since the first intermolecular halo is well separated from the rest of the scattering.

REFERENCES

1. P.J. Flory, "Principles of Polymer Chemistry", Cornell Univ. Press, Ithaca, N.Y., (1953)
2. P.J. Flory, "Statistical Mechanics of Chain Molecules", Interscience, N.Y., (1969)
3. A. Ciferri, C.A.J. Hoeve, P.J. Flory, J. Am. Chem. Soc., 83, 1015, (1961)
4. P.J. Flory, A. Ciferri, Chiang, ibid., 83, 1023, (1961)
5. T.G. Fox, S. Loshaek, J. Appl. Phys., 26, 1080, (1955)
6. T.G. Fox, S. Gratch, S. Loshaek, in "Rheology", edited by F.R. Eirich, Academic Press, New York, 1965, vol.I, p.431
7. H.N. Campbell, M.D. Allen, Ind. Eng. Chem., 43, 413, (1950)
8. S.M. Aharoni, J. Macromol. Sci., B7(1), 73, (1973)
9. F.J. Balta Calleja, J. Polymer Sci., Part C, 16, 4311, (1969)
10. M.I. Kashmiri, R.P. Sheldon, ibid., B7, 51, (1969)
11. K. Katayama, T. Amano, K. Nakamura, Kolloid-Z. Polymere, 226, 125, (1968)
12. P.V. McKinney, C.R. Foltz, J. Appl. Poly. Sci., 11, 1189, (1967)
13. M.S. Ali, R.P. Sheldon, ibid., 14, 2619, (1970)
14. G.S.Y. Yeh, J. Macromol. Sci., B6(3), 451, (1972)
15. V.A. Kargin, J. Polymer Sci., 30, 247, (1958)
16. V.A. Kargin, A.I. Kitaigorodsky, G.L. Slonimsky, Colloid J. (USSR), (English Transl.), 19, 141, (1957)
17. V.A. Kargin, Z.Ya. Berestnava, V.G. Kalashnikova, Usp. Khim., 36, 203, (1967)
18. V.A. Kargin, N.F. Bakeev, S.Kh. Fakirov, N.I. Nikonorova, Dokl. Akad. Nauk. SSSR, 165, 604, (1965)
19. T.G.F. Schoon, R. Kretschmer, Kolloid-Z, 197, 51, (1964)
20. T.G.F. Schoon, O. Teichmann, ibid., 197, 35, (1964)
21. T.G.F. Schoon, R. Kretschmer, ibid., 197, 45, (1964)
22. G.S.Y. Yeh, P.H. Geil, J. Macromol. Sci., B1(2), 235, (1967)
23. G.S.Y. Yeh, P.H. Geil, ibid., B1(2), 251, (1967)

24. S.H. Carr, P.H. Geil, E. Baer, ibid., B2(1), 13, (1968)

25. A. Siegmann, P.H. Geil, ibid., B4(2), 239, (1970)

26. A. Siegmann, P.H. Geil, ibid., B4(2), 273, (1970)

27. R. Hosemann, For example: J. Appl. Phys., 34, 25, (1963)

28. J.J. Klement, P.H. Geil, J. Macromol. Sci., B5(3), 505, (1971)

29. G.S.Y. Yeh, ibid., B6(3), 465, (1972)

30. R.E. Robertson, J. Phys. Chem., 69, 1575, (1965)

31. C.A.J. Hoeve, J. Chem. Phys., 35, 1266, (1961)

32. W.R. Pechhold, Blasenbury, 2nd Europhysics Conference of the section of Macromolecular Physics, European Physical Society, Sorrento (Naples), 1-3 May 1974

33. V.P. Privalko, V.S. Lipatov, Die Makromolekulare Chemie, 175, 641, (1974)

34. P.J. Harget, A. Siegmann, J. Appl. Phys., 43, 4357, (1972)

35. W. Lin, E.J. Kramer, ibid., 44, 4288, (1973)

36. R.G. Kirste, 2nd Europhysics Conference of the section of Macromolecular Physics, European Physical Society, Sorrento (Naples), 1-3 May 1974

37. K. Nagai, J. Chem. Phys., 49, 4212, (1968)

38. A.N. Gent, V.V. Vickroy, J. Polymer Sci., A2, 5, 47, (1967)

39. G.S.Y. Yeh, Conference on Supramolecular Structure in Glassy Polymers, Institute of Chemical Industry, London January 1974

40. R.L. Addleman, Ph.D. Thesis, Dept. Mech. Eng., Imperial College, London (1974)

41. C. Tanford, "Physical Chemistry of Macromolecules", Wiley, N.Y., (1961)

42. J.R. Katz, Z. Phys. Chem. A, 125, 321, (1927)

43. J.R. Katz, Trans. Faraday Soc., 32, 77, (1936)

44. G.D. Coumoulos, Proc. Roy. Soc., (London), A182, 166, (1943)

45. Stewart, Phys. Rev., 31, 174, (1928)

46. S. Krimm, J. Phys. Chem., 57, 22, (1953)

47. F. Zernicke, J.A. Prins, Z. Physik, 41, 184, (1927)

48. G.L. Simard, B.E. Warren, J. Am. Chem. Soc., 58, 507, (1936)

49. T. Ino, J. Phys. Soc. Japan, 8, 92, (1953)

50. A. Bjornhaug, O. Ellefsen, B.A. Tonnesen, J. Polymer Sci., 12, 621, (1954)

51. H.G. Kilian, K. Boueke, ibid., 58, 311, (1962)

52. S.M. Wecker, T. Davidson, J.B. Cohen, J. Mat. Sci., 7, 1249, (1972)

53. G.S. Markova, J.K. Ovchinnikov, E.B. Bokhyan, J. Polymer Sci., Part C, 42, 671, (1973)

54. G.D. Wignall, G.W. Longman, J. Mat. Sci., 8, 1439, (1973)

55. G. Natta, P. Corradini, I.W. Bassi, Del Nuovo Cimento, 15, 69, (1960)

56. B.K. Vainshtein, "Diffraction of X-rays by Chain Molecules", Elsevier, (1966)

57. L.E. Alexander, "X-ray Diffraction Methods in Polymer Science", Wiley, (1969)

58. M.E. Milberg, J. Appl. Phys., 29, 64, (1958)

59. F. Hajdu, Acta Cryst., A28, 250, (1972)

60. F. Hajdu, G. Palinkas, J. Appl. Cryst., 5, 395, (1972)

61. J.A. Victoreen, J. Appl. Phys., 20, 1141, (1949)

62. B.E. Warren, R.L. Mozi, Acta Cryst., 21, 459, (1966)

63. C.W. Dwiggins, D.A. Park, ibid., A27, 264, (1971)

64. J. Krogh-Moe, ibid., 9, 951, (1956)

65. N. Norman, ibid., 10, 370, (1957)

66. A. Bienenstock, J. Chem. Phys., 31, 570, (1959)

67. R. Kaplow, S.L. Strong, B.L. Averbach, Phys. Rev., 138, A1336, (1965)

68. G.S. Cargill, J. Appl. Cryst., 4, 277, (1971)

69. D.H. Ender, J. Macromol. Sci., B4, No.3, (1970)

70. E.H. Andrews, G.M. Levy, J. Willis, J. Mat. Sci., 8, 1000, (1973)

71. G. Farrow, I.M. Ward, Polymer, 1, 330, (1960)

72. M.F. Milagin, N.I. Shishkin, Polymer Science USSR, 14, 400, (1972)

73. C.W. Bunn, Proc. Roy. Soc. (London), A180, 67, (1942)

74. H. Tadokoro, Y. Chatani, H. Kusanagi, M. Yokoyama, Macromolecules, 3, 441, (1970)

APPENDIX

APPENDIX A

A Fortran IV Programme to Generate Radial Distribution Functions

This programme was written to operate on the CDC 6400 computer at Imperial College. Part One was used separately to first correct and then normalise the experimental data. Part Two was then attached to perform the required Fourier transformation.

A.1 Part One : Data Correction and Normalisation

Data for the experimental X-ray intensity, scattering factor for hydrogen and for the double scattering function Q are initially read into the programme. The scattering factors for carbon and oxygen are generated using Hajdu's analytic functions as are the Compton intensities (the Compton intensity for hydrogen is neglected).

The experimental intensity is corrected for polarisation and coherent and incoherent absorption. Using the Newton divided-difference polynomial (see section A.3), this corrected intensity is then converted to the $s = (4\pi/\lambda)\sin\theta$ scale by interpolating at equal s intervals of 0.05. The intensity curve is then extrapolated by eye to zero intensity at s = 0. Optimum normalisation is obtained by using both methods described in Chapter III. The Compton intensity profile is adjusted so that the two methods yield normalisation constants which are to within 1% of each other and no peak close to r = 0 is detected in the RDF.

A.2 Part Two : The Fourier Transformation

The radial and cylindrical distribution functions are calculated at r intervals of 0.1Å and displayed in table form. The Numerical integration is performed using Simpson's Rule. The radial functions needed approximately 20 seconds of computer time while the cylindrical functions required upwards of 300 seconds.

A.3 Interpolation with Finite Divided-Differences

Newton's fundamental formula for n^{th}-degree interpolation can be written as

$$f(x) = P_n(x) + R_n(x)$$

where f(x) is the true function, $P_n(x)$ the approximating polynomial and $R_n(x)$ an error or remainder term. The n^{th}-degree divided-difference interpolating polynomial $P_n(x)$ has the form

$$P_n(x) = f\left[x_o\right] + (x - x_o)f\left[x_1, x_o\right] + \dots + (x - x_{n-1})f\left[x_n, x_{n-1}, \dots, x_o\right]$$

where $x_o, x_1, \dots x_n$ are (n + 1) discrete base points and

$$f\left[x_o\right] = f(x_o)$$

$$f\left[x_1, x_o\right] = \frac{f(x_1) - f(x_o)}{x_1 - x_o}$$

$$f\left[x_n, x_{n-1}, \dots x_o\right] = f\left[x_n, x_{n-1}, \dots x_1\right] - f\left[x_{n-1}, x_{n-2}, \dots, x_o\right]$$

are the zero, first, ..., n^{th} order finite divided differences.

The corresponding remainder term $R_n(x)$ is given by

$$R_n(x) = \left[\prod_{i=0}^{n} (x - x_i)\right] f\left[x, x_n, x_{n-1}, \dots x_o\right]$$

A great advantage of this method of interpolating is that the (n + 1) discrete base points need not be equally spaced.

```
C***********************************************************************
C
C
C      .....RADIAL DISTRIBUTION ANALYSIS.....
C
C      .....PART ONE - DATA CORRECTION AND NORMALISATION.....
C
C
C***********************************************************************
      COMMON R(303),RDF1(303),RDF2(303),H(13),FH(401),SH(13),TINC(401)
      COMMON COH(401),BETA(401),CO(401),Q(10),CSCAT(401),FC(401),FO(401)
      COMMON SGFS(401),UC(401),QTTH(10),XTTD(401),SQR(401),TIS(401)
      COMMON X(207),Y(207),CT(228),XTTH(401),TTH(230),OR(207),DMOS(251)
      COMMON SPLOT(401),TCR(401),TABLE(207,12),COMP(401),TPLOT(209)
      COMMON K,DEL,NUM,IEFM(10),U(401),XTTM(251),TOMO(123),DMO(134)
      COMMON TIF(163),SI(163)
C
C
      READ (5,100) (CT(I),I=1,216),(DMO(J),J=1,132),(H(L),L=1,13),
     1  (Q(M),M=1,7),(QTTH(N),N=1,7)
      II=0
      JJ=0
      KK=0
      LL=0
      SH(1)=0.0
      DO 18 I=2,11
   18 SH(I)=SH(I-1)+1.257
C     .....NUMBER OF ATOMIC SPECIES IN MONOMER UNIT.....
      HN=8.0                                                              PS
      CN=8.0                                                              PS
      ON=0.0                                                              PS
      Z=64.0*ON+36.0*CN+HN
      SGZSS=Z**2
      SAVM=HN*1.00797*0.435+CN*12.01115*4.60+ON*15.9994*11.50
      DSC=SGZSS/(SAVM*10000.0)
C     .....TTH-THE SCANNING ANGLE (TWO THETA).....
      TTH(1)=0.0
      TTH(2)=6.0
      DO 53 I=3,90
   53 TTH(I)=TTH(I-1)+0.5
      DO 54 I=91,200
   54 TTH(I)=TTH(I-1)+1.0
C     .....XTTH-THE SCANNING ANGLE CORRESPONDING TO TABULAR S .....
      XTTH(1)=0.0
C     .....SPLOT-S USED FOR PLOTTING.....
      SPLOT(1)=0.0
      DO 59 I=2,341
   59 SPLOT(I)=SPLOT(I-1)+0.05
      A=4.0*3.1416/1.5418
      ASQ=A**2
      B=360.0/3.1416
      DO 55 I=1,161
      SS=SPLOT(I)**2
      ARG=SPLOT(I)/SQRT(ASQ-SS)
   55 XTTH(I)=B*ATAN(ARG)
C***********************************************************************
      A=4.0*3.1416/0.7107
      ASQ=A**2
      B=360.0/3.1416
      DO 11 I=93,341
      SS=SPLOT(I)**2
      ARG=SPLOT(I)/SQRT(ASQ-SS)
      L=I-92
   11 XTTM(L)=B*ATAN(ARG)
      DO 57 I=162,341
      L=I-91
   57 XTTH(I)=XTTM(L)
      DO 58 I=1,341
      SS=SPLOT(I)**2
      ARG=SPLOT(I)/SQRT(ASQ-SS)
   58 XTTD(I)=B*ATAN(ARG)
C***********************************************************************
C     .....POLARISATION AND ABSORPTION CORRECTIONS.....
C***********************************************************************
      RADF=2.0*3.1416/360.0
      TALPHA=26.59
      XX=(COS(TALPHA*RADF))**2
      V=4.4505                                                            PS
      T=0.15
      W1=RADF*17.0/6.0
      W2=RADF*17.0
      CK=0.04852*1.04*(3.0*1.22*(1.5418**2)-4.0*0.0142*(1.5418**3))
      OK=0.04852*1.04*(3.0*3.18*(1.5418**2)-4.0*0.0554*(1.5418**3))
      HK=0.04852*1.04*(3.0*0.0127*(1.5418**2)-4.0*0.00000466*1.5418**3)
      PK=HN*HK+ON*OK+CN*CK
```

```
      CR(1)=0.0
      YY=5.0
      DO 16 I=2,200
      ALF1=SIN(TTH(I)*RADF)/(2.0*V*W1)
      AC1=1.0-ALF1*(1.0-EXP(-(1.0/ALF1)))
      CM=2.0*V+PK*(SIN(TTH(I)*RADF/2.0))**2
      ALF1=SIN(TTH(I)*RADF)/(CM*W1)
      ACM1=1.0-ALF1*(1.0-EXP(-(1.0/ALF1)))
      PC=(1.0+XX*((COS(YY*RADF))**2))/(1.0+XX)
      IF (I.LE.97) YY=YY+0.5
      IF (I.GT.97) YY=YY+1.0
   16 CR(I)=CT(I+7)*AC1/(ACM1*PC)
C*************************************************************************
      DO 2 I=1,341
      SS=(SPLOT(I)/(4.0*3.1416))**2
      FC(I)=1.8563*EXP(-0.4124*SS)+1.5280*EXP(-10.0750*SS)
     1   +0.3173*EXP(-20.3260*SS)+2.3965*EXP(-30.7790*SS)-0.1096
      FO(I)=1.3721*EXP(-0.3870*SS)+2.0624*EXP(-5.5416*SS)
     1   +3.0566*EXP(-12.3320*SS)+1.0743*EXP(-25.6800*SS)+0.4348
    2 CONTINUE
      DO 4 I=1,341
      SSS=SPLOT(I)/(4.0*3.1418)
      CC(I)=(6.0-(FC(I)**2)/6.0)*(1.0-0.4972*(EXP(-1.8438*SSS)
     1   -EXP(-7.8917*SSS)))
      CO(I)=(8.0-(FO(I)**2)/8.0)*(1.0-0.3933*(EXP(-1.2843*SSS)
     1   -EXP(-32.6820*SSS)))
    4 CONTINUE
C*************************************************************************
      IC=0

   13 N=200
      IF (IC.EQ.1) N=7
      IF (IC.EQ.2) GO TO 73
      IF (IC.EQ.3) N=11
C     .....X AND Y ARE THE INTERPOLATION ARRAYS .....
      DO 1 I=1,N
      IF (N.EQ.7) GO TO 5
      IF (N.EQ.11) GO TO 20
      X(I)=TTH(I)
      Y(I)=CR(I)
      GO TO 1
   20 X(I)=SH(I)
      Y(I)=H(I)
      GO TO 1
    5 X(I)=QTTH(I)
      Y(I)=Q(I)
    1 CONTINUE
C*************************************************************************
C     .....COMPUTE AND PRINT DIVIDED DIFFERENCES.....
      M=12
      IF (IC.EQ.1) M=6
      IF (N.EQ.11) M=10
      CALL DTABLE (X,Y,TABLE,N,M,TRUBL,N)
      IF (TRUBL.NE.0.0) CALL EXIT
      NM1=N-1
      DO 6 I=1,NM1
      L=I
      IF (I.GT.M) L=M
    6 CONTINUE
C     .....READ XARG AND IDEG, CALL ON FNEWT TO INTERPOLATE.....
      IF (N.EQ.200) LT=1
       IF (N.EQ.200) MT=161
      IF (N.EQ.7) LT=1
      IF (N.EQ.7) MT=341
      IF (N.EQ.11) LT=1
      IF (N.EQ.11) MT=252
      DO 56 I=LT,MT
      IF (N.EQ.200) XARG=XTTH(I)
      IF (N.EQ.7) XARG=XTTQ(I)
      IF (N.EQ.11) XARG=SPLOT(I)
      IDEG=6
      IF (I.GE.72) IDEG=1
      IF (IC.GE.1) IDEG=3
      YINTER=FNEWT(X,Y,TABLE,N,M,IDEG,XARG,TRUBL,N)
      II=II+1
      IF (N.EQ.7) JJ=JJ+1
       IF(N.EQ.200) TCR(II)=YINTER
C     .....DSCAT-DOUBLE SCATTERING INTENSITY.....
      IF (N.EQ.7) DSCAT(JJ)=YINTER*DSC
      IF (N.EQ.11) LL=LL+1
      IF (N.EQ.11) FH(LL) = YINTER
   56 CONTINUE
C
   73 IC=IC+1
      IF (IC.LE.3) GO TO 13
```

```
C*************************************************************************
C     .....SGFS-SIGMA F-SQUARED CALCULATED FROM ANALYTIC FITTING.....
C     .....COMP-COMPTON SCATTERING CALCULATED FROM ANALYTIC FITTING.....
C*************************************************************************
      DO 3 I=1,341
      COMP(I)=CN*CC(I)+ON*CO(I)
      IF (I.LE.252) SGFS(I)=CN*(FC(I)**2)+ON*(FO(I)**2)+HN*(FH(I)**2)
      IF (I.GT.250) SGFS(I)=CN*(FC(I)**2)+ON*(FO(I)**2)
    3 CONTINUE
      TCR(1)=0.0
      TCR(2)=500.0
      TCR(3)=1500.0
      TCR(4)=3500.0
      TCR(5)=6000.0
      TCR(6)=8000.0
      TCR(7)=12000.0
      TCR(8)=16500.0
      TCR(9)=21300.0
      TCR(10)=27000.0
C*************************************************************************
C
C
C     .....NORMALISATION.....
C
C*************************************************************************
      GC=0.75
      XMA=0.024
      XMB=0.4
      XMC=0.2
      GD=1.0
C     .....METHOD ONE-BETA=THEORETICAL/EXPERIMENTAL INTENSITY.....
      TFAC=0.0
      BETA(1)=0.0
      TINC(1)=0.0
      DO 70 I=2,161
      IF (I.LE.109) PER=1.0-XMA*SPLOT(I)
      IF (I.EQ.109) PPER=PER
      IF (I.GT.109) PER=PPER-XMB*(SPLOT(I)-SPLOT(109))
      IF (I.EQ.140) PPER=PER
      IF (I.GT.140) PER=PPER-XMC*(SPLOT(I)-SPLOT(140))
      TINC(I)=GC*COMP(I)*PER
   70 BETA(I)=(SGFS(I)+TINC(I)+GD*DSCAT(I))/TCR(I)
C     .....METHOD TWO-KROGH-MOE EQUATION.....
      MM=1
      DO 21 I=MM,161
      SS=SPLOT(I)**2
      L=I-MM+1
   21 U(L)=SS*TCR(I)*EXP(-TFAC*SS).
      K=1
      NUM=162-MM
      DEL=0.05/3.0
      CALL SIMP
      DO 22 I=MM,161
      SS=SPLOT(I)**2
      L=I-MM+1
      TTS(I)=SGFS(I)+TINC(I)+GD*DSCAT(I)
   22 U(L)=SS*TTS(I)
      K=2
      NUM=162-MM
      DEL=0.05/3.0
      CALL SIMP
      RHO=0.0
      XMK=(TERM(2)-2.0*RHO*(3.1416**2)*Z)/TERM(1)
      DO 15 I=1,161
   15 SCR(I)=TCR(I)*XMK
C     .....COH- THE COHERENT INTENSITY.....
      DO 23 I=1,161
   23 COH(I)=SCR(I)-TINC(I)-GD*DSCAT(I)
C*************************************************************************
C     .....THE INTERFERENCE FUNCTION.....
C*************************************************************************
      DO 24 I=1,161
      TIF(I)=SCR(I)-TTS(I)
   24 ST(I)=SPLOT(I)*TIF(I)
      WRITE (6,3000) GC
      DO 60 I=1,161
      WRITE (6,101) SPLOT(I),XTTH(I),TTS(I),SCR(I),TIF(I),ST(I),
     1     BETA(I),TINC(I)
   60 CONTINUE
      WRITE (6,5000) XMK
```

```
C***********************************************************************
C
C       ..... PART TWO - THE FOURIER TRANSFORMATION .....
C
C***********************************************************************
      R(1)=0.0
      DO 8 I=2,301
    8 R(I)=R(I-1)+0.1
      DO 25 I=1,301
      DO 26 J=1,161
   26 U(J)=SI(J)*SIN(R(I)*SPLOT(J))
      K=3
      NUM=161
      DEL=0.05/3.0
      CALL SIMP
      RDF1(I)=TERM(3)*2.0/3.1416
   25 RDF2(I)=R(I)*RDF1(I)
      DO 61 I=1,151
      WRITE(6,102) R(I),RDF1(I),RDF2(I),R(I+150),RDF1(I+150),RDF2(I+150)
   61 CONTINUE
  102 FORMAT (1H ,6F20.3)
C***********************************************************************
C       ..... FORMATS FOR INPUT AND OUTPUT STATEMENTS.....
  100 FORMAT (18(12F6.0/),11(12F6.0/),13F6.3/7F7.2/7F7.2/)
 3000 FORMAT (1H1,5HG0 = ,F8.4)
  101 FORMAT (1H ,2F7.2,4F12.3,F12.6,F12.3)
 5000 FORMAT (1H ,19HKROGH-MOE FACTOR = , F12.6)
      STOP
      END
```

```
      SUBROUTINE SIMP
C
      COMMON R(303),RDF1(303),RDF2(303),H(13),FH(401),SH(13),TINC(401)
      COMMON GOH(401),BETA(401),CO(401),Q(10),DSCAT(401),FC(401),FO(401)
      COMMON SCFS(401),GG(401),DTTH(10),XTTO(401),SUR(401),TTS(401)
      COMMON X(207),Y(207),CT(228),XTTH(401),TTH(230),CR(209),OMUS(251)
      COMMON SPLOT(401),TCF(401),TABLE(207,12),COMP(401),TPLOT(20?)
      COMMON K,DEL,NUM,TERM(10),U(401),XTTM(251),TDMO(123),DMO(134)
      COMMON TIF(163),SI(163)
      UE=0.0
      UO=0.0
      NUM1=NUM-1
      DO 30 J=2,NUM1
      RJ=J
      RJH=RJ/2.0
      JH=J/2
      XJH=JH
      IF (XJH.NE.RJH) GO TO 32
      UE=UE+U(J)
      GO TO 30
   32 UO=UO+U(J)
   30 CONTINUE
      TERM(K)=(U(1)+U(NUM)+4.0*UE+2.0 UO)*DEL
      RETURN
      END
```

```
      SUBROUTINE DTABLE (X,Y,TABLE,N,M,TRUBL,K)
C
C     DTABLE COMPUTES THE FINITE DIVIDED DIFFERENCES OF Y(1)...Y(N) FOR
C     ALL ORDERS M OR LESS AND STORES THEM IN THE LOWER TRIANGULAR
C     PORTION OF THE FIRST M COLUMNS OF THE FIRST N-1 ROWS OF THE MATRIX
C     TABLE. FOR INCONSISTENT ARGUMENTS, TRUBL=1.0 ON EXIT. OTHERWISE,
C     TRUBL=0.0 ON EXIT.
      DIMENSION X(N), Y(N), TABLE(K,K)
C
C     .....CHECK FOR ARGUMENT CONSISTENCY.....
      IF (M.LT.N) GO TO 2
      TRUBL=1.0
      RETURN
C
C     .....CALCULATE FIRST ORDER DIFFERENCES.....
    2 NM1=N-1
      DO 3 I=1,NM1
    3 TABLE(I,1)=(Y(I+1)-Y(I))/(X(I+1)-X(I))
      IF (M.LE.1) GO TO 6
C
C     .....CALCULATE HIGHER ORDER DIFFERENCES.....
      DO 6 J=2,M
      DO 5 I=J,NM1
      ISUB=I+1-J
    5 TABLE(I,J)=(TABLE(I,J-1)-TABLE(I-1,J-1))/(X(I+1)-X(ISUB))
C
    6 TRUBL=0.0
      RETURN
      END
```

```
      FUNCTION FNEWT (X,Y,TABLE,N,M,IDEG,XARG,TRUBL,K)
C
C     FNEWT ASSUMES THAT X(1)...X(N) ARE IN ASCENDING ORDER AND FIRST
C     SCANS THAT X VECTOR TO DETERMINE WHICH ELEMENT IS NEAREST (.GE.)
C     THE INTERPOLATION ARGUMENT, XARG. THE IDEG+1 BASE POINTS NEEDED
C     FOR THE EVALUATION OF THE DIVIDED DIFFERENCE POLYNOMIAL OF DEGREE
C     IDEG+1 ARE THEN CENTRED ABOUT THE CHOSEN ELEMENT WITH THE LARGEST
C     HAVING THE SUBSCRIPT MAX. IT IS ASSUMED THAT THE FIRST M DIVIDED
C     DIFFERENCES HAVE BEEN COMPUTED BY THE SUBROUTINE DTABLE AND ARE
C     ALREADY IN THE MATRIX TABLE. MAX IS CHECKED TO INSURE THAT ALL
C     REQUIRED BASE POINTS ARE AVAILABLE, AND THE INTERPOLANT VALUE IS
C     COMPUTED USING NESTED POLYNOMIAL EVALUATION. THE INTERPOLANT IS
C     RETURNED AS THE VALUE OF THE FUNCTION .  FOR INCONSISTENT ARGUMENTS
C     TRUBL=1.0 ON EXIT. OTHERWISE, TRUBL=0.0 ON EXIT.
      DIMENSION X(N),Y(N),TABLE(K,K)
C
C     .....CHECK FOR ARGUMENT INCONSISTENCY.....
      IF (IDEG.LE.M) GO TO 2
      TRUBL=1.0
      FNEWT=0.0
      RETURN
C
C     .....SEARCH X VECTOR FOR ELEMENT .GE. XARG.....
    2 DO 4 I=1,N
    4 IF (I.EQ.N.OR.XARG.LE.X(I)) GO TO 5
    5 MAX=I+IDEG/2
C
C     .....INSURE THAT ALL REQUIRED DIFFERENCES ARE IN TABLE.....
      IF (MAX.LE.IDEG) MAX=IDEG+1
      IF (MAX.GT.N) MAX=N
C
C     .....COMPUTE INTERPOLANT VALUE.....
      YEST=TABLE(MAX-1,IDEG)
      IF (IDEG.LE.1) GO TO 13
      IDEGM1=IDEG-1
      DO 12 I=1,IDEGM1
      ISUB1=MAX-I
      ISUB2=IDEG-I
   12 YEST=YEST*(XARG-X(ISUB1))+TABLE(ISUB1-1,ISUB2)
   13 ISUB1=MAX-IDEG
      TRUBL=0.0
      FNEWT=YEST*(XARG-X(ISUB1))+Y(ISUB1)
      RETURN
C
      END
```

A.5 Index of Array and Variable Names

AC1	Coherent absorption correction
ACM1	Incoherent absorption correction
BETA	First normalisation parameter $\beta_i = (\sum f^2 + I_{inc})/ I_{expt}$
CC	Compton scattering intensity for independent C atom
CK	$q = 0.04852\rho(3C\lambda^2 - 4D\lambda^3)$ for C atom
CM	$2\mu + \Delta\mu$
CN	Number of C atoms in the monomer unit
CO	Compton scattering intensity for independent O atom
COH	Coherently diffracted intensity I_{coh}
COMP	Compton intensity for the unit of composition
CR	Experimental intensity corrected for absorption and polarisation (2θ scale)
CT	Uncorrected experimental intensity (input data)
DEL	h/3 where h is the interval used in Simpson's method of numerical integration
DSC	$(\sum z_j^2)/ (\sum A_j u_j\{m\})$ for double scattering equation
DSCAT	Double scattering intensity
DTABLE	Subprogramme to compute finite divided-differences
FC	Atomic scattering factor for C atom
FH	Atomic scattering factor for H atom
FNEWT	Subprogramme to determine the interpolant value YINTER
FO	Atomic scattering factor for O atom
GC	Fraction of theoretical Compton intensity used to obtain best normalisation
H	Atomic scattering factor for H atom (input data)
HK	$q = 0.04852\rho(3C\lambda^2 - 4D\lambda^3)$ for H atom
HN	Number of H atoms in the monomer unit

IDEG	Degree of the divided-difference interpolating polynomial
M	Order of the divided-differences of TABLE
MI	Parameter used to approximate TINC
N	Number of elements in the array to be interpolated
NI	Parameter used to approximate TINC
OK	$q = 0.04852\rho(3C\lambda^2 - 4D\lambda^3)$ for O atom
ON	Number of O atoms in the monomer unit
PC	Polarisation correction
PK	q parameter for the unit of composition
Q	$Q(b,q,\theta,\mu t)$ Double scattering function data
QTTH	2θ for input values of Q
R	Radial distance in Angstroms
RADF	Degrees/radians conversion factor
RDF1	Reduced radial distribution function
RDF2	Reduced radial density function
RHO	Macroscopic sample density
SCR	Normalised experimental intensity corrected for absorption and polarisation
SGFS	$\sum f_j^2$ for the unit of composition
SH	s for input values of H
SIMP	Subprogramme to perform numerical integration by Simpson's Rule
SPLOT	$s = \frac{4\pi}{\lambda}\sin\theta$
ST	$s(I - \sum f^2)$
T	Specimen thickness
TABLE	Finite divided-difference table
TALPHA	$2\theta_M$ where θ_M is the Bragg angle of the monochromator
TCR	Experimental intensity corrected for polarisation and absorption (s scale)

TERM	Simpson's formula
TIF	Interference function $I - \sum f^2$
TINC	Compton intensity corrected for monochromator cut off
TTH	Diffraction angle 2Θ
TTS	$\sum f^2 + I_{d.s.} + I_{comp}$
U	General function used in subroutine SIMP
V	Linear absorption coefficient μ
W1	Beam height (A) at sample (for $\frac{1}{6}^{\circ}$ divergence slit)
W2	Beam height (A) at sample (for 1° divergence slit)
X	General function used in DTABLE and FNEWT
XARG	Interpolation argument
XMA	Parameter used to approximate TINC
XMB	Parameter used to approximate TINC
XMC	Parameter used to approximate TINC
XMK	Second Normalisation Parameter (Krogh-Moe)
XTTH	s values corresponding to TTH values
Y	General function used in DTABLE and FNEWT
YINTER	Interpolated value
Z	$\sum Z_j^2$ for the unit of composition